RICE UNIVERSITY

Seismic response control of structures using novel adaptive passive and semi-active variable stiffness and negative stiffness devices

by

Dharma Theja Reddy Pasala

A Thesis Submitted
in Partial Fulfillment of the
Requirements for the Degree
Doctor of Philosophy

Approved, Thesis Committee:

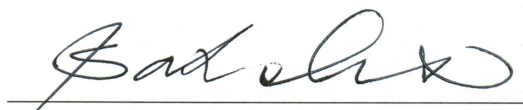

Satish Nagarajaiah, Chair
Professor of Civil and Environmental
Engineering and Mechanical Engineering
and Material Science

Jamie E. Padgett
Assistant Professor of Civil and
Environmental Engineering

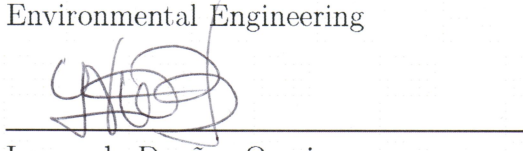

Leonardo Dueñas-Osorio
Assistant Professor of Civil and
Environmental Engineering

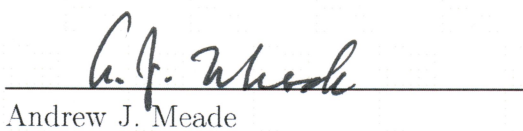

Andrew J. Meade
Professor of Mechanical Engineering and
Material Science

Houston, Texas
August, 2012

ABSTRACT

Seismic response control of structures using novel adaptive passive and semi-active variable stiffness and negative stiffness devices

by

Dharma Theja Reddy Pasala

Current seismic design practice promotes inelastic response in order to reduce the design forces. By allowing the structure to yield while increasing the ductility of the structure, the global forces can be kept within the limited bounds dictated by the yield strength. However, during severe earthquakes, the structures undergo significant inelastic deformations leading to stiffness and strength degradation, increased interstory drifts, and damage with residual drift. The research presented in this thesis has three components that seek to address these challenges.

To prevent the inelastic effects observed in yielding systems, a new concept "apparent weakening" is proposed and verified through shake table studies in this thesis. "Apparent weakening" is introduced in the structural system using a complementary "adaptive negative stiffness device" (NSD) that mimics "yielding" of the global system thus attracting it away from the main structural system. Unlike the concept of weakening and damping, where the main structural system strength is reduced, the new system does not alter the original structural system, but produces effects compatible with an early yielding. Response reduction using NSD is achieved in a two step sequence. First the NSD, which is capable of exhibiting nonlinear elastic stiffness, is developed based on the properties of the structure. This NSD is added

to the structure resulting in reduction of the stiffness of the structure and NSD assembly or "apparent weakening"-thereby resulting in the reduction of the base shear of the assembly. Then a passive damper, designed for the assembly to reduce the displacements that are caused due to the "apparent weakening", is added to the structure-thereby reducing the base shear, acceleration and displacement in a two step process.

The primary focus of this thesis is to analyze and experimentally verify the response reduction attributes of NSD in (a) elastic structural systems (b) yielding systems and (3) multistory structures. Experimental studies on 1:3 scale three-story frame structure have confirmed that consistent reductions in displacements, accelerations and base shear can be achieved in an elastic structure and bilinear inelastic structure by adding the NSD and viscous fluid damper. It has also been demonstrated that the stiffening in NSD will prevent the structure from collapsing. Analogous to the inelastic design, the acceleration and base shear and deformation of the structure and NSD assembly can be reduced by more than 20% for moderate ground motions and the collapse of structure can be prevented for severe ground motions.

Simulation studies have been carried on an inelastic multistoried shear building to demonstrate the effectiveness of placing NSDs and dampers at multiple locations along the height of the building; referred to as "distributed isolation". The results reported in this study have demonstrated that by placing a NSD in a particular story the superstructure above that story can be isolated from the effects of ground motion. Since the NSDs in the bottom floors will undergo large deformations, a generalized scheme to incorporate NSDs with different force deformation behavior in each storey is proposed. The properties of NSD are varied to minimize the localized inter-story deformation and distribute it evenly along the height of the building. Additionally, two semi-active approaches have also been proposed to improve the performance of NSD in yielding structures and also adapt to varying structure properties in real time.

The second component of this thesis deals with development of a novel device

to control the response of structural system using adaptive length pendulum smart tuned mass damper (ALP-STMD). A mechanism to achieve the variable pendulum length is developed using shape memory alloy wire actuator. ALP-STMD acts as a vibration absorber and since the length is tuned to match the instantaneous frequency, using a STFT algorithm, all the vibrations pertaining to the dominant frequency are absorbed. ALP-STMD is capable of absorbing all the energy pertaining to the tuned-frequency of the system; the performance is experimentally verified for forced vibration (stationary and non-stationary) and free vibration.

The third component of this thesis covers the development of an adaptive control algorithm to compensate hysteresis in hysteretic systems. Hysteretic system with variable stiffness hysteresis is represented as a quasi-linear parameter varying (LPV) system and a gain scheduled controller is designed for the quasi-LPV system using linear matrix inequalities approach. Designed controller is scheduled based on two parameters: linear time-varying stiffness (slow varying parameter) and the stiffness of friction hysteresis (fast varying parameter). The effectiveness of the proposed controller is demonstrated through numerical studies by comparing the proposed controller with fixed robust $\mathcal{H}_\infty$ controller. Superior tracking performance of the LPV-GS over the robust $\mathcal{H}_\infty$ controller in different displacement ranges and various stiffness switching cases is clearly evident from the results presented in this thesis. The LPV-GS controller is capable of adapting to the parameter changes and is effective over the entire range of parameter variations.

Contents

Illustrations

Tables

Acknowledgments

First and foremost, I would like to thank my advisor Dr. Satish Nagarajaiah for his motivation, unwavering support, encouragement and guidance. Without his invaluable ideas, suggestions and insight this work would not have been possible.

I thank Dr. Andrei Reinhorn, Dr. Michael Constantinou and Mr. Apostolos Sarlis for all the help, guidance in the experimental testing at the University at Buffalo-SUNY and also making my stay memorable in Buffalo. I extend my thanks to Dr. Jamie Padgett, Dr. Leonardo Dueñas-Osorio and Dr. Andrew Meade for serving on my committee and Dr. Angelo Miele for his advices and inspiration.

I thank all my friends, group members and fellow graduate students for their help and friendship. Finally, I thank my wife, mom and dad for their love, encouragement and relentless support. It is to them I dedicate this thesis.

This research is supported by National Science Foundation, No. NSF-CMMI-0601672 and NSF-CMMI-0830391. This support is gratefully acknowledged.

Chapter 1

Introduction

Experience from the past demonstrated that the earthquakes have a tremendous socioeconomic impact, a huge loss of life and property damage on the endured communities. The recent, Haiti earthquake that occurred on January 12, 2010 resulted in an estimated death toll of 316,000 and property damage of about 14 billion dollars [1]. In the 21st century, the worldwide death toll due to earthquakes is over 815,000 and the property damage is about 150 billion dollars [1]. The damage due to the earthquake disasters cannot be completely avoided but the effects can be significantly subdued by exercising the proper design practices. The field of earthquake engineering has stemmed to tackle the issues involved in seismic resistant structural design. The objective of earthquake engineering is to design, construct and maintain structures to perform during earthquakes.

Designing structures to withstand seismic loads has been well-explored in the structural design community since the 1920s [2]. Based on the experiences from past earthquakes, shake-table tests and analytical studies several specification and guidelines have been incorporated in the design codes. The philosophy of earthquake design for structures, as used in the design codes, is to minimize the structural damage for moderate ground motions and to avoid collapse or serious damage in strong ground motions. In other words, the building should survive a rare, very severe earthquake by sustaining significant damage without collapsing and it should remain safe and serviceable for more frequent, but less severe earthquakes. This is achieved by inelastic

design of structures.

Inelastic design of structures is the standard practice used by the engineers for seismic loads. By increasing the ductility of the structure and allowing the structure to yield, the global forces can be kept within the limited bounds dictated by the yield strength [3]. However, during severe earthquakes, the structures undergo significant inelastic deformations leading to stiffness and strength degradation, increased inter-story drifts, and damage with residual drift. Although the structures do not collapse, they will not be serviceable due to the large residual drifts. These inelastic effects can be reduced significantly by using control devices.

The use of control devices in structural engineering to mitigate the structural response dates back to 1960 [4]. The structural control approaches used in the early stages (vibration isolation, vibrations absorption and vibration damping) were adopted from the aircraft and automobile industry. Structural control is classified into four categories based on the devices used for control: (1) Passive control (2) Active control (3) Semi-active control and (4) Hybrid control.

Despite the progress in advancing the field of structural control for the past five decades there is still a need to develop new devices to overcome the limitations of the existing approaches. The research carried in this thesis attempts to bridge this gap. In this chapter, all the four control approaches are discussed in brief. This chapter also contains a review on all the existing control devices, their advantages and limitations. Towards the end of the chapter, the advantages of the novel devices proposed in this study over the existing devices are discussed in detail.

1.1 Passive Control of Structural Systems

Passive structural control strategies offer very reliable means to protect structures during extreme loading conditions. The simplicity, low-cost and ease of installation makes these devices most widely accepted method to mitigate seismic loads. A passive control system does not require an external power source. The forces exerted by these devices are developed in response to the motion of the structure [5]. Passive control strategies include base isolation, supplemental damping and vibration absorption. Each of the passive control strategies are detailed below

1.1.1 Base isolation

Base isolation, also referred as seismic isolation, is one of the most popular means of mitigating the seismic loads on a structural system [6]. The basic philosophy of base isolation to decouple the superstructure from its substructure (foundation) using isolators. Isolators are very flexible compared to the superstructure. Since the isolators form the intermediate layer between the ground and superstructure, all the energy transmitted from the ground during an earthquake accumulates at the isolation level thus protecting the structure's integrity. Essentially, isolators act as a low pass filter, filtering all the high frequency content in the ground motion [4]. As a result, the natural frequency of the isolator and superstructure assembly can be shifted to the lower frequency to avoid resonance at the dominant frequency of earthquakes. According to the recent statistics, in the United States there are about 125 seismically isolated buildings, in Japan there are more than 13000 buildings and bridges, in China there are several hundred buildings isolated buildings [7]. Excellent review articles of base-isolation systems are presented by Kelly [8, 9], Buckle and Mayes [10], and Soong and Constantinou [11].

Several isolators have been used in the literature over the past five decades and they are classified into shear type and sliding type based on their mode of operation. Lead-rubber bearing, invented by Robinson in 1974 [12], is an example for the shear type isolation system. Lead-rubber bearings bearing consists of alternating horizontal layers of rubber and reinforcing steel shims and the inner core of the bearing has lead plug. Rubber provides the lateral flexibility, steel provides the vertical stiffness and the lead-plug at the center dissipates energy. The lead-rubber bearings without the lead-plug in the center is called an elastomeric bearing [13, 14, 15, 16]. Picture of elastomeric bearing is shown in Figure 1.1(left)

Typical sliding bearings have either a spherical or a flat sliding surface. The spherical sliding surface, invented by Takayoshi and Kotaro [17], utilizes the spherical surface and is the most widely used seismic isolation bearing employed within the United States. In isolation applications, the sliding surface is placed concave down to minimize the possibility of debris collecting on the sliding surface [18]. Zayas et al. [19] developed another type of sliding isolation system called the friction pendulum (FP) system. The desired period of the FP bearing is achieved by choosing the appropriate radius of curvature of the concave surface and the desired damping is achieved by choosing the appropriate friction coefficient. The bearings period, vertical load capacity, damping, displacement capacity, and tension capacity, can all be selected independently [19]. Fenz and Constantinou [20] developed triple friction pendulum isolation system by creating two additional sliding surfaces. In the triple pendulum bearing, three effective radii and three friction coefficients are selected to optimize performance for different strengths and frequencies of earthquake shaking. This allows for maximum design flexibility to accommodate both moderate and extreme motions, including near-fault pulses [21]. Picture of triple friction pendulum bearing

and schematic of cross section is shown in Figure 1.1(right). Researchers have carried experimental studies to study the performance of base-isolated structures subjected to ground motion in two perpendicular directions and also allowing structural uplift [16, 22]. Base isolation is not suitable in regions with soft-soil. Since, the ground motion in soft soils have long periods isolating the base-isolation might amplify the response of superstructure. Also, the excessive deformations at the isolation level for very strong ground motions damage the piping and other installations limits the usage of base-isolation.

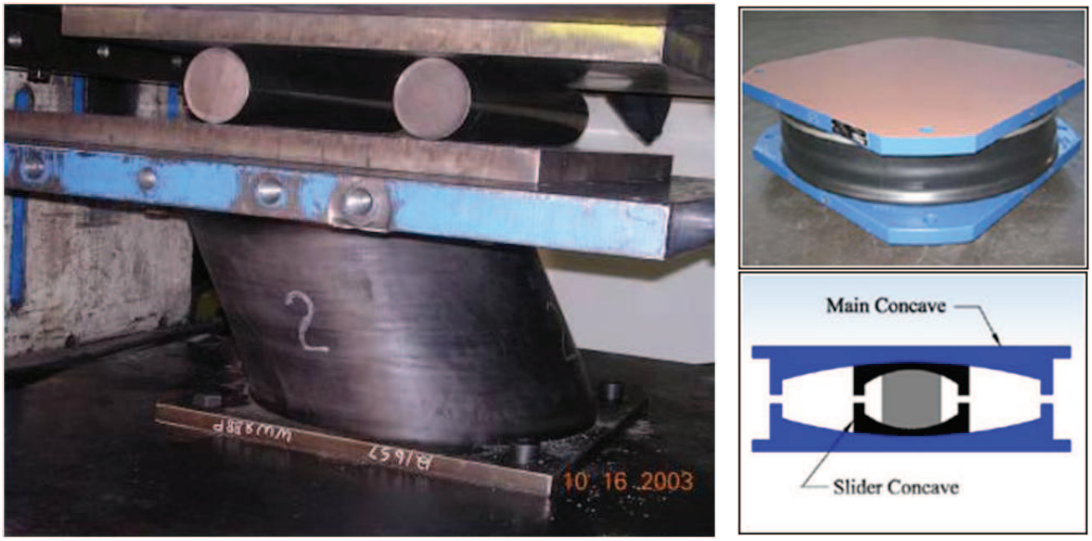

Figure 1.1 : *Left*: Elastomeric bearing. *Right*: Triple friction pendulum bearing.[Courtesy: www.nees.buffalo.edu and Earthquake Protective Systems]

1.1.2 Supplemental damping devices

Energy transferred to the structure from the ground motion constitute strain energy and a small amount of this energy is dissipated due to inherent damping. The inherent damping of the structure comprises of internal stressing, rubbing, cracking and plastic

deformations. Larger the energy dissipation capacity, smaller the strain energy and consequently the amplitudes of vibration will also be reduced. The inherent damping in the structures is very low, generally on the order of 1% of critical damping for steel structures. So the structures undergo large amplitudes of vibration even for moderate earthquakes. By adding the additional devices that dissipate energy, the energy dissipation capacity of the damper and structure assembly increases and as a result the amplitudes of vibration reduces.

Several energy dissipating devices have been proposed and experimentally tested in the past three decades [23]. In general, all the energy dissipating devices are capable of enhancing the energy dissipation in the structural systems in which they are installed. This may be achieved by conversion of kinetic energy to one or more of the following forms: heat, frictional sliding, yielding of metals, phase transformation in metals and deformation of viscoelastic solids or fluids [24]. List of some of the passive damping devices are enumerated next.

Metallic yield dampers

Metallic yield dampers are also referred as hysteretic dampers [25]. The underlying principle of yield-dampers is to capitalize the inelastic deformation of metals to dissipate the energy input to the structure from an earthquake. The idea of utilizing added metallic energy dissipators was first started by the researchers in Newzealand, Kelly et al. [26] and Skinner et al. [25]. Experimental studies on the scaled prototype structure reasserted the effectiveness and energy dissipating capabilities of the the metallic yield dampers [25, 26]. Some of the devices proposed as yield dampers that can yield in torsion, flexure and shear are listed below. The geometric configuration of all the dampers is different but the underlying dissipative mechanism in all

cases is due to inelastic deformation of the metallic elements.

- *Flexural beams*: Flexural-beam damper has a simple cantilever beam of square or circular cross-section designed to operate in direction perpendicular to the beam axis as shown in Figure 1.2(A). So, these dampers are idle to provide damping force at the isolation level (flexibly supported base). The damping force is applied through a link that can accommodate some relative rotation and vertical motion of the beam end.

- *Torsional beams*: These are hysteretic dampers with square or rectangular cross-section and the beams yield in torsion and flexure, with torsion predominating. The beams are designed such that the desired damping is achieved for the design ground motion. These dampers can be installed at the base of the structure where there is large translation as well as uplift. Typical torsional beam is shown in Figure 1.2(B).

- *Flexural plate*: Flexural-plate dampers are special type flexural-beam dampers. These dampers utilize a wider beam to provides a large capacity for loading along a single axis. Two or more pairs of flexural-plate dampers may be combined to form a compact damper as shown in Figure 1.2(C). This damper is suitable for use as a diagonal element in a flexible structural frame.

- *U-strips*: In U-strip dampers, two U-shaped steel strips are rolled between three surfaces in parallel relative motion as shown in Figure 1.2(D). The beam is comparatively flexible in the elastic range and it can exercise large displacements in the inelastic range.

- *Lead and shape-memory-alloy devices*: Lead and shape-memory alloys exhibit

consistent and stable hysteretic behavior, low-cycle fatigue property and long-term reliability. The desirable properties of these materials can be harnessed by making the dampers out of these materials. Sakurai et al. [27], Aiken and Kelly [28] carried numerous analytical and experimental studies to characterize the energy dissipation characteristics of these dampers.

- *X-shaped plate*: X-shaped plate damper also called as added damping and stiffness (ADAS) device is shown in Figure 1.2(E,F). Force-displacement behavior of an ADAS device under constant amplitude displacement controlled cycles has been examined by Whittaker et al. [29]. ADAS consists of multiple X-steel plates as shown in Figure 1.2(E,F) and they are installed in the structure using a chevron connection. The steel plates are chosen in triangular or hourglass shapes so that yielding is spread almost uniformly throughout the material. This is achieved by using the rigid boundary members so that the X-plates are deformed in double curvature. The performance of ADAS is tested on a three story ductile moment resisting frame. Whittaker et al. [29] reported the results of component testing of the ADAS elements that demonstrate the stable hysteresis for a large number of yielding cycles. They also demonstrated that the addition of the ADAS system to the structure limits the frame's response to acceptable levels during severe earthquakes.

- *Triangular plate*: Triangular-plate yielding damper is also referred as triangular added damping and stiffness device (TADAS). TADAS was developed by Tsai et al. [30]; TADAS is obtained by welding triangular plates on ADAS. Tsai et al., demonstrated through experimental studies that a properly welded steel triangular-plate added damping and stiffness device can sustain a large number

of yielding reversals without any stiffness or strength degradation compared to ADAS. They also studied the performance of TADAS at different stiffness ratios of the TADAS element stiffness and the bare frame, and the different ratios of the frame yield strength to the TADAS yield strength.

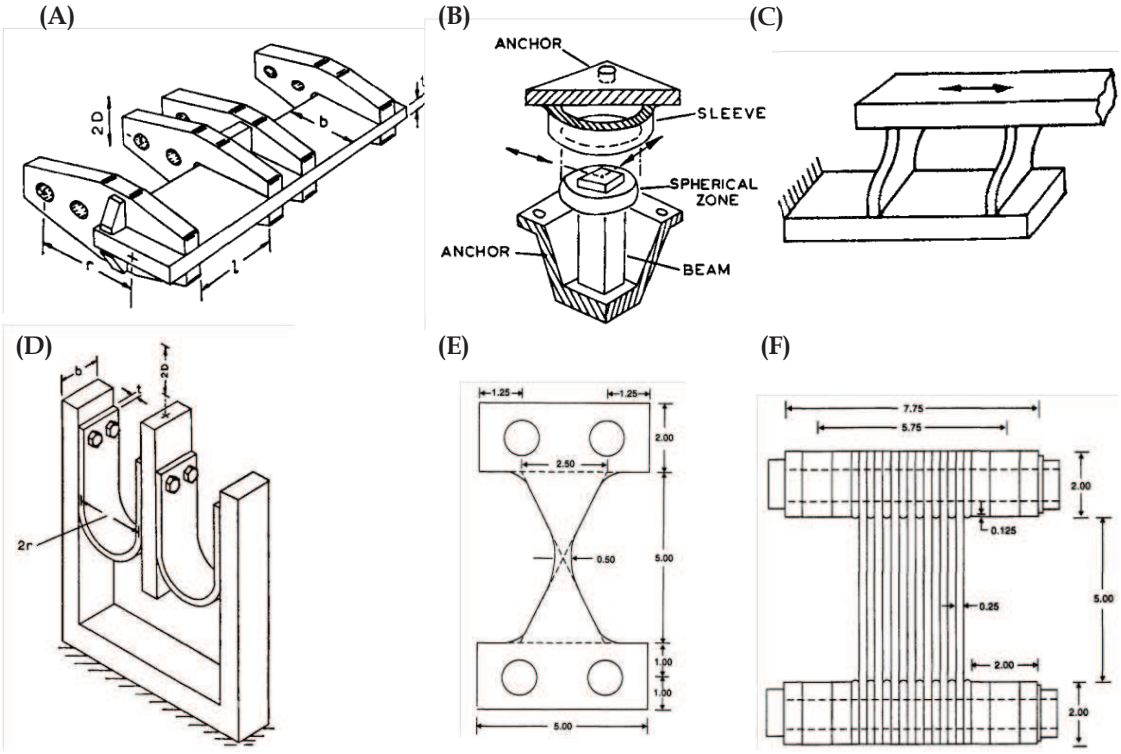

Figure 1.2 : Schematic diagrams of metallic-yield-dampers A: Flexural beams; B: Torsional beams; C: Flexural plate; D: U-strip; E: Cross-section of ADAS; F: ADAS device [Courtsey: Skinner et al. [25], Housner et al. [4]]

Although metallic-yield dampers are simple in principle and expected to be efficient in dissipating energy, there are some issues that hinders the usage of metallic dampers. 1) The choice of appropriate yield displacement for the damper is a critical step. Since these devices start dissipating energy only after yielding, if the yield level is too low then the damper yields even for mild ground perturbations and if the level

is too high then there is a possibility of structural and non-structural damage before the damper engages. 2) Since the damper is connected in parallel to the moment resisting elements of the structure, after an earthquake, any permeant displacement in the damper will result in exerting residual force on the structure. 3) Since the structure is subjected to repeated loading beyond the yield point, the stability of hysteresis loops is a concern. 4) If the displacements are excessive then there is a chance of premature fatigue failure in the yielding elements of the damper.

Friction dampers

Friction is an effective way for dissipate energy and it is one of the most widely accepted form of energy dissipation. As described previously, even in the sliding bearing isolation system friction between the surfaces will result in energy dissipation. In structural engineering, a wide variety of devices have been developed since early 1980s [31]. All the friction dampers differ in the mechanical complexity and the type of sliding materials used as the sliding surface. The coulomb friction has a rectangular hysteresis loop and the structure experiences a sudden jump in the force when the velocity changes its sign; referred as stick-slip phenomenon. It is important that stick-slip phenomena has to be avoided to prevent high frequency excitation. Furthermore, the materials used for the slipping surface should exhibit a consistent coefficient of friction over the intended life of the device.

The Pall device [32] is one of the earliest device used as a passive friction dissipating element. Typically, the Pall friction dampers are installed at the junctions of the cross-braces of the building. The configuration to install the Pall device is shown in Figure 1.3(left). For moderate earthquakes, the friction pads do not slip, and the friction damper acts as an ordinary bracing to stiffen the building. For a

strong earthquake, the force transferred from the ground motion is sufficient for the friction pads to slip, and thus, converting kinetic energy into heat. The effectiveness of these Pall friction dampers is experimentally validated through shake table studies by Filiatrault and Cherry [33].

Sumitomo metal industries of Japan developed a friction damper, commonly referred as Sumitomo friction damper in the literature for railway applications [34]. Figure 1.3(right) shows the schematic cross-section of a typical Sumitomo friction damper and also the configuration of damper in a structure. In Figure 1.3(right) dampers are placed parallel to the floor beams, with one of their ends attached to a floor beam above and the other end attached to a chevron brace arrangement which was attached to the floor beam below. The chevron braces are stiff and the damper is connected to the chevron brace through a swivel connection. The device consists of copper pads impregnated with graphite in contact with the steel casing of the device. The load on the contact surface is developed by a series of wedges which act under the compression of belleville washer springs [35]. Aiken et al. [36] verified the performance of Sumitomo damper experimentally on a 9-storey model structure through shake table studies.

Fitzgerald et al. [37] developed slotted bolted connection (SBC) energy dissipator. Energy dissipation in SBC dissipator is achieved by friction resistance in slotted bolted connections. Laboratory tests proved that the device is capable of reducing the displacement of structure and because of the low cost it has huge potential to be a viable alternative for energy dissipation in seismic design and retrofit applications. Experiment results also confirmed that SBC devices provide consistent performance for different loading amplitudes, frequencies, and even the number of loading cycles. Li and Reinhorn [38] developed the Tekton friction damper. The Tekton friction

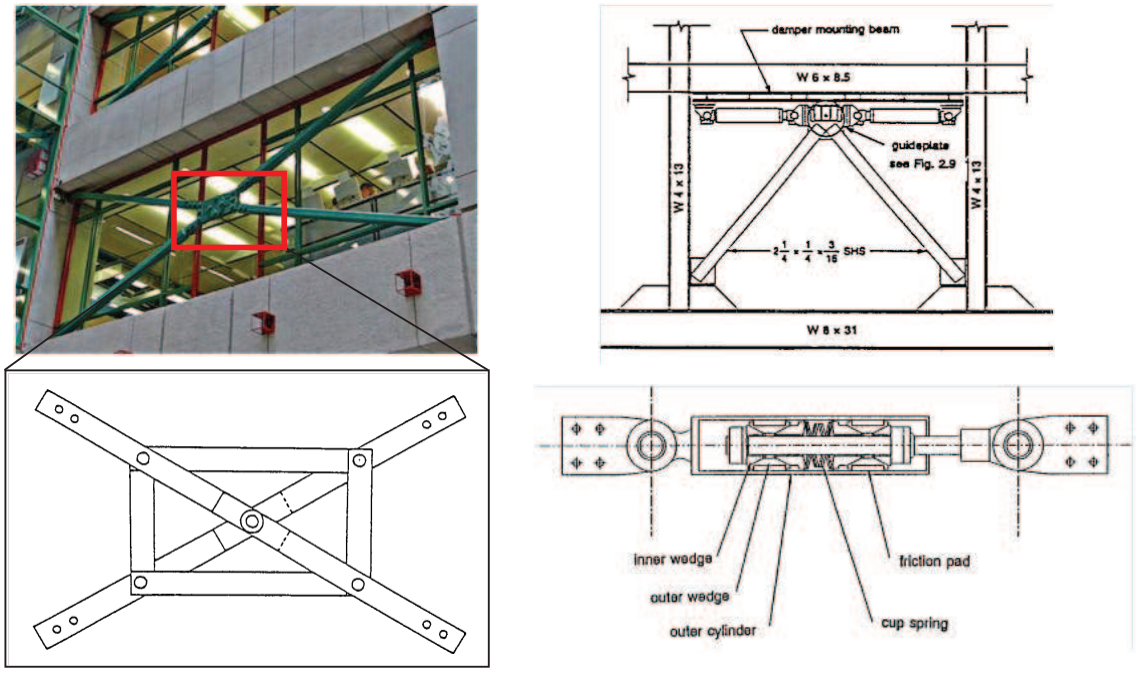

Figure 1.3 : *Left*: Pall friction damper. *Right*: Sumitomo friction damper.[Courtesy: http://www.bcee.concordia.ca and Aiken et al. [36]]

damper is tested on 1:3 scale reinforced concrete frame and the results confirmed the reduction in structural deformations.

For all the friction dampers discussed so far, interface composition plays an important role in the operation of the device on the long run. Also, the device should exhibit uniform frictional behavior for different operating amplitudes and frequencies. Typically, the sliding interfaces consists of steel on steel, brass on steel, or graphite impregnated bronze on stainless steel. Low carbon alloy steels are not desired since they corrode and their interface properties will change with time [4]. Based on the performance of the dampers in existing structures, only steels with high chromium content appear to suffer less corrosion in contact with brass or steel [4].

Little is know about the long-term behavior and durability of the friction devices,

particularly after long periods of inactivity. So, an extensive study is required before adopting friction dampers in the response analysis and design of structures. Experiments carried on the test structures proved that the addition of friction dampers reduce the displacements, while maintaining comparable acceleration levels compared to the unbraced and conventionally braced frames. For an yielding structure, the peak forces in the structure are dictated by the yield level. If friction damper is added to a yielding structure, under a very strong earthquake, the structure with friction damper will experience more accelerations compared to the unbraced structure.

Viscous dampers

Hysteresis dampers and friction dampers are primarily intended for seismic application. These dampers engage only beyond a certain amplitude level. On the other hand, the dampers made of viscous material (solids and liquids) can be dissipate energy at all deformation levels. The concept of viscous dampers originated from the idea that fluids can used to dissipate energy. A viscous damper is a device that removes mechanical energy from a system by converting it to heat. The damper absorbs energy by forcing fluid through orifices, thereby causing the damper to apply a force over a displacement, this force being dissipative [35]. A viscous fluid damper generally consists of a piston in the damper housing filled with a compound of silicone or oil [35, 39]. A typical fluid viscous damper and the schematic are shown in Figure 1.4(left). If the fluid is purely viscous (for instance, Newtonian), then the output force of the damper is directly proportional to the velocity of the piston [40]. The performance of viscous damper is studied both experimentally and analytically by Symans and Constantinou [40]. Arima et al. [41] proposed viscous damping walls in which the fluid flow is laminar instead of the orifice. Viscous damping walls consists

of a plate floating in a thin case made of steel plates (the wall) filled with highly viscous fluid. Actual picture and schematic diagram of the viscous damping walls is shown in Figure 1.4(right).

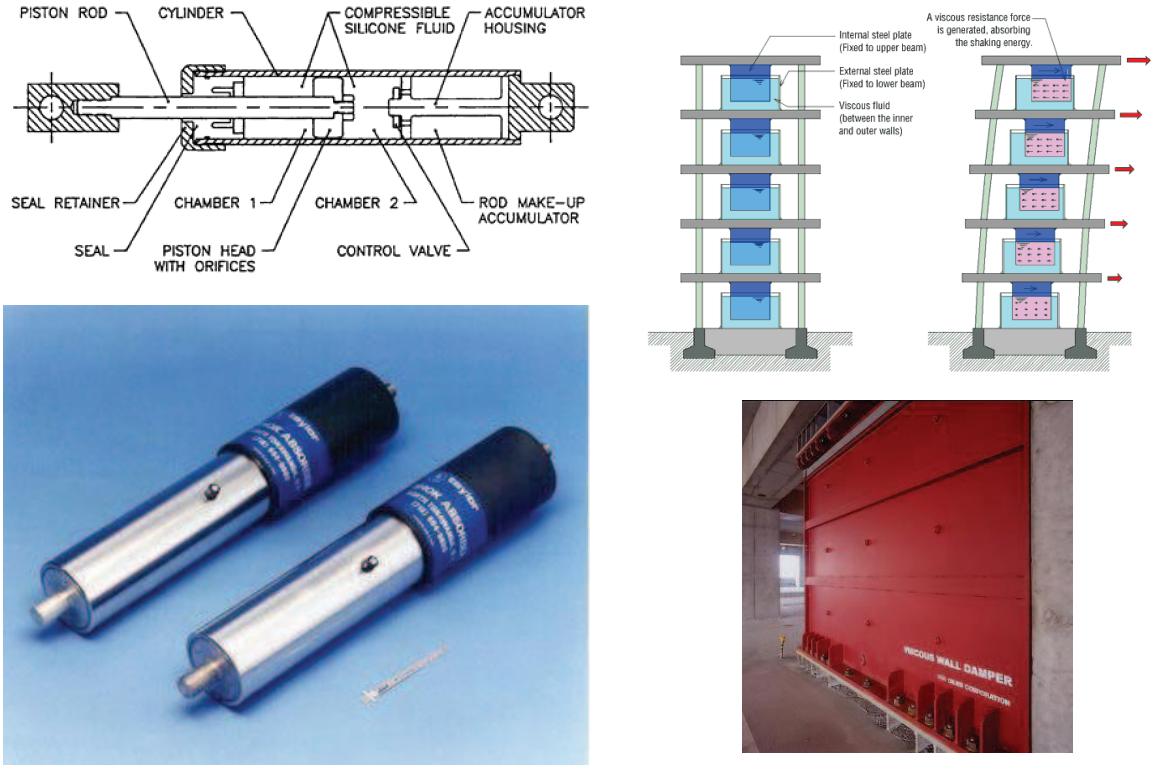

Figure 1.4 : *Left*: Viscous fluid damper. *Right*: Viscous damper wall. [Courtesy: Taylor Devices Inc., Aseismic Devices Co. Ltd. and Aerotek

Viscouselastic dampers

Similar to the viscous fluid dampers, viscoelastic dampers are capable of dissipating energy at all input amplitudes. So, these dampers are also effective in damping the wind-induced vibrations. The force deformation behavior of viscoelastic dampers has characteristics of a elastic material and a viscous fluid–hence the name viscoelastic.

Viscoelastic materials have been used in vibration control since the 1950s [42], they were used on aircrafts to control the vibration-induced fatigue in airframes. For civil engineering structures, these dampers were first used in 1969 to mitigate the wind load in the twin towers of the World Trade Center [4]. Viscoelastic materials used in the typical damper are made out of copolymers.

The viscoelastic damper developed by 3M Inc. has viscoelastic polymer bonded on the steel plates as shown in Figure 1.5. These dampers dissipate energy through shear deformation in the viscoelastic layers. The force deformation behavior of viscoelastic materials depends on vibrational frequency, strain, and ambient temperature [43]. Chang et al. demonstrated the performance of viscoelastic dampers analytically and experimentally on 2:5 scale steel moment frame. In Japan, Hazama Corporation developed devices using copolymers, and Shimizu Corporations developed viscoelastic walls in which solid thermoplastic rubber sheets are sandwiched between steel plates [44].

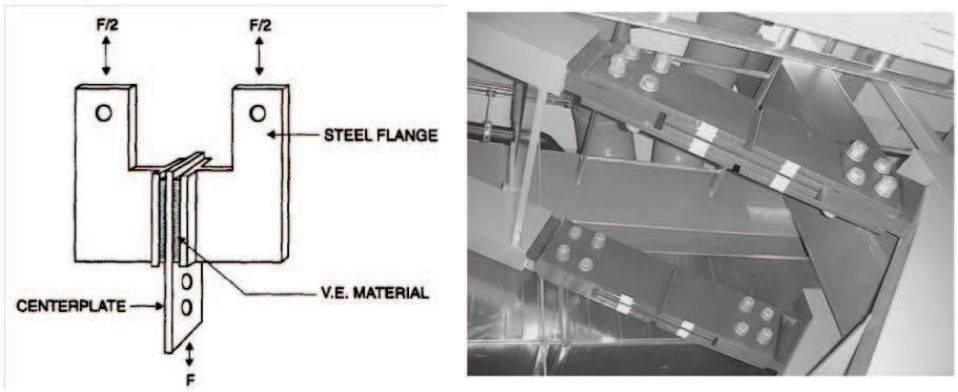

Figure 1.5 : Viscouselastic damper. [Courtesy: Housner et al. [4], Chalmers Microelectronics Laboratory

Some of the important contributions in the vibration control using supplemental

damping devices include (1) A study on the performance of a combination of dampers, a friction damper to prevent the structural damage due to severe earthquake motion and a viscoelastic damper to mitigate the low energy excitation, such as wind forces or mild ground movements [45]. (2) Application of supplemental damping devices (friction dampers and viscous dampers) in the seismic retrofit of reinforced concrete structures [38, 46, 47]. Pradlwater et al. proposed and studied the performance of bidirectional friction dampers [48].

1.1.3 Vibration absorbers

The idea of vibration absorbers is to convert the energy imparted from the earthquake ground motion to the energy among vibrating modes of an auxiliary system added to the structure. The vibration absorbers will indirectly increase the energy damping properties of the primary structure by absorbing significant part of the input energy. In civil engineering applications, tuned mass dampers (TMD) and tuned liquid dampers (TLD).

Tuned mass damper (TMD)

The concept of TMD dates back to the 1940s [49]. TMDs consists of a secondary mass with properly tuned spring and damping elements, providing a frequency-dependent hysteresis that increases damping in the primary structure. TMD installed in Taipei 101, Taiwan is shown in Figure 1.6. "Frequency-dependent damping" is the catchphrase always associated with the tuned mass damper. If the frequency of the structural vibrations is much different from the tuned frequency of the TMD, the TMDs become ineffective. The impact of a TMD in reducing seismic-load and wind-excited structural vibrations is very well established. Villaverde and Koyama [50] carried

numerical and experimental studies on three different structures for nine different ground motions to study the impact of TMDs in reducing seismic response of structures. Experimental results have shown that the effectiveness of TMDs on reducing the response of the same structure during different earthquakes, or of different structures during the same earthquake is significantly different [50]. From the reported results, in some cases, response of structure with TMD significantly reduced and in some cases there is little or even no effect. This confirms the frequency-dependent damping characteristics of TMD. The observed response reduction is large for resonant ground motions and diminishes as the dominant frequency of the ground motion gets further away from the structure's natural frequency to which the TMD is tuned. Also, TMDs are of limited effectiveness under pulse-like seismic loading [50].

In general, the response of a structure with TMD tuned to the fundamental frequency of the structure can be substantially reduced but, the higher modal responses may only be marginally suppressed or even amplified [51]. To overcome the frequency-related limitations of TMDs in a MDOF system, more than one TMD in a given structure, each tuned to a different dominant frequency, can be used. Clark [52] proposed the concept of multiple tuned mass dampers (MTMDs) together with an optimization procedure to control two modes of the structure. Since then, a number of studies have been conducted to understand the behavior of MTMDs [53, 54]. Setareh has proposed doubly tuned mass damper (DTMD), consisting of two masses connected in series to the structure [55]. Analytical results reported by Setareh have shown that DTMDs are more efficient than the conventional single mass TMDs over the whole range of total mass ratios, but are only slightly more efficient than TMDs over the practical range of mass ratios [55]. A more detailed discussion on the literature of TMD is give in Chapter 8.

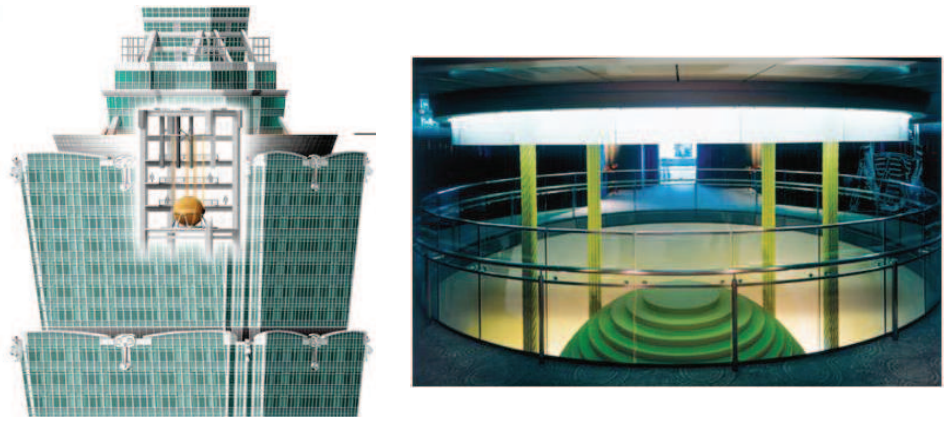

Figure 1.6 : Tuned mass damper installed in Taipei-101 in Taiwan. [Courtesy: [5]]

Tuned liquid damper

Similar to the TMD, the tuned liquid damper (TLD) and tuned liquid column damper (TLCD) impart indirect damping to the system. TLD absorbs input energy by means of viscous actions of the fluid and wave breaking. TLCD absorbs input energy by the passage of liquid through an orifice with inherent head loss characteristics [56]. TLDs have been used in many practical applications to mitigate the wind-induced vibrations. Sun demonstrated the performance of a TLD in SDOF under sinusoidal excitations [57, 58]. Welt and Modi demonstrated the effectiveness of TLD in building through experimental and simulation studies [59]. Bauer [60] suggested the use of a rectangular container completely filled with two immersible fluids to dampen response through the motion of the interface. Fujino et al. [61] proposed a TLD with rectangular or circular containers partially filled with water. Many other types of TLDs and TLCDs have been proposed and tested experimentally [62, 63].

So far, all the existing passive control devices used to reduce the structural response have been discussed. These devices does not required external power to operate

and hence they are called passive devices. These devices are very well understood and accepted in the research community and also the engineering community as a means for mitigating the effects of dynamic loading on structures [5]. However, these passive control devices are not capable of adapting to the structural changes and to the varying loading conditions. Active control is a more sophisticated approach to overcome the limitations suffered by the passive control devices. Active control is discussed in detail next.

1.2 Active Control

In the passive control, the objective is to control the displacements by adding supplemental dampers or to reduce the acceleration by isolating the superstructure. If the control objective is very specific and involves controlling more than one response characteristic for a specified set of external loads, then the desired objective can only be achieved by using a feedback control. In active-control of structures, the structural response is attenuated using actuators. The force exerted by the actuator is calculated in real-time using a control algorithm and feedback from sensors. Measured feedback signal could be the excitation and/or response of structure. Block diagram showing the working principle of feedback-control system is shown in Figure 1.7. Actuators and sensors are connected to the structure at strategic locations (depending on the control scheme used). Sensors measure the response of structure and communicates to the controller, the information communicated by the sensor is called feedback-signal. Potentiometers, linear variable differential transformer (LVDTs) and accelerometers are the common sensors used to measure the feedback-signal. The controller, generally a computer or a micro-processor, has an in built algorithm to calculate the desired actuator force based on the measured feedback signal. The control command from

the actuator drives the actuator. This cycle repeats at a predefined sampling rate. In short, the actuator exerts a force on the structure to achieve a desired response subjected to set of external disturbances.

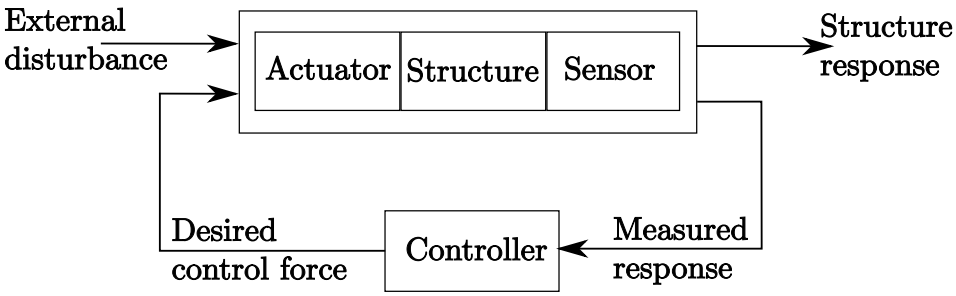

Figure 1.7 : Block-diagram of a typical feedback-control system

Unlike the passive control, the active control is not well received in the civil engineering community sice its introduction in late 80s [4]. Active mass damper is the only active-control devices that have been used in real life applications. Although the active-control is more efficient than passive-control, high power requirement and continuous measurement of feedback signal limit it's applications. Much of the focus in active control is limited to laboratory testing and developing control algorithms.

1.2.1 Active mass damper

The active mass damper (AMD) system, developed by the Kobori research group in 1989 [64], is the full-scale application of active control to a building. The AMD has a large mass whose motion is controlled by a turn screw actuator. AMD comprises of large suspended mass, sensors to measure the acceleration, and activate hydraulic pumps to drive the mass. Hydraulic actuators to move the suspended mass to counteract the building's motion caused due to earthquake or strong wind forces [65]. This

AMD was first installed in the Kyobashi Seiwa Building in Tokyo, Japan, and has performed well during many earthquakes and strong winds [66]. Since then, single axis TMD is installed in couple of buildings in Japan. Actual picture and Schematic diagram of AMD installed in Kyobashi Seiwa building is shown in Figure 1.8(left). Dual-axis active mass damper is shown in Figure 1.8(right).

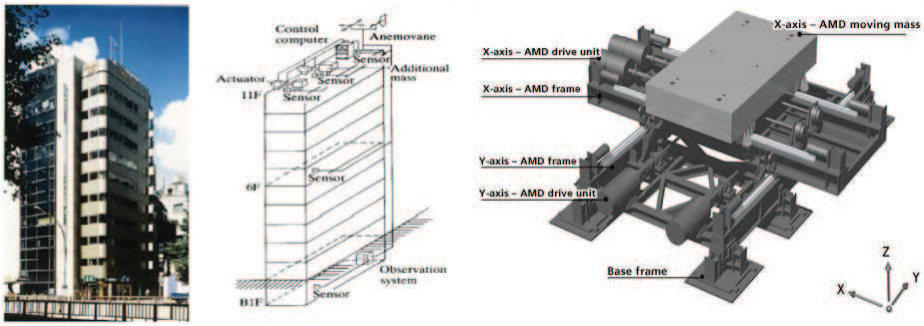

Figure 1.8 : *Left*: Active mass damper installed in the Kyobashi Seiwa building, Japan; *Right*: Dual axis active mass dampers. [Courtesy: IHI Infrastructure systems Co., Ltd.]

Since the installation of first active mass damper, many versions of the AMDs and algorithms to calculate the actuator force have been suggested. Researchers have developed the active bracing system [67] and active tendon devices [68] for the vibration control of structures subjected to multiple support excitation. The algorithms for control using active bracing system include: optimal control [69, 70, 71, 72, 73], stochastic control [74, 75, 76], adaptive control [77, 78], intelligent control [79, 80, 81, 82, 83], sliding mode [84, 85, 86, 87] and robust control [72, 88, 89, 90]. Many researchers have proposed hybrid algorithms in which two algorithms are combined to overcome the limitations of the individual schemes [91, 92].

Use of active control devices has faced serious challenges since the deployment of the first device two decades ago in Japan. These challenges include: (1) high capital

cost and maintenance cost (2) actuators rely heavily on external power and the sensor feedback (3) many active-control devices lack robustness and sometimes destabilize the system in case of sensor failure (4) need for high capacity actuators (for large infrastructure like bridges the desired active control force cannot be achieved by using off-the-shelf actuators). Hybrid and semiactive control strategies are particularly promising in addressing the challenges faced by the active control. Next, some of the hybrid control systems and strategies employing both the active devices and passive devices are discussed.

1.3 Hybrid Control

Hybrid control devices features the best of both the active and passive control devices. They possess the reliability of passive devices, yet maintain the versatility and adaptability of fully active systems. Many researchers have investigated various hybrid control strategies to increase the overall reliability and efficiency of the controlled structure [93, 94]. By adding multiple control devices (hybrid control systems), the limitations of each control device, separately, can be overcome and the advantages of both the devices can be harnessed. Thus, higher levels of performance may be achieved. Research in the area of hybrid control systems has focused primarily on two types of systems: (1) hybrid mass damper systems and (2) active base isolation.

1.3.1 Hybrid mass damper

Hybrid mass damper (HMD) is a combination of a TMD and an active control actuator. The ability of this device to reduce structural responses relies mainly on the natural motion of the TMD. The role of the actuator is to increase the efficiency and also to increase the robustness to change in the dynamic characteristics of the

structure. The energy and forces required to move the mass in HMD are 70% less compared to active mass driver system of comparable performance . The hybrid mass damper (HMD) is the most common control device employed in full-scale civil engineering applications.

Significant contributions have been made by researchers to develop HMDs that are compact, efficient, and practically implementable. A number of innovative, long-period devices have also been proposed. For example, Tanida et al. [95] developed an arch-shaped HMD that has been employed in a variety of applications, including bridge tower construction, building response reduction, and ship roll stabilization. An arch-shaped hybrid mass damper was used during erection of the bridge tower of the Rainbow suspension bridge in Tokyo to reduce large-amplitude vortex-induced vibrations caused due to wind [95]. The mass of the hybrid damper used for the Rainbow bridge tower was 0.14% of the first modal mass of a structure, whereas a comparable passive TMD would require 1% of the modal mass ratio to achieve a similar level of performance.

Koike et al. modified arc-shaped HMD and developed the V-shaped HMD [96]. Fundamental period of V-shaped HMD can be easily adjusted. Three of these devices were installed in the Shinjuku Park Tower. V-shaped HMD used in Shinjuku park tower is shown in Figure 1.9left. Yamazaki et al. [97] developed multistep pendulum type HMDs. Two of these multistep pendulum HMDs have been installed in the Yokohama Landmark Tower, the tallest building in Japan [98]. Multistep pendulum damper used in landmark Yokohama tower are shown in Figure 1.9 (left).

Additionally, the DUOX HMD [99, 100], which attains high control efficiency with a small actuator force, has been proposed and employed in two buildings in Japan. Iemura and lzuno [101] developed and studied another pendulum type device.

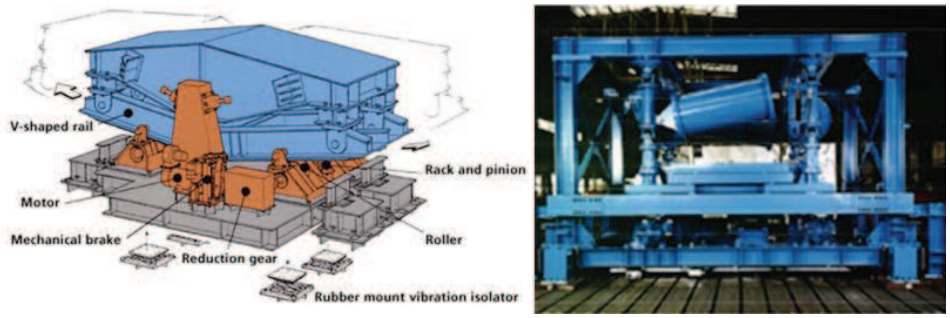

Figure 1.9 : *Left*: V-shaped HMD used in Shinjuku park tower, Japan; *Right*: Multistep pendulum damper used in landmark Yokohama tower [Courtesy: IHI Infrastructure systems Co., Ltd.]

Otsuka et al. [102] conducted experiments in which a roller-pendulum-based HMD was applied to control the response of a tower under seismic excitation. Cheng et al. [103] proposed a HMD system combining a control actuator with a passive tuned liquid damper to control wind-induced vibration of the Nanjing tower in Nanjing, China. Cheng and Tian [104] also studied similar hybrid control approaches. All the hybrid mass dampers discussed so far have only been implemented in Japan and in some buildings in China. Most of the work on hybrid controls in the United States has been focused on combining base isolation with some form of active control to limit excessive displacements, which is discussed next.

1.3.2 Hybrid base isolation

As discussed previously, base-isolation systems are passive systems and are limited in their ability to adapt to changing demands for structural response reduction and large deformations at the isolation level limits the application of base-isolation system. Hybrid base-isolation system, consists of a passive base-isolation system combined with an external actuator to supplement the effects of the base-isolation system.

With the addition of an active control device to a base-isolated structure, a higher level of performance can be potentially achieved without a substantial increase in the cost [105], which is very appealing from a practical viewpoint. Since the base isolation by itself can reduce the interstory drift and the absolute acceleration of the structure at the expense of large absolute base displacement, the combination of base isolation system with an active control device will be able to achieve both low interstory drift and, at the same time, limit the maximum base displacement.

Many researchers proposed robust control approach for uncertain linear base-isolated structures [106, 107, 108]. Reinhorn and Riley [109] performed analytical and experimental studies of a small-scale bridge with a sliding hybrid isolation system in which a control actuator was employed between the sliding surface and the ground to supplement the base-isolation system. They also proposed another type of hybrid base-isolation system that employs a semiactive friction-controllable fluid bearing in the isolation system. Feng et al. [110] employed friction bearings in a hybrid base-isolation system in which the pressure in the fluid could be varied to control the amount of friction at the isolation surface. Yang et al. [111] investigated the use of continuous sliding mode control and variable structure system for a base-isolated structure with friction-controllable bearings.

Since base-isolation systems exhibit nonlinear behavior, many researchers have also developed nonlinear control strategies including fuzzy control [112], neural network based control [13], and adaptive nonlinear control [113]. In the case of base isolation using linear springs the design of the active controller is by conventional linear optimal control theory. Although the hybrid control system is more reliable due to the presence of passive devices, the actuators in hybrid control systems still need to rely on measured feedback signal and external power. To overcome these lim-

itations, semiactive control has evolved which rely on local-feedback and they operate on battery power.

1.4 Semiactive Control

Semiactive control devices offer the adaptability of active control devices without requiring the associated large power sources [5]. Thus, semiactive systems have received considerable attention in the recent past. Semiactive systems operate on battery power, which is critical during seismic events when the main power source to the structure may fail. Semiactive are more sophisticated than the regular passive systems. The underlying principle of a semiactive system is to vary the stiffness and/or damping of the device depending on the measured local-feedback [5, 114]. Semiactive devices are designed to exhibit a force-displacement behavior which upon the addition of structure will result in an adaptive system having superior characteristics compared to the original structure. Generally, the objective is to achieve a non-resonant system.

According to presently accepted definitions, a semiactive control device is one which cannot inject mechanical energy into the controlled structural system, but exhibit properties that can be changed to optimally reduce the responses of the system [5, 115]. Therefore, in contrast to active control devices, semiactive control devices do not have the potential to destabilize (in the bounded input/bounded output sense) the structural system. Preliminary studies indicate that appropriately implemented semiactive semiactive systems perform significantly better than passive devices and have the potential to achieve the majority of the performance of fully active systems, thus allowing for the possibility of effective response reduction during a wide array of dynamic loading conditions [115]. Many researchers have proposed and tested a variety of semiactive control devices. Based on the working principle the semiactive

devices are classified as: (1) Variable stiffness device (2) Variable damping device (3) Variable friction dampers (4) Semiactive tuned mass dampers (5) Controllable fluid dampers

1.4.1 Variable stiffness devices

Variable stiffness device (VSD) change the stiffness of the structure adaptively or based on the measured feedback signal. First variable stiffness system was developed by Kobori et al. at Kajima Research Institute, Japan. The objective of the VSD is to maintain a non-resonant state under seismic excitation by altering the stiffness, and thus natural frequencies, of a building based on the nature of the earthquake [64]. The stiffness is varied by engaging and disengaging the braces in each story of the structural framing system. The hydraulic devices connected between the chevron braces and the floor beams above are used to engage and disengage the bracing system in an on-off manner, thus producing abrupt (discontinuous) changes in stiffness.

To overcome the limitations of the variable stiffness system, Nagarajaiah et al. developed a Semi-Active Instantaneously Variable Stiffness (SAIVS) system which varies the structural stiffness continuously and smoothly so as to maintain a non-resonant state [116]. The SAIVS device is a mechanical device consisting of four springs arranged in a rhombus configuration. The SAIVS device, which has been experimentally tested and shown to be effective, has been incorporated within a smart variable stiffness tuned mass damper (STMD) [114] and smart base isolated structures [6, 15, 117]. Since it requires considerable space, the SAIVS device can only be implemented in an STMD at the top of a fixed-base building or at the base of a base-isolated structure. Due to space constraints, it cannot be implemented within the bracing system of fixed-base structures. SAIVS device is shown in Figure 1.10.

Also, Yang et. al [87] have developed and shown the effectiveness of a Resetting Semi-Active Stiffness Device (RSASD).

1.4.2 Variable damping device

As described earlier in section 1.1.2, by changing the diameter of the orifice the effecting damping of the fluid dampers will also change. Banking on this idea, variable-damping device is developed by using a controllable, electromechanical, variable-orifice valve to alter the resistance to flow of a conventional hydraulic fluid damper. Hence this damper is also refereed as variable-orifice damper. A schematic of such a device is given in Figure 1.10. The concept of applying this type of variable-damping device to control the motion of bridges experiencing seismic motion was first proposed by Feng and Shinozuka [118]. Subsequently, variable-orifice dampers have been studied extensively at the National Center for Earthquake Engineering Research in Buffalo, New York [40, 119]. Variable damping devices change the damping properties of the structure continuously or in multiple stages based on the measured feedback signal. Symans et al. have developed variable damping systems that utilize variable orifice fluid dampers for structural systems and experimentally tested them at both the component level and within multi-story building frames and base isolated structures [40]

Sack and Patten [120] conducted experiments in which a hydraulic actuator with a controllable orifice was implemented in a single-lane model bridge to dissipate the energy induced by vehicle traffic. The effectiveness of variable-orifice dampers in controlling seismically excited buildings has been demonstrated through both simulation and small-scale experimental studies [120, 121, 122].

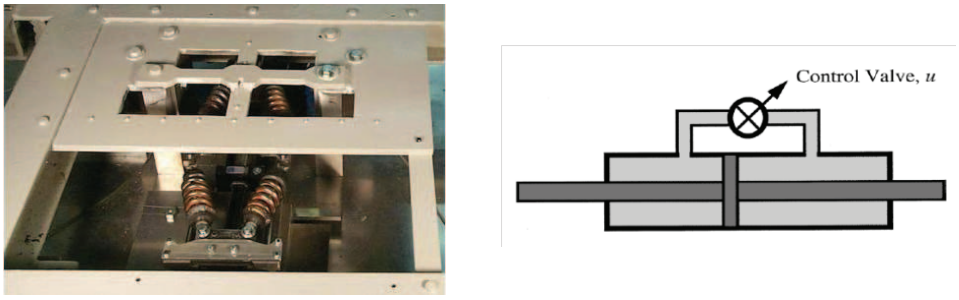

Figure 1.10 : *Left*: SAIVS developed by Nagarajaiah; *Right*: Schematic of variable orifice damper [5]

1.4.3 Variable friction dampers

Similar to the case of variable damping devices, in which the thickness of damping loop can be modified by changing the diameter of the orifice, Akbay and Aktan [123] and Kannan [124] proposed a variable friction device to change the friction loop width have been proposed that utilize forces generated by surface friction to dissipate vibratory energy in a structural system. Variable-friction device consists of a friction shaft that is rigidly connected to the structural bracing. The force at the frictional interface was adjusted by allowing slippage in controlled amounts. A similar device was developed at the University of British Columbia [125, 126]. Dowdell and Cherry carried analytical studies to demonstrate the ability of these semiactive devices to reduce the interstory drifts of a seismically excited structure. In addition, Feng et al. and Yang et al. proposed a semiactive friction-controllable fluid bearing in parallel with a seismic isolation system [110, 111].

1.4.4 Semiactive tuned mass dampers

The response reduction of structures with TMDs is large for resonant ground motions and diminishes as the dominant frequency of the ground motion gets further away from the structure's natural frequency. Since the tuned mass dampers are effective only if the dominant frequency of the system is close to the tuned frequency researchers have explored the semiactive alternatives for these devices to improve their effectiveness in reducing structural responses. Semiactive tuned liquid dampers and smart tuned mass dampers are two examples of semiactive tuned mass dampers.

Semiactive tuned liquid dampers utilize the motion of a sloshing fluid or a column of fluid to reduce the responses of a structure. These liquid dampers are derived from the passive tuned liquid dampers (TLD) and TLCD defined previously in section 1.1.3. Lou et al. [127] proposed a semiactive device based on the passive TSD, in which the length of the sloshing tank could be altered to change the properties of the device. Haroun et al. [128] presented a semiactive device based on a TLCD with a variable orifice.

The concept of smart tuned mass dampers was developed by Nagarajaiah [129, 130]. The STMDs are capable of continuously varying its stiffness and re-tuning its frequency due to real-time control, and is robust to changes in building stiffness and damping [114]. In comparison, the passive TMD can only be tuned to the first mode frequency of the building. The building fundamental frequency can change due to damage or other reasons. The STMDs developed by Nagarajaiah [114] overcomes the limitations of the TMD (i.e. detuning) by retuning the frequency in real time and requires an order of magnitude less power [129, 131].

1.4.5 Controllable fluid dampers

All the semiactive control devices discussed thus far utilize electrically controlled valves or mechanisms. Mechanical components can be problematic in terms of reliability, maintenance and long term usage. Another class of semiactive devices uses controllable fluids. The advantage of controllable fluid devices is that they contain no moving parts other than the piston, which makes them very reliable. The essential characteristic of controllable fluids is their ability to reversibly change from a free-flowing, linear viscous fluid to a semisolid with a controllable yield strength in milliseconds when exposed to an electric (for ER fluids) or magnetic (for MR fluids) field. Two fluids that are viable contenders for development of controllable dampers are: (1) electrorheological (ER) fluids; and (2) magnetorheological (MR) fluids. Although the discovery of both ER and MR fluids dates back to the late 1940s (Winslow 1947; Winslow 1949; Rabinow 1948), the application of these materials in civil engineering has not began till the early 90s.

A number of ER fluid dampers have recently been developed, modeled, and tested for civil engineering applications since 1992 [132, 133, 134, 135, 136], but the MR fluids were not implemented in may structures mainly because they are (1) sensitive to impurities (2) sensitive to temperature changes (3) have low energy density (5) Large current is required to align the particles.

MR fluids are an attractive alternative to ER fluids for use in controllable fluid dampers [137]. MR fluids are magnetic analogs of electro-rheological fluids and typically consist of micron-sized, magnetically polarized particles dispersed in a carrier medium such as mineral or silicone oil. When a magnetic field is applied to the fluid, particle chains form, and the fluid becomes a semisolid and exhibits viscoplastic behavior similar to that of an ER fluid. Transition to rheological equilibrium can be

achieved in a few milliseconds, allowing construction of devices with high bandwidth. Researchers have demonstrated experimentally that the achievable yield stress of an MR fluid is an order of magnitude greater than its ER counterpart and that MR fluids can operate at temperatures from -40C to 150C with only slight variations in the yield stress [137]. Moreover, MR fluids are not sensitive to impurities commonly encountered during manufacturing and usage, and little particle/carrier fluid separation takes place in MR fluids under common flow conditions. Further, a wider choice of additives (surfactants, dispersants, friction modifiers, antiwear agents, etc.) can generally be used with MR fluids to enhance stability, seal life, bearing life, and so on, since electrochemistry does not affect the magneto-polarization mechanism. The MR fluid can be readily controlled with a low voltage (12-24V), current-driven power supply outputting only 1-2 amps.

Spencer et al. [137, 138] and Dyke et al. [139, 140, 141] have carried extensive studies to explore the applications of MR dampers for seismic response reduction. Dyke et al. [139, 140, 141] have shown through simulations and laboratory experiments that the MR damper, used in conjunction with acceleration feedback control strategies, significantly outperforms comparable passive configurations of the damper for seismic response reduction. In addition, Carlson and Spencer [137] reported that the design of a full-scale MR damper is scalable to devices appropriate for civil engineering applications. Schematic diagram of controllable fluid damper and a 20 ton MR damper are shown in Figure 1.11.

All the approaches described thus far suffer from one or other limitation:

- active control devices rely on feedback and substantial power;
- semi-active controllers also require feedback but nominal power;

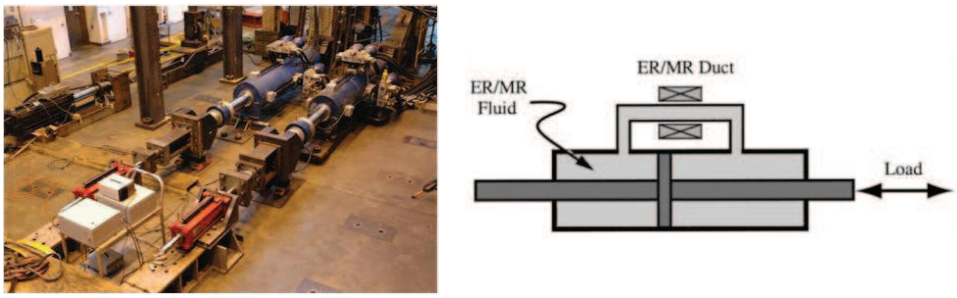

Figure 1.11 : *Left*: MR dampers being tested at the NEES testing facility at Lehigh University *Right*: Schematic diagram of controllable-fluid damper [5]

- passive control devices may reduce displacement but lead to larger base shear and also, the passive devices will not be effective for different loading conditions and change in structure properties

Current seismic design practice promotes inelastic response in order to reduce the design forces. By allowing the structure to yield while increasing the ductility of the structure, the global forces can be kept within the limited bounds dictated by the yield strength. However, during severe earthquakes, the structures undergo significant inelastic deformations leading to stiffness and strength degradation, increased interstory drifts, and damage with residual drift. In this thesis, novel passive and semi-active variable stiffness systems and smart tuned mass dampers are developed to mitigate the vibrations and reduce the large inelastic excursions induced due to strong ground motions.

The NSD together with a viscous damper is called adaptive negative stiffness system or simply adaptive stiffness system (AS). Upon the addition of NSD to the structural system, predesigned reductions of stiffness occur in the combined system or "apparent weakening" occurs; however, it is important to note that the stiffness and the strength of the main structural system remain unchanged in this study (hence,

"apparent"). Unlike the concept of weakening and damping, where the main structural system strength is reduced, the structure and device assembly in "apparent weakening" produces effects compatible with an early yielding, but the original structural system remains unaltered. Addition of the passive damper reduces effectively the displacements that are caused due to the reduction in effective stiffness. The main objective of the adaptive stiffness system is to shift the yielding behavior of the structure to the NSD and reduce the base shear (foundation force) and acceleration of the structure and at the same time limit the maximum deformations of the structure using the viscous damper.

1.5 Outline

The outline of this thesis is as follows:

In chapter 2, the principle of the adaptive negative stiffness system (AS), combination of structure, NSD and damper assembly, proposed in this work is presented. Different feasible configurations of NSD and the role of NSD and damper are sequentially demonstrated in chapter 2. A detailed explanation and working principle of the NSD, simulation studies carried on the AS for periodic and six standard ground motions are also presented.

Chapter 3 focuses on the underlying principle and the development of negative stiffness device. Detailed description of the components, including gap-spring-assembly, in the NSD and their connections. Analytical model of NSD and the derivations pertaining to the development of equation of motion of NSD is also presented in chapter 3. Description of the test setup used to characterize the behavior of NSD and the results comparing the observed experimental behavior and predicted behavior are also presented in this chapter.

Chapter 4 presents the details of all the components in 3SFS and their connections. Design of each of these components, fabrication and assembly on the shake-table is also discussed. Analytical models of 3SFS, NSD and dampers and the installation in the 3SFS is presented. A brief discussion on the instrumentation of the test setup and data acquisition is also given in chapter 4. Experimental results from the testing of 3SFS and the analytical model used to capture the experimental behavior is also presented.

"Apparent-weakening" in elastic structures is verified using the experimental results and simulation studies in chapter 5. The issues involved in the assembly drift when the primary structure undergoes plastic deformation are addressed. Experimental results (response and hysteresis loops) of 3SFS and comparisons with 3SFS assembly equipped with (i) NSD (ii) damper (iii) NSD and damper are presented to highlight the advantages of AS. The second and third floors of the 3SFS are bracing making it act a SDOF system. The key remarks based on the shake-table studies for a suite of ground motions both on elastic and yielding systems are also presented.

In chapter 6 the advantages of using NSDs in multiple storys is presented. Experimental results on 3SFS (without braces in the moment frame) with NSDs in the first floor are presented for moderate ground motions and for severe ground motions separately. Analytical model for a nine-story 1:3 scale frame used to demonstrate the concept of distributed isolation is presented. Simulation results on the nine-story frame depicting the isolation capabilities of NSD and an optimization scheme to distribute isolation over the height of bottom few floors are also presented for a suite of ground motions.

In chapter 7, details pertaining to the development and implementation of semi-active (SA-NSD) is presented. The pin connecting the lever-arm and pivot plate is

moved to change the properties of NSD in real-time. A doubling-acting hydraulic device is proposed to move the pin. The analytical models for the proposed SA-NSD and the advantages of both the semi-active devices are presented through numerical studies. Simulation results on a SDOF system with the proposed SA-NSD are compared with the passive NSD.

Chapter 8 contains the details on the development of adaptive-length pendulum (ALP) smart tuned mass damper (STMD). Two different approaches to change the length of the pendulum is adjusted in real time using a shape memory alloy (SMA) wire actuator are proposed and verified through experiments on a prototype two-story moment frame. The instantaneous frequency tracking algorithm (STFT), used to find the dominant frequency of the structure from a local feedback signal is also presented. Experimental studies demonstrating the advantages of ALP-STMD in comparison with uncontrolled structure are presented in chapter 8.

Chapter 9 contains the description of the SAIVS system, experimental setup and analytical Bou-Wen model for the SAIVS system. A new formulation showing the representation of Bou-Wen model as a quasi-LPV system is presented. Details pertaining to the design of gain-scheduled controller using LMI approach, control objectives, constraints and and closed-loop performance of the fixed robust $\mathcal{H}_\infty$ controller and LPV-GS controller are also presented in. The tracking results from the numerical studies performed on the SAIVS system are also shown in chapter 9.

Chapter 10 contains the conclusions and also the summary of all the key achievements in this study. Chapter 11 presents the scope of future work and recommendations to enhance the experimental devices and analytical tools developed in this study.

Chapter 2

Apparent-Weakening of Structures: Conceptual Study

Conventional structures designed for loads specified by codes undergo significant inelastic deformations during severe earthquakes, leading to stiffness and strength degradation, increased interstory drifts, and damage with residual drift. These yielding structures however keep the global forces within limited bounds dictated by the yield strength [142]. In chapter 1, several approaches have been discussed to reduce the inelastic effects caused due to strong earthquakes. Passive seismic protection systems in the form of supplemental damping devices have been used in many civil engineering infrastructure to mitigate wind and seismic loads [35, 5, 143, 144]. This approach has emerged as an efficient way to reduce response and limit damage by shifting the inelastic energy dissipation from the framing system to the dampers. Examples of few such passive systems are base isolation systems [22], fluid dampers [35], tuned mass dampers [114], friction dampers [21].

Active-control of structures, wherein the excessive structural response can be attenuated using actuators, can also be used to reduce inelastic behavior. The force exerted by the actuator is calculated in real-time using a control algorithm and feedback from sensors. Measured feedback signal could be the excitation and/or response of structure. Although this approach is more efficient than passive-control, high power requirement and continuous measurement of feedback signal limit its applications. Semiactive control strategies combine the best features of both passive and active

control systems. Semiactive control devices offer the adaptability of active control devices without requiring the associated large power sources [5]. Thus, semiactive systems have received considerable attention in the recent past. Semiactive systems operate on battery power, which is critical during seismic events when the main power source to the structure may fail. Even in semi-active control local feedback is unavoidable.

2.1 Adaptive Systems

In this study, a new concept - "apparent weakening", an adaptive structural system - "Adaptive Negative Stiffness System" (AS) and a novel "Negative Stiffness Device" (NSD) are proposed and developed in detail. Adaptive systems belong to the category of passive seismic protection systems but they are more sophisticated than the regular passive systems. An adaptive system consists of adaptive stiffness and/or damping devices which are capable of changing the stiffness and/or damping of the device depending on the displacement amplitude [20, 114]. These devices are designed to exhibit a force-displacement behavior which upon the addition of structure properties will result in an adaptive system having superior characteristics compared to the original structure.

Recently, Iemura and Pradono [145] proposed pseudo-negative-stiffness dampers (PNSD) that are hydraulic or semiactive or active devices capable of producing negative-stiffness hysteretic loops. It has been shown in their investigations that by adding negative-stiffness hysteretic loops, the total force would be lowered significantly. Common passive dampers that act in parallel with the stiffness of structure add to the total force rendering the shear force larger than that due to stiffness of the base-structure alone. It must be noted that the passive hydraulic dampers can-

not "push" the structure in the same direction as the structural displacement; the adaptive NSD proposed in this study can. A hydraulic device that is fully active or semiactive as in the case of PNSD can generate a pseudo-negative stiffness in which case feedback control would be needed to generate the negative stiffness. The passive negative stiffness friction damper-a convex frictional interface or bearing, opposite of the well known frictional pendulum base isolation bearing, that is essentially an unstable friction bearing–proposed by Imeura and Pradono [145] can generate the pseudo negative stiffness. The pseudo negative stiffness is by virtue of the fact that horizontal force at the convex frictional bearing assists the motion in either direction; however, this type of a system is primarily applicable to base isolated structures, wherein such frictional bearings are used. An additional complication of the pseudo negative stiffness friction bearing is that the structure to which it is attached has to accommodate significant vertical motion in additional to the horizontal displacement.

Soong [31] proposed an active control approach to experimentally simulate yielding structure. An active control algorithm has been proposed to reduce the stiffness of structure in real time without any damage to the structure. Different types of active control methods and possible configurations of the actuator to implement the proposed approach has been suggested. The only objective of Soong's approach is to develop an yielding structure out of an elastic structure without any damage to the structure. Essentially, a closed loop system that behaves like an nonlinear-inelastic system is generated. The NSD proposed in this work is an adaptive device with out any external power supply or feedback signal and the main objective of the device is to reduce the response characteristics of the assembly. Structure and the NSD assembly simulates a nonlinear-elastic system (not a hysteretic system).

In this study, a new passive device is developed, as it does not need any feedback

signal or external power supply to generate the desired force. Detailed analytical and experimental study on the NSD is presented in Chapter 3. In brief, The NSD consists of (a) a self contained highly compressed spring in a double negative stiffness magnification mechanism and (b) a "gap spring assembly" (GSA) mechanism which delays the engagement of negative stiffness until the structural system undergoes a prescribed displacement. The NSD employs double chevron braces that self-contain the large vertical forces needed for the development of the horizontal negative stiffness without transferring these forces to the structure.

By adding the NSD, yielding is emulated in a structural system and "yielding" is shifted away from the main structural system-leading to the new idea of "apparent weakening" that occurs ensuring structural stability at all displacement amplitudes. This is achieved through an adaptive negative stiffness system (AS), combination of NSD and a nonlinear damper. By engaging the NSD at an appropriate displacement (simulated yield displacement), which is well below the actual yield displacement of the structural system, a composite structure-device assembly, behaves like a yielding structure [146]. The NSD has a re-centering mechanism thereby avoiding permanent deformation in the composite structure-device assembly unless the main structure itself yields. Essentially, a yielding-structure is "mimicked" without any, or with minimal permanent deformation or yielding in the main structure. In summary, the main structural system suffers less accelerations, less displacements and less base shear, while the AS "absorbs" them. This thesis presents comprehensive details on development and study of the AS/NSD. Through numerical simulations, the effectiveness and the superior performance of the AS/NSD as compared to a structural system with supplemental passive dampers is presented.

Combination of adaptive negative stiffness and damping device can result in re-

duction in base shear and displacement response of the structure. However, to date truly negative stiffness systems have received relatively little attention as compared to aforementioned semiactive or pseudo negative stiffness systems and thus represent a significant gap. Hence, development of new true negative stiffness devices is necessary to shift the yielding behavior from the structural system to AS/NSD. AS/NSD can reduce damage in frames by reducing the base shears and deformations and they can also eliminate residual inter-storey drifts. An alternate explanation on the need for negative stiffness in adaptive systems to reduce the acceleration is discussed next. Working principle of AS is explained with schematic diagrams in section-2.4 and simulation studies demonstrating the concept of "apparent-weakening" are presented in section-2.5.

2.2 Importance of Negative Stiffness Device: Alternate Explanation

Analytically, active control is the most effective, robust way for reducing the response of structure. But, from practical implementation point of view it suffers with two limitations:

1. large external power to drive the actuator and
2. dependency on the structural-response feedback.

Recently, researchers have developed algorithms to break down the control force, calculated from any active control algorithm, into a combination of passive forces and the remaining marginal amount as an active force–a concept termed as "integrated design of inelastic controlled structural systems" by Reinhorn et al. [147] using the concept "weakening" introduced by Reinhorn et al. [142], Viti et al. [143], and Cimellaro et

al. [144]. Due to the limitations and unreliability of the active control devices during extreme events, the objective was to let the passive components take the maximum amount of force, which are more reliable, leaving very little for the actuators that impart active control force.

Consider a linear multi degree of freedom system with mass M, stiffness K and damping C subjected to a ground motion $\ddot{x}_g$. The equation of motion is shown in Eq. 2.1. x is the relative displacement vector of the structure and F_a is the desired active control force required to control the structure. F_a can be calculated easily using standard LQR control algorithms. Active control force can be represented as shown in Eq. 2.2. G_2 and G_2 are constant gain matrices. Using optimization, the gain matrices H_1 and H_2 can be found such that the error between F_a and F_p is minimized. H_1 and H_2 are the gain matrices that are directly associated to the additional damping and stiffness forces that need to be add to the structure using passive devices. The remaining force $F_a - F_p$ is implemented through an active device [144].

$$M\ddot{x} + C\dot{x} + Kx = -M\ddot{x}_g + F_a \tag{2.1}$$

$$F_a = G_1 x + G_2 \dot{x} \tag{2.2}$$

$$F_p = H_1 x + H_2 \dot{x} \tag{2.3}$$

The control force F_p is exerted through four passive components, namely: (i) Positive damping device ($C_1\dot{x}$), (ii) Negative damping device ($C_2\dot{x}$), (iii) Positive stiffness device ($C_3 x$) and (iv) Negative stiffness device ($C_4 x$).

The constants C_1, C_2, C_3 and C_4 are representative of properties of the devices. Positive and negative damping force can be implemented using fluid dampers. Positive stiffness can be easily implemented by adding supplemental braces; the only force that

is hard to incorporate is the true negative stiffness. In this study a new concept of "apparent softening and weakening" is introduced wherein the "yielding" is shifted to the AS/NSD. A mechanism is proposed to develop the true negative stiffness to simulate global yielding.

2.3 Weakening and Damping of Structural Systems

Reinhorn et al. [148] and Viti et al. [143] introduced the concept of weakening structures (reducing strength), while introducing supplementary viscous damping to reduce simultaneously total accelerations and inter-story drifts. Design methodologies for changing the stiffness of structures and adding damping devices using control theory have been proposed by Gluck et al. [149] to determine the magnitude and the locations of changed structural elements (often requiring softening rather than stiffening) and the added damping, while insuring structural stability. More recently, the design of weakened (reduced strength) structures with supplemental damping was introduced by Reinhorn et al. [147], using principles of structural control. In the latter approach, a two-stage design procedure was suggested:

1. first using a nonlinear active control algorithm, to determine the new structural parameters while insuring stability, then

2. determine the properties of equivalent structural parameters of passive system, which can be implemented by removing, or weakening, some structural elements, or connections, reducing the yield capacity of the structure and by addition of energy dissipation systems.

Passive dampers and weakened elements are designed using an optimization algorithm to obtain a response as close as possible to an actively controlled system. The

weakening of structures leads to an early yielding of the structural system resulting in damage and permanent deformation. The adaptive negative stiffness system AS/NSD, developed in this study is designed to prevent such damage due to inelastic excursions and permanent deformation, but still exhibit the yielding desirable for reduction of base shear.

2.4 Adaptive Negative Stiffness System

2.4.1 Working principle

Assume a perfectly-linear single degree of freedom structure with stiffness, K_e, and no damping, a NSD with stiffness K_{NSD} and a passive damper with damping coefficient C. All the three elements are shown in Figure 2.1(a) and the force displacement plots are shown in Figure 2.2(a). By adding NSD to the structure, schematically shown in Figure 2.1(b), the assembly stiffness reduces to $K_a = K_e - K_{NSD}$ beyond the displacement u'_y (shown in Figure 2.2(b)). If, F_2 and u_2 are the maximum restoring force and maximum displacement of a perfectly-linear system (green line in Figure 2.2(b)) then for the same load the maximum restoring force and maximum displacement of the assembly are F_3 and x_3 (blue line in Figure 2.2(b)), respectively. K_{NSD} is designed to achieve the desired reduction in base shear. Force exerted by the NSD is shown as red line in Figure 2.2(b). Although the reduction in base shear is achieved the maximum deformation of adaptive system is substantially increased in the process when compared with an elastic system.

Deformation of this assembly can be reduced by adding a passive damping device in parallel to the NSD, schematically shown in Figure 2.1(c). A linear viscous damper is used as a passive damping device. By adding the viscous damper to the structure

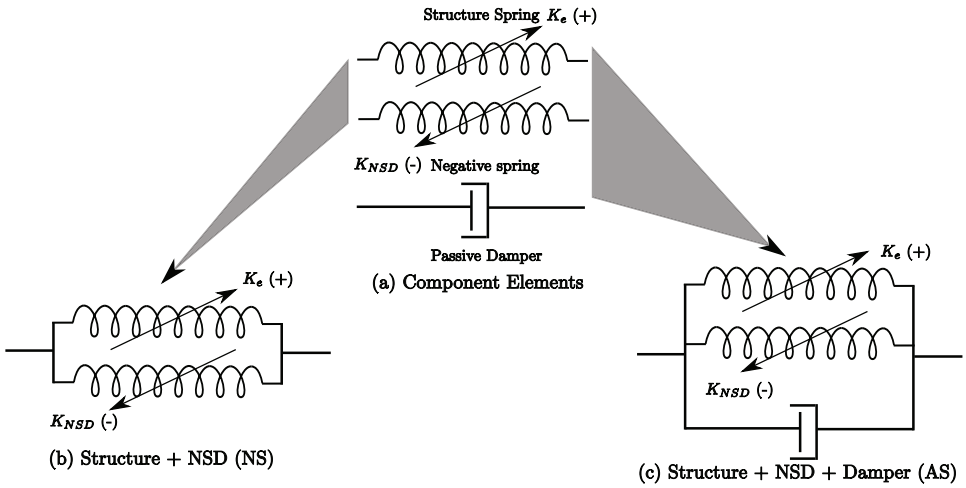

Figure 2.1 : Schematic diagram showing the components in AS and NS

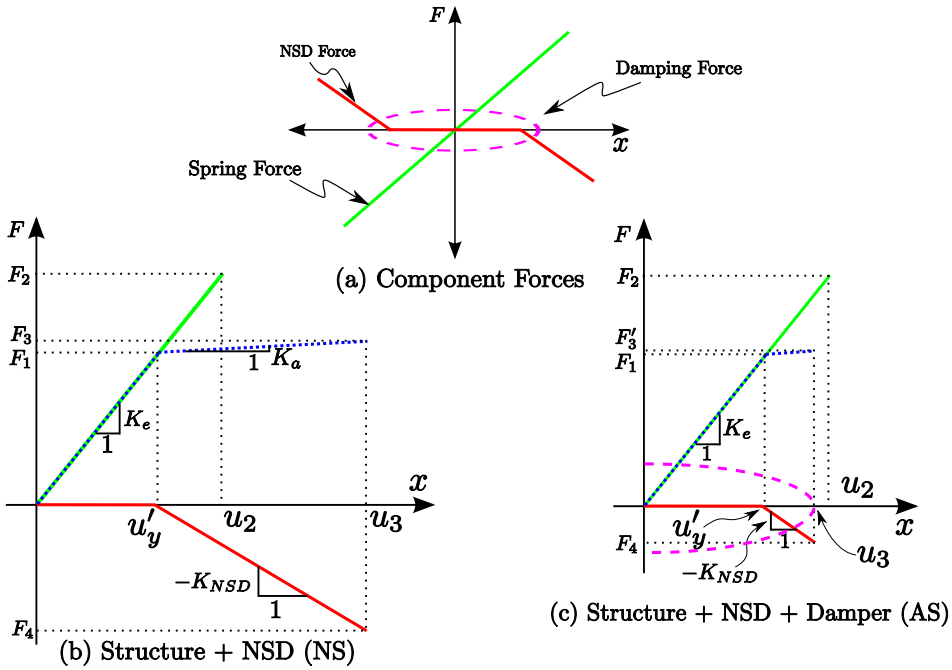

Figure 2.2 : Schematic force-deformation plots of (a) components (b) components and assembly of NS (c) components and assembly of AS

along with NSD, maximum displacement is reduced resulting in $x_3' < x_2$ shown in Figure 2.2(c). Since the assembly of structure and NSD acts like a nonlinear elastic system, viscous damper even with a very small damping coefficient can be effective. It should be noted that by adding a damper to structure and NSD assembly base shear of the assembly is not significantly increased.

At this stage, there is one important constraint that is imposed on the NSD. From Figure 2.1(a,b,c) it can be seen that there is an offset displacement, u_y', called as "apparent yield-displacement", before the negative stiffness device is engaged. This is to avoid excessive response at relatively small external excitations. For displacements u such that $|u| < u_y'$ the structure and NSD assembly behaves like the actual structure. This initial gap is provided by the horizontal spring with elastic-bilinear behavior that has been implemented using a pair of mechanical springs [150].

2.4.2 Challenges in inelastic structures

Another important constraint on NSD comes into picture when the structural system starts yielding. Assume an elastic-purely-plastic structure and NSD assembly, schematically shown in Figure 2.3(a). Force displacement plots of the base structure and NSD are shown separately in Figure 2.3(b). If the structure is subjected to loads that will take it beyond the yield displacement, u_y, there are two limitations (refer to Figure 2.3(c)). F_y is the yield force of the structure. First, the tangential stiffness of the adaptive system becomes negative i.e., for displacements greater than u_y, the slope is negative, as shown in Figure 2.3(c). This signifies an unstable condition and this behavior is not desired as it would result in the collapse of structure. Fortunately, an NSD that has constant negative stiffness is physically not realizable [151]. The stiffness of the NSD changes at large displacements to positive stiffness, which

provides the desired hardening effects.

The second limitation is the increased base shear. In Figure 2.3(c), the structure yields first in the positive direction then after the first load reversal, when the structure yields in the negative direction, the peak base shear of the structure and NSD assembly, F_b, is greater than the base shear that is targeted, F_t, i.e. $|F_b| > |F_t|$. So the negative stiffness of the NSD has to be modified, once the structure starts yielding, to avoid this condition. Similar behavior is observed in the case of a bilinear system if the post-elastic stiffness of the base structure is less than the negative stiffness of the NSD.

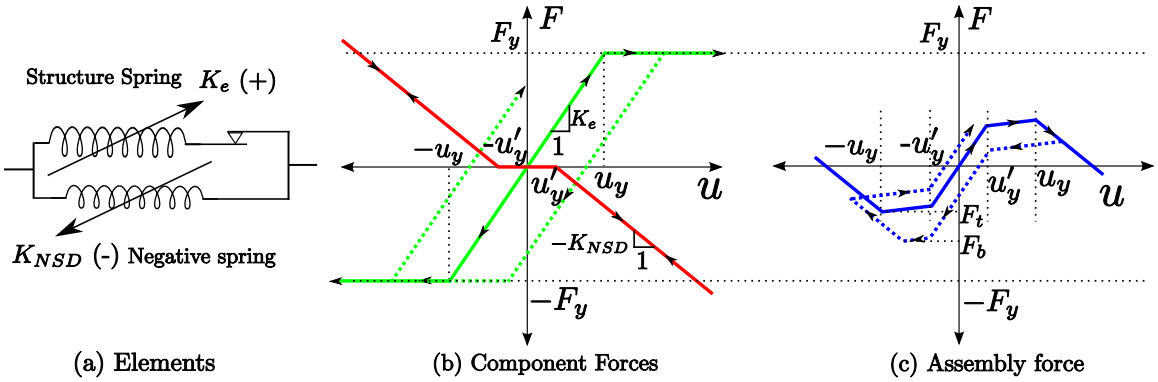

Figure 2.3 : Working principle of Adaptive system. (a) Schematic representation of components (b) component F-D plots (c) assembly behavior [(Green line) : Base-structure, (Red line) : NSD, (Blue line) : Assembly]

The three possible ways of exerting the negative stiffness are:

1. Having a constant negative stiffness for all displacements beyond u'_y, shown in Figure 2.4(a)

2. Keeping the force exerted by the NSD constant beyond u_y (shown in Figure 2.4(b))

3. Stiffening the NSD beyond u_y (shown in Figure 2.4(c))

Three curves, shown in Figure 2.4, are for the base-structure (SF), NSD (NF) and the structure with NSD (TF). Figure 2.4(a) is the response of an NSD with constant negative stiffness, K_{NSD}, and without any constraints on the negative force generated, which is not possible as described earlier. Figure 2.4(b and c) is for second and third approaches respectively.

From Figure 2.4, clearly both the second and third approaches i.e., saturating or stiffening of the NSD after the structure undergoes deformation beyond yield point, will definitely work. Impact of the second approach is shown more clearly in Figure 2.5. Schematic diagram of an elastic-purely-plastic structure and NSD assembly is shown in Figure 2.5(a). Force-displacement behavior of the base structure and NSD are shown separately in Figure 2.5(b). Force-displacement behavior of the structure with NSD is shown in Figure 2.5(c). The second approach is an idealistic case and is hard to develop a passive device that is capable of exhibiting this force-displacement behavior.

The NSD developed and tested in this work is based on the third approach that is capable of exhibiting the hardening behavior beyond a certain displacement. A semi-active method is also proposed to achieve the F-D behavior of second approach by changing the configuration of the elements in NSD using a hydraulic device; this is presented in chapter 7. The NSD is referred as adaptive device because the F-D behavior of the device can be adjusted by varying the geometrical and mechanical properties. The device can be predesigned (adjusted/adapted) to exhibit different stiffnesses at different displacement ranges.

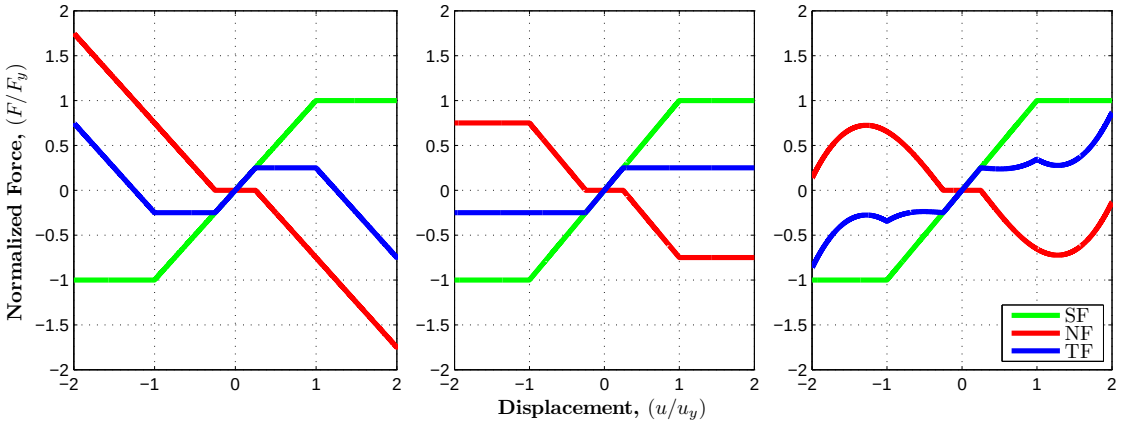

Figure 2.4 : Different feasible force-displacements of structure-device assembly for yielding systems (a) no constraints on the force exerted by NSD (b) keeping the force exerted by the NSD constant beyond u_y (c) stiffening the NSD beyond u_y [SF: Spring Force; NF: NSD Force; TF: Total Force]

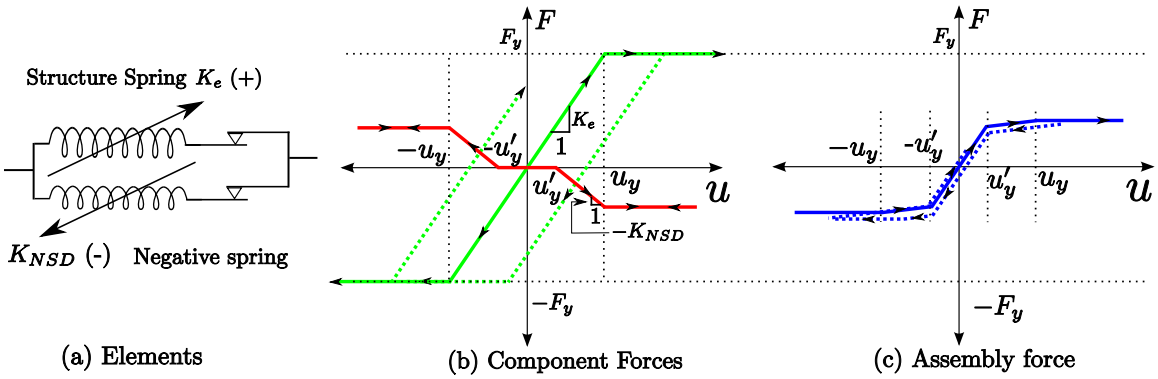

Figure 2.5 : Instability in nonlinear systems with added negative stiffness. (a) Schematic representation (b) component F-D plots (c) assembly behavior [(Green line) : Base-structure, (Red line) : NSD, (Blue line) : Assembly]

2.5 Simulation studies

The main objective of the adaptive system is to reduce the base shear (foundation force) of the structure and at the same time limit the maximum displacement and acceleration of structure. It will be uneconomical and unrealistic to design devices

that will retain the structure in elastic state, without any yielding, after a major earthquake. So, all the cases considered in this chapter involve structure whose properties are representative of a real building and the loading cases for which there is yielding in the structure.

The model used as the test structure in the simulations is calculated from the capacity curve of the test-setup presented in chapter 4, obtained using the commercial softwares with the exact detailing. The strength reduction factor of the three-story frame, $R_{oy} = F_o/F_y = 1.25$, which is a conservative design. F_o is the maximum force in the elastic system for the suite of the ground motions used in this simulation study and F_y is the yield force of the three-story structure. As per the seismic code, ASCE-07, the desired strength reduction factor for moment resisting steel structures should be 4. The NSD is designed such that the strength reduction factor, $R'_{yy} = {}^{F_y}/_{F'_y} = 4$, where, F'_y is the apparent-yield-strength (force in the NSD and structure assembly at u'_y). Hence, the NSD and structure assembly has a strength reduction factor, $R'_{oy} = {}^{F_o}/_{F'_y}$ of 5. The strength reduction factor R'_{yy} should not be greater than 4 due to safety considerations. Sivaselvan-Reinhorn model [152] is used to capture the hysteretic behavior. The Governing equation of motion for the structure is

$$m\ddot{u} + \left(2\xi\sqrt{K_e m}\right)\dot{u} + \alpha K_e u + (1-\alpha)\,K_e u_y z = -m\ddot{u}_g \tag{2.4}$$

$$\dot{z} = \left(1 - |z|^{\eta}(\gamma \mathrm{sgn}(z\dot{u}) + \beta)\right){}^{\dot{u}}/_{u_y} \tag{2.5}$$

Eq. 2.5 can be represented in the displacement differential form as

$$\frac{dz}{du} = \frac{\left(1 - |z|^{\eta}(\gamma \mathrm{sgn}(z\dot{u}) + \beta)\right)}{u_y} \tag{2.6}$$

where, m is the mass of structure, ξ is the damping ratio, α is the post-yield stiffness ratio. γ, η and β are constant parameters that determine the shape of bilinear hysteretic loops. $z = {}^{F_{hys}}/_{F_y}$, is the ratio of hysteretic force to the yield force. The tangential stiffness of the hysteretic part is proportional to ${}^{dz}/_{du}$. K_e is the initial elastic stiffness and αK_e is the post-yielding stiffness of the structure obtained from the push over curve. The tangent stiffness of the system can be then represented by the following relation; shows low stiffness after yielding ($z \to 1$):

$$K_{tangent} = K_e \left(\alpha + (1-\alpha)\left[1 - |z|^{\eta}(\gamma \mathrm{sgn}(z\dot{u}) + \beta)\right]\right) \tag{2.7}$$

The values for remaining parameters are obtained using nonlinear interior-point optimization algorithm by minimizing the error between the capacity curve and the analytical model. The force deformation behavior of the structure, NSD and the assembly are shown in Figure 2.6. The displacement and forces in Figure 2.6 are normalized with the yield displacement and yield force. Viscous damper is used as the supplemental passive damper in the simulations. Equations to calculate the force exerted by the NSD are presented in chapter 3.

2.5.1 Periodic ground motion

A periodic input consisting of five cycles sine function is used as an excitation with a frequency identical to the natural frequency of the base structure, $\omega_n = \sqrt{K_e/m}$.

Elastic systems

For those systems that will remain in elastic region for the design ground motion. NSD is found to be very effective. NSD will reduce the base shear of the structure

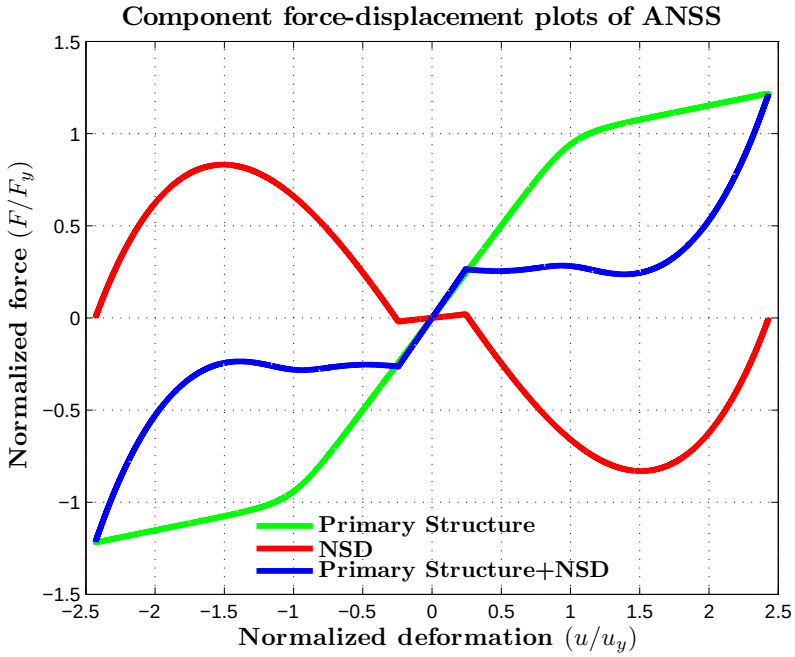

Figure 2.6 : Force deformation behavior of structure, NSD and assembly

substantially. To demonstrate this point, a periodic ground motion is applied to the structure. Amplitude of the ground motion is chosen such that the structure and NSD assembly will remain in elastic region. Response time histories comparing the actual structure and adaptive system are shown in Figure 2.7. Adaptive system (AS) here refers to the structure, NSD and viscous damper with 0% damping. BS refers to base-structure (bilinear system). It can be seen from the plots in Figure 2.7 that all the response characteristics i.e., displacement, velocity and acceleration of the BS case have higher amplitude compared to the AS case. Comparison of the column forces and damper forces in BS and AS are shown in Figure 2.8. The component forces acting in the AS are shown in Figure 2.9(a) and F-D behavior of the assembly forces are shown in Figure 2.9(b). "Apparent yield displacement" for the NSD is at a

normalized displacement of 0.25, since R'_{yy}=4. It is evident from the results in Figure 2.8 and 2.9 that in the case of AS the primary structure remains in the elastic region (displacement of the AS is less than the yield displacement of the primary structure, u_y), whereas in the case of base structure the primary structure yields. It should be noted that passive damper is not yet included for the results shown in Figure 2.7, 2.8 and 2.9. NSD alone is effective for reducing base shear, without any increased deformations, in elastic structures. A passive damper can be added to reduce the deformation of structure along with the base shear, which is considered next.

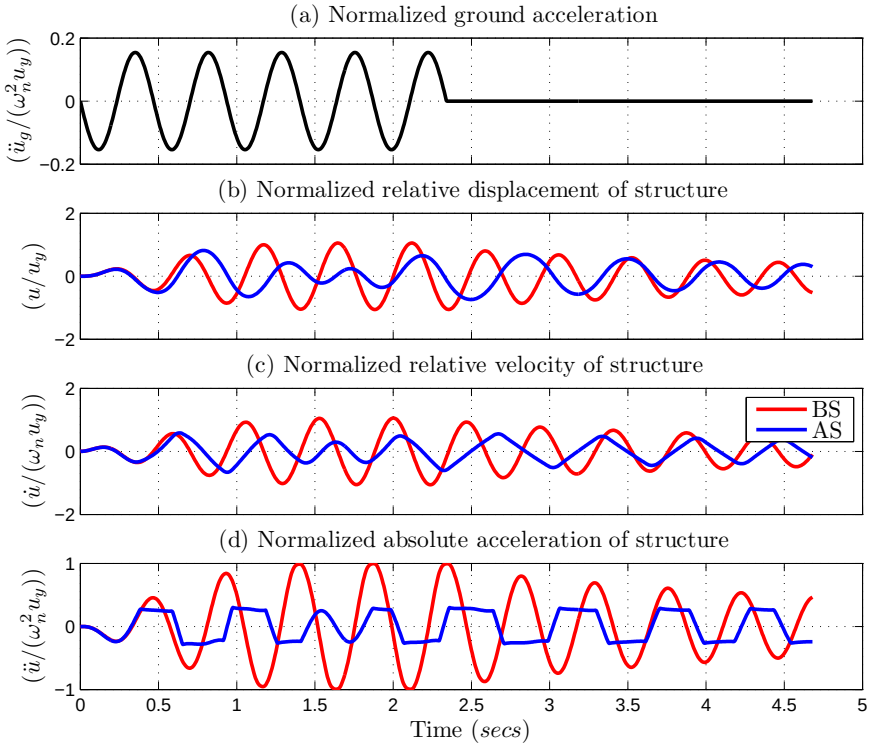

Figure 2.7 : Response of AS and BS for periodic input in elastic structure

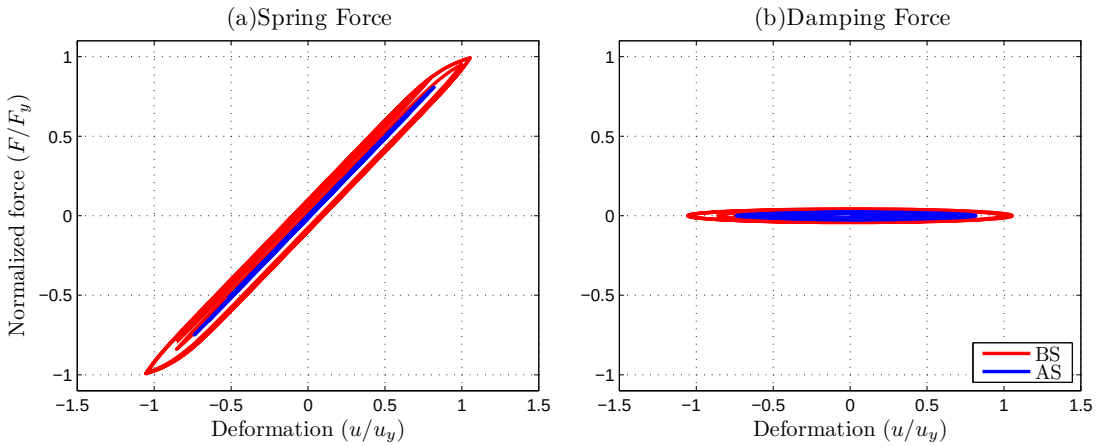

Figure 2.8 : F-D behavior of columns and dampers in elastic structure

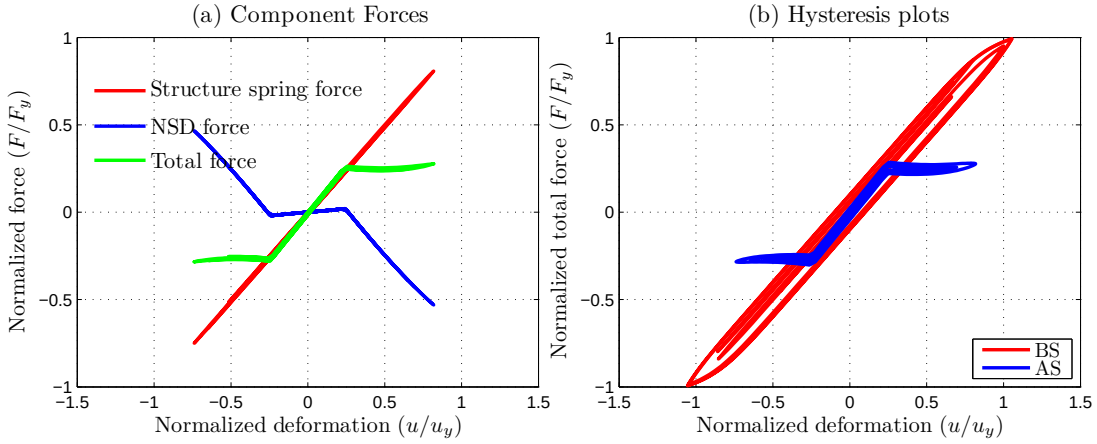

Figure 2.9 : F-D behavior of the (a)components of AS and (b)assembly forces

Inelastic systems

The performance of the NSD is further verified for higher input amplitudes. Amplitude of input periodic ground motion is increased so that the adaptive system starts yielding. As discussed earlier with NSD alone the deformation of the adaptive system will increase due to reduction of stiffness. Passive viscous damper with 20%

damping ratio is used to contain the increased displacements that occur in the AS due to reduction in total stiffness of the system. Simulation results for three systems are compared in Figure 2.10-2.13 after the addition of passive viscous damper: (i) Bilinear system (referred to as BS), (ii) Bilinear system with passive damper (referred to as PS) and (iii) Bilinear system with passive damper and NSD (referred to as AS).

For all these systems response time histories are shown in Figure 2.10, column forces and damper forces are compared in Figure 2.11, hysteresis loops of components of PS and AS are shown in Figure 2.12 and the assembly forces are shown in Figure 2.13. For the periodic input with input-frequency, ω_n, and five cycles, the structure yields; the addition of passive damper results in the deformation of the structure being reduced substantially with a higher base shear. Figure 2.10 shows the reduction in all the responses of an adaptive system (base-structure with NSD and passive damper). Maximum deformation of adaptive system and passive system are comparable in Figure 2.10 and Figure 2.13, but the acceleration of adaptive system is 40% less-compared to passive system and base-structure. Forces exerted by the passive damper in case of both adaptive and passive system, shown in Figure 2.11(b), are comparable. The shear forces experienced by the columns in the two cases of AS and PS is approximately the same, shown in Figure 2.11(a).

In the AS, the base shear (force transferred to the structure's base) is reduced substantially, whereas in the PS case the base shear is larger than the BS case, shown in Figure 2.13. Also, the accelerations reduce substantially in AS case, as compared to both BS and PS cases, which is a significant benefit as the secondary systems can be protected preventing severe post earthquake losses. From Figure 2.10-2.13, it can be concluded that the three main objectives of the adaptive system are clearly achieved.

1. Base shear of the structural system has been reduced substantially. In case of passively damped system the base shear is greater than the base structure, the column shears remain approximately the same in AS and PS as both experience approximately the same displacement

2. The accelerations are substantially reduced in the case of AS as compared to BS and PS

3. Deformation of the AS is also reduced when compared to the BS and is of similar magnitude as the PS

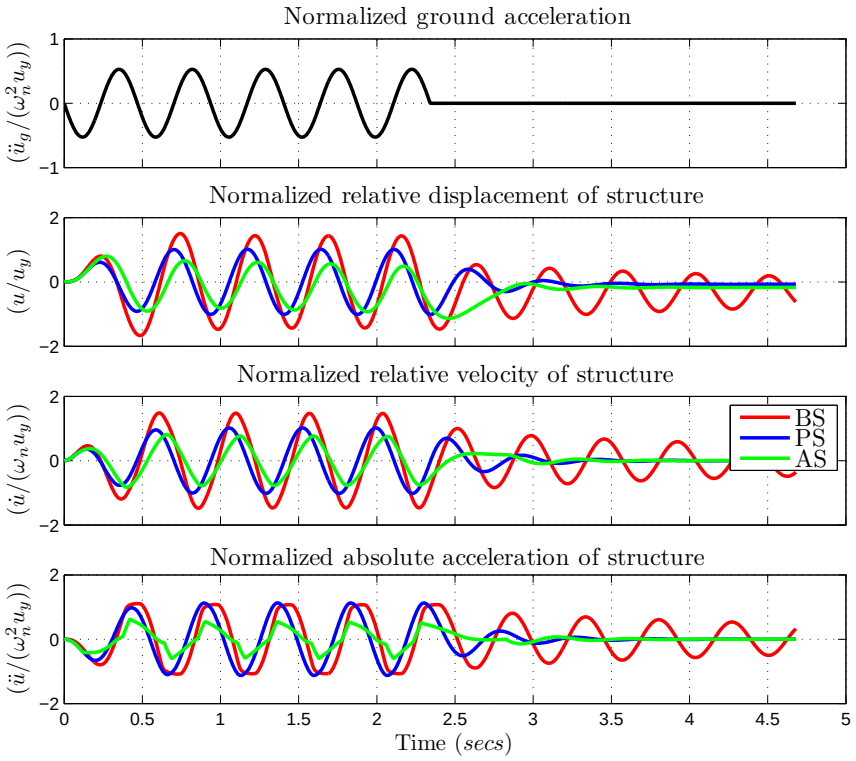

Figure 2.10 : Response of AS and BS for periodic input in yielding structure

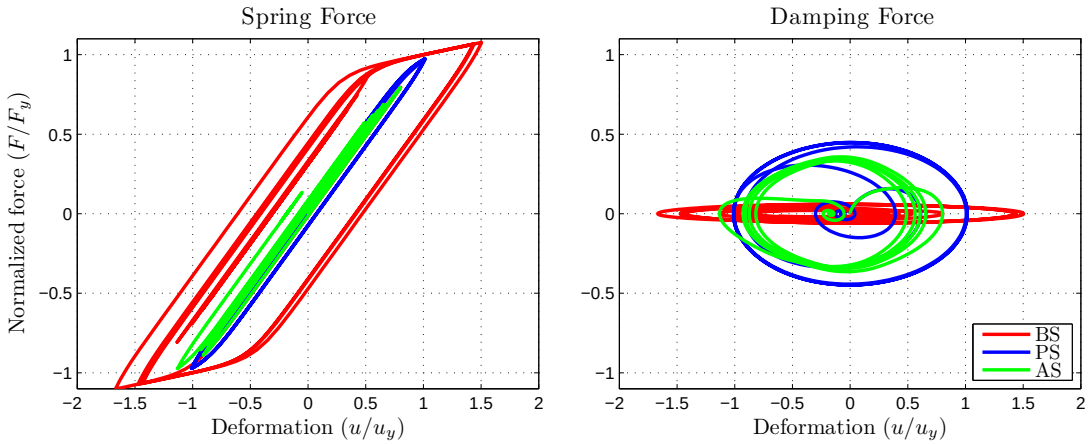

Figure 2.11 : F-D behavior of columns and dampers in yielding structure

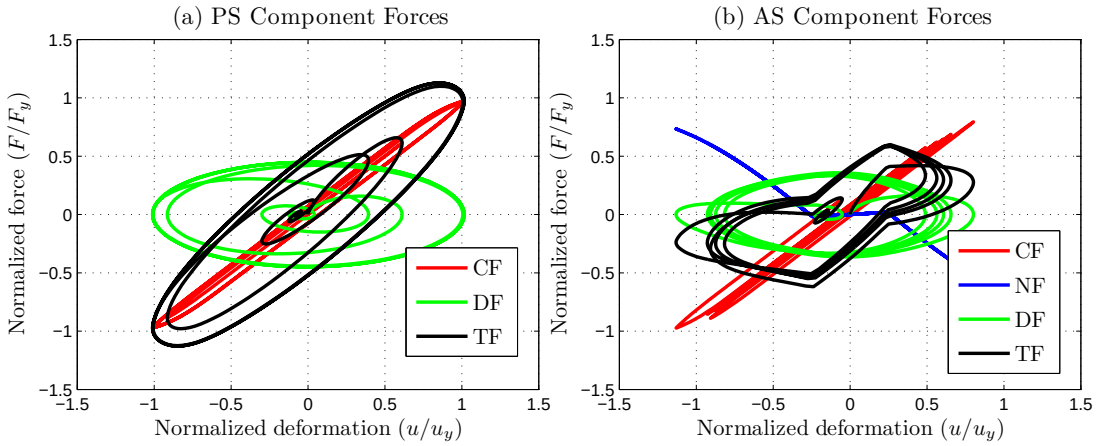

Figure 2.12 : F-D behavior of the components of PS and AS

Response to ground motion

To demonstrate the efficiency of the AS for earthquake ground motions, four standard performance criteria suggested for nonlinear benchmark structures [153], are used to evaluate and compare the performance of AS with passively-controlled-structure and original structure. Performance functions are shown in Table 2.1. There are minor

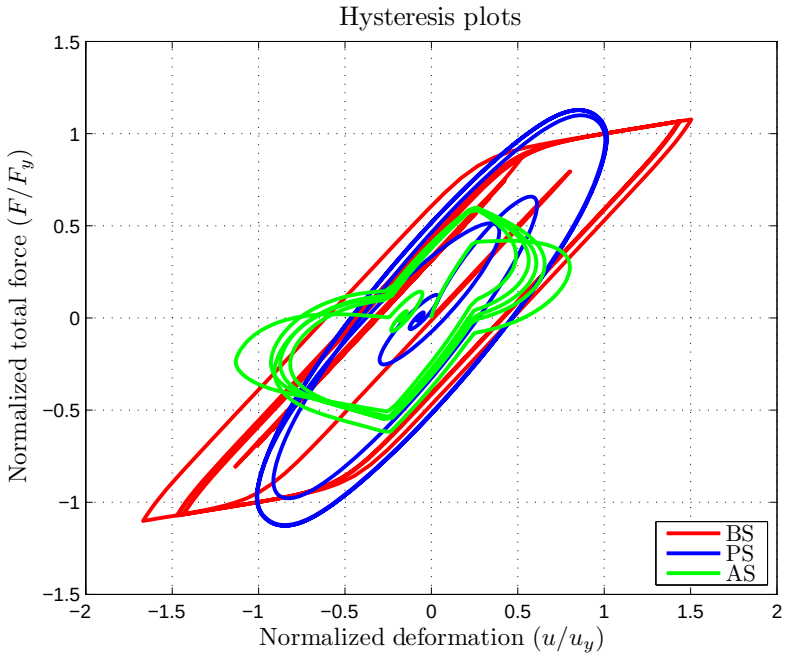

Figure 2.13 : Comparison of the assembly F-D behavior in yielding structures

modifications in the indices used in this study compared to the benchmark indices; formulae for all the indices are listed in Table 2.1. In Table 2.1, u_y is the yield displacement, K_e is elastic stiffness of the structure, F_{TF} is the base shear (structure force with NSD force and PD force), F_{col} is the force experienced by the columns. Seven standard ground motions are used to evaluate the performance of the AS/NSD developed in this study. The ground motions chosen are representative of both the far field and near-fault earthquakes. The performance indices of all the three systems for seven ground motions are listed in Table 2.2. From the results in Table 2.2, it can be seen that absolute accelerations (J_2) of AS is lower than BS by 40% to 60% and it is lower than PS by 16% to 45%. Base shear (J_3) of AS is lower than the BS by 55% to 70% and it is lower than PS by 40% to 65%. Inter-storey displacements (J_1)

Table 2.1 : Performance indices used to evaluate different systems

Name	Evaluation Parameter	Formula
J_1	Inter-storey drift	$\max_t \left({}^{u(t)}/_{u_y}\right)$
J_2	Abs. acceleration	$\max_t \left({}^{\lvert\ddot{u}(t)+\ddot{u}_g(t)\rvert}/_{\max(\lvert\ddot{u}_g(t)\rvert)}\right)$
J_3	base shear	$\max_t \left({}^{\lvert F_{TF}\rvert}/_{K_e u_y}\right)$
J_4	Column force	$\max_t \left({}^{\lvert F_{col}\rvert}/_{K_e u_y}\right)$

of AS in some cases are 30% more than the PS but they are consistently less than BS by 20% or more. It should be noted that a simple viscous damper is adopted in these simulations. Although the base shear (J_3) of the AS is lower than the PS by 55% or more, the force experienced by the columns (J_4) follows the same trend as the inter-story displacement (shown in Table 2.2).

Response characteristics of all the three systems (BS, PS and AS) for Kobe #5 fault-normal (FN) ground motion are shown in Figure 2.14. Column forces and damper forces of different systems for Kobe ground motion are shown in Figure 2.15. AS and PS have slightly yielded but the BS has significantly yielded and undergone permanent deformation, shown in Figure 2.15(a,b). The shear forces and damper forces in AS and PS are similar. Hysteresis loops and component forces of AS and PS are shown in Figure 2.16. "Apparent-weakening" is evident from the component plots in Figure 2.16(b). In the AS, when compared with PS, peak acceleration and base shear have been reduced by 40%, shown in Figure 2.17. Peak inter-storey deformation in the case of AS is 30% more than the PS and the peak damping force of AS is 35% less than the PS, shown in Figure 2.17. Adding NSD to the base structure reduced the base shear significantly and the deformations of the assembly are contained with the addition of damper.

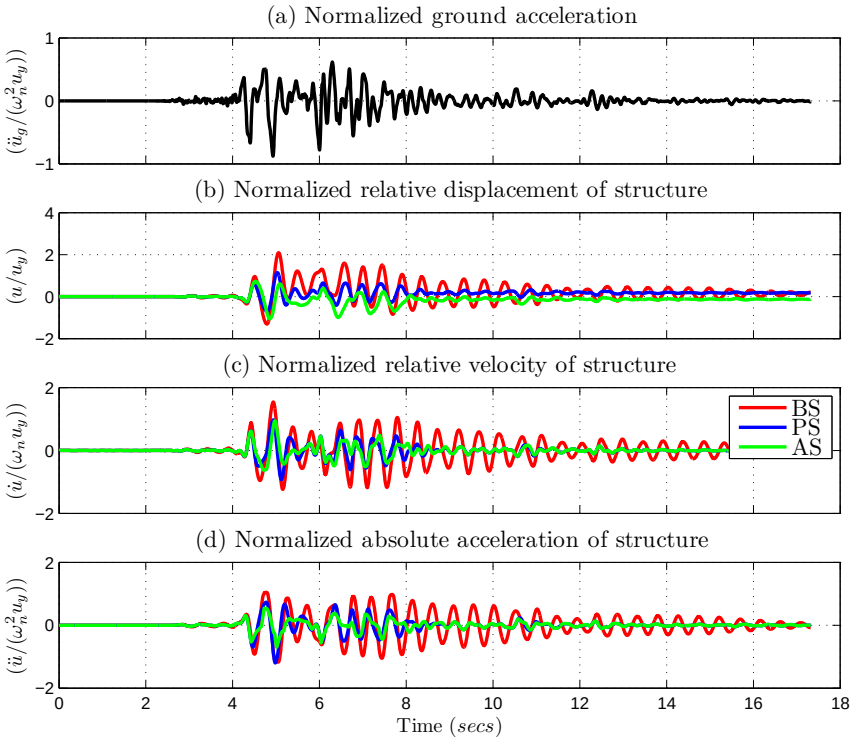

Figure 2.14 : Response of AS and BS for Kobe ground motion

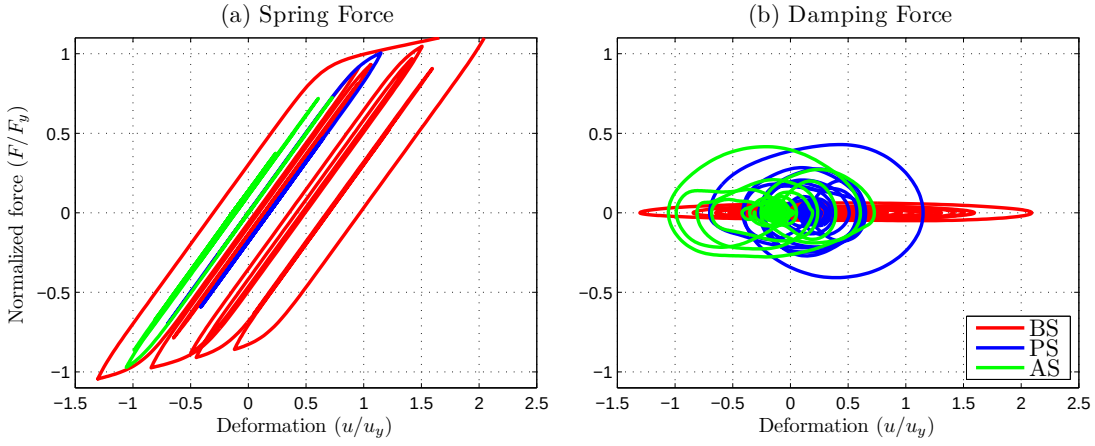

Figure 2.15 : F-D behavior of columns and dampers for Kobe ground motion

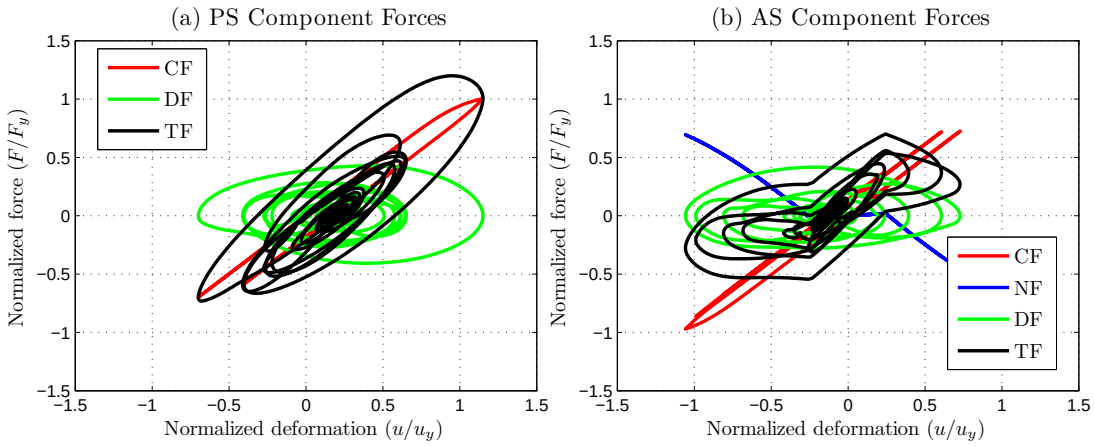

Figure 2.16 : F-D behavior of the components of PS and AS for Kobe ground motion

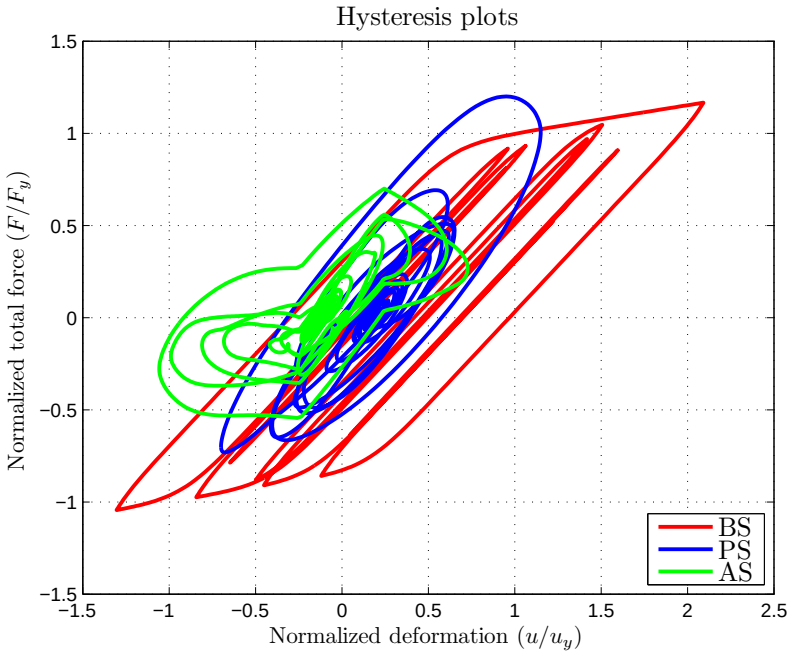

Figure 2.17 : Comparison of the assembly F-D behavior for Kobe ground motion

To demonstrate that the proposed adaptive negative stiffness device is effective for a range of structural systems (systems with different natural frequencies) response

Table 2.2 : Summary of simulation results for recorded ground motions

PI	System	ElCentro #5 FN	Lucerne Valley FN	Rinaldi FN	Erzincan NS	Newhall FN	Sylmar FN	Pacoima
J_1	BS	0.72	0.98	1.00	0.68	1.66	1.24	0.61
	PS	0.48	0.47	0.64	0.45	0.93	0.65	0.45
	AS	0.64	0.69	0.83	0.56	0.93	0.78	0.55
J_2	BS	4.01	7.86	2.90	3.42	1.81	6.46	2.30
	PS	2.83	4.19	2.05	2.41	1.63	4.79	1.81
	AS	2.30	3.52	1.36	1.96	0.99	2.66	1.40
J_3	BS	0.72	0.93	0.97	0.68	1.10	1.03	0.61
	PS	0.48	0.47	0.64	0.45	0.90	0.65	0.45
	AS	0.29	0.28	0.30	0.27	0.31	0.30	0.27
J_4	BS	0.72	0.93	0.97	0.68	1.10	1.03	0.61
	PS	0.48	0.47	0.64	0.45	0.90	0.65	0.45
	AS	0.64	0.69	0.82	0.56	0.90	0.78	0.55

spectra are generated for BS, PS and AS. Responses are presented in dimensionless π-terms, displacement $u\omega_p^2/a_p$, base shear-F_{shear}/ma_p, acceleration-$\ddot{u}/a_p$and frequency-T_s/T_p. Where, a_p is the pulse-amplitude of the acceleration, ω_p is the frequency of the pulse, T_s and T_p are the time-periods of structure and pulse, respectively. Makris and Black [154, 155] have developed cycloidal pulses that are representative of the actual recorded ground motions. These cycloidal pulses and recorded ground motion data are used to test the performance of the AS. Response spectra is generated for both cycloidal pulses and recorded ground motions. Response-spectra plots are represented in dimensionless π-terms proposed by Makris and Black [155]. All the earthquake motions responses are represented by equivalent pulses and the corresponding amplitudes and time-periods for normalization. Response spectra of C_1 pulse type ground motion and Sylmar FN ground motion are shown in Figure 2.18 and Figure 2.19, respectively. For C_1 ground motion, the pulse-period, T_p=0.5 seconds is used to gen-

erate spectra in Figure 2.18. The Sylmar FN ground motion can be approximated by a C_2 pulse with a period (T_p) of 2.3 seconds and an acceleration peak (a_p) of 64.6 in/sec^2, which is used to normalize the spectra in Figure 2.19.

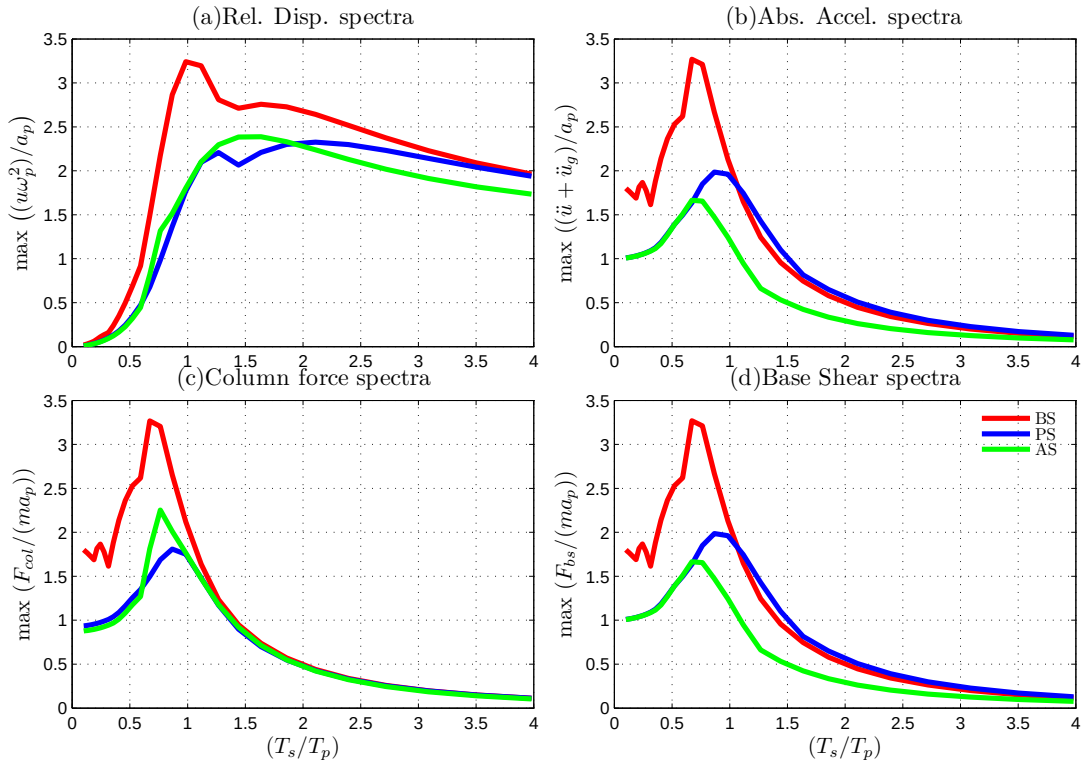

Figure 2.18 : Comparison of response spectra for C_1 type cycloidal pulse

For highly stiff structures ${}^{T_s}/_{T_p} < 0.5$, the response of the PS and AS are similar because the normalized displacement of the structure remains less than u'_y, shown in Figure 2.18(a),2.19(a). For $0.5 < {}^{T_s}/_{T_p} < 1.5$ peak acceleration and base shear of the AS is more than 30% lower than BS and PS because of the NSD, shown in Figure 2.18(b,c),2.19(b,c). The peak displacement of AS in the same region is 20% higher than the PS but 50% less than BS. For ${}^{T_s}/_{T_p} > 3$, all the three systems (BS,PS and AS) start yielding and the NSD starts stiffening so the peak acceleration and base

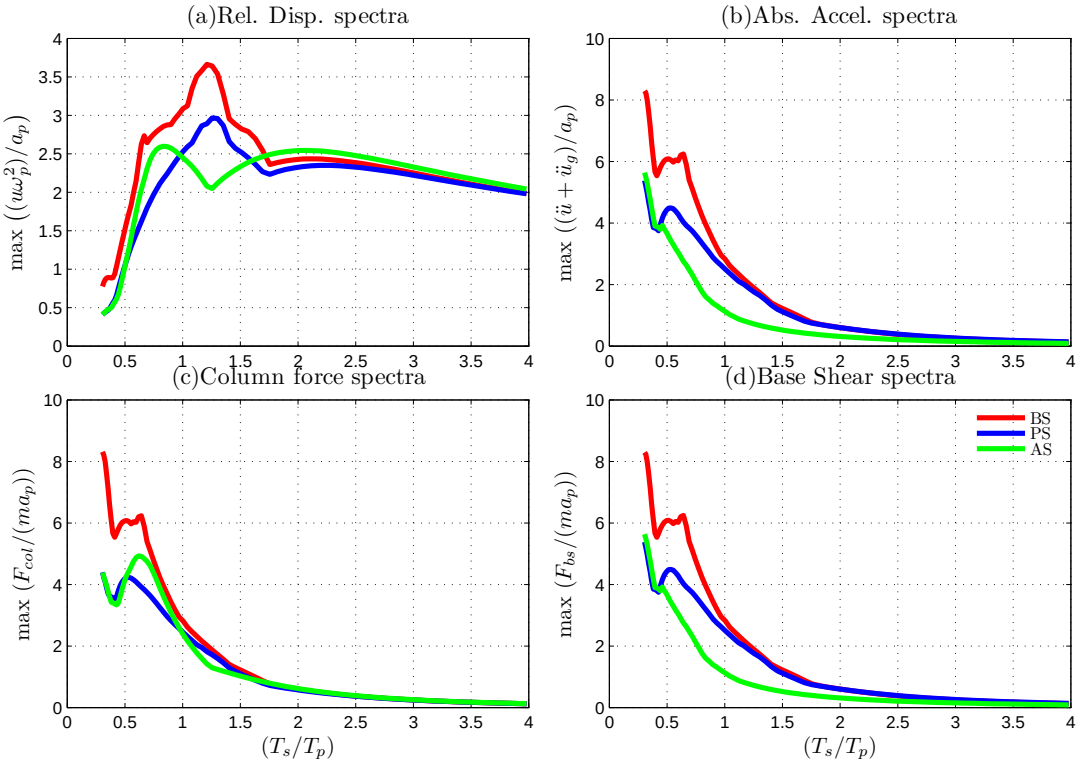

Figure 2.19 : Comparison of response spectra for Sylmar ground motion

shear of all the systems are same, shown in Figure 2.18(b,d),2.19(b,d). Column force in the AS is slightly higher than the PS around the peak in the spectra plots and it is almost identical for all other time-periods. Peak relative displacement of BS is always greater than the PS and AS. Key observations based on the response spectra plots of pulses and ground motion data are listed in Table 2.3.

2.6 Summary

The new idea of an "apparent weakening" is a novel concept that is proposed in this study. An "apparent weakening" is introduced in the structural system using a complementary negative stiffness device (NSD) that mimics "yielding" of the global

Table 2.3 : Summary of response spectra for cycloidal pulses

T_s/T_p Range	Description
$T_s/T_p < 0.5$	PS and AS have same response characteristics but they have a superior spectral characteristics compared to BS due to the passive damper
$0.5 < T_s/T_p < 1.5$	PS and AS have same response characteristics but they have a superior spectral characteristics compared to BS due to the passive damper
	Peak column force of AS is higher than PS
	Displacement has mixed behavior for PS and AS
$1.5 < T_s/T_p < 3.0$	AS has superior characteristics compared to PS and BS in peak acceleration and base shear
	And the column force of AS is same as PS
	Displacement has mixed behavior for PS and AS
$3.0 < T_s/T_p$	All the three systems yield in this region
	NSD starts stiffening resulting in increased peak acceleration and base shear responses
	All the systems exhibit same spectral characteristics

system thus attracting it away from the main structural system. Unlike the concept of weakening proposed earlier (summarized by Reinhorn et al., [147]), where the main structural system strength is reduced, the new system does not alter the original structural system, but produces effects compatible with an early yielding.

Adaptive negative stiffness system (AS) is an assembly of primary structure, NSD and passive damper (PD). AS is referred as adaptive system or adaptive stiffness system. The main objective of the adaptive system is to shift the yielding behavior of the structure to the NSD and reduce the base shear (foundation force) of the structure and at the same time limit the maximum displacement and acceleration of structure.

Adaptive systems belong to the category of passive seismic protection systems but they are more sophisticated than the regular passive systems. The adaptive system that is developed in this work consists of two components that are designed in a two step sequence, similar to the approach developed by Reinhorn et al. [147]. First an adaptive negative stiffness device, which is capable of changing its stiffness during lateral displacement, is developed based on the properties of the structure. This NSD is designed to exhibit negative stiffness behavior which upon the addition of structure properties will result in reduction of the stiffness of the structure and NSD assembly or "apparent weakening" thereby resulting in the reduction of the base shear of the assembly. Then a passive damper is designed for the assembly to reduce the displacements that are caused due to the "apparent weakening"-thereby reducing the base shear and displacement in a two step process.

This thesis presents comprehensive details of principles and the study of the behavior of the AS. The NSD is described in detail in the next chapter. Through numerical simulations and simulation studies it is shown that the concept of AS is very effective in elastic and some inelastic structural systems. The effectiveness and the superior performance of the AS as compared to a structural system with supplemental passive dampers when subjected to periodic and random input ground motions is demonstrated by numerical results.

Chapter 3

Negative Stiffness Device

True negative stiffness means that the force must assist motion, not oppose it as in the case of a positive stiffness spring. A passive device capable of exhibiting true negative stiffness, negative stiffness device (NSD), without external power supply is developed and studied in this work. The approach used to generate the negative stiffness is similar to the idea proposed by Nagarajaiah and Reinhorn [112]. A precompressed spring is used to generate the force to push the structure and a lever-mechanism is adapted to amplify the generated force. The concept of using springs to achieve a low stiffness system was first introduced by Molyneaux [156] for vibration isolation in aircraft systems. More recently, Platus [157, 158] developed ultra sensitive vibration isolation devices to isolate the the structure from horizontal-vibrations using pre-compressed springs. Thus far the application of negative stiffness devices has been limited to vibration isolation of small scale systems. Due to the large compression forces (usually of the order of self weight of structure) required to generate the desired negative stiffness, in the case of large structural systems, using pre-compressed springs was not perceived. So, a dual amplification mechanism is adapted along with the pre-compressed spring idea to achieve the desired level of forces to emulate a yielding system ("apparent weakening").

This chapter is organized as follows: Section-3.1 contains the detailed description of various components in the NSD and their connections. Working principle of NSD and the derivations pertaining to the development of equation of motion of NSD

is presented in section-3.2. More detailed model including the inertial terms and other nonlinear terms are presented in section-3.3. Description of the test setup used to characterize the behavior of NSD and the experimental results are summarized in section-3.4. Conclusions based on the comparisons between the observed experimental and predicted results are discussed in section-3.5.

3.1 NSD Description

The NSD is fabricated by Taylor Device Inc., Tonawanda. All the elements of NSD are made with mild steel. Schematic diagram and photograph of the NSD with labeled components is shown in Figure 3.1. NSD consists of (1) pre-compressed spring (2) two chevrons (CB1 and CB2) (3) two channel sections (4) pivot plate (5) lever-arm (6) two double pinned columns and (6) two gap spring assemblies (GSA).

Each channel section is welded to the loose ends of chevrons; bottom channel is welded to the bottom chevron (CB1) and the top channel is welded to the top chevron (CB2). One leg of each chevron is made out of steel-flats and the other leg is made of hollow square section (HSS). The two chevrons are coupled such that the steel flats of CB1 engulf the HSS of CB2 and viceversa. Pre-compressed spring (CS), made out of cylindrical steel tube by machining a helical groove along the axis of the cylinder, is placed vertically between the two chevron braces CB1 and CB2, as shown in Figure 3.1. Since the CS is pre-loaded, it will exert force to push the chevrons closer. To retain the chevrons at certain spacing, two double pinned columns (DPC) are connected to the channels of chevrons braces at either ends. Essentially, the pre-load force stored in the CS is balanced by the tension in DPCs; hence, NSD is self-contained for the vertical forces.

As mentioned earlier, an amplification mechanism is also incorporated using a

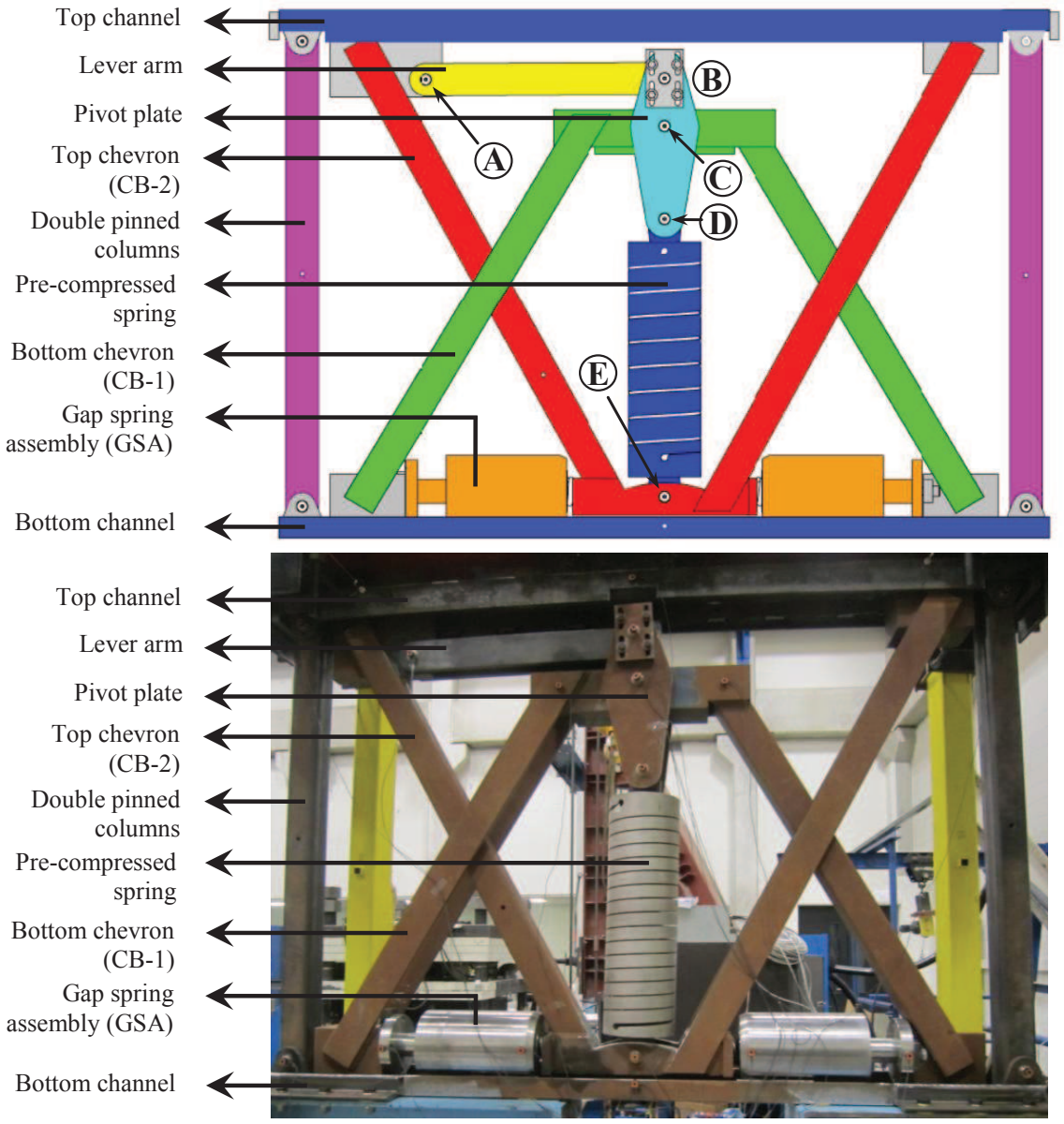

Figure 3.1 : Schematic diagram and photograph of NSD

simple lever principle. To achieve this, pivot-plate and lever-arm are added to the device. Pivot-plate is connected to the top of CB1 using 1 *in.* diameter pins. Instead of connecting the top of CS directly to the CB1, it is connected to the bottom of

pivot-plate. The top of pivot plate is connected to the lever-arm which in turn is connected to the top channel of NSD. Two elastic-bilinear springs, referred as gap-spring assemblies (GSA), are placed horizontally, connecting CB2 and the bottom channel of NSD.

GSA has three coil-spring and is equivalent to series connection of two coil-springs, two soft springs (S_1',S_1'') and a stiff spring (S_2), as shown in Figure 3.2. S_2 sits inside the cup and flushes against the CB2. GSA has a circular plate on one end and it is bolted horizontally to the bottom channel. The circular plate is connected to the rest of the assembly with a steel rod that can apply force and compress S_1' and S_1''. The working principle of NSD and GSA are explained in the next section.

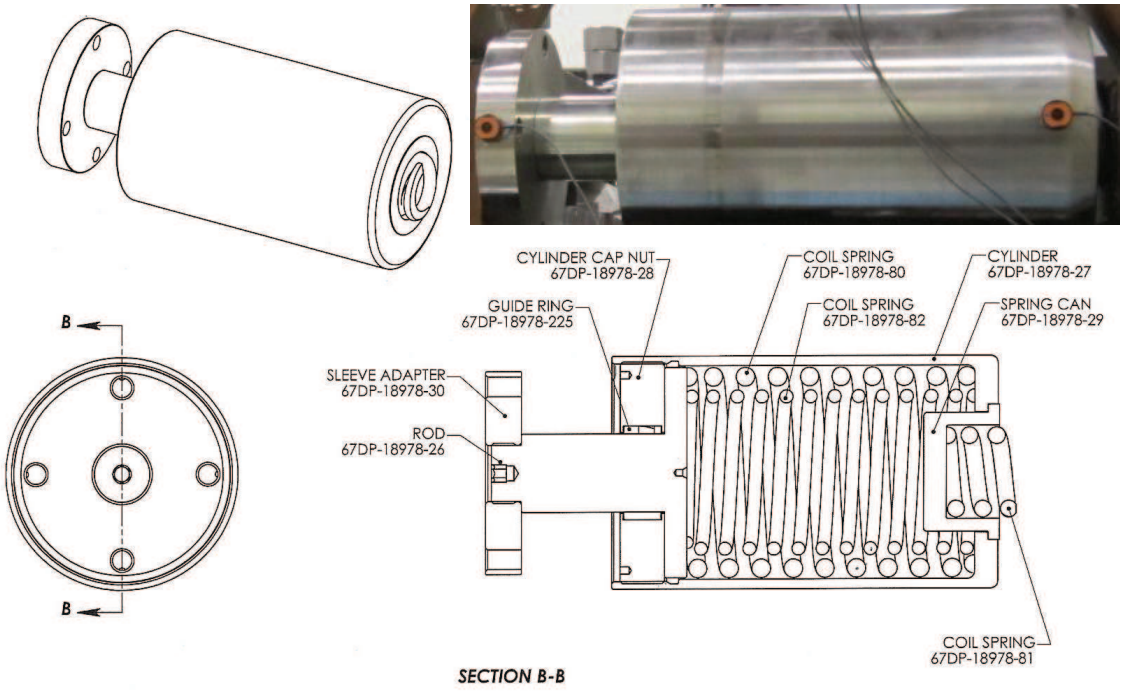

Figure 3.2 : Fabrication drawings of GSA showing the coil-springs. Inset: Photograph of GSA

3.2 Analytical Model

Consider a floor in the structure in which "apparent-weakening" is desired, the NSD should be bolted to the bottom of floor and the top of NSD is connected to the ceiling of the floor using a end-angle assembly that will transfer only the horizontal forces, described in detail in the next chapter. Five crucial points (pin-joints in the device) are marked in Figure 3.1 to explain the working principle of the device. Any inter-story structural deformation will result in the deformation of the top channel, CB2 and the lever-arm. Since the lever-arm is connected to the pivot plate (point-B) and the pivot plate is fixed at point-C, any deformation of point-B will result in rotation of pivot-plate about point-C. As a result, point-D will displace in the opposite direction to that of point-B. Also, the bottom of CS is connected to CB2, so, point-E will undergo same deformation as point-B. The total lateral deformation of the CS is magnified by comparison to the displacement of point A (a) by the ratio CD to BC and (b) due to the movement of point E in the opposite direction to D. Essentially, any deformation at the top of NSD will result in the horizontal deformation of CS both at the top and bottom; this is the dual amplification mentioned previously.

Assuming all the elements are rigid, deformed shape, undeformed shape and free body diagram of NSD for an arbitrary horizontal displacement of the structure, u, is shown in Figure 3.3. The pivot plate rotates by angle ψ, the CS rotates by an angle of θ and the lever-arm rotates by an angle of θ_{lv}. When the top of NSD moves horizontally, the DPCs rotate and all the elements connected to the top channel and CB2 undergo a vertical displacement h', given in Eq. 3.1

$$h' = h\left(1 - \sqrt{1 - \left(\frac{u}{h}\right)^2}\right) \tag{3.1}$$

where, h is the height of DPCs. Points A and E displaces horizontally by a distance u, same as the structure displacement, shown in Figure 3.3(b). Point-B moves by a $u' < u$ due to the rotation of the lever-arm. θ_{lv} and u' are coupled together by the compatibility equation given by Eq. 3.2-3.3

$$u' = u + l_{lv}\left(\cos(\theta_{lv}) - 1\right) \tag{3.2}$$

$$\theta_{lv} = \sin^{-1}\left(\frac{l_2 - h' - \sqrt{l_2^2 - (u')^2}}{l_{lv}}\right) \tag{3.3}$$

The simultaneous equations, Eq. 3.2 and 3.3, are transcendental equations. The solution is calculated numerically at each time step using Newton-Rhapson iteration. From the numerical study, it has been found that the solution converges in 6 to 10 iterations. However, since the maximum rotation of θ_{lv} is less than 3°, so θ_{lv} is assumed to be zero and $h = h'$. Since $u' \ll l_2$ and $h' \approx 0$, θ_{lv} only depends on the ratio l_2/l_{lv}. The angles ψ and θ are calculated using Eq. 3.4-3.5

$$\psi = \sin^{-1}\left(\frac{u'}{l_2}\right) \tag{3.4}$$

$$\theta = \tan^{-1}\left(\frac{\left[u + u'\frac{l_1}{l_2}\right]}{\left[l_p + l_1\left(1 - \cos(\psi)\right) + h'\right]}\right) \tag{3.5}$$

where, l_1 and l_2 are the lengths of pivot-plate CD and BC, respectively. l_p is the initial length of compressed spring, when $u = 0$. Once the points D and E move in opposite direction, length of the CS increases. Length of the CS in deformed configuration, l_{extd}, is calculated using Eq. 3.6

$$l_{extd} = \sqrt{\left(l_p + l_1(1 - \cos(\psi)) + h'\right)^2 + \left(l_1 \sin(\psi) + u\right)^2} \tag{3.6}$$

In the deformed configuration, the axial force exerted by CS, F_{sc}, is calculated using Eq. 3.7

$$F_{sc} = P_{in} + K_{sc}\,(l_{extd} - l_p) \tag{3.7}$$

where, P_{in} is the initial compressive force in the spring and K_{sc} is the stiffness of compressed spring. The axial force in lever arm, F_{lv}, is given by Eq. 3.8

$$F_{lv} = F_{sc}\frac{l_1 \sin(\psi + \theta)}{l_2 \cos(\psi - \theta_{lv})} \tag{3.8}$$

The total lateral force exerted by the NSD at the top of the device (without GSA), F_{vs}, is equal to the sum of horizontal forces at point-B and point-D (Eq. 3.9).

$$F_{vs} = F_{sc}\sin(\theta) + F_{lv}\cos(\theta_{lv}) \tag{3.9}$$

Assuming $\theta_{lv} = 0$ and $h = h'$, lateral force exerted by the NSD (without GSA) is given by

$$F_{vs} = F_{sc}\left[\sin\theta + \frac{l_1}{l_2}\frac{\sin(\theta + \psi)}{\cos\psi}\right] \tag{3.10}$$

Since the NSD consists of many moving elements, equation of motion for the NSD including the inertial terms is also developed. However, in the operating frequency range, the contribution of inertial terms is insignificant. For the sake of completeness, these derivations are presented next.

3.3 Dynamic Equation of Motion for the NSD

Free-body diagram of the components of NSD with dimensions is shown in Figure 3.4 for all the dimensions. Δ is the precompression in the spring. D_1 and D_2 are the densities (mass per unit length) of the two rotating elements (lever and spring

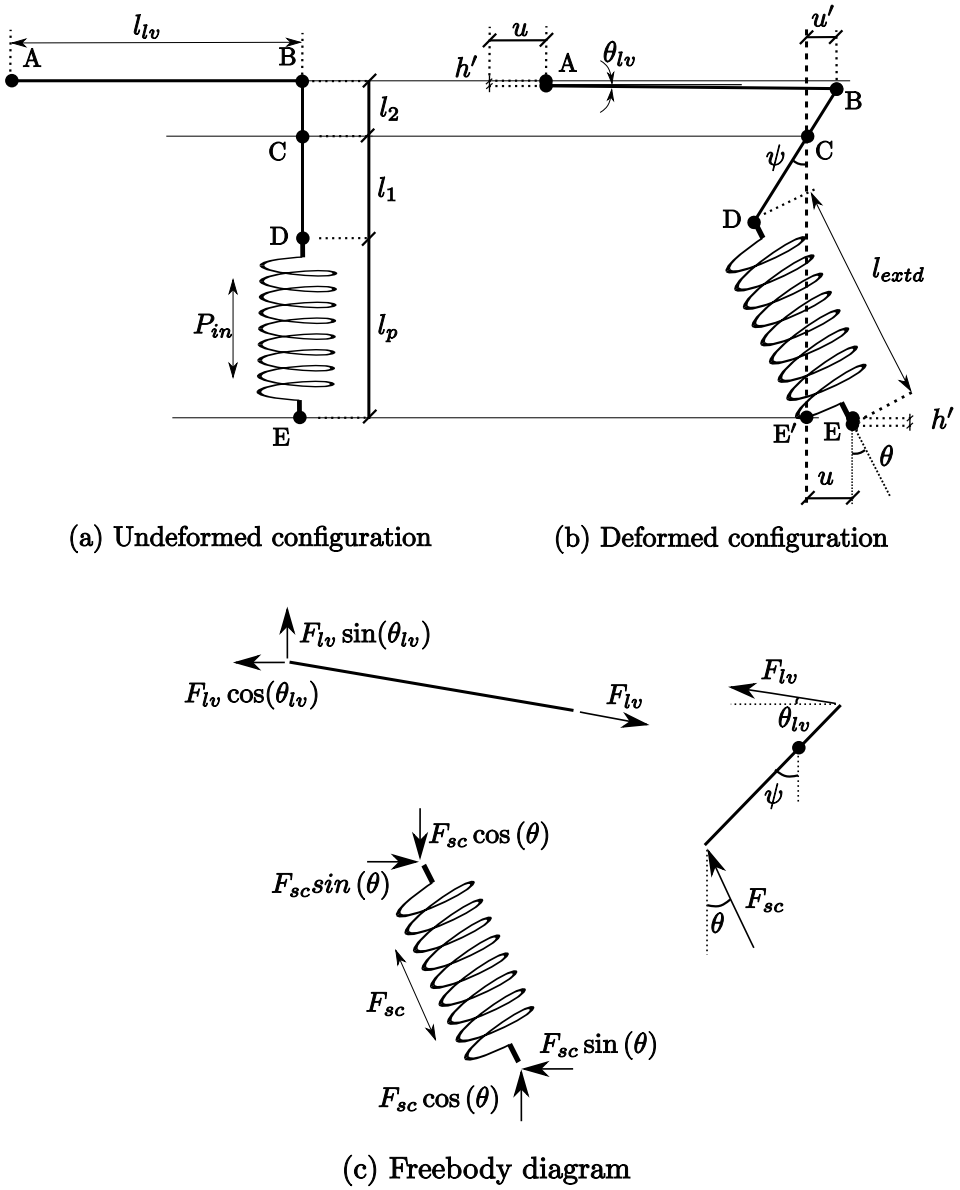

(a) Undeformed configuration (b) Deformed configuration

(c) Freebody diagram

Figure 3.3 : Undeformed shape, deformed shape and free body diagrams of components in NSD

respectively). I_1 and I_2 are the moment of inertias of the two rotating elements about their corresponding rotational axes (lever and spring respectively). M_2 is the mass of spring. θ is the rotation of the precompressed spring, ϕ is the rotation of the lever

arm and x_2 is the translational displacement of the spring. The drop in height of top channel (CB2) and rotation of lever-arm are neglected.

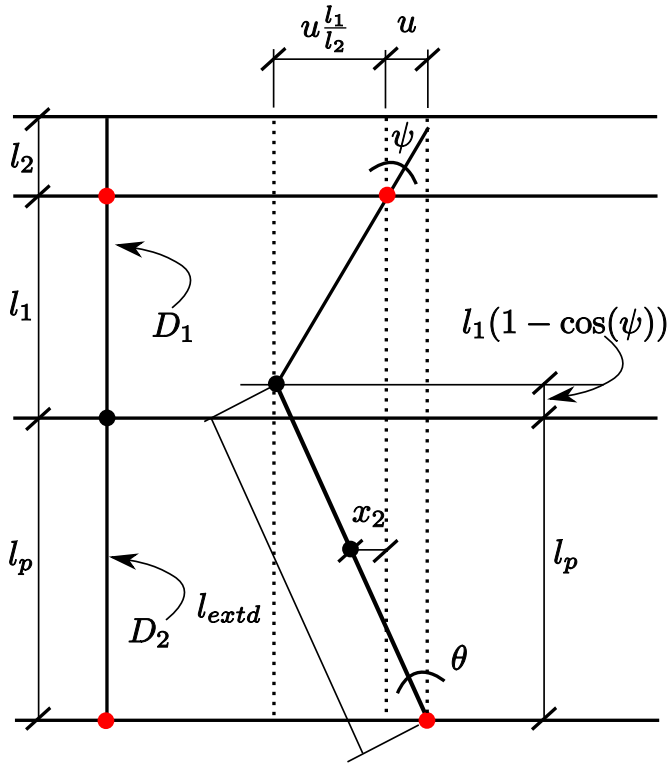

Figure 3.4 : Deformed shape of the NSD device

Angles θ and ψ are related to u by the Eq. 3.11-3.12

$$\theta = \sin^{-1}\left(\frac{u}{l_{extd}}\left(1+\frac{l_1}{l_2}\right)\right) \tag{3.11}$$

$$\psi = \sin^{-1}\left(\frac{u}{l_2}\right) \tag{3.12}$$

$$x_2 = \frac{l_{extd}}{2}\sin(\theta) - u \tag{3.13}$$

Extended length of the spring is

$$l_{extd} = \sqrt{\left(u + u\frac{l_1}{l_2}\right)^2 + \left(l_p + l_1\left(1 - \cos(\psi)\right)\right)^2} \tag{3.14}$$

$$= \sqrt{\left(u + u\frac{l_1}{l_2}\right)^2 + \left(l_p + l_1\left(1 - \frac{\sqrt{l_2^2 - u^2}}{l_2}\right)\right)^2} \tag{3.15}$$

Moment of inertia of the two elements about their corresponding rotational axes are

$$I_1 = D_1\left[\frac{(l_1 + l_2)^3}{12} + \frac{(l_1 + l_2)(l_1 - l_2)^2}{4}\right] \tag{3.16}$$

$$I_2 = D_2\frac{l_p l_{extd}^2}{3} \tag{3.17}$$

$$\dot{I}_2 = D_2\frac{2l_p l_{extd}}{3}\frac{\partial l_{extd}}{\partial u}\dot{u} \tag{3.18}$$

$$M_2 = D_2 l_p \tag{3.19}$$

Lagrangian of the system can be expressed as

$$\mathcal{L} = \mathcal{U} - \mathcal{K} \tag{3.20}$$

Potential energy, $\mathcal{U}$, is given by (ignoring the drop in the potential energy due to the vertical motion of the rotating masses)

$$\mathcal{U} = \frac{1}{2}K_{sc}\left(-\Delta + (l_{extd} - l_p)\right)^2 \tag{3.21}$$

Kinetic energy, $\mathcal{K}$, is given by (ignoring the kinetic energy due to translational motion of the rotating lever arm)

$$\mathcal{K} = \frac{1}{2}I_1\dot{\psi}^2 + \frac{1}{2}I_2\dot{\theta}^2 + \frac{1}{2}M_2\dot{x}_2^2 \tag{3.22}$$

Equation of motion for the system is obtained from

$$\frac{\partial \mathcal{L}}{\partial u} - \frac{d}{dt}\left(\frac{\partial \mathcal{L}}{\partial \dot{u}}\right) = 0 \tag{3.23}$$

$$\implies \quad \frac{\partial \mathcal{U}}{\partial u} - \frac{d}{dt}\left(\frac{\partial \mathcal{U}}{\partial \dot{u}}\right) - \frac{\partial \mathcal{K}}{\partial u} + \frac{d}{dt}\left(\frac{\partial \mathcal{K}}{\partial \dot{u}}\right) = 0 \tag{3.24}$$

Now, each term in the Eq. 3.24 are calculated in the subsequent sections

$$\frac{\partial \mathcal{U}}{\partial u} = K_{sc}\left(-\Delta + (l_{extd} - l_p)\right)\frac{\partial l_{extd}}{\partial u} \tag{3.25}$$

$$\frac{\partial l_{extd}}{\partial u} \quad = \quad \left[\frac{\left(1+\frac{l_1}{l_2}\right)^2 + \left(l_p + \frac{l_1}{l_2}\left(l_2 - \sqrt{l_2^2 - u^2}\right)\right)\frac{l_1}{l_2}\frac{1}{\sqrt{l_2^2-u^2}}}{\sqrt{\left(u + u\frac{l_1}{l_2}\right)^2 + \left(l_p + l_1\left(1 - \frac{\sqrt{l_2^2-u^2}}{l_2}\right)\right)^2}}\right] u \tag{3.26}$$

Let,

$$\rho = \left(1 + \frac{l_1}{l_2}\right) \quad , \quad X_0 = \sqrt{1 - \left(\frac{u}{l_2}\right)^2} \tag{3.27}$$

$$\frac{\partial X_0}{\partial u} = -\frac{u}{l_2^2 X_0} \quad , \quad X_1 = u\rho \tag{3.28}$$

$$X_2 = l_p + l_1\left(1 - X_0\right) \quad , \quad \frac{\partial X_2}{\partial u} = \frac{l_1 u}{l_2^2 X_0} \tag{3.29}$$

$$\frac{\partial^2 X_2}{\partial u^2} \quad = \quad \frac{l_1}{l_2^2}\left(\frac{1}{X_0} - \frac{u}{X_0^2}\frac{\partial X_0}{\partial u}\right) \tag{3.30}$$

$$X_3 = \rho^2 + \left(\frac{X_2}{X_0}\right)\left(\frac{l_1}{l_2^2}\right) \tag{3.31}$$

$$\frac{\partial X_3}{\partial u} = \left(\frac{l_1}{l_2^2}\right)\left(\frac{l_1 u}{l_2^2 X_0^2} + \frac{u X_2}{l_2^2 X_0^3}\right) \tag{3.32}$$

Eq. 3.26 can be written as

$$\frac{\partial l_{extd}}{\partial u} = \left(\frac{X_3}{l_{extd}}\right) u \tag{3.33}$$

$$\frac{\partial^2 l_{extd}}{\partial u^2} = \left(\frac{X_3}{l_{extd}} + \frac{u}{l_{extd}}\frac{\partial X_3}{\partial u} - \frac{X_3 u}{l_{extd}^2}\frac{\partial l_{extd}}{\partial u}\right) \tag{3.34}$$

$$\frac{\partial \mathcal{U}}{\partial \dot{u}} = 0 \tag{3.35}$$

$$\frac{\partial \mathcal{K}}{\partial u} = I_1\dot{\psi}\frac{\partial \dot{\psi}}{\partial u} + I_2\dot{\theta}\frac{\partial \dot{\theta}}{\partial u} + \frac{D_2 l_p l_{extd}\dot{\theta}^2}{3}\frac{\partial l_{extd}}{\partial u} + M_2\dot{x}_2\frac{\partial \dot{x}_2}{\partial u} \tag{3.36}$$

$$\frac{\partial \mathcal{K}}{\partial \dot{u}} = I_1\dot{\psi}\frac{\partial \dot{\psi}}{\partial \dot{u}} + I_2\dot{\theta}\frac{\partial \dot{\theta}}{\partial \dot{u}} + M_2\dot{x}_2\frac{\partial \dot{x}_2}{\partial \dot{u}} \tag{3.37}$$

$$\begin{aligned}\frac{d}{dt}\left(\frac{\partial \mathcal{K}}{\partial \dot{u}}\right) = {} & I_1\ddot{\psi}\frac{\partial \dot{\psi}}{\partial \dot{u}} + I_2\ddot{\theta}\frac{\partial \dot{\theta}}{\partial \dot{u}} + I_1\dot{\psi}\frac{d}{dt}\left(\frac{\partial \dot{\psi}}{\partial \dot{u}}\right) + I_2\dot{\theta}\frac{d}{dt}\left(\frac{\partial \dot{\theta}}{\partial \dot{u}}\right) + \dot{I}_2\dot{\theta}\frac{\partial \dot{\theta}}{\partial \dot{u}} \\ & + M_2\ddot{x}_2\frac{\partial \dot{x}_2}{\partial \dot{u}} + M_2\dot{x}_2\frac{d}{dt}\left(\frac{\partial \dot{x}_2}{\partial \dot{u}}\right)\end{aligned} \tag{3.38}$$

Contribution from kinetic energy terms is

$$\begin{aligned}\frac{\partial \mathcal{K}}{\partial u} - \frac{d}{dt}\left(\frac{\partial \mathcal{K}}{\partial \dot{u}}\right) = {} & \left[I_1\dot{\psi}\frac{\partial \dot{\psi}}{\partial u} + I_2\dot{\theta}\frac{\partial \dot{\theta}}{\partial u} + \frac{D_2 l_p l_{extd}\dot{\theta}^2}{3}\frac{\partial l_{extd}}{\partial u} + M_2\dot{x}_2\frac{\partial \dot{x}_2}{\partial u} + \dot{I}_2\dot{\theta}\frac{\partial \dot{\theta}}{\partial \dot{u}}\right] \\ & - \left[I_1\dot{\psi}\frac{d}{dt}\left(\frac{\partial \dot{\psi}}{\partial \dot{u}}\right) + I_2\dot{\theta}\frac{d}{dt}\left(\frac{\partial \dot{\theta}}{\partial \dot{u}}\right) + M_2\dot{x}_2\frac{d}{dt}\left(\frac{\partial \dot{x}_2}{\partial \dot{u}}\right)\right] \\ & - \left[I_1\ddot{\psi}\frac{\partial \dot{\psi}}{\partial \dot{u}} + I_2\ddot{\theta}\frac{\partial \dot{\theta}}{\partial \dot{u}} + M_2\ddot{x}_2\frac{\partial \dot{x}_2}{\partial \dot{u}}\right]\end{aligned} \tag{3.39}$$

Each of the terms in Eq. 3.36-3.38 are calculated in the following sections. From Eq. 3.12,

$$\frac{d\psi}{dt} = \frac{du}{dt}\frac{d\psi}{du} \tag{3.40}$$

$$\dot{\psi} = \dot{u}\frac{1}{l_2\sqrt{1-\frac{u^2}{l_2^2}}} = \frac{\dot{u}}{l_2 X_0} \tag{3.41}$$

$$\frac{\partial\dot{\psi}}{\partial u} = \frac{u\dot{u}}{l_2^3\left(\sqrt{1-\frac{u^2}{l_2^2}}\right)^3} = \frac{u\dot{u}}{l_2^3 X_0^3} \tag{3.42}$$

$$\frac{\partial\dot{\psi}}{\partial\dot{u}} = \frac{1}{l_2\sqrt{1-\frac{u^2}{l_2^2}}} = \frac{1}{l_2 X_0} \tag{3.43}$$

$$\frac{d}{dt}\left(\frac{\partial\dot{\psi}}{\partial\dot{u}}\right) = -\frac{1}{l_2 X_0^2}\frac{\partial X_0}{\partial u}\dot{u}\ ,\ \frac{d\dot{\psi}}{dt} = \frac{d}{dt}\left(\frac{\dot{u}}{l_2 X_0}\right) \tag{3.44}$$

$$\frac{d^2\psi}{dt^2} = \frac{\ddot{u}}{l_2 X_0} + \frac{u\dot{u}^2}{l_2^3}\frac{1}{\left(\sqrt{(1-\frac{u^2}{l_2^2})}\right)^3} \tag{3.45}$$

$$\ddot{\psi} = \frac{\ddot{u}}{l_2 X_0} + \frac{u\dot{u}^2}{(l_2 X_0)^3} \tag{3.46}$$

From Eq. 3.11

$$\frac{d\theta}{dt} = \frac{d\wp}{dt}\frac{d\theta}{d\wp} \tag{3.47}$$

assuming,

$$\wp = \frac{\rho u}{l_{extd}} \tag{3.48}$$

Derivatives of the variable θ are given below

$$\frac{d\theta}{d\wp} = \frac{l_{extd}}{\sqrt{l_{extd}^2 - \rho^2 u^2}} = \frac{l_{extd}}{X_2} \tag{3.49}$$

$$\frac{d\wp}{dt} = \frac{\rho\dot{u}}{l_{extd}} - \frac{\rho u}{l_{extd}^2}\frac{dl_{extd}}{dt} = \frac{\rho\dot{u}}{l_{extd}} - \frac{\rho u\dot{u}}{l_{extd}^2}\frac{\partial l_{extd}}{\partial u} \tag{3.50}$$

$$\dot{\theta} = \frac{\rho\dot{u}}{X_2}\left(1 - \frac{u}{l_{extd}}\frac{\partial l_{extd}}{\partial u}\right) \tag{3.51}$$

$$X_4 = \left(1 - \frac{u}{l_{extd}}\frac{\partial l_{extd}}{\partial u}\right)\ ,\ \dot{\theta} = \frac{\rho\dot{u}}{X_2}X_4 \tag{3.52}$$

$$\frac{\partial\dot{\theta}}{\partial u} = -\frac{\rho\dot{u}}{X_2^2}\frac{\partial X_2}{\partial u}X_4 + \frac{\rho\dot{u}}{X_2}\frac{\partial X_4}{\partial u} \tag{3.53}$$

$$\frac{\partial X_4}{\partial u} = -\left(\frac{1}{l_{extd}}\frac{\partial l_{extd}}{\partial u} - \frac{u}{l_{extd}^2}\left(\frac{\partial l_{extd}}{\partial u}\right)^2 + \frac{u}{l_{extd}}\frac{\partial^2 l_{extd}}{\partial u^2}\right) \tag{3.54}$$

$$\frac{\partial\dot{\theta}}{\partial\dot{u}} = \frac{\rho}{X_2}\left(1 - \frac{u}{l_{extd}}\frac{\partial l_{extd}}{\partial u}\right) = \frac{\rho X_4}{X_2} \tag{3.55}$$

$$\frac{d}{dt}\left(\frac{\partial\dot{\theta}}{\partial\dot{u}}\right) = \left(\frac{\rho}{X_2}\frac{\partial X_4}{\partial u}\dot{u} - \frac{\rho X_4}{X_2^2}\frac{\partial X_2}{\partial u}\dot{u}\right) \tag{3.56}$$

$$\frac{d\dot{\theta}}{dt} = \frac{\rho X_4}{X_2}\ddot{u} + \frac{\rho\dot{u}^2}{X_2}\frac{\partial X_4}{\partial u} - \frac{\rho X_4\dot{u}^2}{X_2^2}\frac{\partial X_2}{\partial u} \tag{3.57}$$

Derivatives of the variable x_2 are given below:

$$\frac{dx_2}{dt} = \frac{d}{dt}\left(\frac{l_{extd}}{2}\sin(\theta) - u\right) = \frac{d}{dt}\left(\frac{\rho u}{2} - u\right) \tag{3.58}$$

$$\dot{x}_2 = \left(\frac{\rho}{2} - 1\right)\dot{u} \tag{3.59}$$

$$\frac{\partial \dot{x}_2}{\partial u} = 0 \ , \ \ddot{x}_2 = \left(\frac{\rho}{2} - 1\right)\ddot{u} \tag{3.60}$$

$$\frac{\partial \dot{x}_2}{\partial \dot{u}} = \left(\frac{\rho}{2} - 1\right) \ , \ \frac{d}{dt}\left(\frac{\partial \dot{x}_2}{\partial \dot{u}}\right) = 0 \tag{3.61}$$

3.3.1 Numerical Simulations

Numerical values used for this simulation studies are shown in Table-3.1. A set of

Table 3.1 : Numerical values used in the simulations

Variable	Value	Value	Variable
l_1	10 in	5.13 in	l_2
l_p	30 in	10.5 kip	P_{in}
K_{sc}	3 kip/in	3.5 in	Δ
D_1	5×10^{-6}	7.5×10^{-6}	D_2

displacement, velocity and acceleration profiles are used to find the dynamic characteristics of NSD. Normalized response-profiles are shown in Figure 3.5. Frequency of the response is 2 Hz. Profile of angles as a function of displacement are shown in Figure 3.6. Moment-of-inertia of lever and spring are shown in Figure 3.7. Moment of inertia of lever remains constant but the moment of inertia of spring increases as the length of spring increases. Differentials of variables ψ, θ and x_2 are shown in Figures 3.8,3.9 and 3.10, respectively. Force displacements comparing all the terms is shown in Figure 3.11. In Figure 3.11, red colored line is the F-D plot due to precompression

in the spring and it is independent of the external excitation. Black colored line is due to the inertial terms and is proportional to the acceleration, $\ddot{u}$. The green colored line is the contribution from nonlinear term, $\dot{u}^2$. Total dynamic force is the sum of contributions from nonlinear-term and inertial term, shown as purple line in Figure 3.11. Total force exerted by the NSD on the structure is shown as a blue line.

The force contribution due to the dynamics of the device at different frequencies is shown in Figure 3.13. Effective force exerted by the NSD is shown in Figure 3.12.

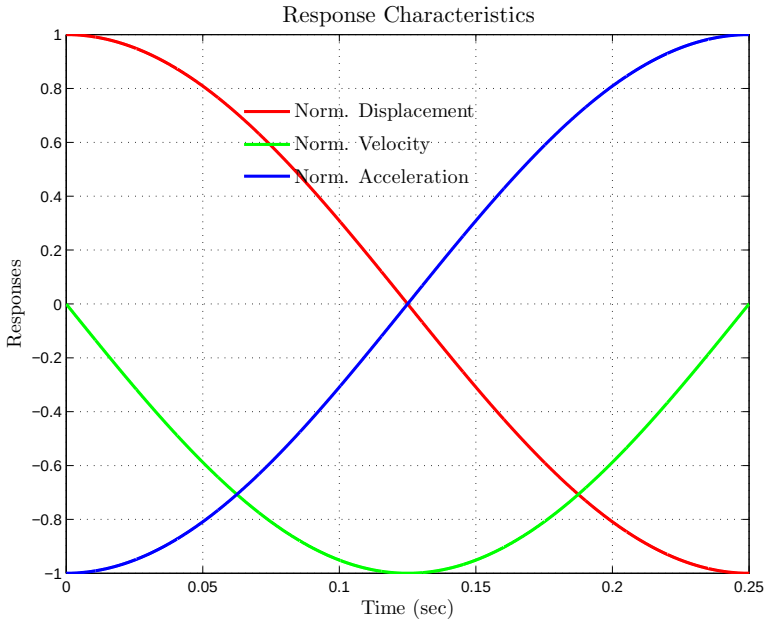

Figure 3.5 : Normalized response profiles used for u, $\dot{u}$ and $\ddot{u}$

Next, the working principle and the analytical model for the GSA is presented.

3.3.2 Gap spring assembly

"Apparent yield-displacement", described in section-2.4.1, is achieved using the the GSA. Two GSAs are present in each NSD and each GSA exhibits bilinear elastic

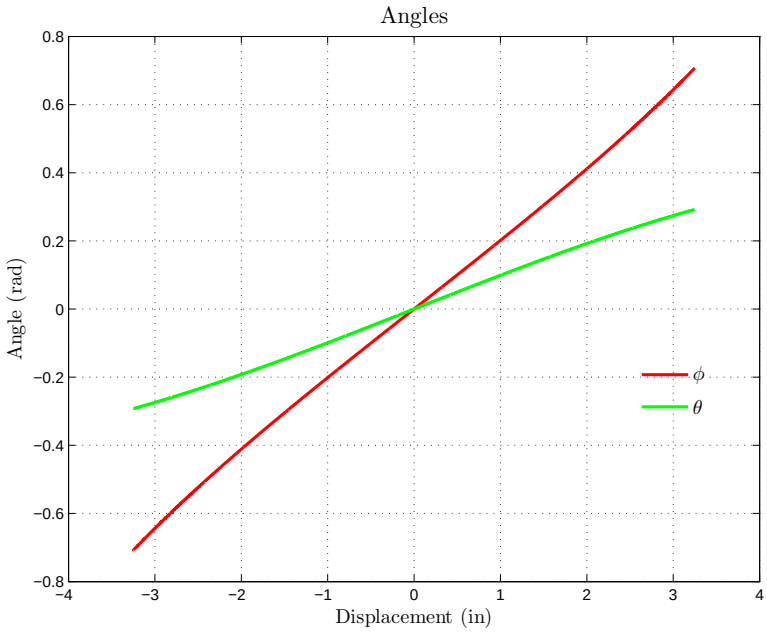

Figure 3.6 : Behavior of various parameters: ψ and θ as a function of displacement

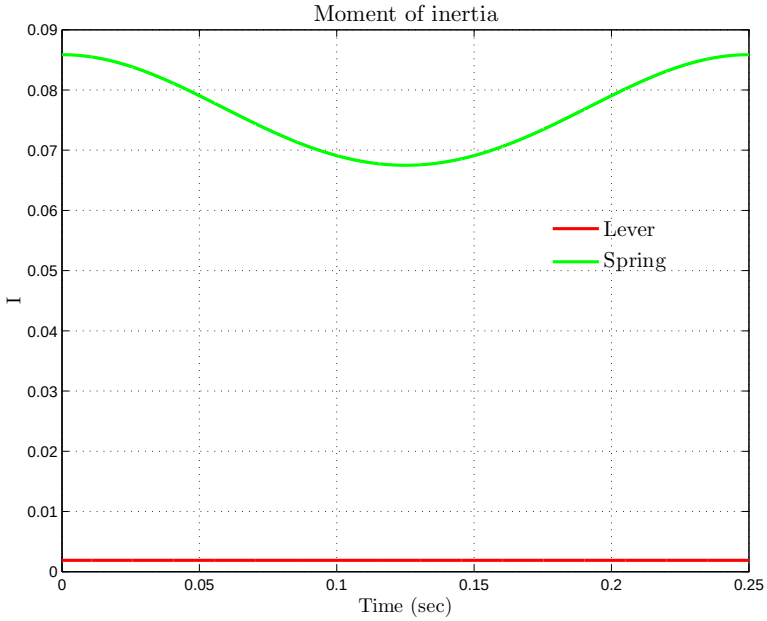

Figure 3.7 : Moment of inertia of rotating elements as a function of time

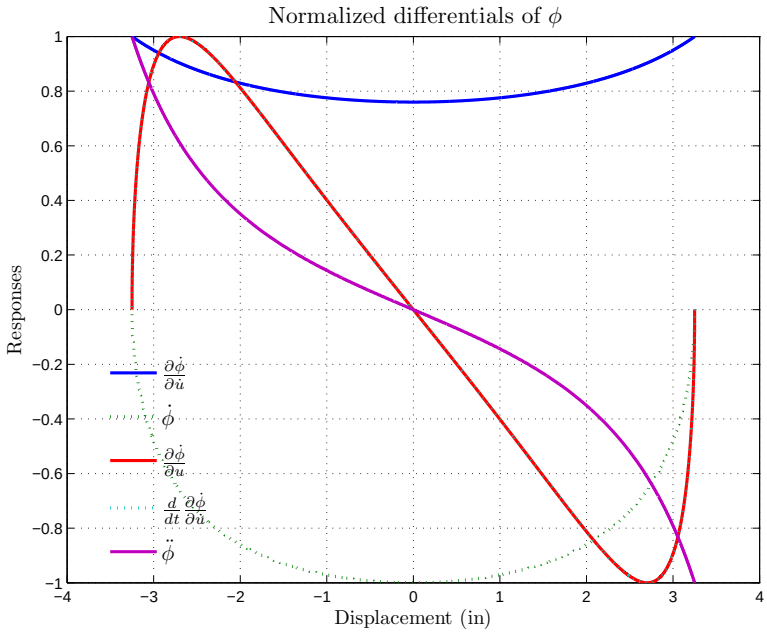

Figure 3.8 : Comparison of the inertial and differential terms in the EOM of NSD

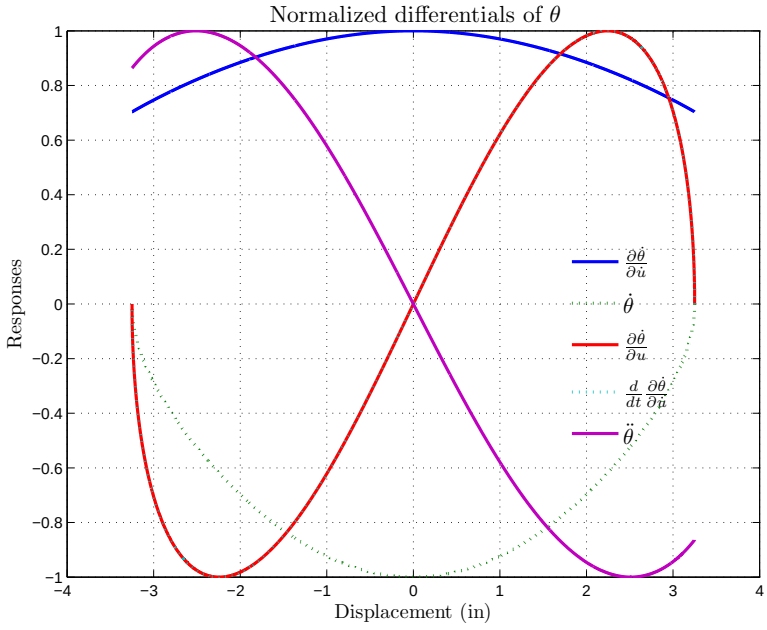

Figure 3.9 : Differentials of θ as a function of displacement

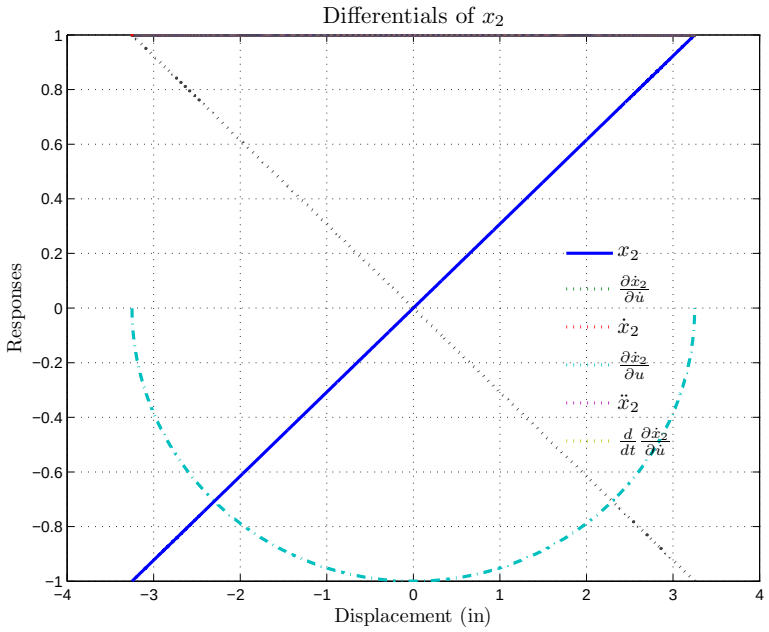

Figure 3.10 : Differentials of x_2 as a function of displacement

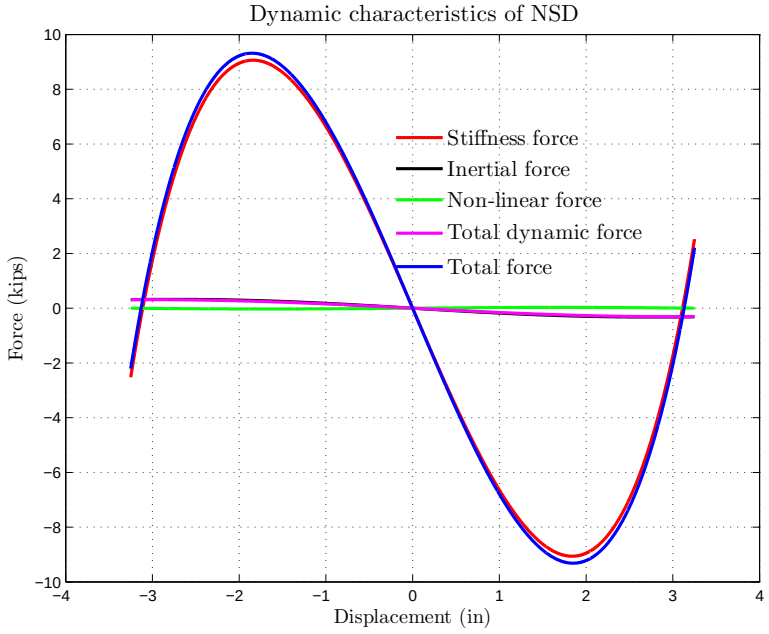

Figure 3.11 : Comparing force-deformation plots of different terms

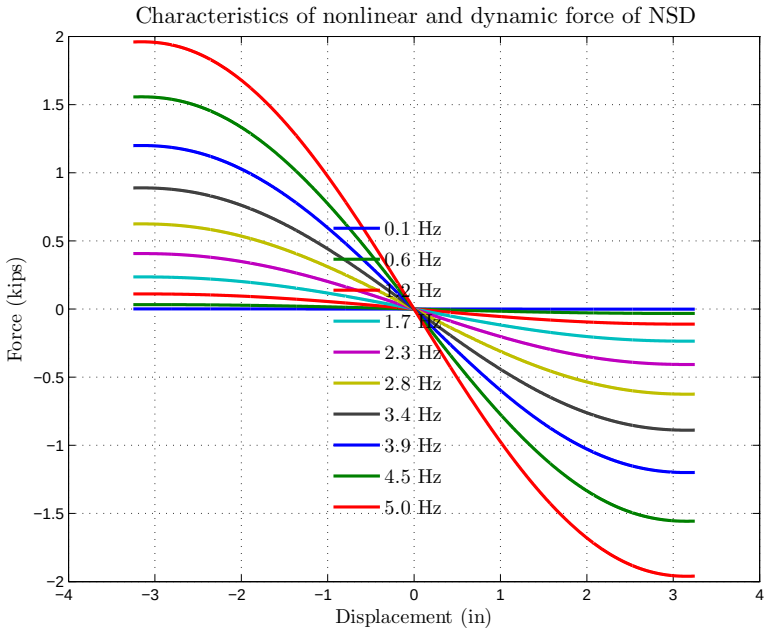

Figure 3.12 : Comparing force-deformation plots of different terms

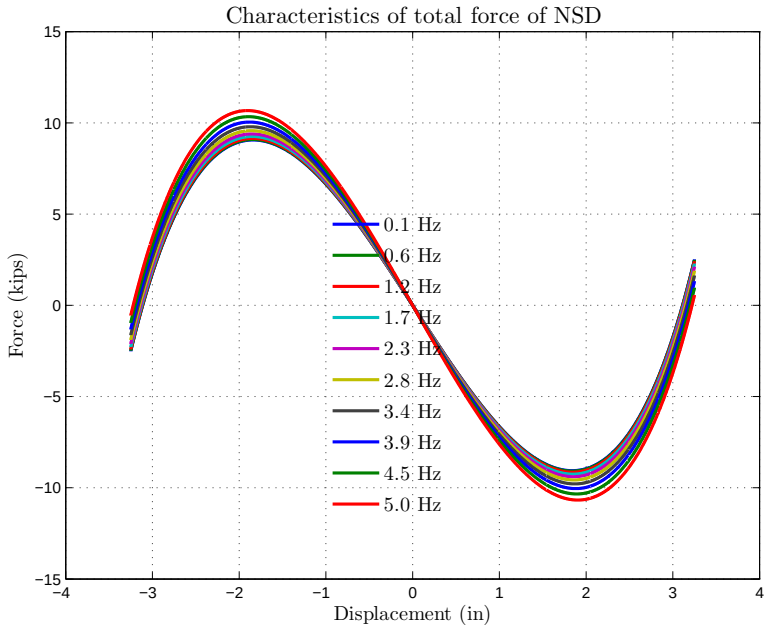

Figure 3.13 : Comparing the total force exerted by NSD at different frequencies

behavior. They are designed in such a way that one GSA engages for positive displacements and the other for negative displacements. Equivalent system for the GSA is shown in Figure 3.14. GSA consists of (1) soft spring (S_1) with a stiffness of, K_{S1}, and a pre-load, P_{S1} (2) stiff spring (S_2) with a stiffness, K_{S2}, in series to achieve bilinear-elastic structure. Free length of S_1 is L_{S1} and the installed length is L'_{S1}. Pre-load in S_1 is calculated using Eq. 3.62

$$P_{S1} = K_{S1}\left(L_{S1} - L'_{S1}\right) \tag{3.62}$$

When a load, F_g, is applied on the GSA, since spring-S_1 is pre-loaded, spring-S_2 deforms until the compression-force in S_2 reaches P_{S1}. Once the external load is greater than P_{S1}, both S_1 and S_2 deform. The force exerted by GSA is given in Eq. 3.63

$$F_g = \begin{cases} K_{S2}u & \text{if } |u| \leq \frac{P_{S1}}{K_{S2}}, \\ P_{S1} + \frac{K_{S1}K_{S2}}{K_{S1}+K_{S2}} & \text{if } |u| > \frac{P_{S1}}{K_{S2}} \end{cases} \tag{3.63}$$

For the GSA used in this study, the desired stiffness of the soft spring is 0.15 *kip/in.* A coiled-spring with 0.15 *kip/in* was not available so two soft-springs, S'_1 and S''_1, with stiffness of 0.11 *kip/in* and 0.04 *kip/in*, respectively and they have a free length of 25.9 *in.*. They are compressed to 9.7 *in.* (a pre-load of 2.25 kips, together) and placed inside the cylindrical case. The spring S_3, has a stiffness of 7.5 *kip/in* and is placed in a cup outside the cylindrical case. The correlation between the spring stiffness and the desired NSD properties is explained next.

Force displacement characteristics of the pre-compressed spring, GSA and the NSD are shown in Figure 3.15(a),(b) and (c) respectively. Five distinct points are shown in Figure 3.15(a). Point "0" is the initial position and lateral force exerted

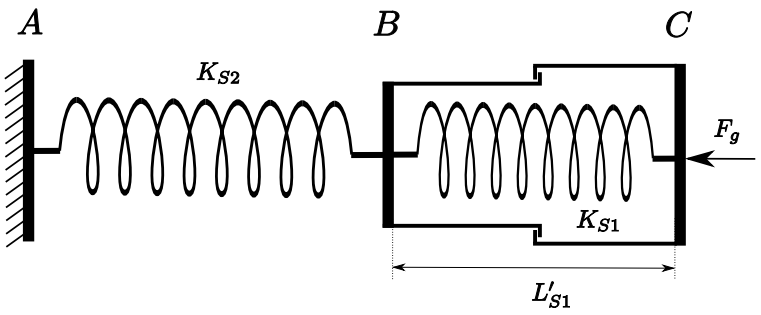

Figure 3.14 : Schematic of the equivalent system of GSA

by the vertical spring, F_{vs}, is zero. When the precompressed vertical spring is displaced to an inclined position at angle θ from the vertical, the axial force in the pre-compressed spring, F_{sc}, is given by Eq. 3.7. At point-"1" in Figure 3.15(a) the secant stiffness $(-F_{vs1}/u'_y)$ and tangential stiffness (slope at point-"1") are both negative. At point-"2" the secant stiffness $(-F_{vs2}/u_2)$ is still negative and tangential stiffness reaches zero. At point-"3" the secant stiffness $(-F_{vs3}/u_3)$ is still negative but the tangential stiffness becomes positive. At point-"4" secant stiffness becomes zero and the tangential stiffness remains positive. At point-"4", $l_{extd} = l_p + P_{in}/K_{sc}$, hence the net axial force in the inclined spring becomes zero, $F_{sc} = 0$, or all the pre-compression force is lost; thus $F_{vs} = 0$. At point-"5" both the secant stiffness and tangential stiffness are positive.

The horizontal spring exhibits elastic-bilinear behavior, the transition in stiffness occurs at displacement u'_y and stiffness of the spring is zero for $|u| > u'_y$, as shown in Figure 3.15(b). Since it is not possible to achieve zero stiffness beyond u'_y, a soft spring is used in the GSA used in this study. The total force-displacement characteristics of the NSD is shown in Figure 3.15(c). The initial stiffness of the horizontal spring, F_{g1}/u'_y, is designed to match (or be greater than) the initial negative

stiffness of the inclined spring resulting in zero stiffness for the NSD till $|u| \leq u'_y$ i.e., $F_{g1} - F_{v1} = 0$. The stiffness of the horizontal spring, K_g, beyond u'_y is chosen to be zero (or a very low value); hence, essentially the behavior of vertical spring is reflected in the NSD for displacements beyond u'_y. NSD exhibits positive secant and tangential stiffness beyond point-"3", as shown in Figure 3.15(c). The total lateral force, F_{NSD}, combination of pre-compressed spring and GSA, is given by Eq.

$$F_{NSD} = F_{vs} + F_g \tag{3.64}$$

The NSD behaves like a nonlinear-elastic spring with variable stiffness as described above. All the equations developed so far in this chapter are based on the assumption that all the elements are rigid. Assuming that CB1, CB2 and the top channel are flexible, the force exerted by NSD on the structure is given by,

$$F_{NSD} = F_{vs} + F_g + K_f u_f \tag{3.65}$$

where, K_f stands for the equivalent stiffness due to the flexibility of CB1, CB2 and top channel. u_f is the equivalent deformation due to the flexing of the chevron braces.

The impact of preload in the CS, P_{in}, and the stiffness of CS, K_{sc}, on the overall behavior of NSD is studied next. F-D behavior of NSD with different K_{sc} and $P_{in} =$ 3.7 *kip* is shown in Figure 3.16 and the behavior of NSD with $K_{sc} = 1$ *kip/in* and different P_{in} are shown in Figure 3.17. For the plots shown in Figure 3.16 and 3.17, $l_1 = 10$, $l_2 = 5$ and $l_p = 30$ are used and GSA is not added. By changing the K_{sc} value, keeping P_{in} same, initial stiffness of NSD remains the same but the rate at which NSD looses the preload increases as a result the NSD stiffens faster with

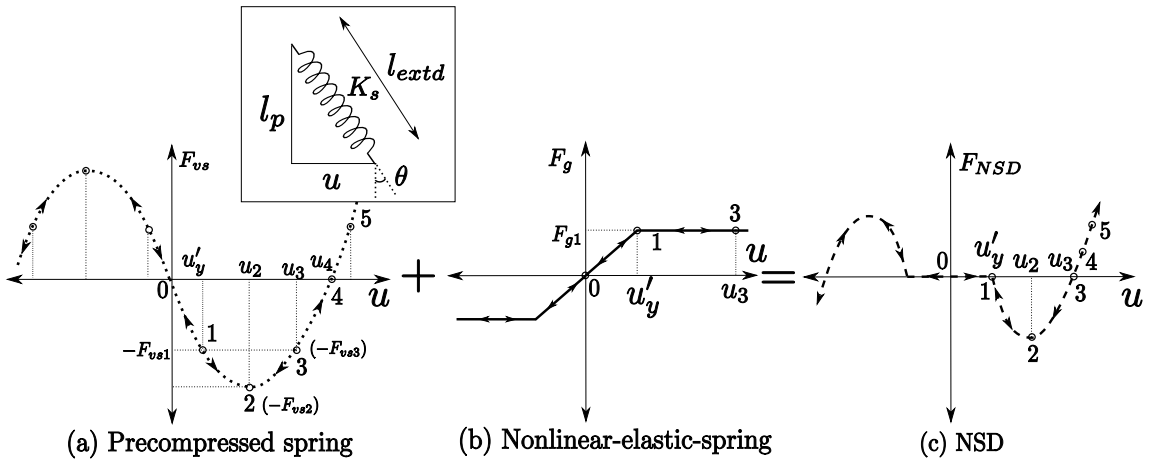

Figure 3.15 : Schematic diagram of the force displacement plots of NSD

higher stiffness of CS. By keeping the stiffness of CS same and increasing the preload, initial stiffness and stiffening point are proportional to the amount of pre-load but the stiffness beyond the stiffening point remains the same.

3.3.3 Significance of dual amplification

Using a pre-compressed spring to achieve negative stiffness has already been implemented in aerospace and automobile industry, but the real advantage of NSD comes from the dual amplification adapted in the device. The two amplification approaches are (1) double brace mechanism, wherein the point-E moves with the structure and (2) lever mechanism to amplify the deformation of point-D. To elucidate the advantage of the NSD developed in this study, three NSDs with different configurations are compared. The three systems are (1) the actual NSD (NSD-1), equivalent schematic diagram shown in Figure 3.18(a) (2) NSD without the double chevron connection (NSD-2), schematic diagram shown in Figure 3.18(b) and (3) NSD without double chevron brace and the lever arm (NSD-3), schematic diagram shown in Figure 3.18(c).

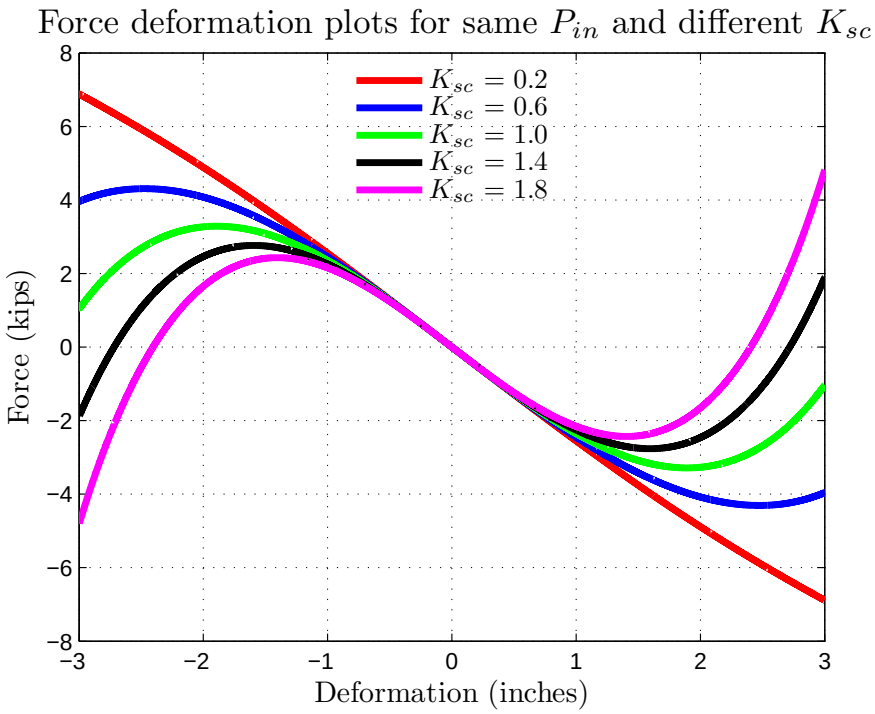

Figure 3.16 : The behavior of NSD with the change in K_{sc} value

Although double chevrons are used in NSD-3, they do not amplify the deformation of NSD; it is just a provision to reduce the length of CS instead of spanning the floor height. In NSD-2, the point-E is directly connected to the bottom of NSD, so only the lever-mechanism amplify the deformation of point-D.

Since the connections and the geometry of the system has changed, the force

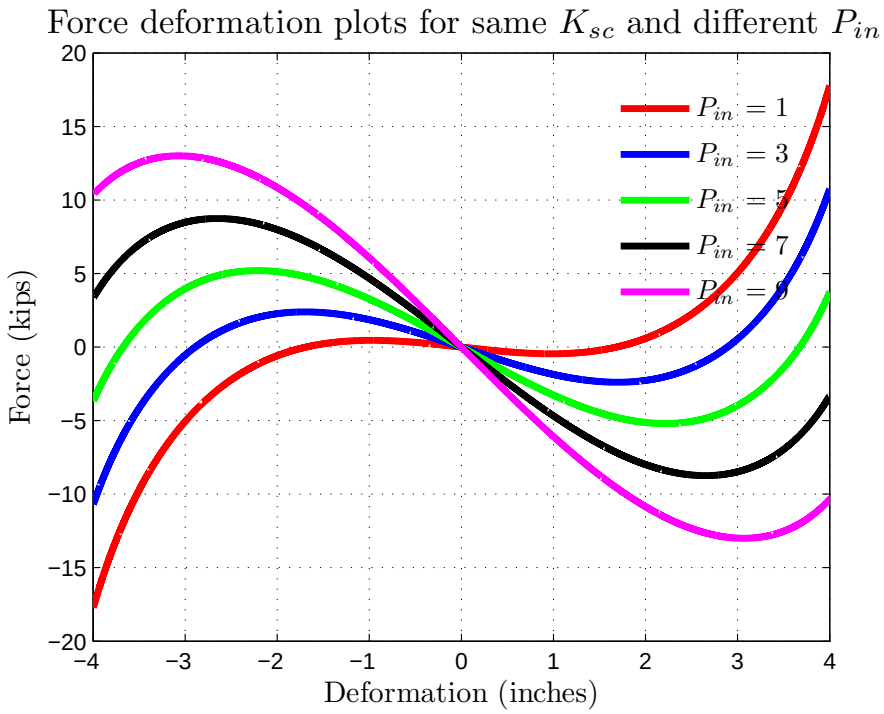

Figure 3.17 : The behavior of NSD with the change in P_{in} value

exerted by NSD-2 is calculated using Eq. 3.66-3.70

$$F_{NSD2} = F_{sc}\frac{\sin(\theta+\psi)}{\cos(\psi)} \tag{3.66}$$

$$F_{sc} = \left((l_{extd} - l_p) - {}^{P_{in}}/_{K_{sc}}\right) K_{sc} \tag{3.67}$$

$$\sin(\psi) = \frac{u}{l_2} \tag{3.68}$$

$$\tan(\theta) = \frac{u^{l_1}/_{l_2}}{l_{extd}} \tag{3.69}$$

$$l_{extd} = \sqrt{\left(u^{l_1}/_{l_2}\right)^2 + \left(l_p + l_1\left(1-\cos(\phi)\right)\right)^2} \tag{3.70}$$

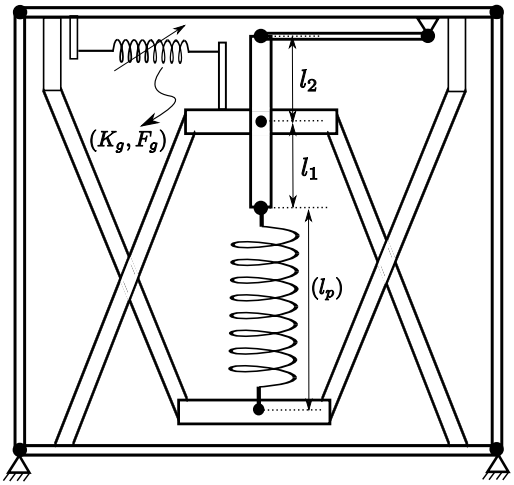

(a) Equivalent schematic diagram of the NSD

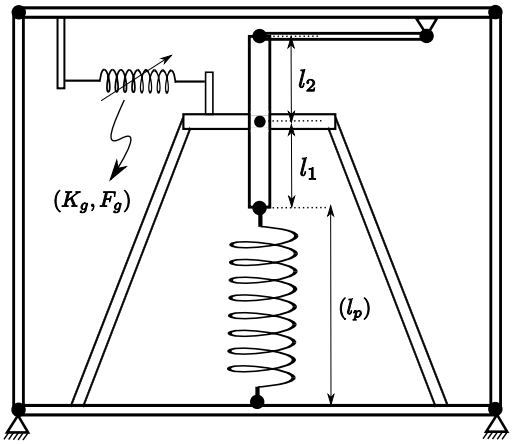

(b) Schematic diagram of the NSD-1 without double chevron connection

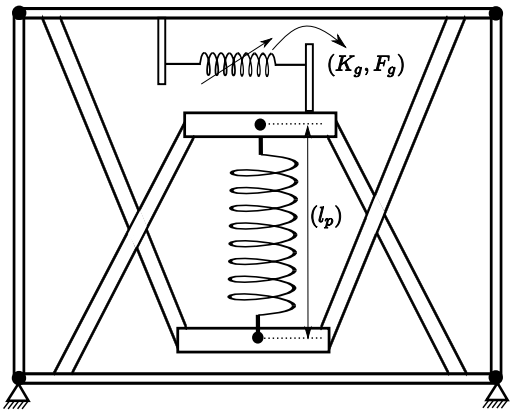

(c) Schematic diagram of the NSD-2 without lever and double chevron connection

Figure 3.18 : Schematic diagram of the NSD-3

The force exerted by NSD-3 is given by Eq. 3.71-3.74

$$F_{NSD3} = F_{sc}\sin(\theta) \tag{3.71}$$

$$F_{sc} = \left((l_{extd} - l_p) - {}^{P_{in}}/_{K_{sc}}\right) K_{sc} \tag{3.72}$$

$$\sin(\theta) = \frac{u}{l_{extd}} \tag{3.73}$$

$$l_{extd} = \sqrt{u^2 + l_p^2} \tag{3.74}$$

Assuming the dimensions l_p, l_1 and l_2 are constant, the values of P_{in} and K_{sc} desired to achieve the same force-displacement behavior in all the three case is shown in Table 3.2. For NSD-1 and NSD-2 two cases are presented with different lever ratio, $\epsilon = 1$ and $\epsilon = 2$. The force-deformation behavior of all the five systems is shown in Figure 3.19. In Table 3.2, the values of P_{in} and K_{sc} are scaled with the yield-strength and the stiffness of the structure for which they are designed and shown in parenthesis. Increasing the lever ratio will reduce the required stiffness of the CS by more than nine folds and the desired preload is reduced by more than three folds (compare the data of $\epsilon = 1$ and $\epsilon = 2$ in Table 3.2). The double chevron connection will reduce the demand on the stiffness and preload of the CS by 50%. With just the CS (NSD-3), the value of K_{sc} is two orders more than the NSD-1 and P_{in} is one order more than NSD-1. The preload and stiffness of CS in the case of NSD-1 ($\epsilon = 2$) shows that "apparent weakening" is practically feasible even in structures with large mass. Next, the experimental setup used to test the NSD and the observed experimental results are compared with simulation results using the analytical models used in this chapter.

Table 3.2 : Summary of the values used for different configurations of NSDs

Variable	NSD-1 ($\epsilon = 2$)	NSD-1 ($\epsilon = 1$)	NSD-2 ($\epsilon = 2$)	NSD-2 ($\epsilon = 1$)	NSD-3
l_p (in)	30	30	30	30	30
l_1 (in)	10	10	10	10	-
l_2 (in)	5	10	5	10	-
K_{sc} (kip/in)	2.7 (0.23)	25 (2.1)	4.5 (0.4)	76 (6.3)	1220 (101.7)
P_{in} (kip)	8.9 (0.74)	27.2 (2.3)	11.5 (1)	47 (3.9)	15.83 (15.8)

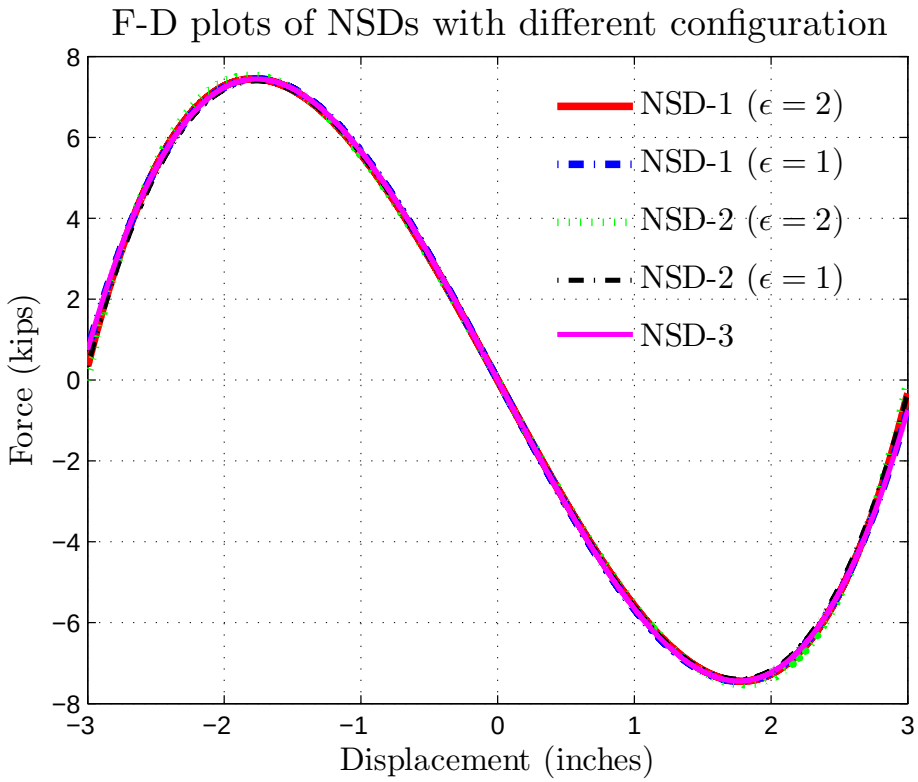

Figure 3.19 : Comparing the F-D behavior of NSDs with different configuration

3.4 Experimental Study

The force-deformation behavior of the NSD is very crucial for "apparent weakening" in yielding systems. So, characterizing the behavior of NSD is very crucial before the installation in the test structure. The experimental setup used to test the NSDs is briefed next.

3.4.1 Experimental setup

The setup used for testing the NSD is shown in Figure 3.20. The setup has a steel girder (bottom frame) and a support frame bolted to the concrete floor along North-South direction. Two spacers (also, steel girders shown in cyan color in Figure 3.20)

are placed on the bottom frame and the bottom-channel of NSD is bolted to the top of spacers. Another steel girder (top frame) is placed on top of the device and two vertical actuators are connected to either ends of top frame to carry the weight of the frame. Lateral swaying of the frame is prevented by the lateral restraint frame (LRF). LRF has "U"-shaped hollow square sections (HSS), shown in yellow color in Figure 3.20, bolted to the bottom frame and the free ends of the frame has steel plate assembly with bearings to avoid friction force between the top frame and LRFs. A horizontal actuator is connected to one end of the top frame and the support frame as shown in Figure 3.20. End angle assembly is used to connect the top of the NSD to the top frame. End angle assembly has "L"-shaped section with gussets and slotted holes, shown in Figure 3.21. One leg of the end angle assembly is bolted to the top-frame and the other leg is polished and flushed against the ball-transfer plate of NSD. The miniature ball transfer plate (BTP) is a 3/16 *in.* thick plate with 18 ball bearings (3/8 *in.* diameter) embedded in the steel plate as shown in Figure 3.21. BTPs are bolted to the ends of NSD with two counter-sunk bolts. Bearings of BTP sit against the polished surface of end angle assembly and they prevent transfer of any vertical load from the NSD to the structure.

Two accelerometers and five string potentiometers are installed on the device to measure the acceleration and deformation of various points on the device. The deformations and force exerted by the NSD are measured using the in-built load cells and linear variable displacement transducers (LVDTs) of actuators. Data from all the sensors mentioned above is recorded in the Flex-test data acquisition system. Krypton K600 camera system is also used to measure the deformation of all the elements in NSD. Light emitting diode (LED) sensors are placed at 17 points on the NSD and the deformation of the device is captured for all the tests. All the three

actuators are operated in the displacement control mode. The two vertical actuators are programmed to maintain a specific distance between the bottom and top frames and the horizontal actuator is programmed to track a periodic signal with definite time-period and amplitude. The experimental results from these tests are discussed next.

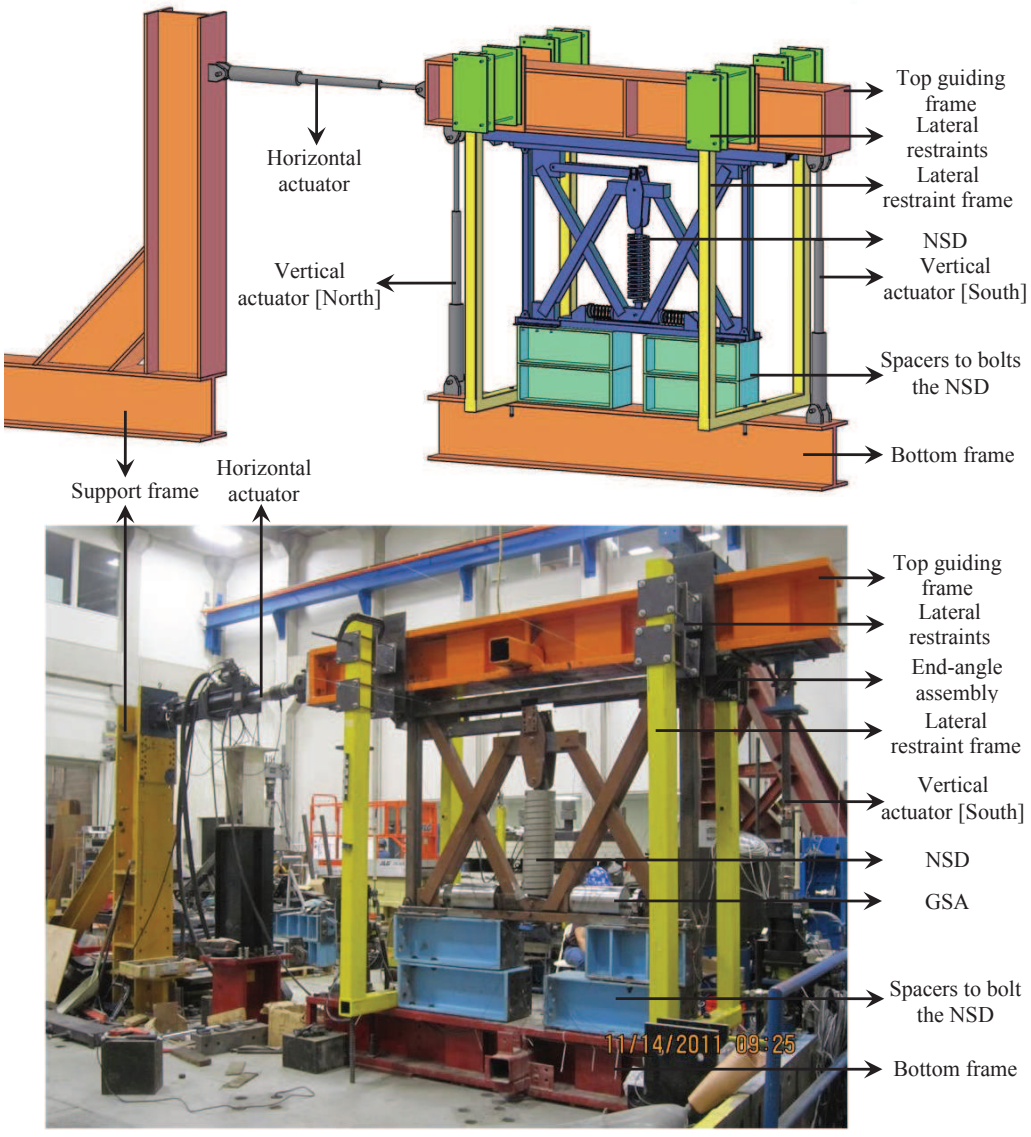

Figure 3.20 : Schematic diagram and the photograph of NSD test setup

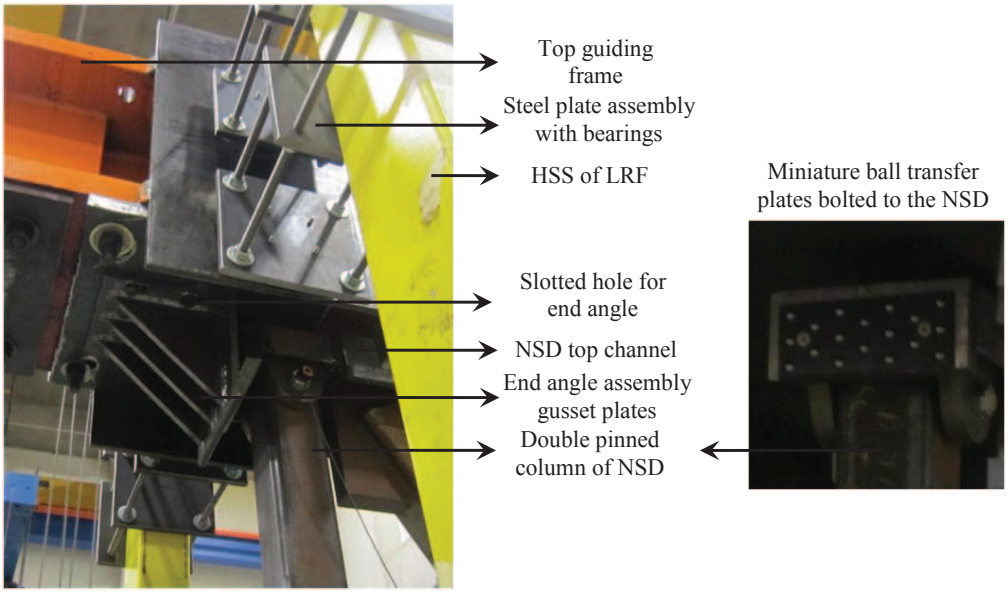

Figure 3.21 : NSD connection with the top frame using end-angle assembly and the miniature ball transfer plates used to transfer the NSD load to topo frame

3.4.2 Experimental results

Two NSDs (NSD-East and NSD-West) are tested with this setup. Response of both the NSDs is calculated for three cycles of sinusoidal input at two different frequencies (0.1 *Hz* and 0.01 *Hz*). To obtain the dynamic properties of the NSD, the device has to be tested at frequencies higher than 0.1 *Hz*. However, the tests couldn't be carried at higher frequencies because of the flexing in the restraining-frames. Each device is tested at 1.5 *in.* amplitude first and then the amplitude is increased in steps of 0.5 *in.* First step in testing the NSD is to characterize the behavior of test-rig and use that information to compensate the NSD test data.

Since the top-frame sitting on the two vertical actuators is like an inverted pendulum, the setup itself exhibits negative stiffness. The test rig is subjected to periodic displacement of 3 *in.* amplitude and 0.01 *Hz* frequency. The force deformation be-

havior of the NSD test rig is shown in Figure 3.22(a) and the measured actuator displacement and actuator force is shown in Figure 3.22(b,c). Test-rig has a negative stiffness of 67 *lb/in.* and a consistent friction loop width of 200 *lb.*, as shown in Figure 3.22(a). The force-displacement loops of the NSDs obtained from the test data should be compensated for the inverse-pendulum action of the test-rig. The actuator force measured using the load-cell is noisy so a low-pass butterworth filter is used to obtain clear data. Similar test has been performed at 0.1 *Hz* frequency but the obtained data is inconsistent due to slipping and vibration of the LRF. Since the top frame is held in position using the side-restraining frames the friction significantly increased at high frequencies.

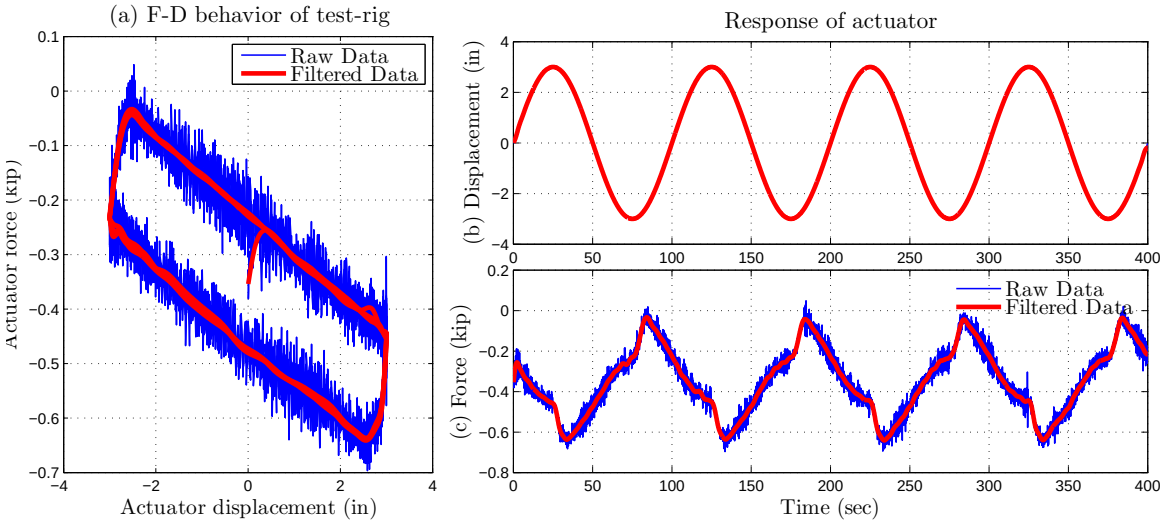

Figure 3.22 : Force-deformation behavior of the test-rig

After calculating the slope and loop width of the test-rig from the F-D plots, NSD-West is placed in the test rig and tested at a displacement of 2.5 *in.* amplitude and 0.01 *Hz* frequency for three cycles of sinusoidal input. The choice of the displacement amplitude is based on the estimated maximum deformation of the device in the 3SFS

tests. The F-D behavior measured from the load-cell and LVDT data is shown in Figure 3.23(a). The hysteresis loop in Figure 3.23(a) is due to the friction in the test setup and also the friction in the joints of NSD. As mentioned previously, the observed behavior of the NSD has to be corrected for the inverted pendulum action and the F-D loop of the device has to be centered. The compensated behavior of the NSD-West is shown in Figure 3.23(b). For the three cycles of the test, forward loop and the reverse loop are separated and averaged, shown in Figure 3.23(b). F-D behavior of individual loops (average of the forward and reverse loops) and mean of all the loops is also shown in Figure 3.23(b). It is clear from Figure 3.23 that the the NSD-West exhibits symmetric and retraceable force-deformation behavior. "Apparent yield-displacement" of the NSD-West is equal to 0.2 *in.*, peak negative force exerted is 7 *kip* at a displacement of 1.5 *in.* and the CS looses all the compression force at 2.5 *in.* displacement.

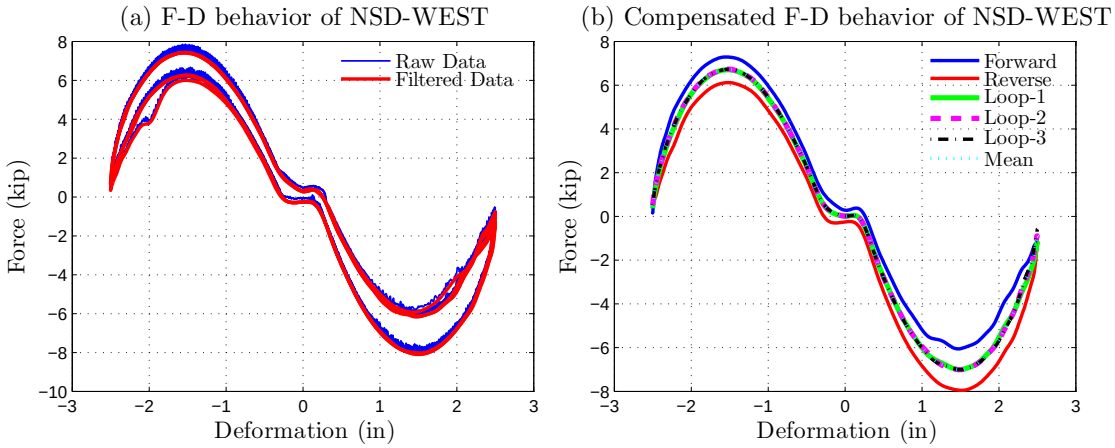

Figure 3.23 : Observed experimental force-deformation behavior of NSD-West

For the same test, using the experimental data from the Krypton camera system, the flexibilities of all the elements can be studied. The points A, B and E of the NSD

(Figure 3.1) have the same displacement as shown in Figure 3.24(a). This confirms that (1) lever-arm undergoes very small rotations ($u = u'$) and (2) CB2 is not flexible for NSD-West. The deformation of point-C and point-D are compared with point-A in Figure 3.24(b) for the NSD-West. The ratio of the deformations of point-D and point-A, shown in Figure 3.24(b), is equal to the lever ratio of the device and this confirms that there is no flexing in the pivot plate. The point-C of NSD-West has undergone little or no deformation (<0.03 *in.*) which means the CB1 is also not flexible for NSD-West. Two LEDs are also placed on the steel casing of the GSAs and the measured deformation is shown in Figure 3.24(c). Since the LEDs are on the steel casing the deformation shown in Figure 3.24(c) is only the deformation of the softer springs (S_1' and S_1''). Each GSA deforms on one side as shown in Figure 3.24(c). The gap in which the GSA-left and GSA-right remain undeformed, shown in Figure 3.24(c), is equal to 0.4 *in.* This confirms with the force-deformation plots or NSD-West, shown in Figure 3.23, that the "apparent yield-displacement" is 0.2 *in.* which means that the stiff springs of both GSAs (S_2) deforms for the first 0.2 *in.* on either side.

NSD-East is also tested in same setup to ensure that both the devices exhibit the desired behavior. NSD-East is also tested at a displacement of 2.5 *in.* amplitude and 0.01 *Hz* frequency for three cycles of sinusoidal input. The F-D behavior measured from the load-cell and LVDT data is shown in Figure 3.25(a) and the compensated behavior of the NSD-West is shown in Figure 3.25(b). For the three cycles of the test, averaged individual loops are shown in Figure 3.25(b). Unlike NSD-West, the F-D behavior of NSD-East is asymmetric but the loops are retraceable. The peak force in the positive direction is 7 *kip* at 1.3 *in.* and the peak force for negative displacements is 9.5 *kip* at 1.7 *in.* Also, the stiffness of the stiff spring in GSAs is significantly larger

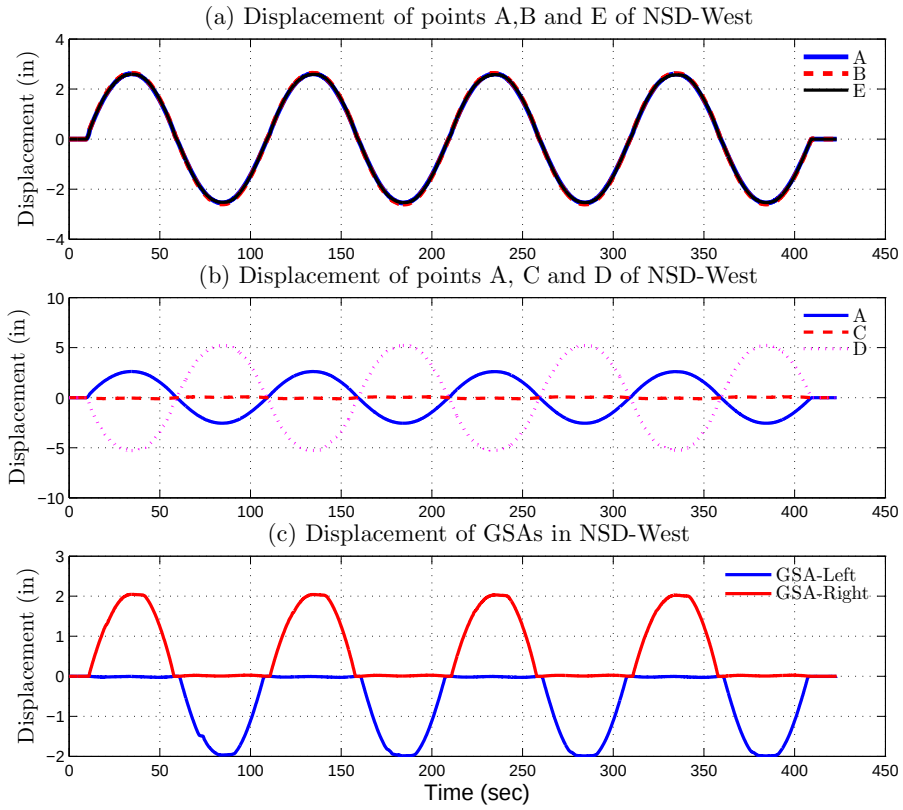

Figure 3.24 : Comparison of the displacements of various points on NSD-West

than the negative stiffness of the CS; hence the NSD-East exhibit positive stiffness for deformations $|u| < 0.2$. "Apparent yield-displacement" of the NSD-East is also equal to 0.2 *in.*

The displacement of points A, B and E of NSD-East are similar and they are symmetric about zero displacement as shown in Figure 3.26(a). The deformation of point-C and point-D are compared with point-A in Figure 3.26(b). The deformations of point-D is not symmetric about the zeros-axis, shown in Figure 3.24(b). This could be because of the differential flexibilities of chevron braces CB1 and CB2. The point-C of NSD-East has undergone a deformation of 0.06 *in.*) which means that

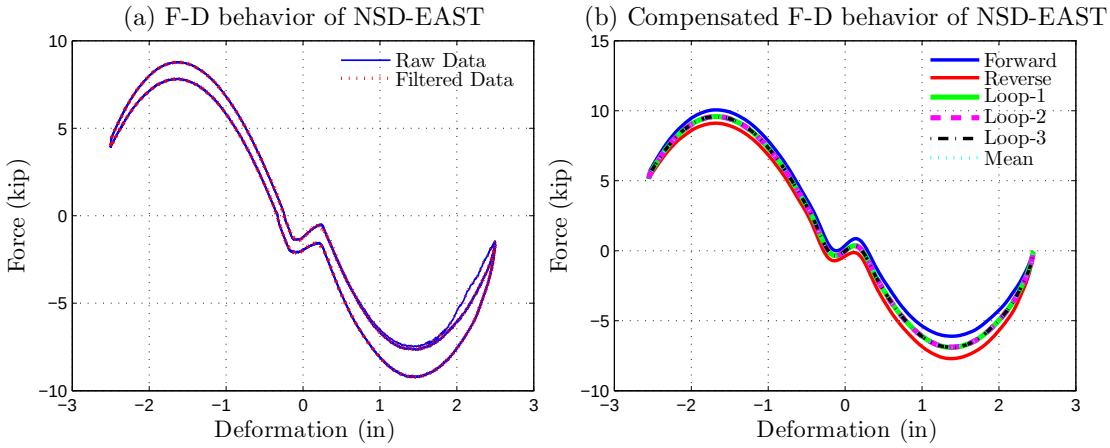

Figure 3.25 : Observed experimental force-deformation behavior of NSD-East

CB1 of NSD-East is also more flexible than the NSD-West. The deformation of the GSAs is shown in Figure 3.24(c). GSA-left has undergone 0.3 *in.* more deformation than the the GSA-right, shown in Figure 3.24(c). This also confirms the differential flexibilities of chevron braces in NSD-East. Next, the analytical models presented in this chapter are used to capture the observed experimental behavior.

3.4.3 Analytical results

NDS-West and NSD-East designed to exhibit identical properties, however, because of the uncertainty in the material properties and the connections different F-D behavior has been observed in the experimental results. Some of the variables in the analytical are measured (L_1, L_2 and L_p) and the feasible range for the remaining variables is also known. Set of feasible values for these variables are determined by calibrating the analytical model with the observed experimental results. Comparison of the experimental and predicted F-D loops of the NSD-West are shown in Figure 3.27(a) and the components of the analytical model are shown in Figure 3.27(b). Since the

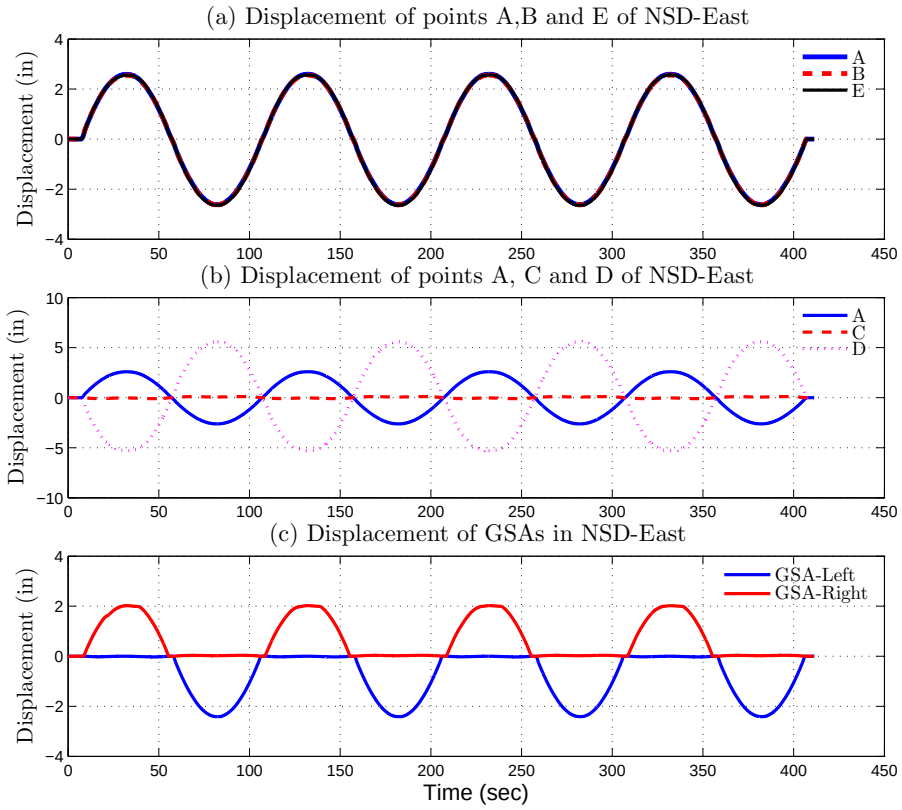

Figure 3.26 : Comparison of the displacements of various points on NSD-East

observed behavior of NSD-West is symmetric, the analytical model developed in this chapter can capture the observed behavior very accurately. Calibrated values of all the variables used for the analytical model of NSD-West are shown in Table 3.3. From Figure 3.27, it is clear that all the key features including, "apparent yield-displacement", peak NSD force and the initial stiffness of NSD for both experimental data and the analytical model are in good agreement. Bilinear-elastic behavior of the GSAs in NSD-West and the lateral force exerted by the CS are shown in Figure 3.27.

Since the NSD-East tend to exhibit asymmetric loops, this behavior can be cap-

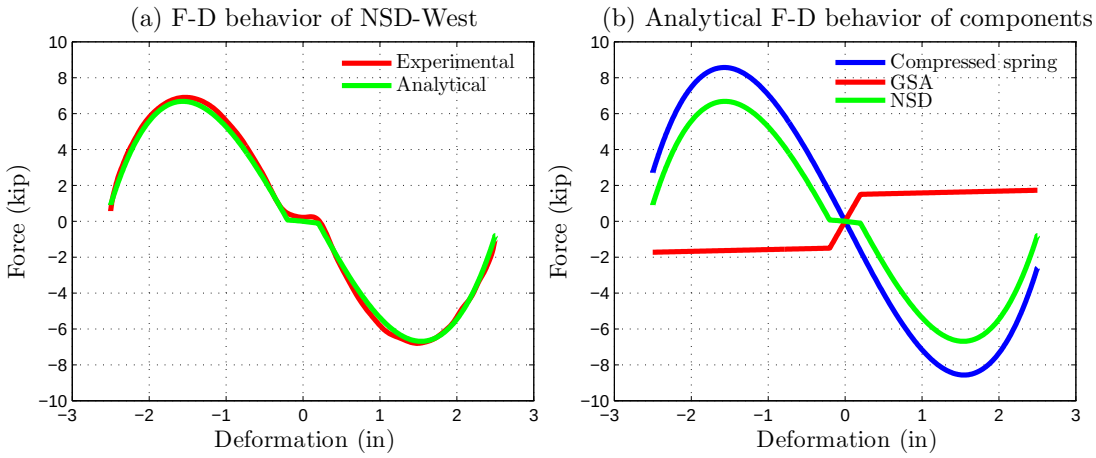

Figure 3.27 : Comparison of the experimental and analytical F-D behavior of NSD-West

tured analytically by writing Eq. 3.65 as

$$F_{NSD}(u) = F_{vs}(\tilde{u}) + F_g(u) + K_f(u) + P_o \tag{3.75}$$

where, $\tilde{u} = u - u_o$ is the linear transformation of u and it is introduced to shift the F-D curve of CS along the displacement-axis and P_o is the constant force added to shift the F-D curve along the force-axis. It should be noted that the shift is created only for the CS and not for the GSA or the chevrons. The need for creating this shift in the NSD equation of motion is explained next.

GSAs, shown in Figure 3.2, have a through threaded-rod that maintains the pre-compression load in the soft-spring. The same threaded-rod is used to bolt the GSAs to the bottom-angle of NSD. The stiff-spring is just placed in the cup and flushed against the bottom of CB2. The GSAs are designed to not exert any force on the CB2 in the undeformed configuration $u = 0$. However, due to the misalignment and tolerances in springs and the threaded-rod of GSAs, there will be a net force acting

on CB2 even when the NSD (and structure) is in undeformed position. This residual force is addressed through an artificial shift as given in Eq. 3.75. Using the modified equation, the experimental and analytical F-D loops of NSD-East are compared in Figure 3.28(a). The F-D behavior of components shown in Figure 3.28(b) clearly shows the translation of the displacement and force of CS. The values of all the variables used to capture the behavior of NSD-East are shown in Table 3.3.

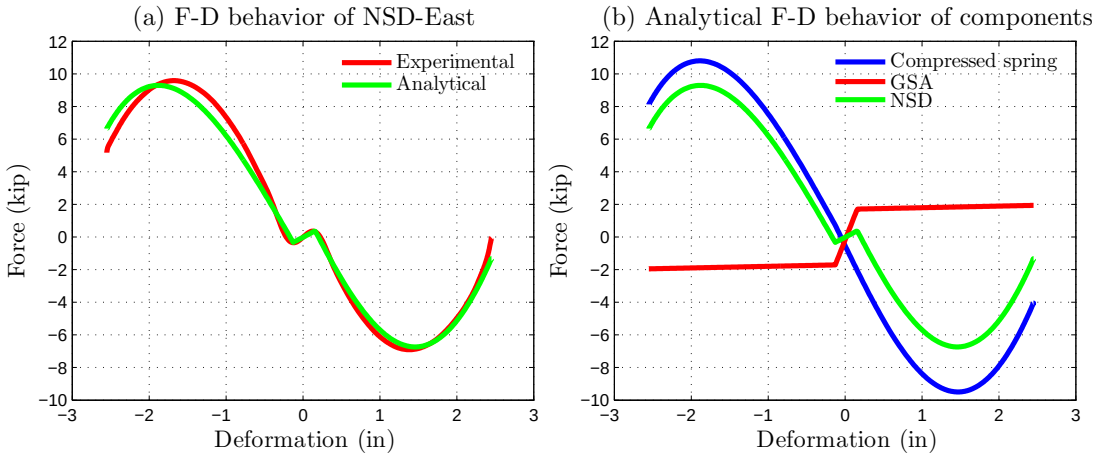

Figure 3.28 : Comparison of the experimental and analytical F-D behavior of NSD-East

3.5 Summary

In this chapter, detailed description of the working principle and the analytical models of the NSD are presented. The key feature of the device, the dual amplification achieved from the double chevron and the lever-arm mechanism, is highlighted with a numerical study. From the practical point of view, it has been shown that the demand on the preload requirements to achieve the desired negative stiffness in real life structures can be significantly reduced using the NSD. The fact that the device

Table 3.3 : Values of the parameters used in NSDs

Variable	Unit	NSD-West	NSD-East
l_1	inch	10	40
l_2	inch	5.13	4.99
l_p	inch	30	30
K_{sc}	kip/in	3.8	3.8
P_{in}	kip	2.8	3.25
K_{S1}	kip/in	0.1	0.1
K_{S2}	kip/in	7.5	12
P_{S1}	kip	1.5	1.6
K_{CB1}	kip/in	122	65.4
K_{CB2}	kip/in	400	400
P_o	kip	-	0.75
u_o	inch	-	0.14

is completely passive and still has the adaptability to change the device properties offline makes it a very powerful tool in structural control.

An experimental study carried to characterize and evaluate the behavior of NSDs has also been reported. The force-deformation loops obtained from the experiments have confirmed that the NSDs exhibits elastic behavior. The behavior of NSDs predicted using the analytical models is in excellent agreement with the observed experimental results.

Chapter 4

Experimental Setup and Component Testing

The goal of the experimental study is to

1. show the effectiveness of "apparent weakening" in elastic and mild-yielding single degree of freedom (SDOF) systems
2. study the behavior of structure and NSD assembly in heavy-yielding systems
3. study the impact of NSDs in multi-story structures

It has been found from the preliminary analytical study that for the heavy-yielding tests, all the four columns in first story will yield after every ground motion test. Since it is extremely time consuming and uneconomical to disassemble the entire structure to replace the columns, a versatile and generic test structure is needed that can be used to achieve all the three goals with minimum cost and effort. The three-story frame structure (3SFS) built and tested in this study posses all these attributes.

3SFS was first developed by Kusumastuti et al. [159] to study the behavior of structural systems near collapse. The first structural model developed was a one-third scale, three-story three-bay steel structure. 3SFS is designed to have sacrificial elements (components that will be severely damaged for strong ground motions) that can be readily replaced upon damage and the structure can be further tested without disassembling the entire frame. Using the versatility of the model, Kusumastuti et al. [159] also tested and characterized the behavior of irregular-structures for a suite

of ground motions. 3SFS has two independent support systems: moment resisting frames or simply the moment frames (MFs) to bear the lateral inertial forces exerted on the structure and gravity frames (GFs) to carry the gravity load of the entire structure. Since the two frames are completely decoupled and the entire gravity load is borne by the GFs, the sacrificial elements in the MFs can be replaced easily without disassembling the entire structure.

In this study, the experiments on the 3SFS were carried at the NEES equipment site at University at Buffalo, SUNY. Two NSDs and a viscous damper are installed in the first floor. The experiments on the 3SFS have been performed in two phases. In the first phase, the top two floors of the 3SFS are braced, essentially making the 3SFS a SDOF system. The SDOF system is subjected to a series of ground motion with increasing peak-ground-acceleration (PGA) to demonstrate the concept of "apparent weakening" in elastic and yielding structures. In the second phase, the braces in the top two floors are removed and the behavior of NSDs in MDOF systems is studied. Three different types of systems are tested in both the phases for five ground motions from PEER database:

1. 3SFS or the base structure (BS): NSDs and the damper are disconnected
2. 3SFS and the NSD assembly (NS): NSDs are connected and the damper is disconnected
3. 3SFS, NSDs and damper assembly (AS): both NSDs and the damper connected

Since replacing columns after every heavy-yielding test was expensive, only NS and(or) AS are tested for all the ground motions. To compare all the three systems, response of the missing system is simulated using the calibrated analytical models.

The contents in this chapter are organized as follows: Section-4.1 presents the details of all the components in 3SFS and their connections. In section-4.2, the analytical models of NSD and dampers and the installation in the 3SFS is presented. A brief discussion on the instrumentation of the test setup and data acquisition is given in section-4.3. Section-4.4 presents the experimental results of the testing of 3SFS and the analytical model used to capture the experimental behavior. The key observations from these test results and comparisons are summarized in section-4.5

4.1 Three-story frame structure (3SFS)

The 3SFS is also a one-third scale three-story fixed base structure, similar to the structure developed by Kusumastuti et al. [159], but it only has one-bay. 3SFS is installed on a single-axis shake table is shown in Figure 4.1, the picture is taken from the East. The shake table is aligned to move the structure in north-south direction (longitudinal direction). A support frame (orange color in Figure 4.1), located to the south of the shake table, is used for the installation of string-potentiometers to measure the displacement at various heights of 3SFS. Megadac data acquisition system, located at the foot of support frame, is used to record the experimental data. Overhead crane is used to install the 3SFS on shake-table and also to hold the 3SFS as a precautionary measure, in case if the 3SFS collapse during the tests.

3SFS has three components, shown separately in Figure 4.2 (1) moment resisting system, designed to resist the inertial forces of the floor system (2) vertical support system, designed to carry the gravity load of the floor system (3) floor system containing three 3.5 *in.* thick steel plates that form the floor slabs. The damageable lateral load resisting system and the undamageable vertical load system are completely disjoint and they are connected to the floor system separately. Details of

these components and their assembly is discussed next.

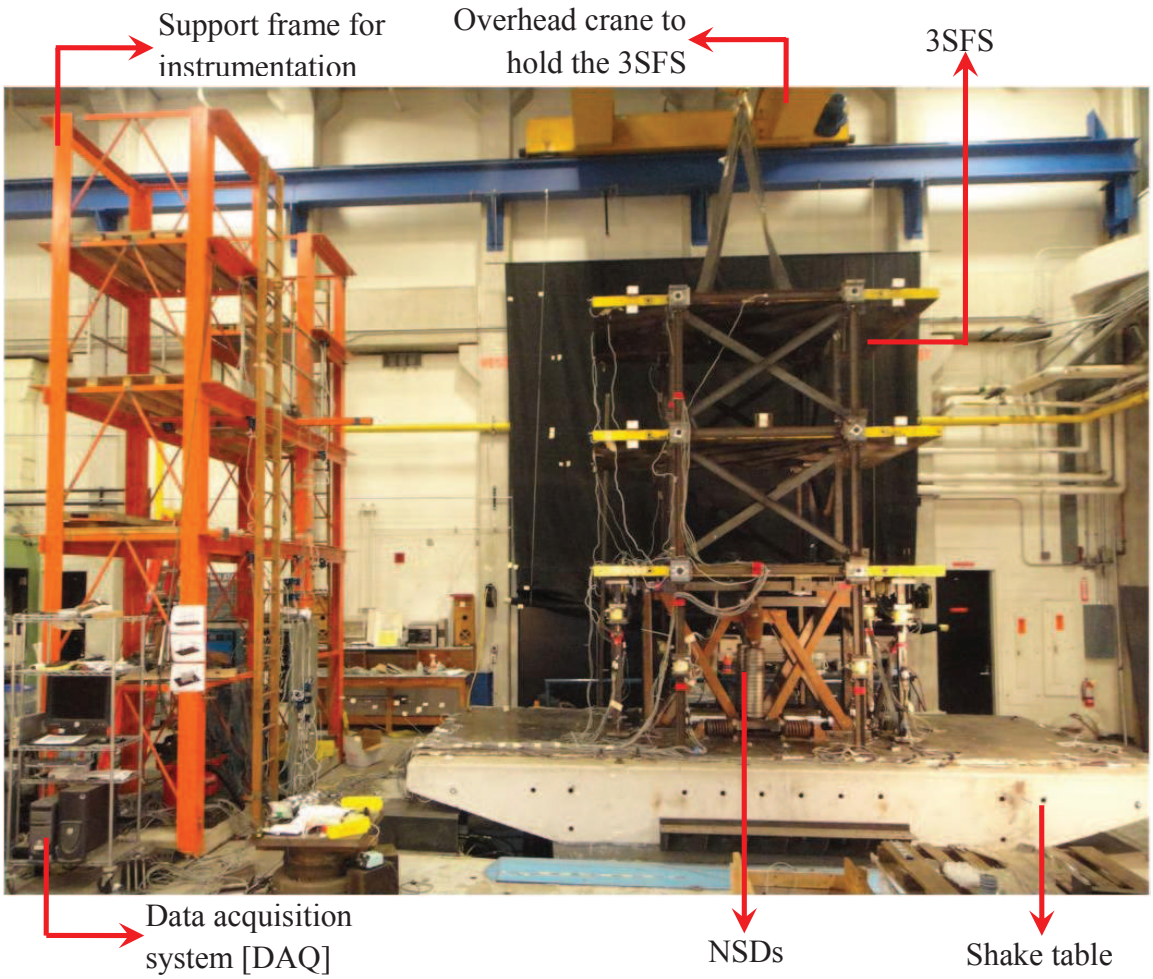

Figure 4.1 : 3SFS installed on the shake table at NEES equipment site, University at Buffalo, SUNY

4.1.1 Moment resisting system

The moment resisting system has two moment frames (MF), MF-east and MF-west, aligned along the north-south direction as shown in Figure 4.2(a) (also shown as red colored frames in Figure 4.3 and Figure 4.4). Each moment frame has five com-

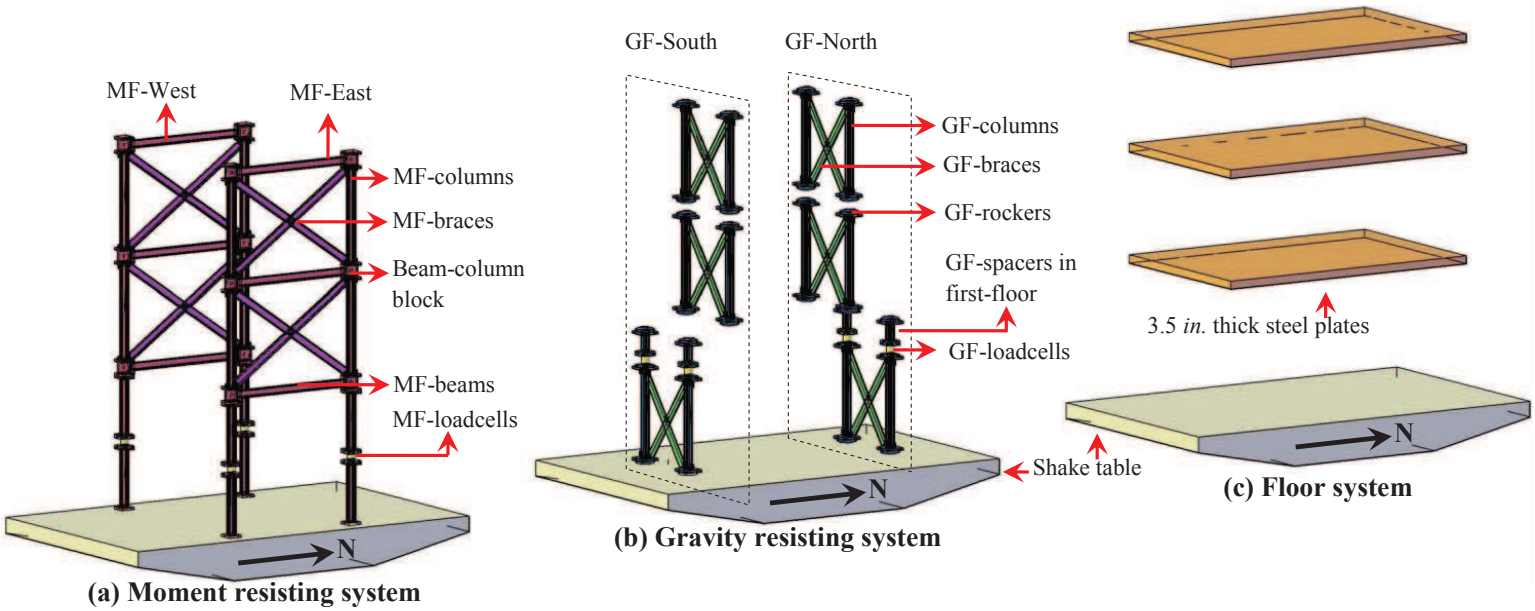

Figure 4.2 : Schematic diagram showing the components in 3SFS

ponents: columns, beams, beam-column blocks, cross-braces and load-cells; all the components are marked in Figure 4.2(a), 4.3 and 4.4. Columns and beams in all the three stories are made of standard steel section S3×5.7 and they have 1 *in.* thick steel plates with through holes welded on either sides. Schematic drawings of all the elements, with dimensions are shown in Appendix-A.

The columns and beams are connected to the beam-column block, shown in Figure 4.5. Beam-column block is a machined steel block ("I"-shaped cross-section) with threaded holes in the vertical direction to connect the columns and through holes along longitudinal direction to connect the beams. It also has a slotted hole ($1^1/_{16}$ *in.* diameter and 2 *in.* long) in east-west direction to connect the moment frames to the steel-slabs as shown in Figure 4.5. The MFs are connected to the steel slabs with a one inch bolt that passes through the vertical slotted hole of beam-column block and is threaded into the steel slab. The bolt can freely move in the vertical slot of the beam-column block so the gravity load of slabs cannot be exerted on the moment frame. The entire gravity load is carried by the gravity frame. When the MF sways in the longitudinal direction, the inertial forces of the steel slabs are transferred to the MFs through the one inch bolt and the slack in the vertical slot will prevent the transfer of gravity load to MF columns. To avoid the frictional forces between the beam-column block and the bolt a teflon washer is placed on either side of the block. Accelerometer and the string-pot holder placed on the beam-column block can be seen in Figure 4.5.

For the tests in the first two phase of this study, the behavior of AS in SDOF system has been studied. So, the top two stories of the moment frame are braced using steel sections C3x4.1 making the structure essentially a SDOF system as shown in Figure 4.2(a), 4.3 and 4.4. The diagonal braces are also bolted at the center. The

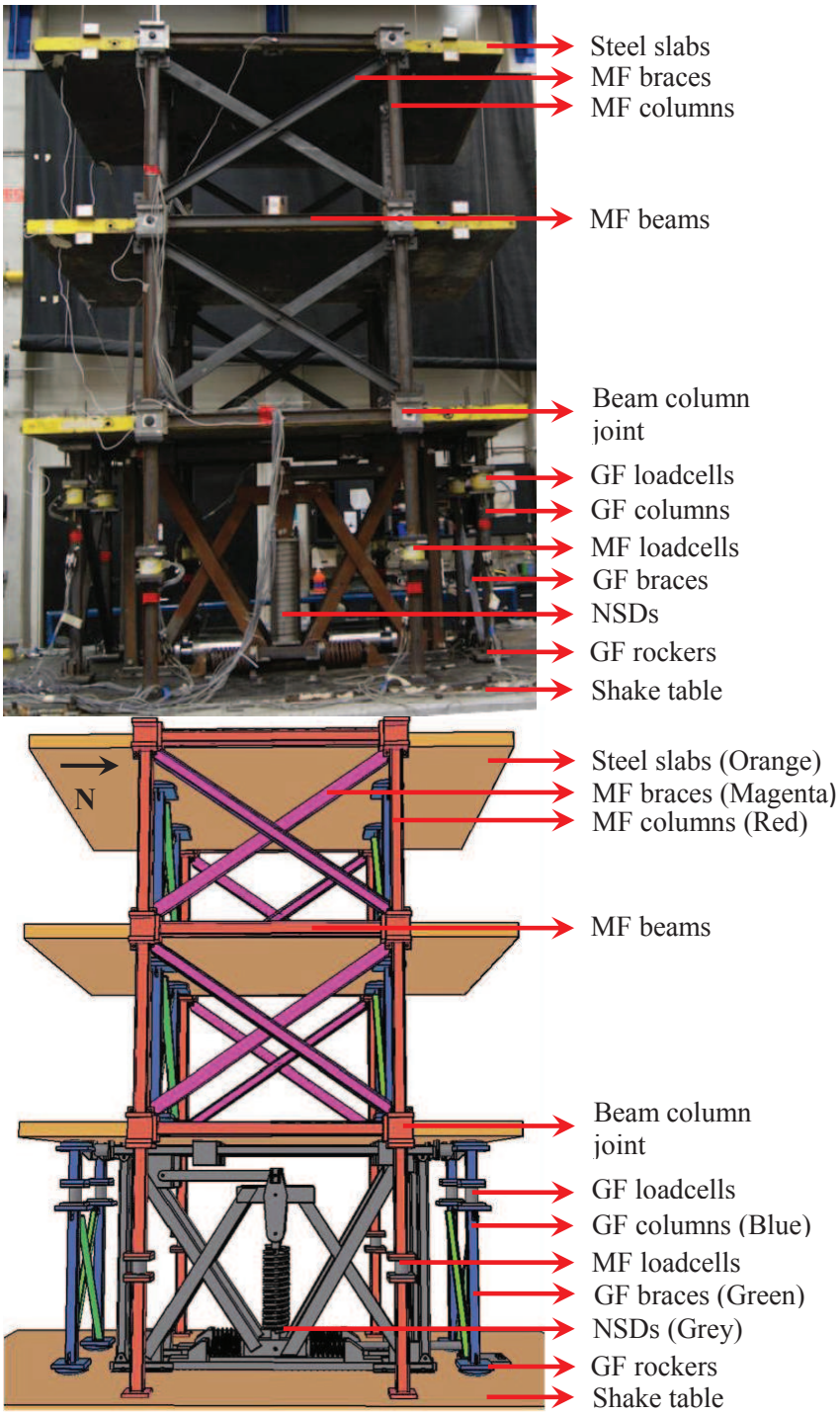

Figure 4.3 : Photograph and schematic diagram of 3SFS (Elevation)

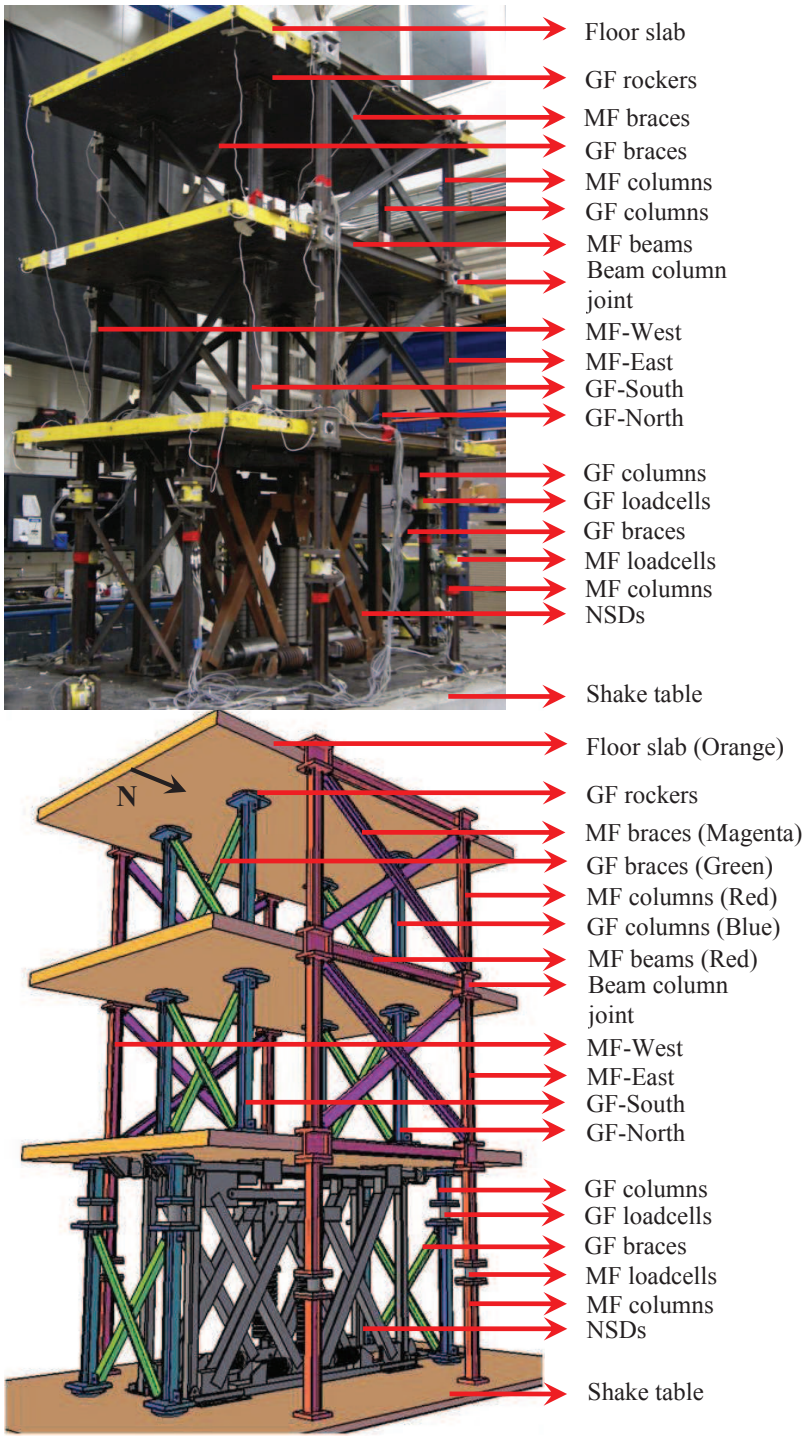

Figure 4.4 : Photograph and schematic diagram of 3SFS (Isometric view)

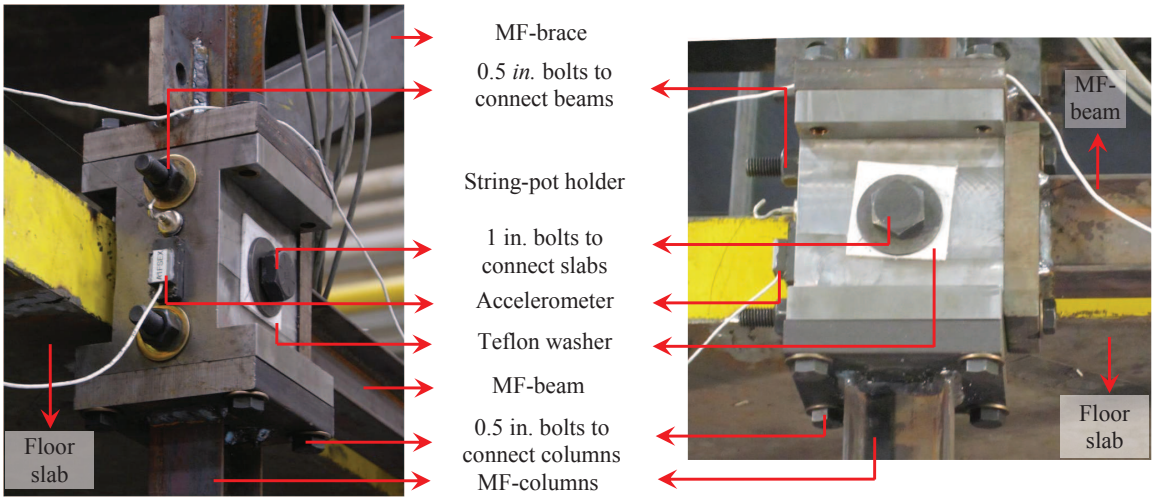

Figure 4.5 : Beam-column block showing the connections

columns and braces of the second and third floor of MF have the same configuration and dimensions. In the first floor since the floor height is taller than the other two and also the load-cells are added the configuration is different. To measure the base shear experienced by the columns in first story one load-cell is added to each column. Since the shear in the middle of the columns in first story is very low, load-cells are strategically placed at this point. The clear spacing between the two MFs is equal to 78.75 in (same as the width of steel slab, details in Appendix-A).

4.1.2 Vertical support system

Vertical support system is designed to carry the gravity load and it cannot provide any resistance to the lateral load. This is achieved by creating a hinge-hinge end connection for all the gravity columns. Each story has two gravity frames (GFs), GF-North and GF-South, aligned in the east-west direction (perpendicular to the plane of motion) symmetrically on either side of the center line of steel slabs as

shown in Figure 4.2(b). Gravity frame consists of two S3x5.7 columns and each column has hinge connections at either end. Opposite corners of the gravity columns in each gravity frame are connected with L2x2x0.25 braces to prevent torsion in the 3SFS, shown in Figure 4.2(b), 4.4 and 4.6. Gravity column hinges are made out of a steel plate having a convex surface with a 10 *in.* radius on one side, and a flat surface on the other side, shown in Figure 4.6. The convex side of the hinge-plate sits against the steel slabs or base plate to provide axial support and the flat surface faces the gravity column end plate. Four oversize holes were provided in the hinge-plate, gravity column end-plate, and steel slab. Steel pins are used to connect the end plate of the gravity column to the hinge-plate and the steel slab, preventing any possible slip as shown in Figure 4.6. The steel pins are used just to hold the gravity frames but not to rigidly connect it to the floor. Since the gravity frame has hinge-plates with a convex surface in all the four corners, the gravity frame can rock freely under lateral loads without changing the vertical geometry of the model.

The gravity frames in second and third story are placed between the adjacent columns of MF-east and MF-west as shown in Figure 4.4. In Figure 4.3, the gravity frames in second and third floor cannot be seen clearly because they are right behind the moment frame columns. In the model developed by Kusumastuti et al. [159], gravity frames in all the three stories were aligned. In this study, since the NSDs are placed in the first story and they cannot be accommodated in the clear space available between the gravity frames, they are moved towards the edge in the first story. Similar to the MFs, the gravity columns in first story have load cells to measure the gravity load of the structure and also the shear force in case if the gravity frame provides any lateral resistance. Although the height of first-floor is 13.25 *in.* more than the other two floors, to avoid confusion and to maintain uniformity, six identical

gravity frames are fabricated. To span the entire floor, load cells and spacers are added on top of the GFs in first floor as shown in Figure 4.2(b) and 4.4.

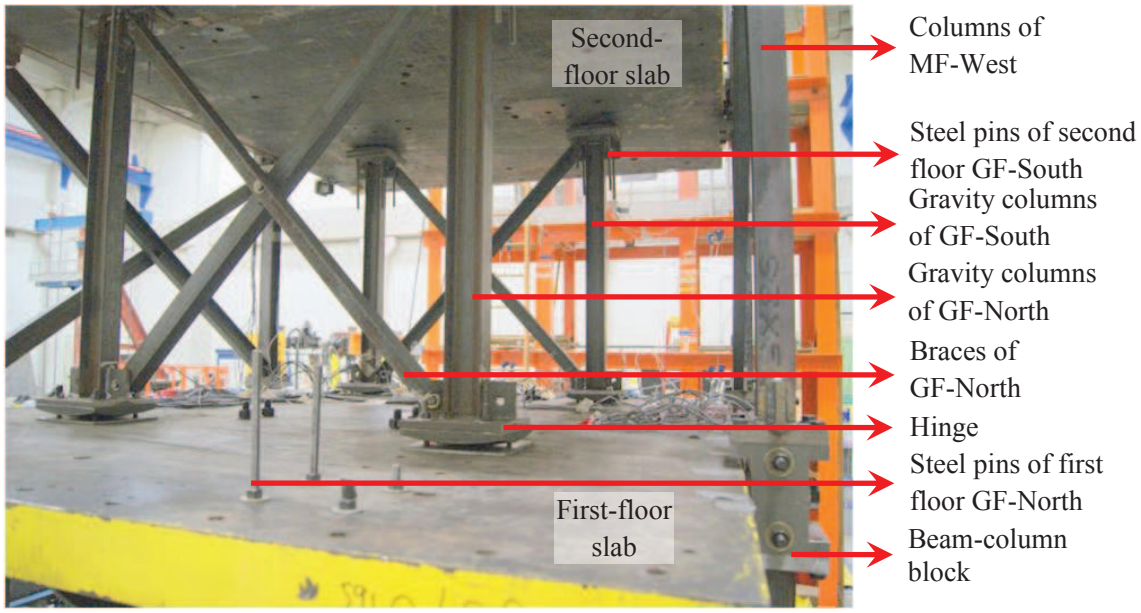

Figure 4.6 : Photograph of gravity frames in the second floor of 3SFS

4.1.3 Floor system

The floor system is required in 3SFS to generate inertia forces. It comprises of three 3.5 *in.* thick steel plates located at a height of 60.5 *in.*, 107.75 *in.* and 155 *in.* from the top of the shake table, shown in Figure 4.2(c), 4.4 and 4.6. Weight of each plate is 8.5 *kip*. The gravity load exerted by the floor system will be of a huge concern during the yielding tests of 3SFS. In case if the columns of the frame has a huge permanent drift, the gravity load of the floor system is sufficient to collapse the structure due to P-Δ effect. To prevent the collapse of structure, two separate support systems (MF and GF) are developed. The weight of all the plates is transferred to the shake table

through the gravity frame. The inertial forces of the floor system are transferred only to the moment frame through the 1 *in.* bolts. The hinges will prevent the transfer of inertial forces to the gravity frame.

4.2 NSD and Damper Installation in 3SFS

To study the role of NSD and damper in AS and also to demonstrate the effectiveness of "apparent-weakening", response of three different systems have to be studied experimentally for each ground motion data. In order to prevent the delays in connecting and disconnecting the NSDs and damper special connections are provided between the 3SFS, NSD and damper. These connection details are presented in this section.

4.2.1 Negative stiffness device

Detailed description of NSD, working principle and the experimental studies to characterize the behavior of NSD are presented in chapter 3. From the preliminary analysis, based on the observed experimental behavior of NSD, it has been found that the negative stiffness of NSDs is more than what is required and the predicted behavior of 3SFS and NSD assembly was not complying with the desired behavior (assembly force should always be in first and third quadrant of F-D plot), shown in Figure 4.7(a). The discrepancy in the stiffness is due to fabrication tolerances and flexibilities of chevron braces in NSD.

The behavior of the assembly can be improved by either reducing the negative stiffness of NSD or adding positive stiffness externally. The negative stiffness can only be reduced by changing the pre-loaded spring (explained in section-3.2) and since it is expensive to replaced the machined spring, two additional GSAs (GSA-2)

are added to the NSDs to reduce the negative stiffness of NSD, as shown in Figure 4.8. GSA-2 is tested separately and using the experimental data, the predicted force deformation behavior of 3SFS and NSD assembly with the addition of GSA-2 is shown in Figure 4.7(b). The behavior shown in Figure 4.7(b) is very close to the desired behavior. Readers should note that the actual NSD has only one GSA (GSA-1) but in this study an extra GSA (GSA-2) is added to the system.

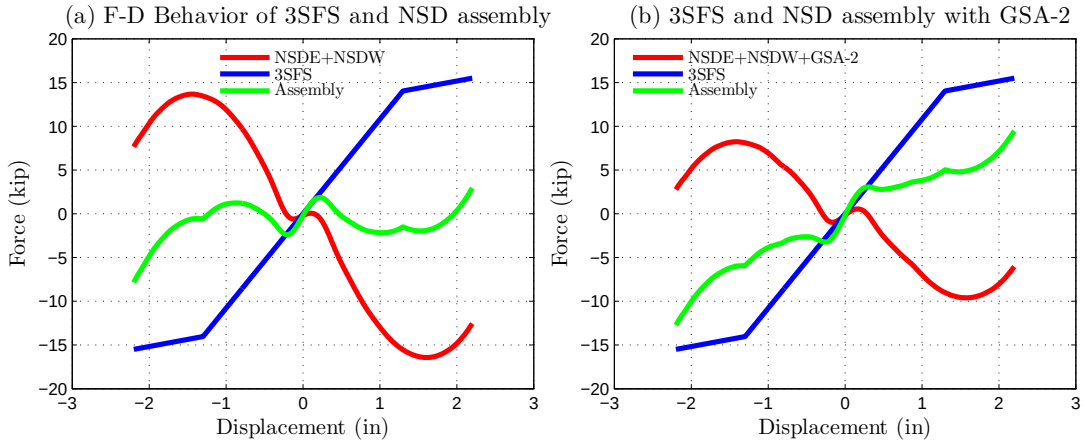

Figure 4.7 : Predicted behavior of 3SFS and NSD assembly w/ and w/o GSA-2

Side view and front view of the NSDs installed in the first floor of 3SFS is shown in Figure 4.9 and 4.10. The bottom of the NSDs is bolted down to the shake table. A clear space of 2 *in.* is provided at the top between the NSD and the first floor slab. Two restrainers are placed around the top channel of NSD and bolted to the first floor slab to prevent any out of plane motion, shown in Figure 4.9. An "L" shaped assembly with gussets referred as end-angle assembly is designed as an interface to connect the NSD to the first story slab, shown in Figure 4.11. One flange of the end-angle assembly is bolted to the first story slab and a load-cell is fastened on the other flange facing the NSD, shown in Figure 4.11. Miniature ball transfer plates

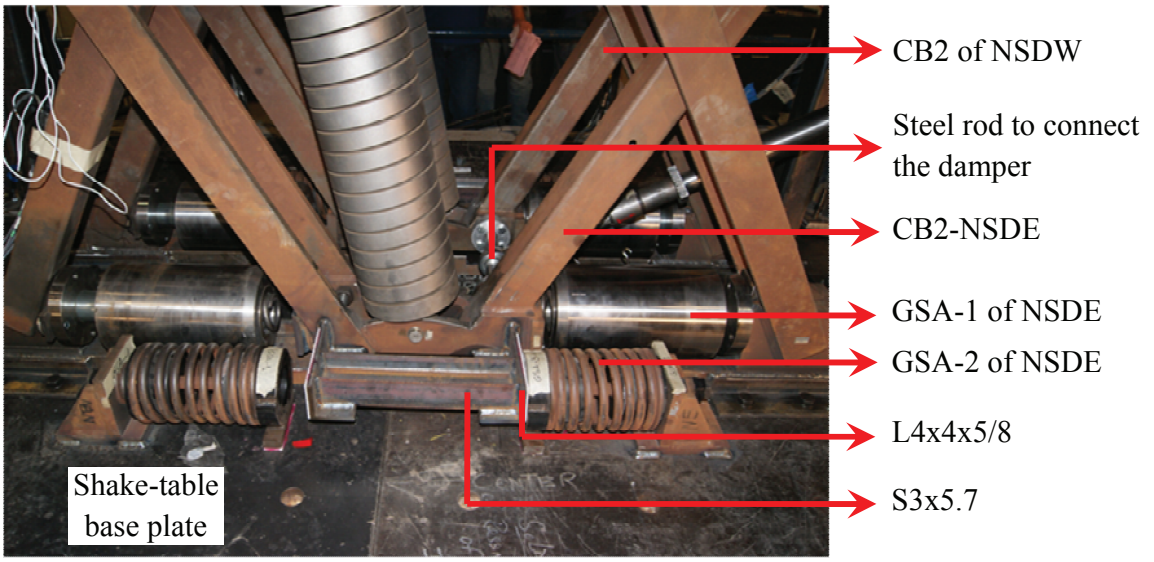

Figure 4.8 : GSA-2 connected to the CB2 of NSD

are fixed to both the ends of NSD (explained in section 3.4.1) and they are flushed against the load-cell connected to the end-angle assembly. The ball transfer plates have very low friction and they can only transmit lateral load and will not exert any vertical force on the structure.

The flange of the end-angle assembly that is connected to the floor-slab has slotted holes (1.5 *in.* long) for eight 1/2 *in.* bolts, shown in Figure 4.11. The slotted holes along with a 1 *in.* spacer, facilitate connecting and disconnecting the NSDS. By moving the end-angle assembly towards the edge of the floor slab and removing the spacer, a clear space of 2.5 *in.* is provided between the end angle assembly and the NSD. Since the maximum deformation of the floor is less than 2 *in.*, the NSDs can be easily connected and disconnected from the 3SFS just with the end angle assembly. Before disconnecting or connecting the end-angle assembly, the preloaded springs of the NSDs are compressed using four 3/4 clamp bolts until the NSD is in

the undeformed configuration. Although the initial stiffness of NSD is positive for this particular NSDs, the preloaded spring is clamped as a safety measure. The role of load-cells placed between the NSD and end-angle assembly is to measure the force exerted by each NSD separately.

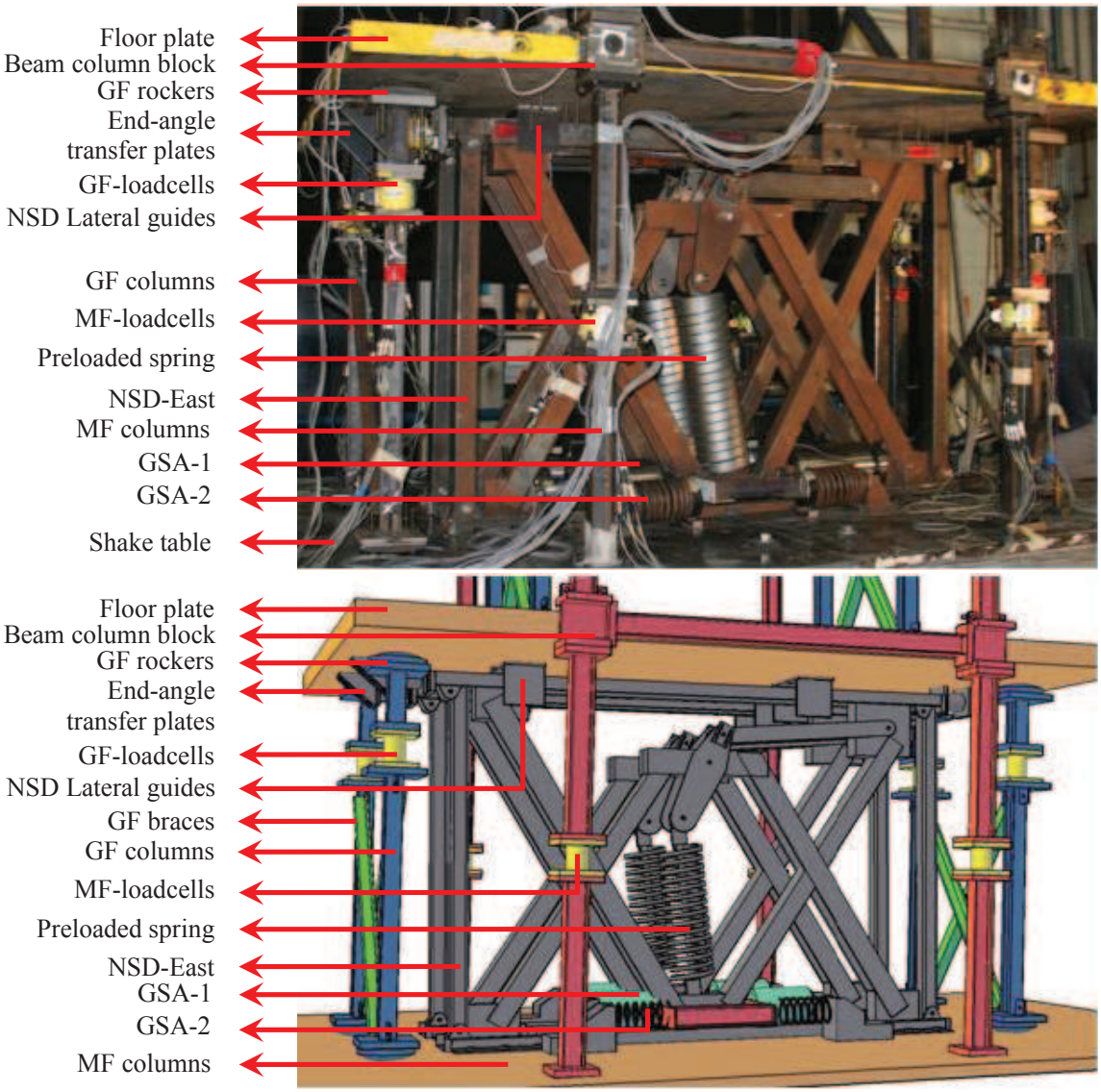

Figure 4.9 : Photograph and schematic diagram of 3SFS (Elevation)

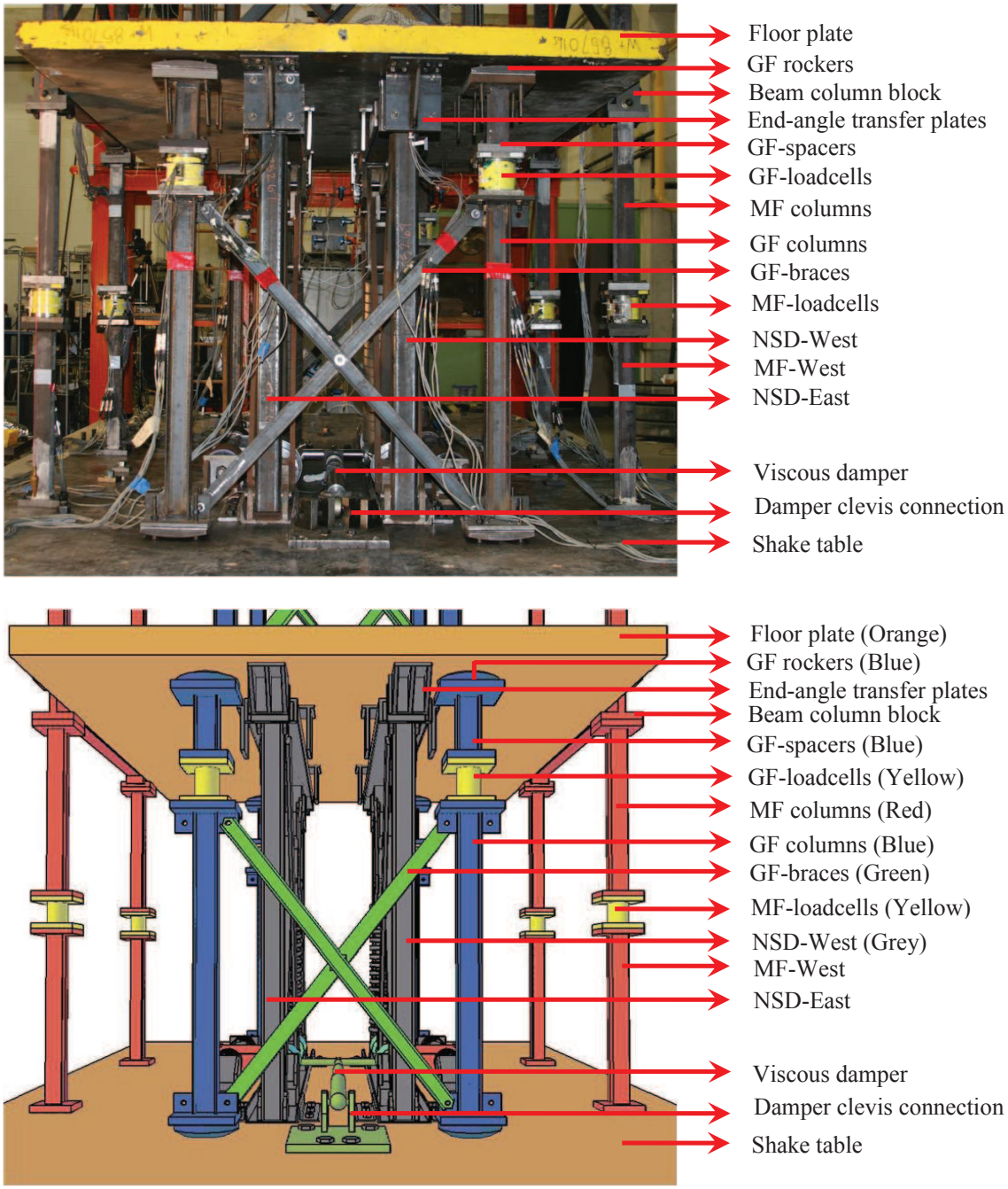

Figure 4.10 : Observed experimental force-deformation behavior of NSD-East

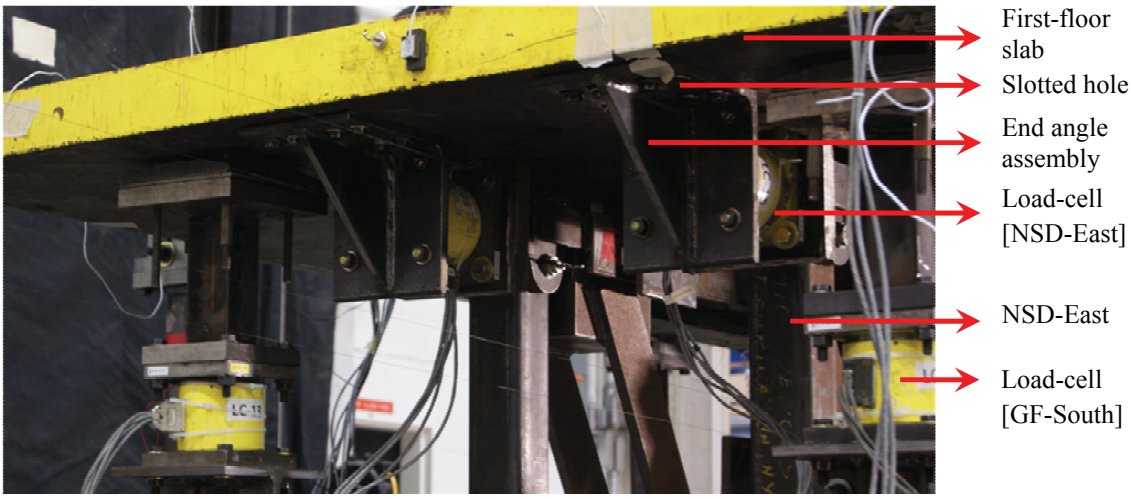

Figure 4.11 : End angle assembly to connect the NSDs to floor slab

Force exerted by the NSD with the additional GSA and all the flexibilities, derived in chapter 3, is given by Eq. 4.1

$$F_{NSD} = -\left(\frac{P_{in} + K_{sc} l_p}{l_{extd}} - K_{sc}\right) \frac{l_1}{l_2} \left(2 + \frac{l_2}{l_1} + \frac{l_p + l_1}{\sqrt{(l_2^2 - u^2)}}\right) u + F_{g1} + F_{g2} + F_f \quad (4.1)$$

where, F_{g1}, F_{g2} and F_f are the forces exerted by GSA-1, GSA-2 and chevron flexing, respectively.

$$F_{g1} = \begin{cases} K^1_{S2} u & \text{if } |u| \leq \frac{P^1_{S1}}{K^1_{S2}}, \\ P^1_{S1} + \frac{K^1_{S1} K^1_{S2}}{K^1_{S1} + K^1_{S2}} & \text{if } |u| > \frac{P^1_{S1}}{K^1_{S2}} \end{cases} \quad (4.2)$$

$$F_{g2} = \begin{cases} K^2_{S2} u & \text{if } |u| \leq \frac{P^2_{S1}}{K^2_{S2}}, \\ P^2_{S1} + \frac{K^2_{S1} K^2_{S2}}{K^2_{S1} + K^2_{S2}} & \text{if } |u| > \frac{P^2_{S1}}{K^2_{S2}} \end{cases} \quad (4.3)$$

$$F_f = \begin{cases} K_{f1} u_f & \text{if } u \leq 0, \\ K_{f2} u_f & \text{if } u > 0 \end{cases} \quad (4.4)$$

Due to the imperfections in NSD fabrication, chevrons exhibit different stiffness for positive and negative deformations as shown in Eq. 4.4. u_f is the deformation of point-C and point-E due to the flexing of chevron braces. Using these equations, the predicted and experimental force deformation behavior of NSD-West and NSD-East are shown in Figure 4.12(a) and 4.13(a), respectively. The predicted behavior is in very close agreement with the observed experimental behavior for both the NSDs. Due to the addition of GSA-2, both the devices exhibit high positive stiffness till $|u| < 0.2$ *in*. The F-D loop of NSD-East is asymmetric, shown in Figure 4.13(a), this is captured in the analytical model through linear transformation explained in Eq. 3.75. The force-deformation behavior of the components, GSA-1, GSA-2 and lateral force due to CS, of both the NSDs are shown in Figure 4.12(b) and 4.13(b). Next, the damper connection in the first floor of 3SFS and the analytical model for the damper is detailed.

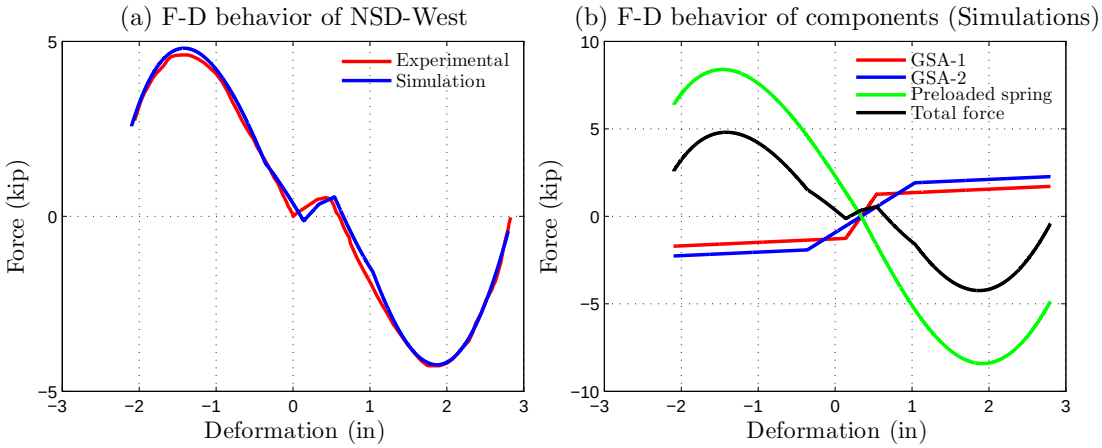

Figure 4.12 : Experimental and predicted behavior of NSD-West

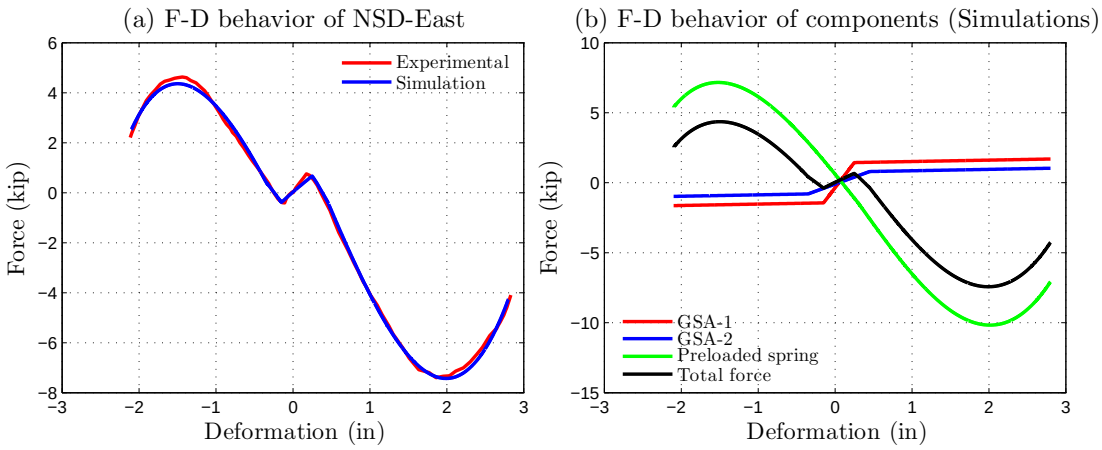

Figure 4.13 : Experimental and predicted behavior of NSD-East

4.2.2 Viscous damper

Viscous damper developed by the Taylor Devices Inc. is used in this experimental study. The damper exhibits linear force-velocity behavior and has a damping coefficient of 0.3769 *kips-sec/in.* A load-cell is attached to the damper to measure the force exerted by the damper. Length of the damper is 20 *in.* and the clear space in the first story is 58.75 *in.* so the damper could not be connected directly in the first-floor. Also, to achieve the desired damping the damper has to be connected horizontally aligning along north-south direction. When the end-angle assembly is connected to the NSD, the bottom of the chevron CB2 will undergo the same deformation as the first story slab as explained in section-3.4.2. So, one end of the damper is connected to a rod that is fixed to the bottom of the CB-2s of NSD-east and NSD-west, shown in Figure 4.10 and the other end of the damper is fixed to the shake table using a clevis connection. To test the structure only with NSD, the damper end that is connected to the shake table is disconnected and is held up using a rope.

Preliminary tests on The viscous damper has revealed that the force-velocity be-

havior of the viscous damper is linear if the velocity is less than 12.5 *in/sec*, but for larger velocities the force-velocity behavior observed was nonlinear as shown in Figure 4.14(a). To capture the behavior of damper for all amplitudes, a higher order term is added to the linear term as shown in Eq. 4.5. The force exerted by the damper, F_{PD}, is given by

$$F_{PD} = 0.312\dot{u} + 1.17 \times 10^{-6}\dot{u}^5 \tag{4.5}$$

Force-velocity behavior of the damper comparing the experimental results with the analytical results (Eq. 4.5) is shown in Figure 4.14(a). The force-deformation of analytical model and experimental results is shown in Figure 4.14(b). The predicted behavior of the damper shown in Figure 4.14 is in very good agreement with the experimental results.

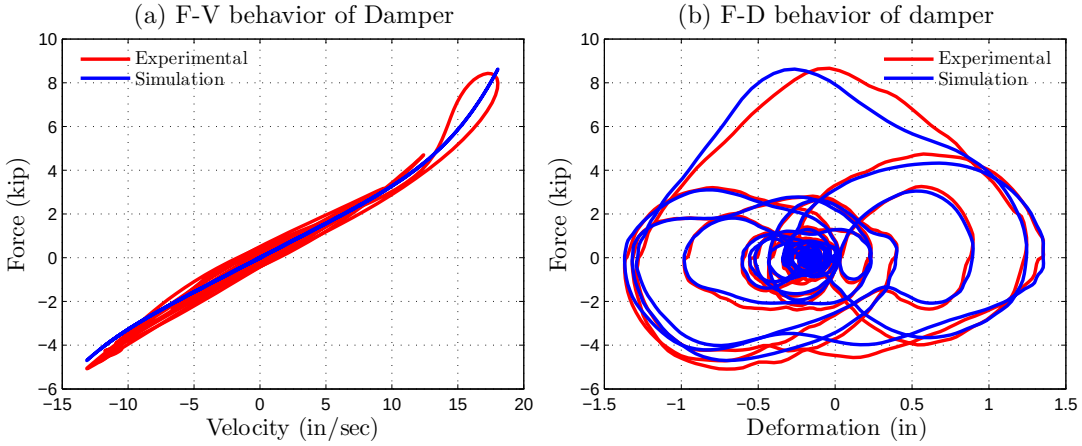

Figure 4.14 : Experimental and predicted behavior of viscous damper

4.3 Instrumentation

Thus far location of 12 multi-axis load-cells (in NSDs, moment-frame columns and gravity columns of first floor) and a uniaxial load-cell (in damper) to measure the force of various components in the structure is presented. Each load-cell measures axial force, shear force (shear-X and shear-Y) and moment (moment-X and moment-Y) at the installed location. Apart from these load-cells, the structure is heavily instrumented with string-potentiometers, strain-gages and accelerometers. Summary of all the instruments and location is summarized in Table 4.1.

In plane displacements and accelerations of the structure at floor level is measured at four different points (one on each moment frame and two on the floor slab) along the transverse direction. Eight accelerometers are placed on the shake-table to measure the in-plane motion, out of plane motion, and rocking of the shake-table. String potentiometers and accelerometers are also placed at all the pin connections in both the NSDs to capture the complete behavior of NSD. Strain gages are attached to the columns and beams of the MF-West, in the first story, to monitor the yielding status of the beams and columns in moment frame. In total, 28 string potentiometers, 24 accelerometers and 12 strain gages are used in this test. String-pots are installed on the support frame, located to the south of shake-table, shown in Figure 4.1. Fishing lines with magnetic holders are used to connect the string pots to the structure, glue-stick is used to attach the accelerometers and epoxy-adhesive is used to attach the strain gages. More than two sensors are used to measure the same response at each floor level to avoid data loss in the case of the sensor malfunctioning.

Megadac data acquisition with 112 channels and in-built signal conditioner is used to record the experimental data. The data is acquired at a rate of 256 samples per second. All the force transducers are calibrated with respect to NIST traceable 20

kip reference load cell. From the calibration tests, it has been found that the moment measured using the multi-axis load-cells exhibit a nonlinear behavior with significant hysteresis. So, the moments recorded in these tests has not been used in the analysis. Data from some of the load cell channels keeps drifting due to the joule-effect in the cables, so all the channels, except the strain-gage channels, are tore before every test.

The shake table used in this study is a five-axis shake table, but in this study it is only used as a single-axis shake table. The shake table has four vertical actuators and two horizontal actuators (25 kN capacity). Plan of the table has 12 *ft.* by 12 *ft.* steel base with a payload capacity of 85 kips (specimen load) and an operating frequency range of 0 to 50 *Hz.* The table is furnished with a reinforced concrete platform of 20 *ft.* by 12 *ft.*. The 3SFS tested on the shake-table exerts a lot of overturning moment for large accelerations. So, the shake table controller is tuned to compensate for the actuator structure interaction. With the addition of NSD, the assembly exhibits bilinear elastic stiffness and the shake table has to be retuned again to achieve the target ground motion. Essentially, two sets of controller properties (tuned parameters) are calculated and used subsequently for all the tests. Despite all the best efforts, it has been observed in the experimental results that shake table was rocking. The observed shake table response for commanded ground motion is slightly different.

In the next section, the experimental results from the preliminary tests, the data processing adapted and the channels used for analyzing the data are discussed.

4.4 Experimental Results

All the elements in 3SFS are connected through bolts, except the end plates of GF and floor slabs. After the installation of structure the shake table is subjected to

Table 4.1 : List of all the sensors used for data acquisition

Sensor	Location	Direction[†‡]	Remarks
Uni-axial load-cell	damper	F-X	Measures the damper force
Multi-axis load-cell	MF columns	F-X,F-Y	In-plane and out of plane shears
	GF columns	F-X,F-Y,F-Z	Dead load of floor slabs and shears due to inertial forces
	NSDs	F-X,F-Y,F-Z	Normal load exerted by the NSDs and friction in vertical direction
String-pots	MF	D-X	One string-pot on each frame (floor level) to measure the displacement and torsion
	Floor slabs	D-X	Two string-pots (SW and SE corner)
	Shake table	D-X	Two string-pots (SW and SE corner)
	NSD-pins	D-X	Located at points-A, B, C, D and E
Accelero-meters	MF	A-X,A-Y	Two per floor for in-plane motion and one each in the first and third floor for out of plane motion
	Floor slabs	A-X,A-Y	Two per floor for in-plane motion and one per floor for out out of plane motion
	Shake table	A-X,A-Y,A-Z	Two for in-plane, two for out of plane and 4 to measure rocking
	NSD-pins	A-X	Located at points A,C and E
Strain gages (SG)	MF-West columns	S-Z	Four SGs on the flanges of columns (2 *in.* from top and bottom)
	MF-West beam	S-X	Eight SGs on top and bottom flanges of the beam at 1/3 distance from both ends

[†] F: force; D:Displacement; A: Accelerometer; S: strain
[‡] X: North-South; Y: East-West; Z: Vertical direction

white noise tests to loosen the elements that were held by friction in the GFs. Then the structure is subjected to Newhall (1994) ground motion and the performance of the sensors and the functionality of the components in 3SFS is verified for BS and AS separately.

The shear force in the columns of first floor can be calculated from the accelerometers installed at the floor level and also from the the load-cells installed in the MF. To ensure that the data measured from different sensors is consistent, first the F-D behavior of first-floor measured using load-cells and the accelerometers is compared in Figure 4.15. The base shear measured with the load-cells is 14% more than the shear calculated from acceleration. Since the accelerometers are more reliable than load-cells and moreover the channels in load-cell are coupled, the load-cell data is scaled to match the shear calculated from acceleration data, shown in Figure 4.15. The base shear in AS can be calculated from accelerometers or by adding the NSD load-cell and MF load-cell data (compensated). For Newhall ground motion the base shear calculated from both the approaches is compared in Figure 4.16. The response calculated from different sensors, shown in Figure 4.16, for AS is accurately matching and this justifies the need for compensating the load-cell data.

The next step is to ensure that there is no torque in the 3SFS and also no relative deformation between the MF and the floor-slabs. Two terms are defined here: Δ_1, a measure of torsion, refers to the difference in the recorded data between two sensors, one in East and one in West, located at the same height; Δ_2 refers to the difference in the recorded data between two adjacent sensors, one on the moment frame and one on the floor-slab. Since the MFs are not bolted tightly to the floor-slabs, the relative motion between the MF and floor-slabs has to be verified to ensure that there is no slack in the 1 *in.* bolts. The shake-table rocking (M_y) for Newhall GM in the case of

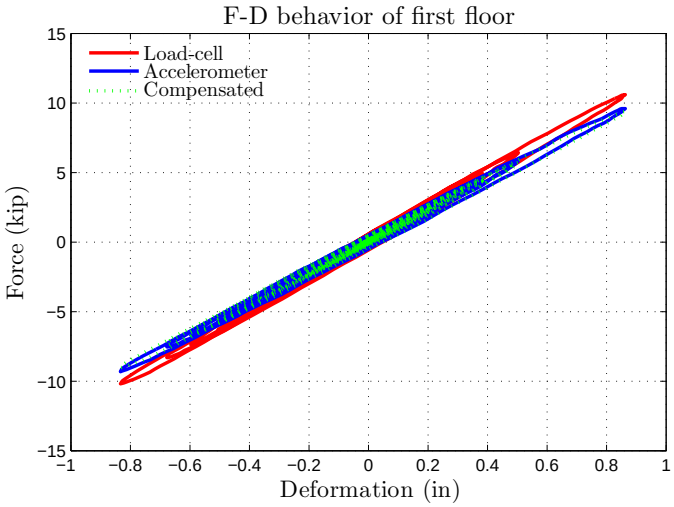

Figure 4.15 : Force deformation loops of the load-cells and accelerometers [BS]

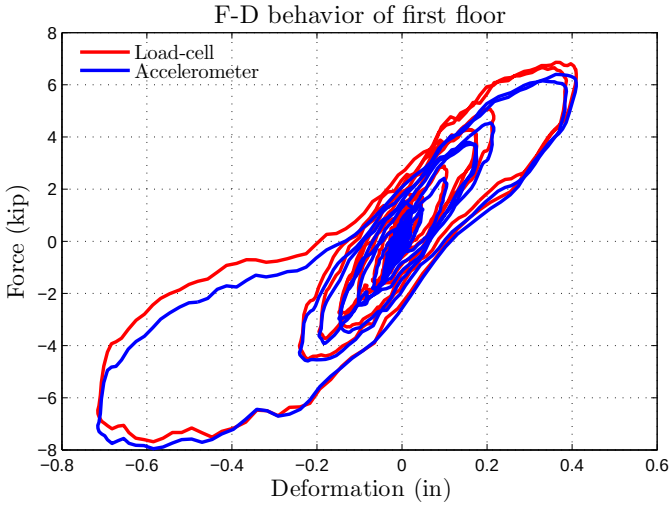

Figure 4.16 : Force deformation loops of the load-cells and accelerometers [AS]

BS is shown in Figure 4.17(a). The PGA of the ground motion is 0.18 g and the peak acceleration due to rocking is 0.04 g (20 % of PGA), so it is important to consider the measured shake-table rocking in the simulation studies. The acceleration of the roof measured on MF-East and MF-West is shown in Figure 4.17(b) and the data

measured from both the sensors is very close confirming that there is no torsion in the case of BS. The percentage difference in the displacement of the roof measured on MF-East and MF-West, $\Delta_1 u$, is shown in Figure 4.17(c). The peak difference in displacement is less than 1.5% which is a sign that the displacements of both the MFs are synchronous. It should be noted that observed 1.5%, shown in Figure 4.17(c), also contains the measurement noise.

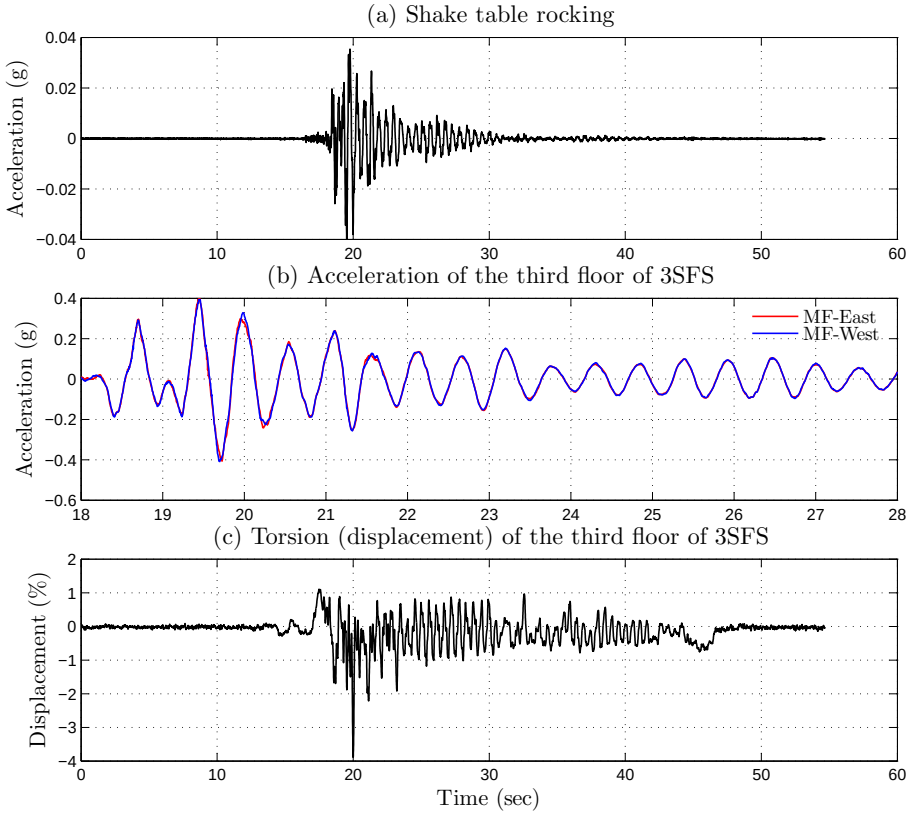

Figure 4.17 : Torsion and rocking in the test structure [BS]

The same analysis is carried on the AS and the response plots are shown in Figure 4.18. Although the commanded PGA is same in the case of BS and AS, the PGA achieved in the case of AS is 0.2 g due to the structure and actuator interaction.

Table 4.2 : Summarized list of torsion and differential response for BS and AS

Location	BS				AS			
	$\Delta_1\ddot{u}$	$\Delta_1 u$	$\Delta_2\ddot{u}$	$\Delta_2 u$	$\Delta_1\ddot{u}$	$\Delta_1 u$	$\Delta_2\ddot{u}$	$\Delta_2 u$
Shake table	3.22	3.41	-	-	2.95	2.46	-	-
First floor	12.85	1.82	1.59	1.99	9.08	2.35	2.65	1.45
Second floor	9.95	3.82	1.57	7.36	9.33	1.71	2.61	4.64
Third floor	9.35	3.89	0.86	1.20	12.70	1.23	2.40	1.09

This difference is much more evident for higher amplitudes. The peak acceleration of shake-table rocking is 0.1 g (50% of PGA). The acceleration of MF-West and MF-East, shown in Figure 4.17(b), shows that the acceleration of both the MFs are close except at the peaks when the NSDs engage. The $\Delta_1 u$ at the roof is less than 1.5% similar to the case of BS.

The response of BS and AS for Newhall ground motion is summarized in Table 4.2. The difference in response ($\Delta_2 u$ and $\Delta_2\ddot{u}$) columns 5 through 8 of Table 4.2 is less than 5% confirming that there is no slack in the connecting bolt between MF and floor-slab. The torsion-displacement, $\Delta_1 u$, is also less than 3% at all floors. However, the torsion-acceleration $\Delta_1\ddot{u}$ is close to 10% in the case of both BS and AS. If this difference is completely due to the torsion, the values of $\Delta_1 u$ and $\Delta_1\ddot{u}$ of second and third floors should be higher than the first-floor. Since the structure is vibrating in the first-mode and still the torsion values are same in all the floors this could be due to the measurement noise in the accelerometers. Next, the analytical model used to capture the behavior of 3SFS is presented.

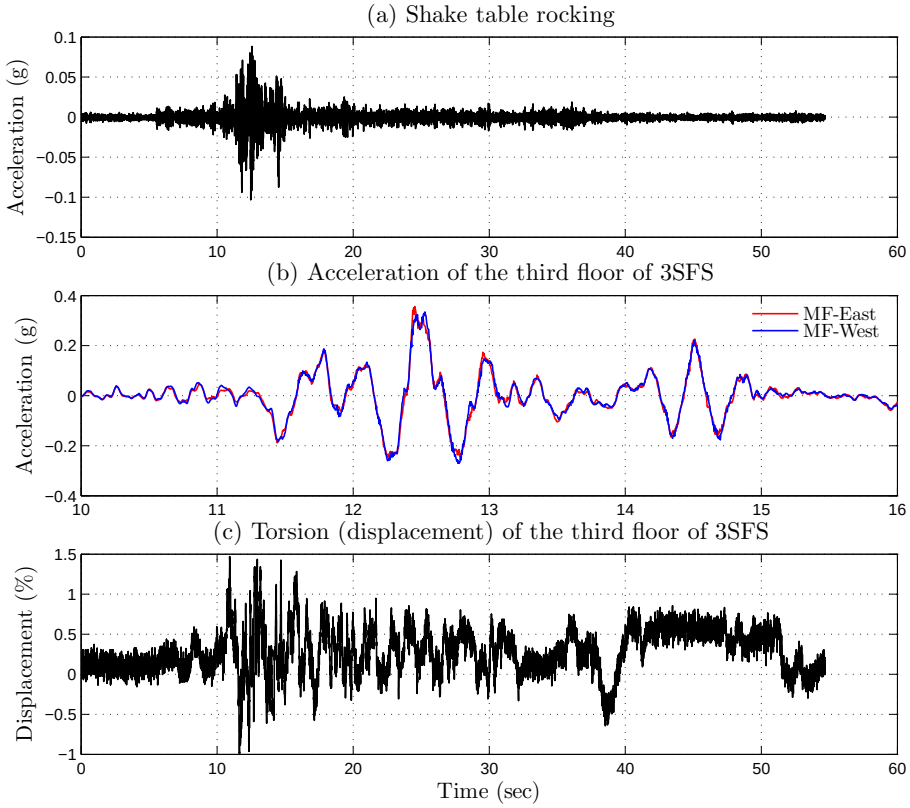

Figure 4.18 : Torsion and rocking in the test structure [AS]

4.4.1 3SFS Analytical Model

Since the primary structure will be yielding in the experiments carried in this study, the columns are modeled using Sivaselvan-Reinhorn model [152]. The structure also has contact forces at three connections (1) NSDs and floor-plates (2) gravity frames and floor-plates (3) beam-column blocks and floor-plates. Due to these connections, a lot of frictional-damping has been observed in the experiments, this is also captured using Sivaselvan-Reinhorn model. First, a set of shake-table tests have been performed with sine-sweep input to estimate the stiffness and damping of three modes of 3SFS. Essentially, the analytical model of each-floor in 3SFS has viscous damping,

friction damping and hysteretic model to capture the column behavior. The values various parameters used in the models is different for the 3SFS with braces in the second and third floor, acting as a SDOF structure, and the 3SFS without braces. Governing equation of motion for the 3SFS is given in Eq. 4.6

$$\mathbf{M\ddot{u}} + \mathbf{C\dot{u}} + \mathbf{F_s(u)} + \mathbf{F_f(u)} = -\mathbf{MI}\ddot{u}_g - \mathbf{ML}\ddot{\theta}_g \tag{4.6}$$

$$F_{si}(u_{ri}) = \alpha_{si} K_{si} u_{ri} + (1 - \alpha_{si}) K_{si} u_{syi} z_{si} \tag{4.7}$$

$$\frac{dz_{si}}{du_{ri}} = \left(\frac{1 - |z_{si}|^{\eta_{si}} \left(\gamma_{si} \text{sgn}(z_{si} du_{ri}) + \beta_{si}\right)}{u_{syi}} \right) \tag{4.8}$$

where, u is the displacement vector of the structure relative to the ground. $\ddot{u}_g$ and $\ddot{\theta}_g$ are the shake table horizontal acceleration and rotation due to shake table rocking. $\mathbf{M}$ and $\mathbf{C}$ are the mass and damping matrices of the structure. $\mathbf{I}$ and $\mathbf{L}$ are the influence coefficient vectors for shake table acceleration and rotation. $\mathbf{F_s(u)}$ and $\mathbf{F_f(u)}$ are the force vectors containing the force due to friction in each floor and the story-columns. The nonlinear stiffness force in each story is calculated using Eqs. 4.7, 4.8. Subscript-i stands for i^{th} story, F_{si} is the nonlinear spring force in i^{th} story, $u_{ri} = u_i - u_{i-1}$ is the inter story deformation of i^{th} story and u_{syi} is the yield displacement. The parameters α_{si}, K_{si}, η_{si}, γ_{si} and β_{si} are the constants in Sivaselvan-Reinhorn model for i^{th} story. The friction force, $\mathbf{F_f(u)}$, is calculated using the equations similar to Eqs. 4.7, 4.8.

Weight of steel slabs in each story is measured (M_1=M_2=M_3=8.6 kips) and used to calculate the mass matrix, $\mathbf{M}$, elastic stiffness of the columns is calculated from individual story stiffness (K_{s1}=10.9 *kip/in*; K_{s2}=56.0 *kip/in*; K_{s3}=35.0 *kip/in*), damping matrix, $\mathbf{C}$, is calculated assuming 1% damping ($\xi = 0.01$) in each floor

($C_1 = 2\xi\sqrt{M_1 K_{s1}}$, $C_2 = 2\xi\sqrt{M_2 K_{s2}}$ and $C_3 = 2\xi\sqrt{M_3 K_{s3}}$). The matrices and the components are shown below

$$\mathbf{M} = \begin{bmatrix} M_1 & 0 & 0 \\ 0 & M_2 & 0 \\ 0 & 0 & M_3 \end{bmatrix} ; \mathbf{C} = \begin{bmatrix} C_1 + C_2 & -C_2 & 0 \\ -C_2 & C_2 + C_3 & -C_3 \\ 0 & -C_3 & C_3 \end{bmatrix} ; \mathbf{I} = \begin{bmatrix} 1 & 1 & 1 \end{bmatrix}$$

$$\mathbf{L} = \begin{bmatrix} 60.5 & 107.75 & 155 \end{bmatrix}$$

$$\mathbf{F_s(u)} = \begin{bmatrix} F_{s1}(u_{r1}) + F_{s2}(u_{r2}) & -F_{s2}(u_{r2}) & 0 \\ -F_{s2}(u_{r2}) & F_{s2}(u_{r2}) + F_{s3}(u_{r3}) & -F_{s3}(u_{r3}) \\ 0 & -F_{s3}(u_{r3}) & F_{s3}(u_{r3}) \end{bmatrix}$$

$$\mathbf{F_f(u)} = \begin{bmatrix} F_{f1}(u_{r1}) + F_{f2}(u_{r2}) & -F_{f2}(u_{r2}) & 0 \\ -F_{f2}(u_{r2}) & F_{f2}(u_{r2}) + F_{f3}(u_{r3}) & -F_{f3}(u_{r3}) \\ 0 & -F_{f3}(u_{r3}) & F_{f3}(u_{r3}) \end{bmatrix}$$

The constants in Sivaselvan-Reinhorn model are estimated by minimizing the error between experimental and analytical hysteresis loop. From the optimization study, $\alpha_{si} = 0.2$, $\eta_{si} = 12$, $\gamma_{si} = 0.84$ and $\beta_{si} = 0.16$. Predicted and the observed experimental force-deformation behavior of all the floors in 3SFS for San Fernando earthquake ground motion [Recorded at Pacoima dam, 164 (CDMG station 279)] (PGA = 0.75g) is shown in Figure 4.19. The analytical predictions are matching with the experimental results very accurately in the first-floor. The experimental force-deformation behavior of the second and third floors is more noisy compared to the first-floor because the shear in first-floor is measured using the load-cells whereas in the second and third floors it is calculated from the floor acceleration. The maximum defor-

mation of second and third floor is less than 0.15 *in.* and the peak deformation of first-floor is 1.95 *in.* First floor deformation and acceleration is shown in Figure 4.20 for the same ground motion. From the comparisons in Figure 4.20, the peak response characteristics and also the frequency-information obtained from the analytical model of 3SFS can capture the observed experimental behavior very accurately. The permanent drift observed in the experiments is 0.21 *in.* and the permanent deformation in the simulations is 0.25 *in.*

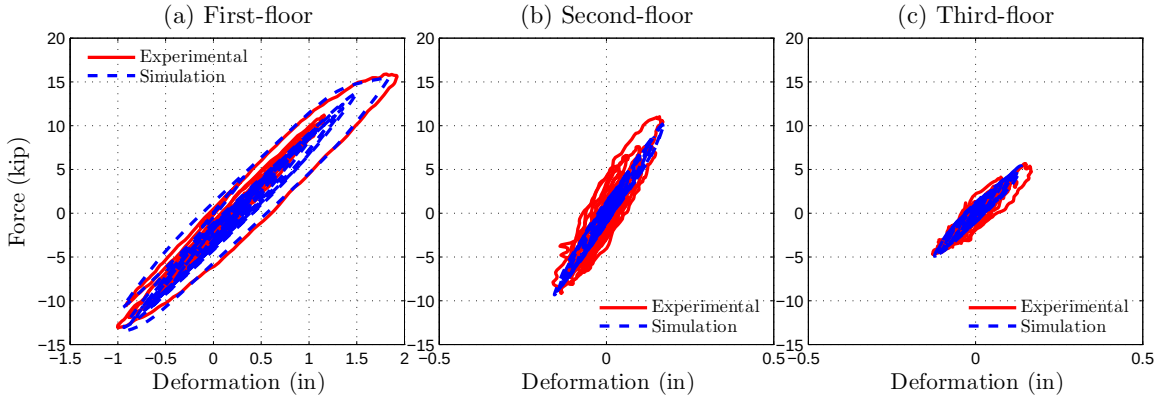

Figure 4.19 : F-D behavior of 3SFS with braces in second and third floor

Next, the behavior of 3SFS without the braces is verified for Kobe ground motion (1995). The experimental force-deformation behavior of all the floors is shown in Figure 4.21. The analytical predictions are matching with the experimental results very accurately in all the first-floor unlike the braced structure, shown in Figure 4.21. The maximum deformation of the second and third floors (Figure 4.21) is 0.75 *in.* and 0.5 *in.* respectively. The elastic stiffness of the columns in each floor is K_{s1}=8.9 *kip/in*, K_{s2}=11.2 *kip/in* and K_{s3}=9.2 *kip/in*. Sivaselvan-Reinhorn model constants are $\alpha_{si} = 0.17$, $\eta_{si} = 6$, $\gamma_{si} = 0.84$ and $\beta_{si} = 0.16$. First floor deformation and acceleration is shown in Figure 4.22; roof deformation and acceleration is shown in

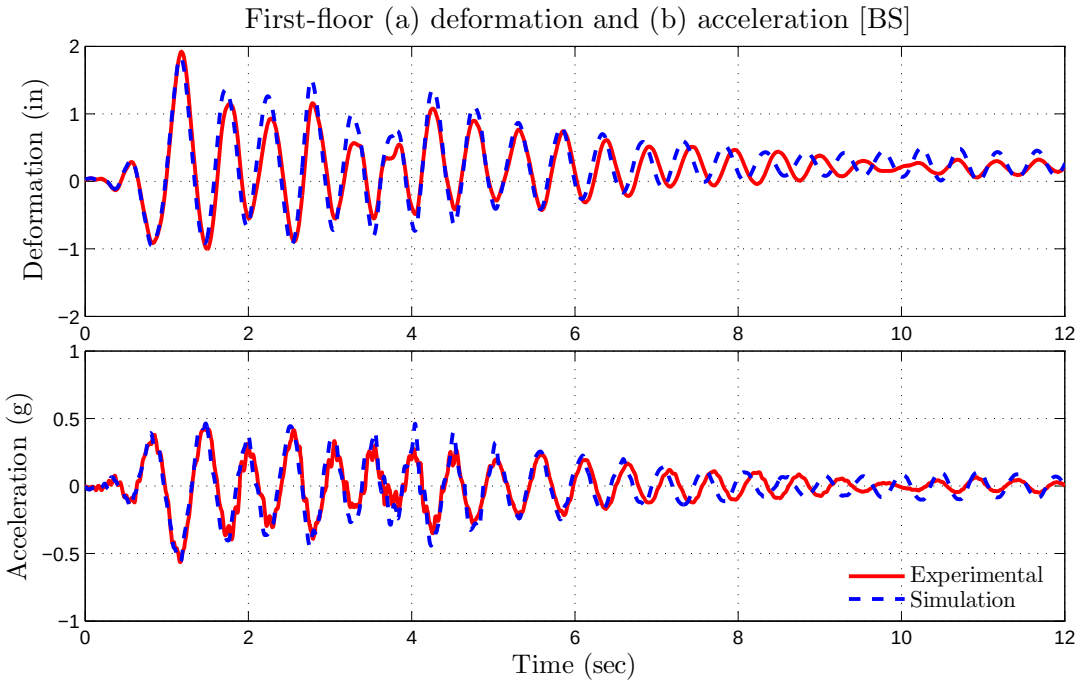

Figure 4.20 : Displacement and acceleration of the first floor of braced-3SFS

Figure 4.23. Similar to the braced structure, the comparisons in Figure 4.22 and 4.23, the peak response characteristics are matching accurately but the frequency-information is slightly off because of the dynamics of the second and third floors. The friction in the second and third floors is also highly nonlinear because of the slipping in the gravity columns.

4.5 Summary

In this chapter, the experimental setup of the three-story frame structure, the connections between the 3SFS, NSD and damper is presented in detail. The analytical models for each of the components is also presented and the models are calibrated using the experimental data from the component testing.

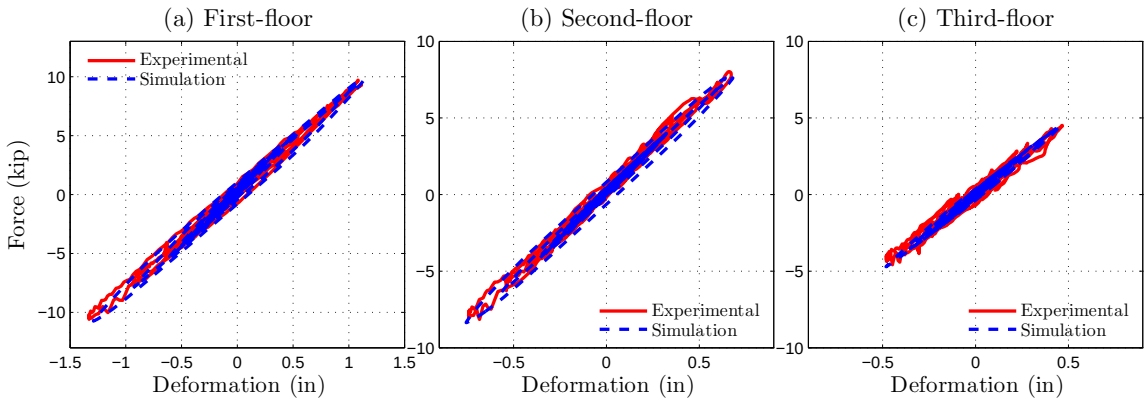

Figure 4.21 : F-D behavior of all the floors in 3SFS

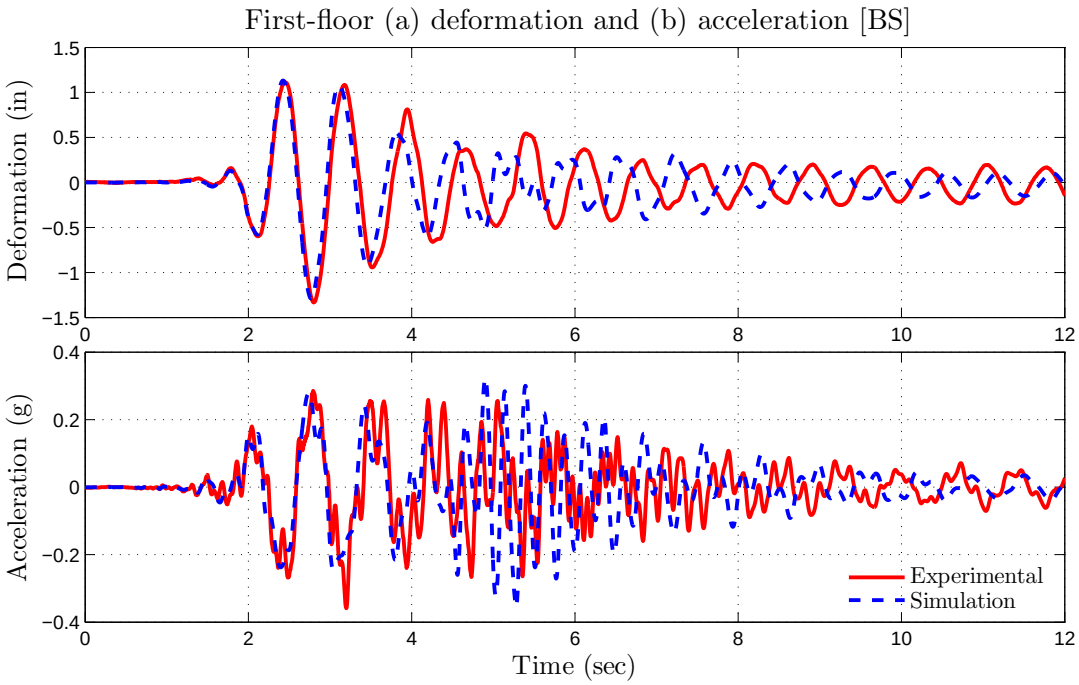

Figure 4.22 : Displacement and acceleration of the first floor of 3SFS

It has been found from the shake-table studies that the 3SFS will undergo very little torsion and can be ignored in the analysis. The data measured from various sensors (many of them redundant) is verified and is found to be consistent. The

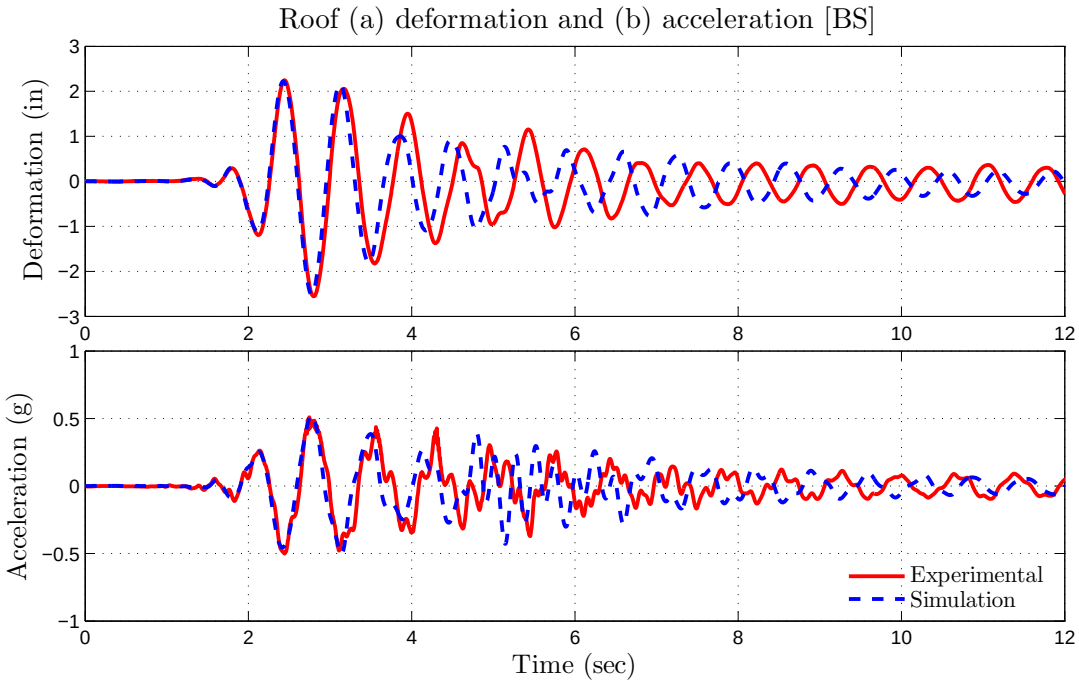

Figure 4.23 : Displacement and acceleration of the roof of 3SFS

experimental data has confirmed that the two support systems (lateral force resisting system and vertical load carrying system) are completely independent and stable; hence it is an ideal test structure to perform yielding tests with NSD. The behavior of the NSD, damper and 3SFS can be modeled and can be very accurately predicted using the analytical models presented in this chapter. The comparisons between the numerical predictions and experimental data is in very close agreement and these component models can also be used to predict the behavior of 3SFS and assembly, which is presented in the next chapter.

Chapter 5

Apparent-Weakening in SDOF Structures: Experimental Study

This chapter presents the results from the experimental study on three-story fixed-base structure (3SFS) that demonstrates the concept of "apparent weakening" in SDOF structural systems. The top two floors of 3SFS are braced making the 3SFS a SDOF structure. First, the effectiveness of "apparent-weakening" in reducing the response of elastic systems is demonstrated. Then the performance of structure and NSD assembly when the primary structure has yielded is evaluated and the issues involved in such systems are presented in detail.

To accentuate the advantages of "apparent-weakening" in structures over the existing passive energy dissipation devices, experimental results of three different systems: 3SFS (BS); 3SFS with NSD (NS); 3SFS with NSD and damper (AS); and analytical results of 3SFS with damper (PS) are compared for a suite of ground motions. Five standard ground motions (see Table 5.1) from the PEER database have been used for the shake-table tests. The ground motions chosen are representative of both the far field and near-fault earthquakes. Analytical models, based on principles of mechanics, describing the behavior of each and all of the three systems (presented in chapter 4) are used to reproduce the experimental results. Also, these models are further used to estimate the response of PS and the missing tests. Since the damper is connected to the structure though the NSD, as explained in section-4.2, 3SFS with the damper (PS) could not be tested experimentally without connecting the NSD. In order to

emphasize the significance of NSD in AS, the response of 3SFS with viscous damper (PS) is simulated and compared with the experimental results of the BS, NS and AS.

Due to the braces in the second and third floors of 3SFS, the columns in the first story will yield first when the frame is subjected to severe ground motion. The strain in the columns of the first-floor is monitored during the tests and they are replaced after they yield. Since replacing the columns after every test is expensive and time consuming, shake-table tests at higher PGA values (tests in which the first floor columns of 3SFS yield) have only been conducted on: 3SFS with NSD and; 3SFS with NSD and damper assembly for different PGA values. For comparisons, the behavior of other systems is predicted using the calibrated analytical models.

The rest of the chapter is organized as follows: "Apparent-weakening" in elastic structures is verified using the experimental results (BS, NS and AS) and simulation studies (PS) in section 5.1. In section 5.2 the issues involved when the primary structure undergoes plastic deformation are addressed. Experimental results (response and hysteresis loops) of 3SFS and comparisons with 3SFS assembly equipped with (i) NSD (ii) damper (iii) NSD and damper are also discussed in section 5.2. Section 5.3 contains the conclusions based on the experimental and simulation studies on SDOF structures.

5.1 Elastic structures

The concept of "apparent-weakening" in elastic and inelastic systems is explained in chapter 2. The main objective of the adaptive negative stiffness system is to shift the yielding behavior from the structure to the NSD and reduce the base shear (foundation) force of the structure while limiting its maximum response displacement and acceleration. The negative stiffness device (NSD), used in this study, exhibits

nonlinear-elastic negative stiffness behavior; by adding NSD to the elastic structure the resulting structure-device assembly behaves like a bilinear-elastic structure [160]. Peak acceleration and base shear experienced by the structures can be reduced by adding the negative stiffness device and the additional deformations caused due to the reduced stiffness can be contained by adding the viscous damper. A short description of the working principle of adaptive negative stiffness system in reference to the 3SFS and NSD developed in this study is presented next.

Assume a single degree of freedom linear elastic structure with stiffness K_e and no damping, the force deformation (F-D) behavior ($F_s(u)$) is shown in Figure 5.1(a,b). At displacements u_1 and u_2, the force in the structure are F_{s1} and F_{s2} respectively, shown in Figure 5.1(b). The F-D behavior of NSD ($F_{NSD}(u)$) is shown in Figure 5.1(a,b); NSD has zero stiffness until $|u| < u_1$ and beyond this displacement it exerts negative nonlinear-elastic stiffness. The displacement at which the NSD engages, u_1, called as "apparent yield-displacement" and the force exerted by the NSD at displacement u_2 is $-F_{NSD2}$ ($F_{NSD2} > 0$), shown in Figure 5.1(b). Although the NSD exhibits nonlinear stiffness beyond u_1, the stiffness of NSD between u_1 and u_2 remains almost constant, K_{NSD}, so the NSD can be assumed to be linear in this region. This argument is also justified using the F-D curves obtained from the experimental results shown in the forthcoming sections. The F-D behavior of the structure and NSD assembly is shown in Figure 5.1(c). At displacement u_1, the assembly force, F_{n1}, is same as the force in the primary structure (F_{n1}= F_{s1}) because the NSD does not exert any force until $|u| > u_1$. At displacement, u_2, the force in the assembly is $F_{n2} = F_{s2} - F_{NSD2}$. The stiffness of the structure and NSD assembly, K_n, is equal to K_e for $|u| < u_1$ and $K_n = K_e - K_{NSD}$ for $u_1 \leq |u| < u_2$. Since the structure and device assembly is elastic and exhibits two stiffness, K_e and K_n, it is called "bilinear elastic" system.

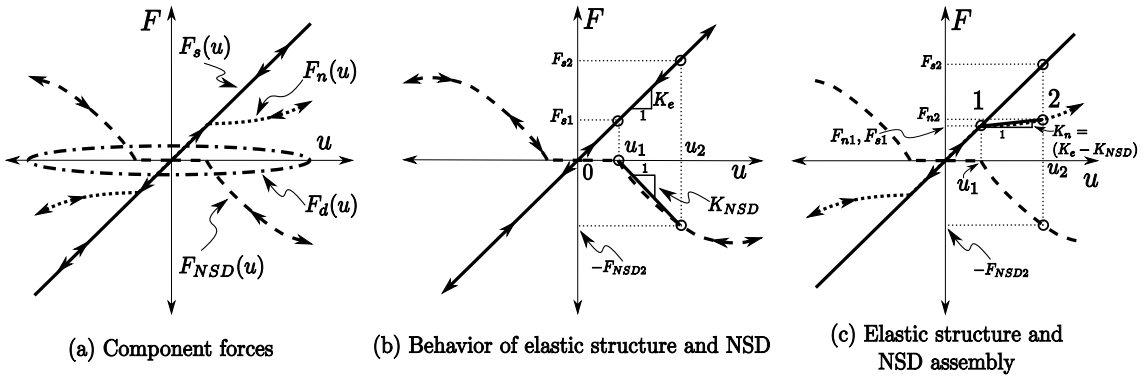

Figure 5.1 : Schematic diagram depicting "apparent-weakening" in elastic systems

In chapter 4, it has been shown that the behavior of the components: 3SFS (BS), NSD-East, NSD-West and the viscous damper; can be captured accurately. Next, the predicted behavior of NS and AS is compared with experimental results to show that the analytical models used in this study are consistent in capturing the observed experimental behavior. The measured ground acceleration and shake-table rocking is used as the ground excitation in the simulation studies. Shear force in the columns is measured using the MF-load-cells, base shear is calculated using the acceleration of all the three floors, force exerted by the NSDs and damper are also measured using the load-cells. Kobe fault-normal ground motion with PGA of 0.29g is used to test the performance of all the four systems in elastic region.

5.1.1 3SFS and NSD assembly

The role of NSD in NS and AS is to reduce the base shear of the structure and as a result reduce the acceleration experienced by the structure. This is depicted in the results shown in Figure 5.2-5.5. Force-deformation curves of the columns in the first-floor of 3SFS and the assemby (3SFS, NSD-East and NSD-West) in NS for the

Kobe FN ground motion is shown in Figure 5.2. The reduction in assembly stiffness with the addition of NSD is evident from Figure 5.2. Force-deformation behavior of the NSD-East and NSD-West is shown in Figure 5.3. Please note that the F-D loops of NSD in Figure 5.3 have significant friction hysteresis, but the models developed previously in section-4.2.1 do not take this into account. Sivaselvan-Reinhorn model is used to account for the friction hysteresis of NSDs.

First-floor deformation, acceleration and base shear are shown in Figure 5.4. The predicted first-floor deformation and base shear is matching the experimental behavior very accurately. The acceleration predicted using the analytical model has high frequency information due to the inclusion of shake table rocking. The experimental and predicted force-deformation loops of all the components in NS are separately shown in Figure 5.5. From Figure 5.5, it is evident that by adding NSDs to the 3SFS the peak assembly force in the first-floor is reduced by 45%. The peak acceleration of the first-floor is also reduced by 25% compared to BS (refer to Table 5.1 and Figure 5.14) but the peak deformation of the first story has increased by 10% in the case of NS. This increase in inter-story deformation is due to the reduction in story stiffness. From Figure 5.5, it is evident that the addition of NSD to 3SFS will result in bilinear elastic behavior of the assembly. It is also clear from all the subplots in Figure 5.2-5.5 that the observed experimental behavior of all the components and the assembly in the NS can be captured very precisely with the analytical model used in this study. Next, the role of viscous damper in AS is demonstrated.

5.1.2 3SFS, NSD and damper assembly

For the same system described previously (3SFS and NSD assembly), by adding the viscous damper the deformation of the assembly is reduced along with the base shear

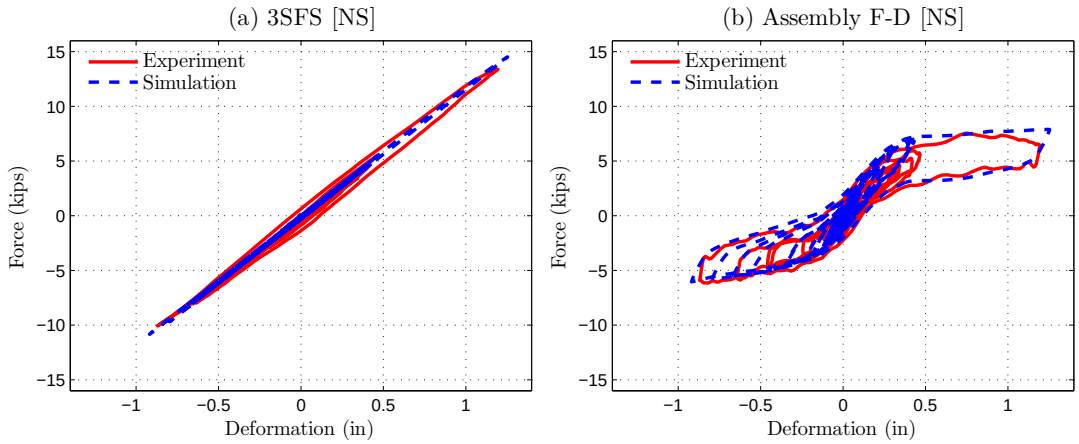

Figure 5.2 : F-D behavior of 3SFS and assembly in NS (Kobe GM; PGA=0.29g)

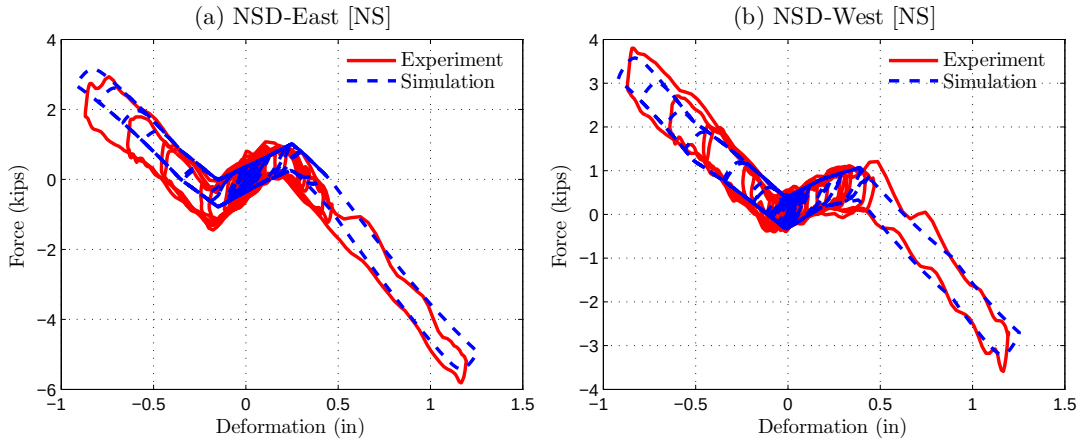

Figure 5.3 : F-D behavior of NSDs in NS (Kobe GM; PGA=0.29g)

and acceleration. The Experimental and predicted force-deformation loops of the first-floor of 3SFS and damper are compared in Figure 5.6. The stiffness of 3SFS in Figure 5.6(a) is 5% higher than the simulations and also Figure 5.2(a) due to the additional connections of NSD. Force-deformation behavior of NSD-East and NSD-West is shown in Figure 5.7. The maximum deformation of NSD has decreased to 0.8 *in.* from 1.2 *in.* (Figure 5.3) with the addition of viscous damper. The F-D behavior

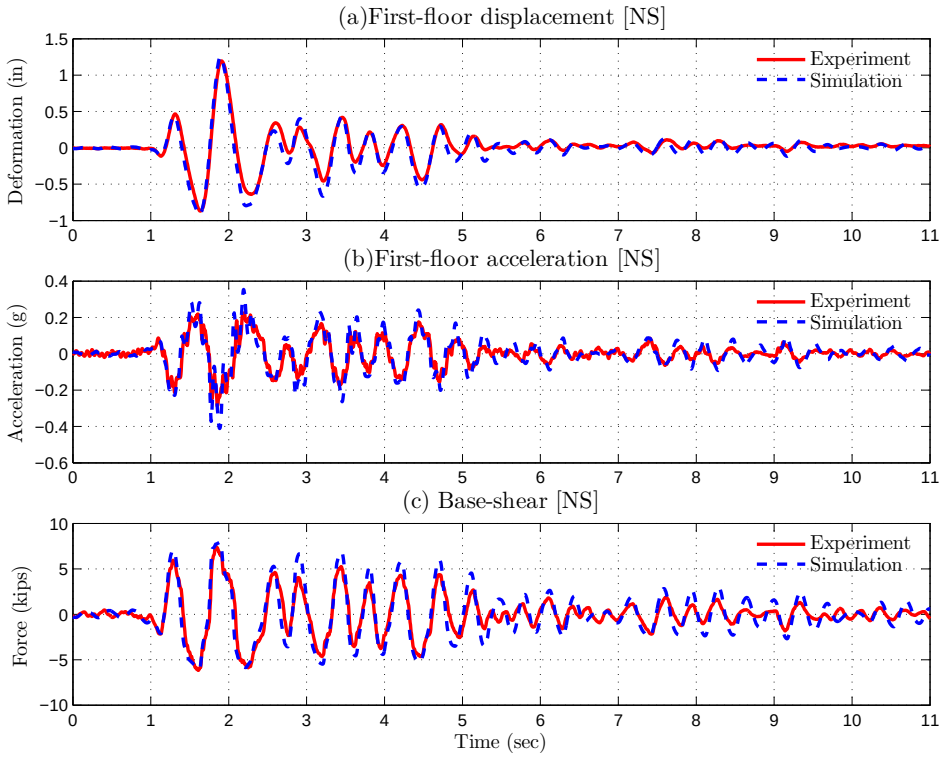

Figure 5.4 : First-floor response and base shear of NS (Kobe GM; PGA=0.29g)

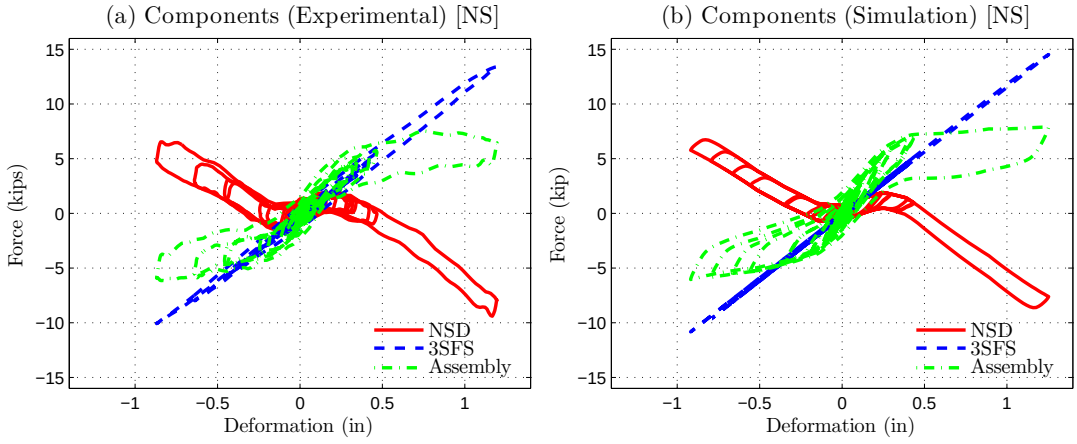

Figure 5.5 : F-D behavior of NS with components (Kobe GM; PGA=0.29g)

of all the components of AS are shown separately for experiments and simulations in Figure 5.8. The first-floor deformation, acceleration and base shear of AS are shown in Figure 5.8. Unlike the case of NS, the acceleration response of simulations and experiments is matching very accurately in the case of AS. The experimental and predicted F-D behavior of AS is compared in Figure 5.10. The analytical hysteresis loop is bigger than the experimental but the overall trend is matching very well.

By adding the viscous damper, the additional damper force exerted on the structure will increase the base shear of the structure by 15% compared to NS but it is still 30% less than the BS (refer to Figure 5.4, 5.9, 5.14 and Table 5.1). The peak acceleration of the AS is same as the NS but the peak deformation of AS is 20% less than the BS this reduction is significant compared to the 10% increase as in the case of NS. By adding the viscous damper the base shear is slightly increased but the significant reduction in inter-story deformation achieved outperforms the increase in base shear.

The observed experimental behavior of all the components and the assembly in the AS is very accurately captured with the analytical model. This confirms that the response of PS predicted using the analytical model should be a very good estimate of the actual response of PS. Next, the response of all the systems is compared to show the effectiveness of AS.

5.1.3 Comparative study

By adding NSD to an elastic structure, the structure and NSD assembly will emulate a bilinear elastic system. Although addition of NSD will result in reduction of base shear and acceleration, it will also result in increased deformations. A viscous damper in conjunction with the NSD will attenuate base shear, accelerations and displacements.

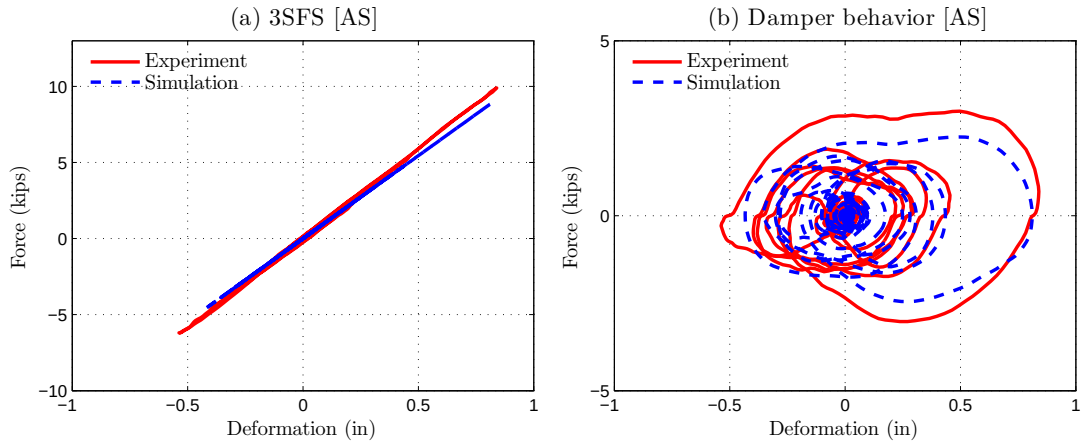

Figure 5.6 : F-D behavior of 3SFS and damper in AS (Kobe GM; PGA=0.29g)

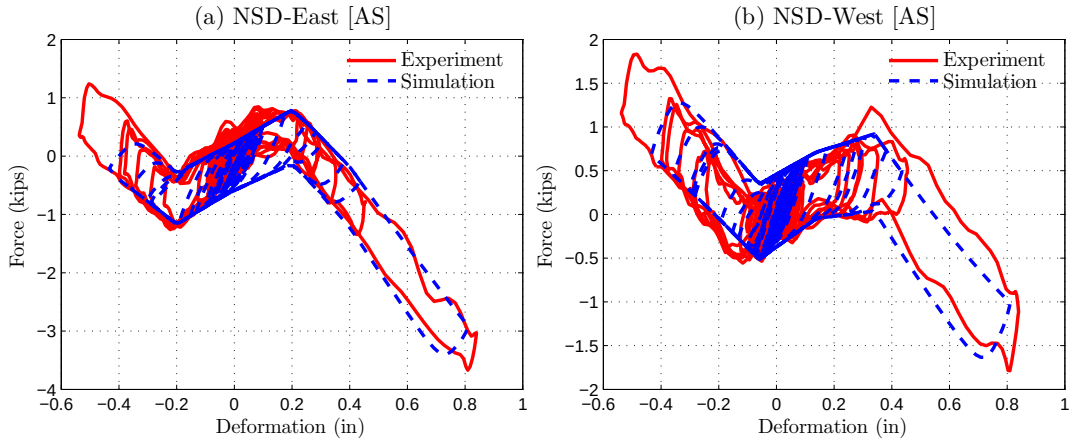

Figure 5.7 : F-D behavior of NSDs in AS (Kobe GM; PGA=0.29g)

In order to justify the usage of the NSD with the damper (AS), the response of AS is compared with PS next. The force-deformation loops of the first-floor in all the systems with the components is shown in Figure 5.11. The assembly F-D behavior is compared in Figure 5.12, first floor deformation, acceleration and base shear are compared in Figure 5.13. The asterisk mark on PS in the figures and tables indicates that the results are predicted and not from the shake-table tests.

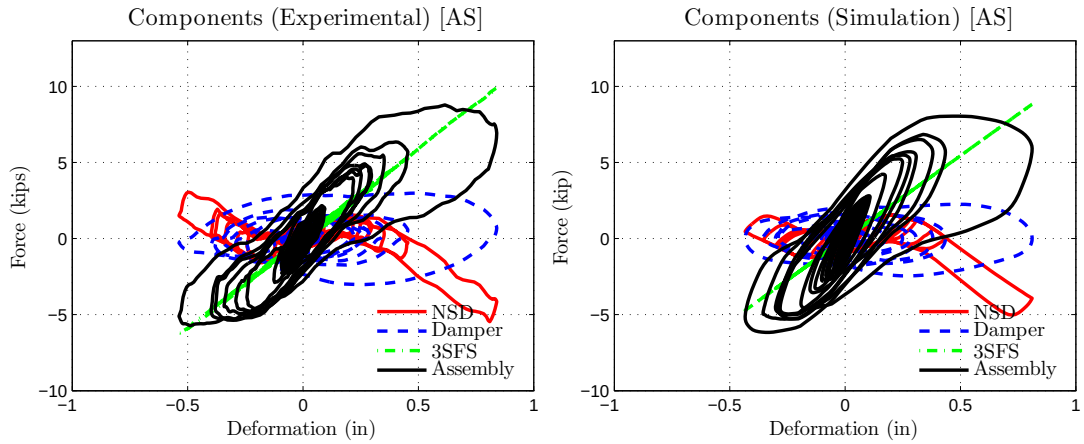

Figure 5.8 : F-D behavior of AS with components in elastic structure (Kobe GM; PGA=0.29g)

In the case of PS, although the peak first-floor deformation of PS is reduced by 20% compared to BS, there is no reduction in the base shear and the acceleration and this underlines the need of NSD in AS, shown in Figure 5.13. From Figure 5.11 and Figure 5.12, it is clear that with the addition of NSD, the assembly exhibits elastic bilinear behavior and as a result the base shear is reduced by more than 45% in the case of NS and 30% in the case of AS when compared to the BS and PS. From Figure 5.13(a), it can be seen that there is no permanent drift in the structure. Due to the presence of viscous damper in the AS, the displacements are reduced by 20% compared to BS and NS, the base shear and acceleration are reduced by 30% and 20% respectively, compared to BS and PS. Addition of viscous damper (PS) will reduce the peak deformation by more than 20% compared to BS, but the structure will experience almost the same acceleration and base shear as the uncontrolled structure, shown in 5.13(b,c). The NSD in conjunction with a viscous damper is capable of simultaneously reducing the base shear, the acceleration and the displacement of the structure.

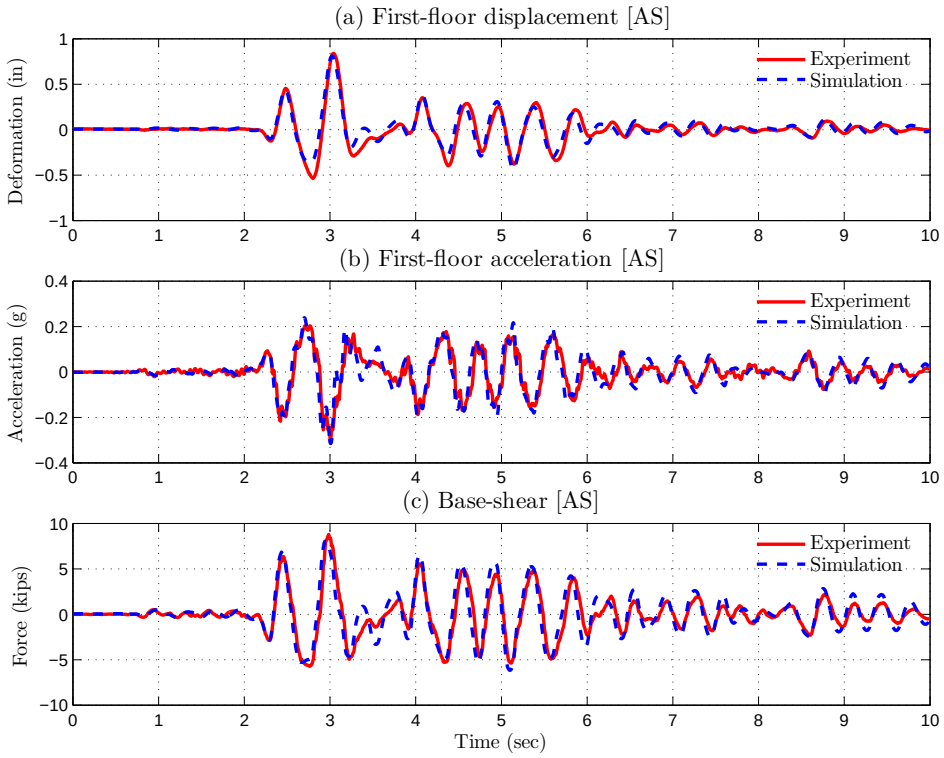

Figure 5.9 : First-floor displacement, acceleration and base shear of AS in elastic structure (Kobe GM; PGA=0.29g)

Similar study has been carried out for four other ground motions from PEER database and the peak response are tabulated in Table 5.1 and shown as bar-graphs in Figure 5.14. As stated previously, the ground motions are chosen to cover both the near-fault and far-field earthquakes. Since the NSD and structure assembly is a highly nonlinear system, NSD designed to reduce response for a structure and specific design ground motion has to be verified through analytical studies. The analytical models developed in this research are representative of the real life structures and can be used to verify the performance of AS for any ground motion data.

All the experimental results of BS, NS, AS and the simulation results of PS, shown in Table 5.1 and Figure 5.14 are summarized below. The key observations from the

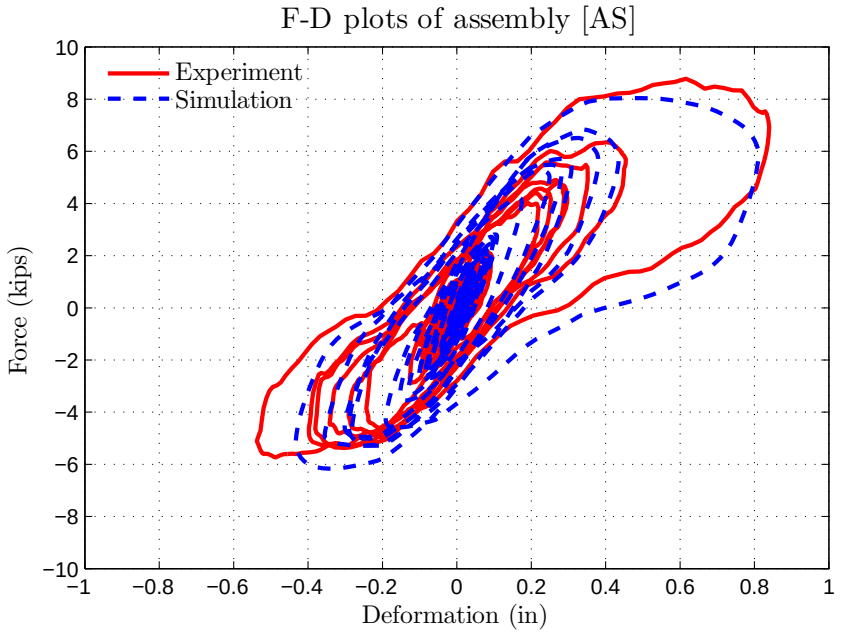

Figure 5.10 : Comparison of F-D behavior of AS (Kobe GM; PGA=0.29g)

results presented in Table 2 are:

- Base shear of the NS and AS is consistently reduced by more than 20% compared to BS and in some cases up to 35% (Pacoima, Chi-Chi and Newhall). Base shear of PS is only reduced by 5% in the case of Kobe and Newhall when compared to the BS and for the other ground motions it is reduced only by 15%.

- In the case of NS the peak deformation of the first-floor has a mixed response when compared with BS. Since there is no damper in the NS, the peak deformations can be larger than BS. For Kobe, Pacoima and Sylmar the peak deformation of NS is 5% more than the BS and for Chi-Chi and Newhall it is 20% less than BS. However, when the viscous damper is connected (PS and AS), the peak deformation is consistently reduced by more than 20%.

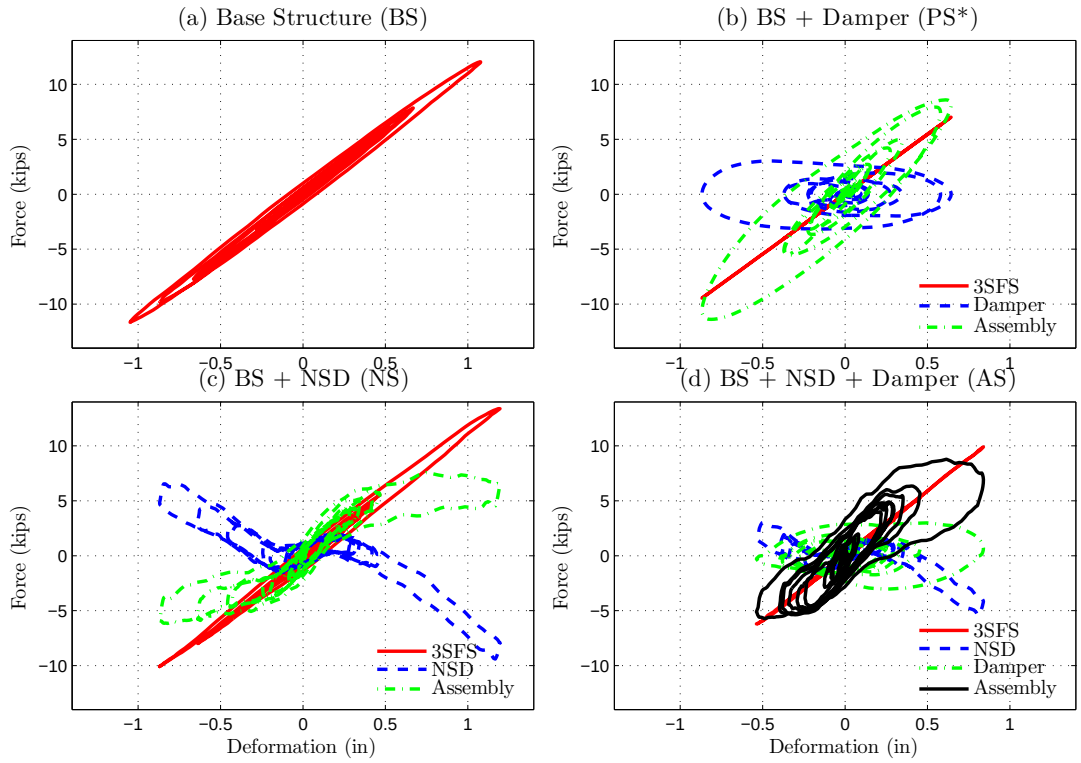

Figure 5.11 : F-D behavior of BS, PS, NS and AS with components in elastic structure (Kobe GM; PGA=0.29g)

- Addition of damper reduces displacements consistently for all the ground motions both in the case of PS and AS. Among the AS and PS the response has mixed behavior; for Pacoima and Sylmar, PS has 10% lesser displacements than AS and for the other three ground motions AS has 5% lesser deformations than PS.

- Peak acceleration of the first-floor in the case of PS is very similar to BS for Kobe and Newhall ground motions and it is reduced by 20% for the other ground motions. With the addition of NSD to the 3SFS along with the damper (AS) these accelerations are reduced by more than 20% and in the case of Pacoima

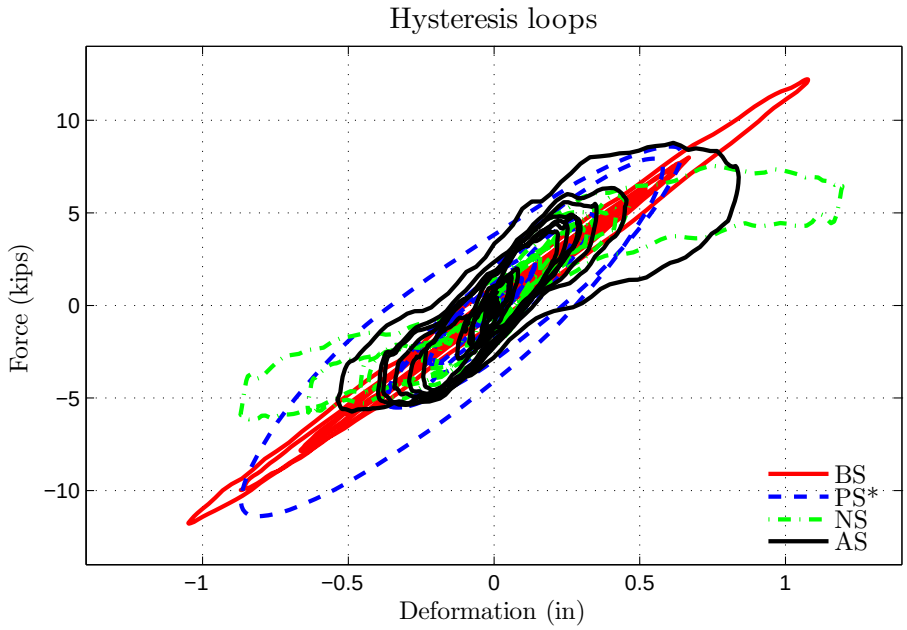

Figure 5.12 : Comparison of assembly force in SDOF elastic structure (Kobe GM; PGA=0.29g)

it is reduced by 40%.

Essentially, adding NSD to the elastic structure, a bilinear elastic system can be emulated and as a result the base shear demands on the main structure during strong earthquakes can be reduced by more than 30%, the peak acceleration experienced by the structure is also reduced by more than 20%. However, the peak displacement of the NSD and structure assembly is increased due to the reduction in stiffness induced by the NSD. These increased deformations are controlled by adding a viscous damper. Consistent response reductions are observed for a suite of ground motions by the addition of the viscous fluid damper. The observed experimental behavior can be reproduced by the presented analytical models at the component level and also for the structure and device assembly. Next the concept is extended to yielding

Table 5.1 : Summary of the peak responses from the shake table tests [Elastic-tests]

Serial number	Ground motion	System	Cmd. PGA (g)	First-floor response		Base shear (kip)
				Deform. (in)	Accel. (g)	
1	Kobe, 1995	BS	0.29	1.08	0.39	12.21
2		PS*	0.29	0.87 (19%)	0.39 (1%)	11.39 (7%)
3		NS	0.29	1.20 (-11%)	0.29 (27%)	7.55 (38%)
4		AS	0.29	0.84 (22%)	0.31 (20%)	8.78 (28%)
5	Pacoima, 1971	BS	0.56	1.20	0.45	13.05
6		PS*	0.56	0.67 (44%)	0.32 (29%)	8.89 (32%)
7		NS	0.56	1.25 (-4%)	0.29 (37%)	7.05 (46%)
8		AS	0.56	0.82 (32%)	0.27 (41%)	7.70 (41%)
9	Sylmar, 1994	BS	0.48	0.89	0.35	10.23
10		PS*	0.48	0.63 (29%)	0.26 (26%)	8.72 (15%)
11		NS	0.48	0.99 (-12%)	0.30 (15%)	6.84 (33%)
12		AS	0.48	0.74 (17%)	0.28 (21%)	8.08 (21%)
13	Chi-Chi, 1999	BS	0.76	1.07	0.44	11.97
14		PS*	0.76	0.70 (35%)	0.34 (23%)	9.48 (21%)
15		NS	0.76	0.86 (19%)	0.33 (24%)	6.43 (46%)
16		AS	0.76	0.59 (45%)	0.35 (21%)	7.88 (34%)
17	Newhall, 1994	BS	0.32	1.32	0.45	13.93
18		PS*	0.32	1.05 (21%)	0.46 (-1%)	13.53 (3%)
19		NS	0.32	1.01 (24%)	0.34 (25%)	8.77 (37%)
20		AS	0.32	1.00 (25%)	0.36 (21%)	9.15 (34%)

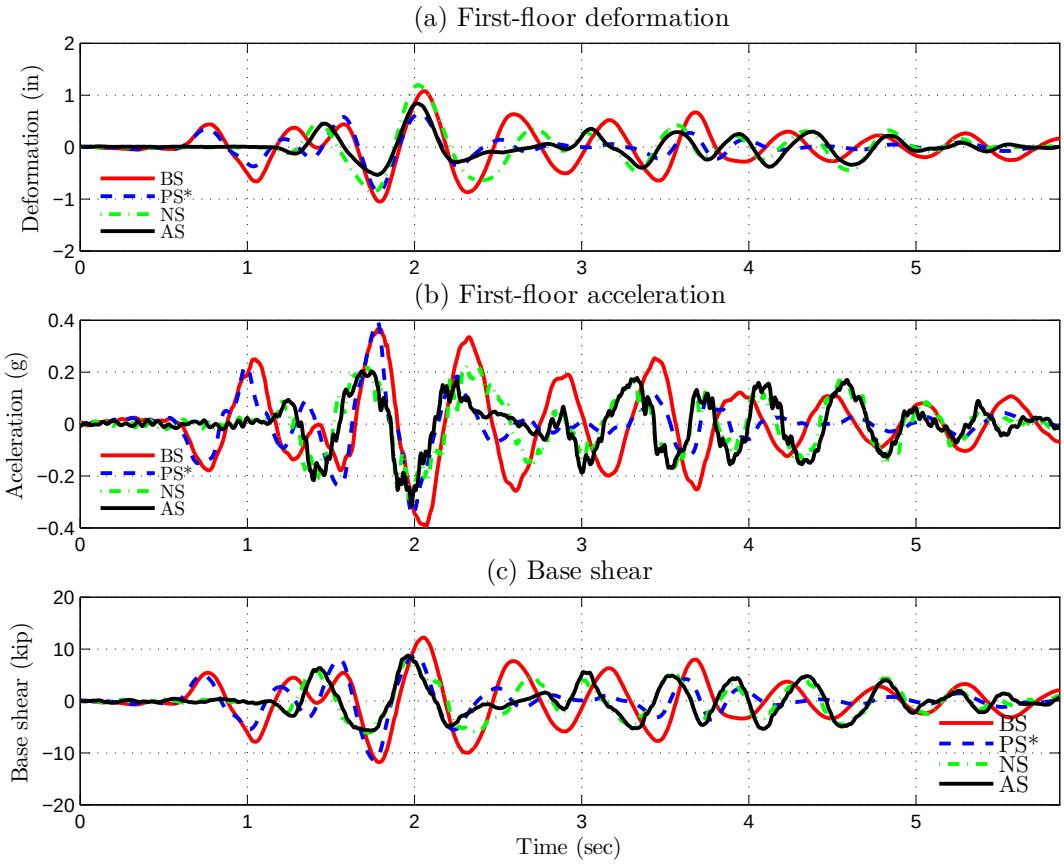

Figure 5.13 : Comparison of first-floor displacement, acceleration and base-shear in elastic structure (Kobe GM; PGA=0.29g)

systems and the complications involved when the primary structure undergo inelastic deformation are discussed.

5.2 Yielding structures

The objective of the adaptive negative stiffness system is to shift the yielding behavior from the structure to the NSD and reduce the base shear (foundation) force of the structure while limiting its maximum response displacement and acceleration using the passive damper. In this chapter, two terms: (1) apparent yield-displacement and

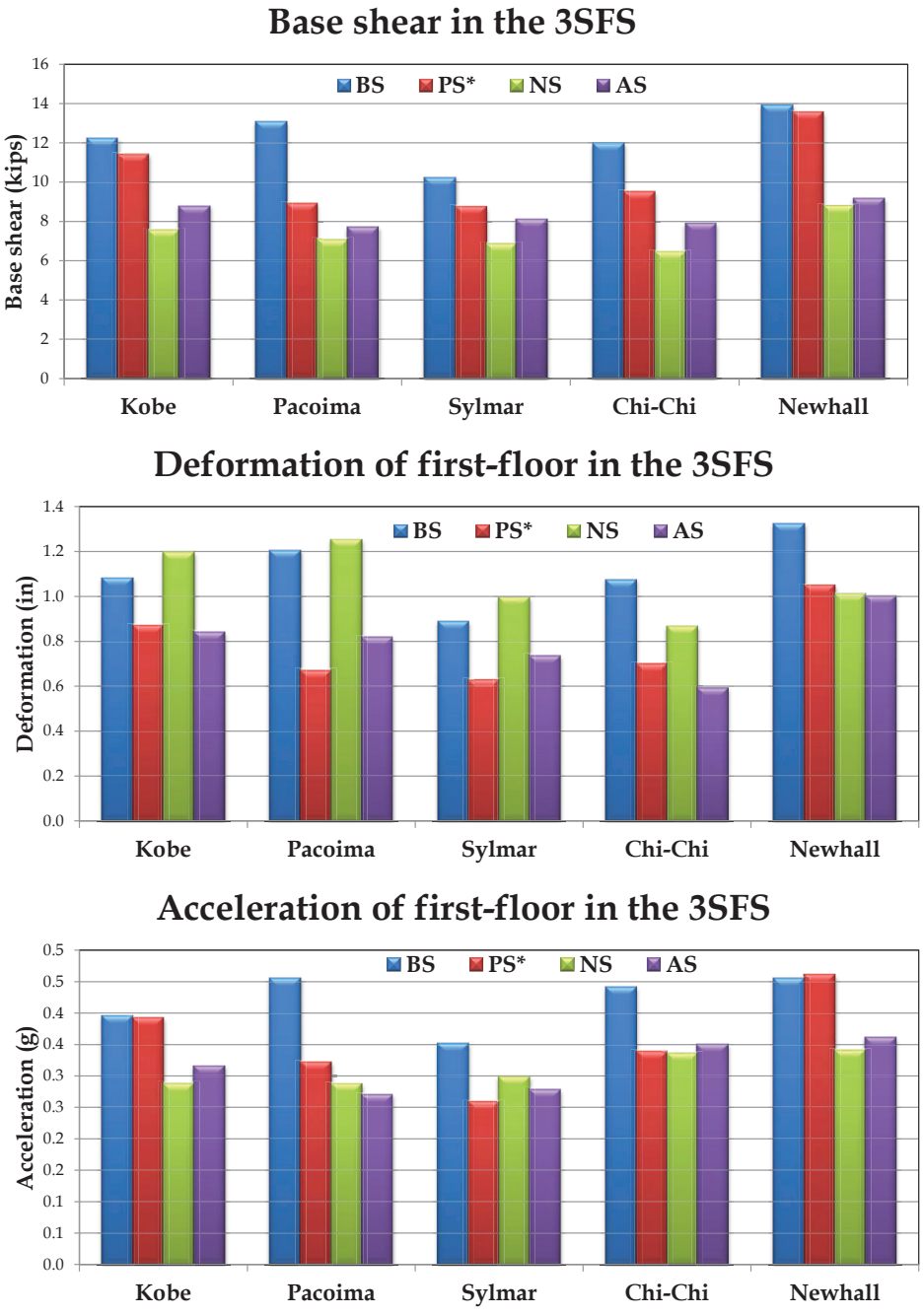

Figure 5.14 : Summary of peak responses in elastic systems

(2) yield displacement will be repeatedly used. To differentiate the two terms the idea of apparent weakening in bilinear inelastic structures is described next.

The force displacement characteristics of the bilinear inelastic structure, NSD and the structure with NSD assembly are shown in Figure 5.15(a), (b) and (c) respectively. Primary structure has a yield displacement u_y and the yield force is F_y, shown in Figure 5.15(a). Three crucial points are marked on the force deformation behavior of the NSD, shown in Figure 5.15(b). Point-1 is the displacement at which NSD engages (also referred as apparent yield-displacement), point-3 is when the NSD starts stiffening (stiffness becomes positive beyond point-3) and point-4 is when the NSD looses all the compression force. Readers should refer to section 3.2 for more details on the behavior of NSD.

By adding the NSD to the primary structure, the resulting force-displacement behavior of the combined system is shown in Figure 5.15(c). The behavior of the structure with NSD will not be altered for $|u| < u'_y$. Beyond u'_y, the stiffness of the combined system reduces until u_3. The structure and NSD assembly behaves like a nonlinear elastic structure for displacements $|u| < u_y$. For displacements larger than u_3, the stiffness of the structure and NSD assembly again increases and the magnitude will be higher than the elastic stiffness. At displacement u_4, the structure and the assembly (primary structure with NSD) will experience the same amount of force, shown in Figure 5.15(c). Beyond u_4, the structure with NSD will have a very high stiffness and also has higher force compared to the primary structure. The stiffening point of NSD, u_3, should be close to the yield displacement of the primary structure, u_y.

From the force deformation behavior of structure and NSD assembly shown in Figure 5.15(c): (1) the assembly exhibits the same behavior as the primary structure

for $|u| < u'_y$ (2) the shear force experienced by the assembly is significantly less than the primary structure for $u'_y < |u| < u4$. (3) the stiffness of the assembly is very high for $|u| > u4$, so the assembly can be prevented from collapsing due to large plastic deformations. Since the primary structure itself is yielding, the permanent deformation of the structure and NSD assembly after a ground motion is discussed next in detail.

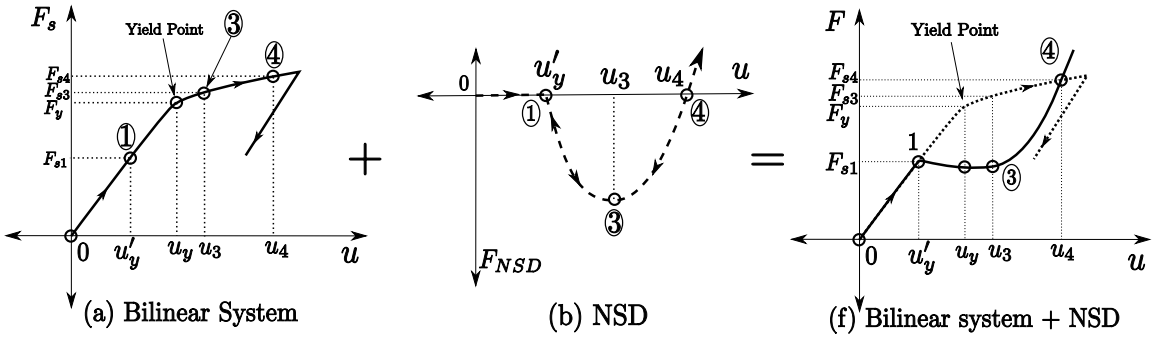

Figure 5.15 : Schematic diagram depicting "apparent-weakening" in yielding systems

The behavior of primary structure itself is inelastic; adding a nonlinear-elastic device to the yielding structure will result in a more involved system. To understand the permanent deformations in the structure and NSD assembly, it is studied in two different regimes: (1) mild yielding systems (2) heavily yielding systems [161].

Mild yielding systems:

The response of the structure and NSD assembly in mild yielding case is shown in Figure 5.16(a). Say, for a given ground motion, the assembly first deforms in the negative direction but the deformation is less than u_y (shown in Figure 5.16(a)); so the assembly will remain nonlinear elastic and retraces its path. Next, the assembly deforms in the positive direction and reaches a peak deformation at point-5, $u_5 > u_y$

(shown in Figure 5.16(a)). Since the peak deformation is greater than u_y, the primary structure will undergo a permanent inelastic deformation and will have a residual drift (plastic deformation). If there are no significant peaks in the subsequent load, the assembly will oscillate at low amplitudes and reaches point-6 (shown in Figure 5.16(a)) at the end of loading cycle. The plastic deformation in the primary structure is $u_{d6} = u_5 - u_y$; subscript-"d" refers to permanent drift. Since the NSD exerts no stiffness for $|u| < u'_y$, the permanent deformation in the assembly is same as the plastic deformation in the primary structure if $|u_{d6}| < u'_y$ as shown in Figure 5.16(a). If the permanent yield deformation in the structure, u_d, is less than u'_y, then the structure is assumed to have undergone mild yielding. The assembly always reaches the point where the assembly force is zero, following a loading cycle. Next, the condition in which, $|ud| > u'_y$, is studied.

Heavily yielding systems:

Assume a particular load in which there are two dominant half-pulses, one in the positive direction and the other in negative direction. For the first pulse, say, the assembly deforms in negative direction with mild yielding as shown in Figure 5.16(b). Then for the next pulse, the assembly deforms in positive direction and reaches a peak deformation u_7. Since there are no other dominant pulses, the assembly oscillates at low amplitudes and reaches point-9, where the assembly force is zero as shown in Figure 5.16(b). The permanent deformation in the assembly is u_{d9}. It should be noted that the assembly force is zero at point-9, but the force in the primary structure is F_{s9} and the force in NSD is F_{NSD9} as shown in Figure 5.16(b). The forces in structure and NSD have save magnitude but with different sign so they nullify each other to result in zero assembly force. The actual plastic deformation in the primary structure is u'_{d9}; which is less than u_{d9} as shown in Figure 5.16(b).

By disconnecting the NSD, the primary structure will move to the displacement u'_{d9}. The difference of the displacements u_{d9} and u'_{d9} is called recoverable permanent-drift or simply recoverable-drift, u_{rd}.

In brief, for heavily yielded systems, the permanent drift in the assembly (u_{d9}) is larger than the plastic deformation in the primary structure (u'_{d9}). Deformation, u_{rd} can be recovered from the assembly to reach u'_{d9}. In the experiments carried on the 3SFS, the connectors between the NSD and primary structure have a slotted hole to disengage the NSD easily and recover u_{rd}. The trend in the permanent deformation of the primary structure and assembly will again be different for deformation larger than u_4 (shown in Figure 5.15(b)). Due to the very high assembly stiffness for displacement greater than u_3, the assembly deformation will never reach u_4. The concept explained using schematic diagrams shown in Figure 5.16 can be extended to multiple loading cycles. Next the experimental results of NS in which the primary structure had yielding is presented. The results are overlapped with predicted results obtained from the analytical models.

5.2.1 Mild-yielding structures

In this section "apparent weakening" in mild and heavily yielding systems is analyzed through shake-table studies on 3SFS and NSD assembly (NS). Since the damper has a maximum stroke of only two inches and the yield displacement is 1.5 inches, the heavy yielding tests could not be carried on the 3SFS, NSD and damper assembly. In elastic systems, experimental results for Kobe FN ground motion are presented in section 5.1. In the case of mild yielding and heavy yielding, 3SFS and NSD assembly is subjected to Pacoima ground motion at two different amplitudes (peak ground acceleration (PGA) of 0.57g and 0.81g).

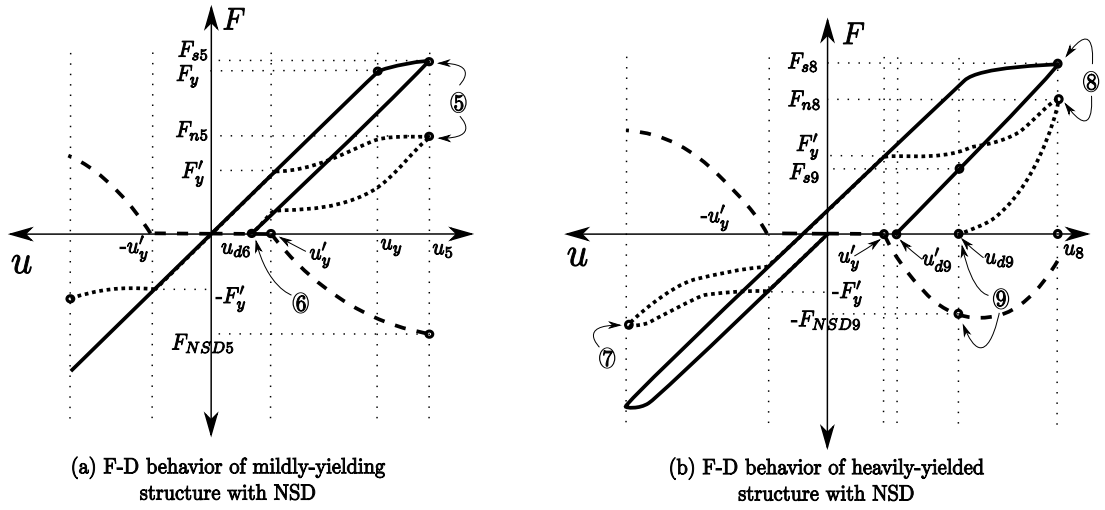

Figure 5.16 : Recoverable drift and residual drift in NSD and bilinear inelastic structure assembly

When the assembly is subjected to the ground motion at PGA of 0.57g there is mild yielding in the primary structure. The force-deformation behavior of the primary structure (3SFS), and the assembly is shown in Figure 5.17; the F-D loops of NDS-East and NSD-West are shown in 5.18. The experimental and analytical force-deformation behavior of the assembly with the components is shown separately in Figure 5.19. First-floor displacement, acceleration and base shear response are shown in Figure 5.20. From force-deformation behavior of primary structure, shown in Figure 5.17(a) and displacement response shown in Figure 5.20(a), it is clear that the 3SFS has yielded at 1.8 seconds when the peak deformation in the structure is 1.7 inches. The structure has undergone plastic deformation and it subsequently vibrates about 0.11 inch displacement. Although the primary structure has yielded, since the plastic deformation is less than the simulated yield displacement, the permanent drift in the assembly is same as the permanent drift in the primary structure. Force-

deformation behavior shown in Figure 5.17(a) and Figure 5.19 confirms that the base shear of the assembly is reduced by more than 50% by adding the NSD to the primary structure. This behavior is consistent in both the predicted analytical results and observed experimental results.

The trace of the force-deformation plots of 3SFS, NSD and assembly (similar to the schematic plots shown in Figure 5.16(a)) is shown in Figure 5.21 for both experimental and analytical results. The trace of force-deformation plots is obtained by removing the friction in the NSDs (Figure 5.18), assembly (Figure 5.17(b)) and discarding the vibrations after 2.5 seconds. From the experimental results in Figure 5.21(a), the permanent drift in the assembly and the plastic deformation in the primary structure are same, 0.11 in. and in the case of simulation results, shown in Figure 5.21(b), it is equal to 0.09 *in.* The plastic deformation in 3SFS and the permanent drift in assembly are same because the simulated yield displacement in NSD is 0.25 *in.* and the permanent drift in the primary structure is less than 0.25 *in.*.

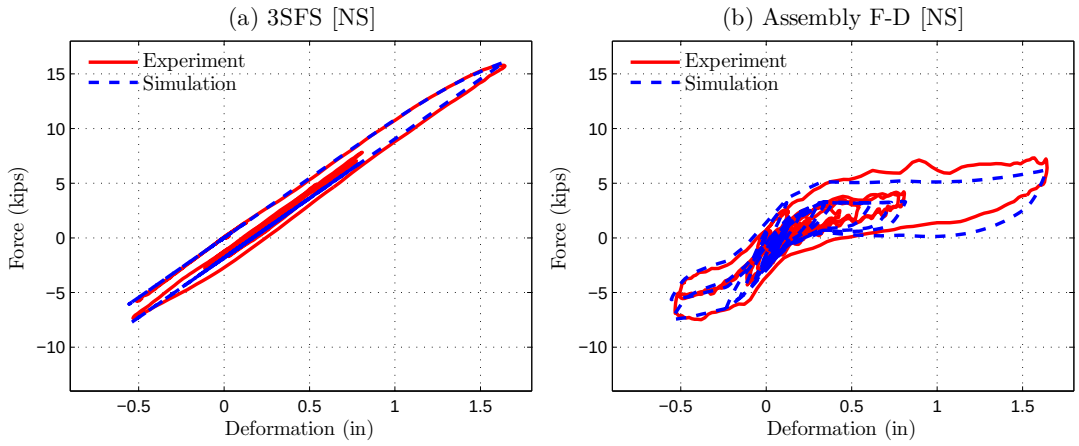

Figure 5.17 : F-D behavior of 3SFS and assembly in NS (Pacoima GM; PGA=0.57g)

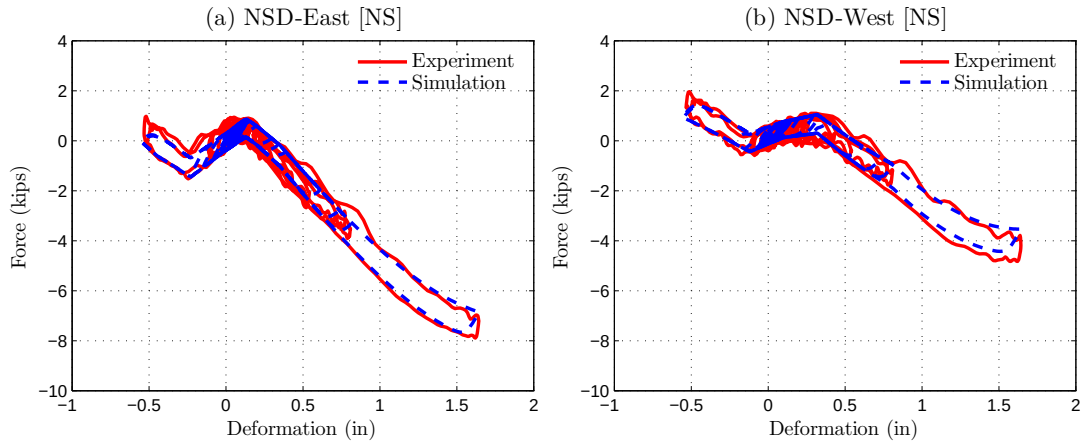

Figure 5.18 : F-D behavior of NSDs in NS (Pacoima GM; PGA=0.57g)

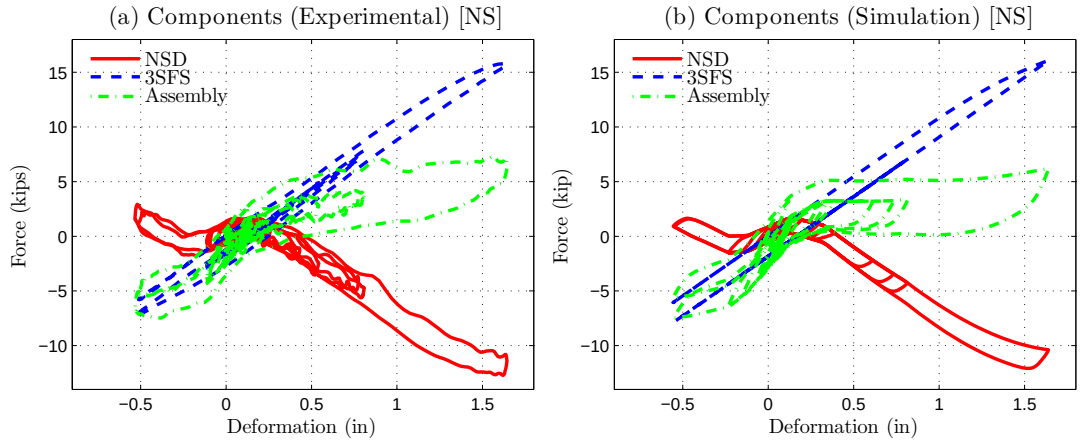

Figure 5.19 : F-D behavior of NS with components in mild-yielding structure (Pacoima GM; PGA=0.57g)

5.2.2 Heavy-yielding structures

When the structure is subject to the ground motion with PGA of 0.81g, the primary structure in NS has yielded significantly. The force-deformation behavior of the primary structure (3SFS) and the assembly are shown in Figure 5.22, and NSDs (NSD-East and NSD-West) are shown in Figure 5.23. The experimental and an-

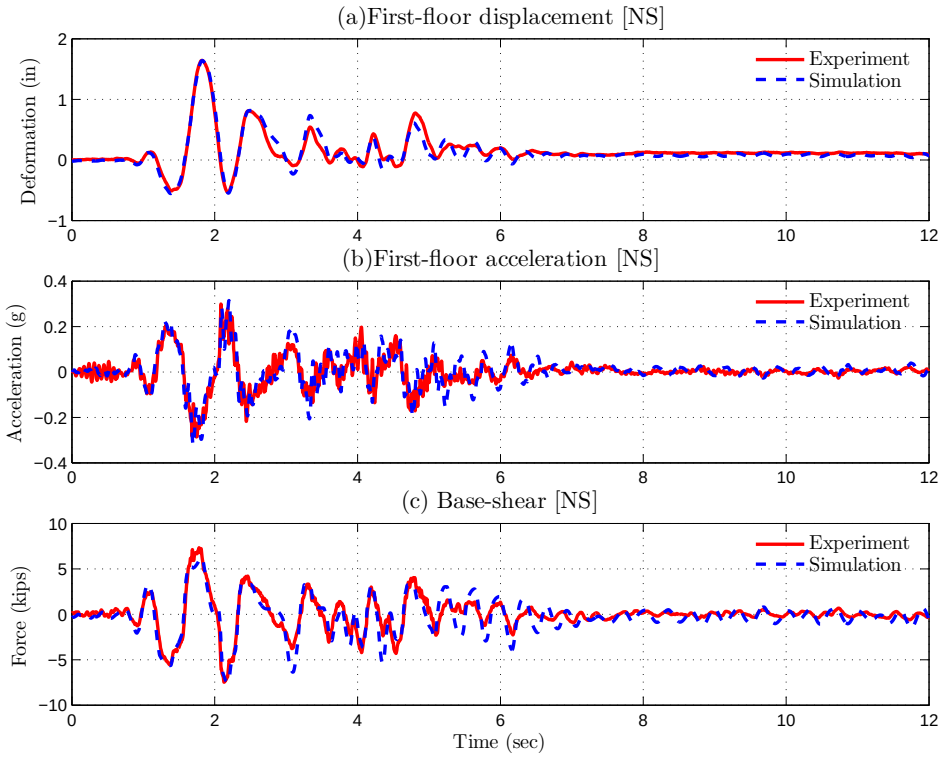

Figure 5.20 : First-floor response and base shear of NS in mild-yielding structure (Pacoima GM; PGA=0.57g)

alytical force-deformation behavior of the assembly with the components is shown separately in Figure 5.24 for the heavy yielding case. First floor displacement and acceleration response of the first-floor are shown in Figure 5.25(a,b), and base shear is shown in Figure 5.25(c). The overall trend in the analytical and experimental behavior depicted in Figure 5.22 and Figure 5.23 is similar, but the peak deformation in the experiments is 2.83 *in.* and the peak deformation in analytical studies is 2.51 *in.*

From the experimental force-deformation behavior of primary structure shown in Figure 5.22(a) and displacement response shown in Figure 5.25(a), 3SFS has yielded at 2.3 seconds when the peak deformation in the structure is 2.83 *in.* The plastic

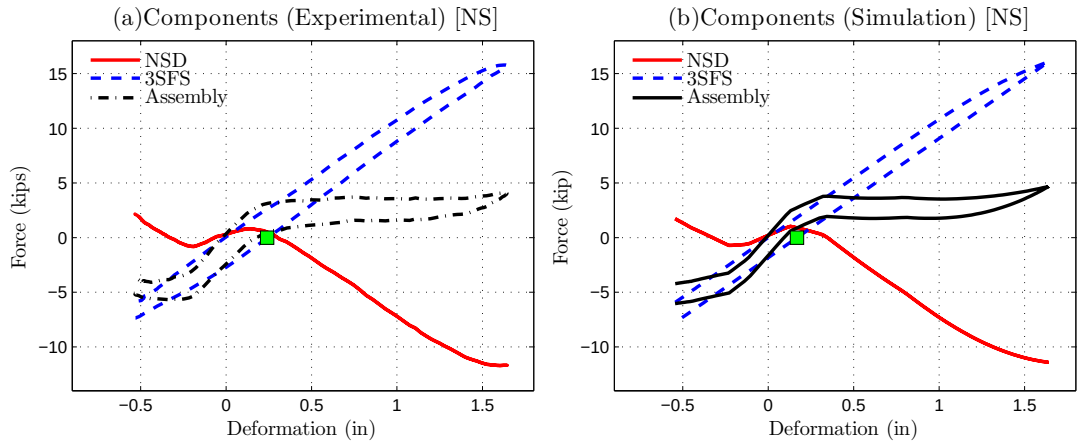

Figure 5.21 : Trace of F-D behavior of NS with components in mild-yielding structure (Pacoima GM; PGA=0.57g)

deformation of the primary structure is 1.14 *in.* as shown in Figure 5.25(a). Since the simulated yield displacement (0.25 *in.*) is significantly less than the plastic deformation in the 3SFS, the permanent deformation of the assembly will be higher than the plastic deformation of the 3SFS due to the presence of NSD as explained in the previous section. The assembly starts stiffening at 2 in displacement resulting in the increase in base shear as shown in Figure 5.24. Once the assembly starts stiffening, the excessive deformation caused due to the initial reduction in stiffness is contained and the structure is prevented from collapsing. Essentially, the accelerations and base shear of the assembly are reduced between the displacements, 0.5 *in.* and 3 *in.* by removing a segment of the force deformation loop of primary structure.

The trace of the force-deformation plots of 3SFS, NSD and assembly (similar to the schematic plots shown in Figure 5.16(b)) is shown in Figure 5.26 for both experimental and analytical results. The trace of force-deformation plots is obtained by removing the friction in the NSDs (Figure 5.23), assembly (Figure 5.22(b)) and

discarding the vibrations after 2.5 seconds. From the experimental results in Figure 5.26(a), the permanent drift in the assembly is 2.1 *in.* and the plastic deformation in the primary structure, shown in Figure 5.25(a) is 1.14 *in.* In the case of simulation results, shown in Figure 5.26(b), the permanent drift in the assembly is 2 *in.* and the plastic deformation in the primary structure, shown in Figure 5.25(a), is 0.89 *in.* Since the plastic deformation in the primary structure is much larger than the simulated yield displacement, the permanent drift in the assembly will be higher than the plastic deformation in the primary structure. So, in the experimental results, the residual drift in the NS will be *in.* in and the recoverable drift is 0.97 *in.* In the deformation plot shown in Figure 5.26(b), the NSD is disengaged from the structure at 9 seconds so the drift in the structure has reduced to 1.14 *in.*

In the next section, the advantages of using NSD in conjunction with the damper to attenuate the acceleration, displacement, base shear and permanent drift response is demonstrated by comparing with three other systems.

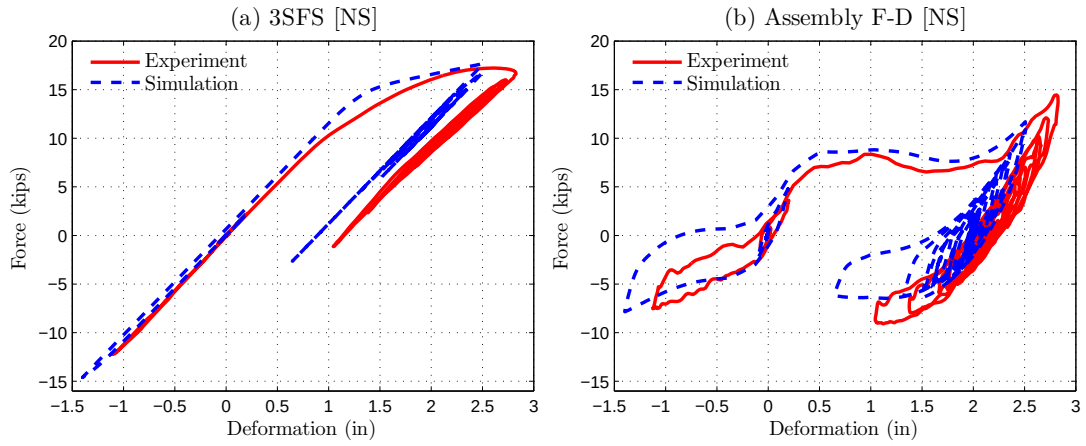

Figure 5.22 : F-D behavior of 3SFS and assembly in NS (Pacoima GM; PGA=0.81g)

Since the columns were yielding significantly after a strong ground motion, only

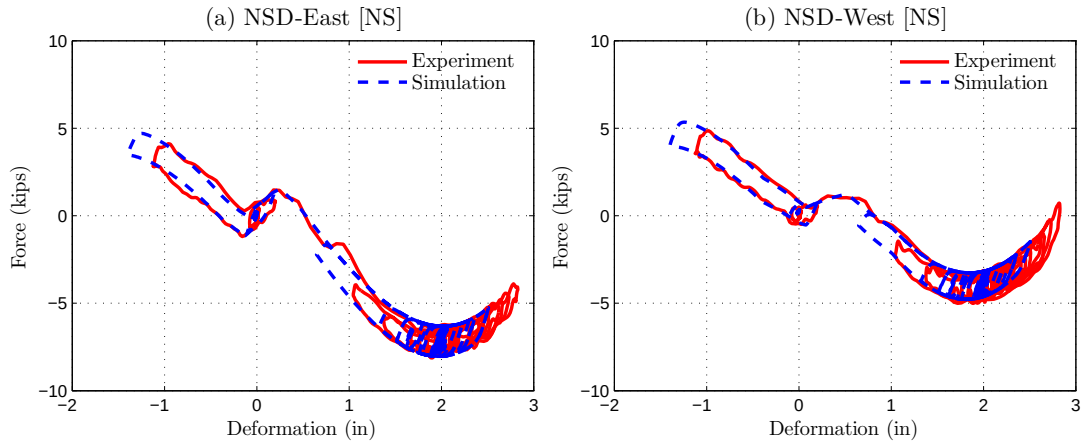

Figure 5.23 : F-D behavior of NSDs in NS (Pacoima GM; PGA=0.81g)

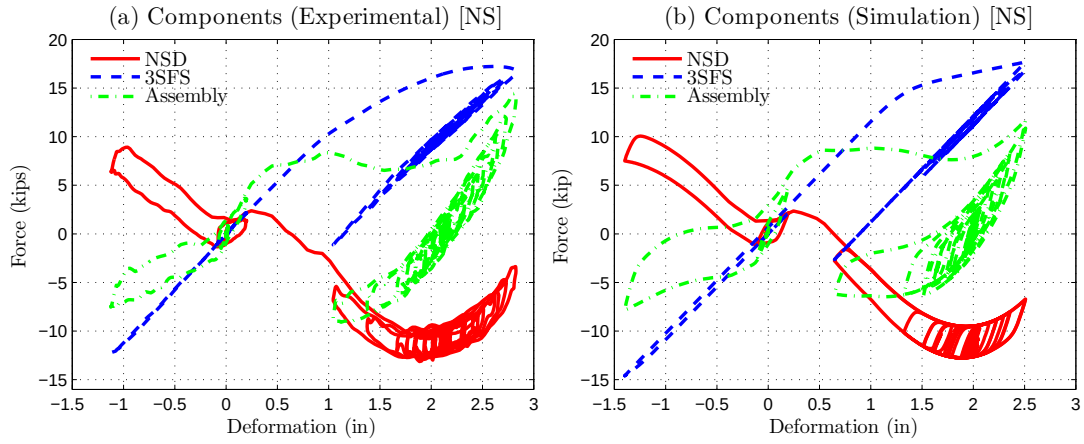

Figure 5.24 : F-D behavior of NS with components in heavy-yielding structure (Pacoima GM; PGA=0.81g)

one yielding experiment for each ground motion has been conducted. For Newhall, Pacoima and Sylmar ground motions, the NS is tested and for Kobe ground motion, the AS is tested. In this section the experimental results of AS and the simulation results of BS, PS and NS are compared to demonstrate the effectiveness of apparent-weakening and damping in yielding structures. The results from other shake table

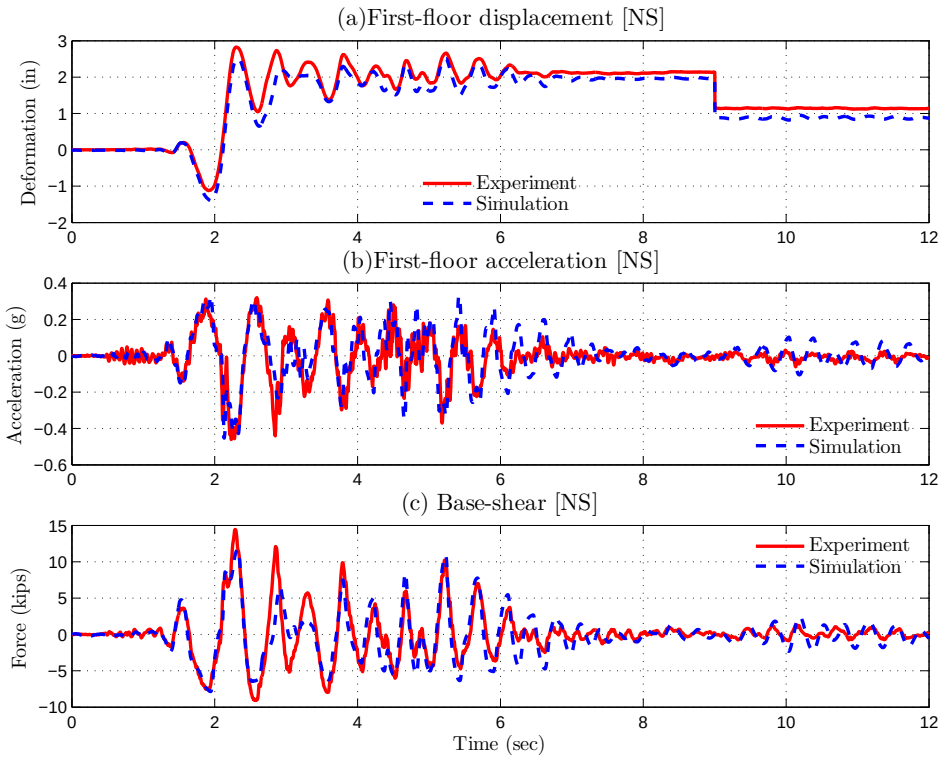

Figure 5.25 : First-floor response and base shear of NS in heavy-yielding structure (Pacoima GM; PGA=0.81g)

tests are summarized in Table 5.2 and Figure 5.30.

Force-deformation loops of all the four systems with components are shown in Figure 5.27 for Kobe-FN ground motion with PGA of 0.65g. Superscript-"*" denotes that the results are simulated using the analytical model. The accelerations, deformations (showing the drifts) and base shears of all the four systems are compared in Figure 5.28. From Figure 5.27(a) and Figure 5.28(a), the BS has undergone plastic deformation in the negative direction first and then in the positive direction. The peak deformation, acceleration and base shear of the first story in the BS are 2.84 *in.*, 0.79g and 17.7 *kips*, respectively, shown in Table 5.2. By adding NSD to the 3SFS (NS) due to the reduction in assembly stiffness beyond 0.5 *in.*, the assembly

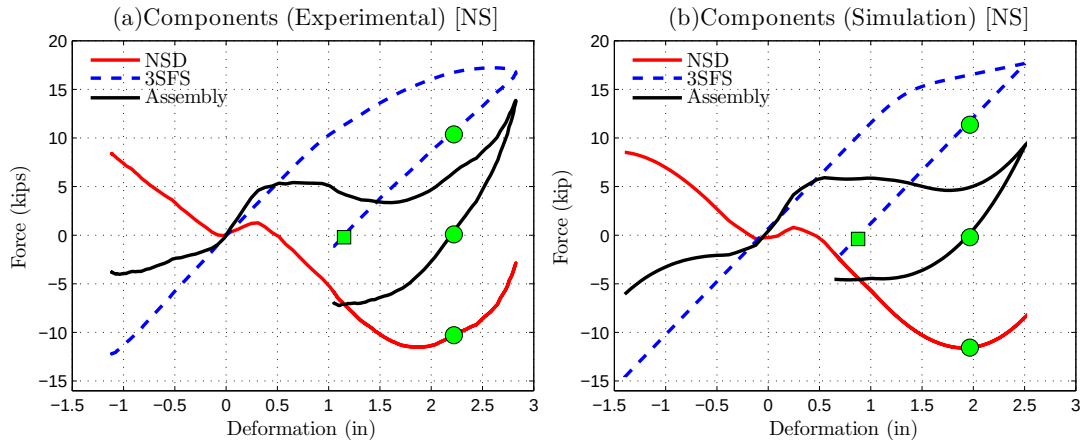

Figure 5.26 : Trace of F-D behavior of NS with components in heavy-yielding structure (Pacoima GM; PGA=0.81g)

has undergone significant deformation until it gets into the stiffening region, shown in Figure 5.27(c). Once the assembly enters the stiffening region, due to the high assembly stiffness and large plastic deformation of the 3SFS, the assembly will remain in the stiffening region. Permanent drift in the assembly after the ground motion is 1.67 *in.* (shown in Figure 5.28(a)) and the plastic deformation in the 3SFS is 0.87 *in.* as shown in Figure 5.27(c). The permanent drift in the NS after disconnecting the NSD at 6 seconds is shown in Figure 5.28(a). So, by adding the NSD, the accelerations and base shears can be reduced and the structure can be prevented from collapsing for large deformations. Although the peak deformations in NS are similar to BS, the global collapse of the assembly is prevented in NS due to the stiffening in NSD.

By adding a viscous damper to the structure along with the NSD, the experimental force-deformation plots of the assembly and components are shown in Figure 5.27(d). With the addition of viscous damper, the excessive deformations caused due to the reduction in assembly stiffness are contained. From Figure 5.27, 5.28, 5.29 and Table

5.2, the peak deformation, acceleration and base shear of the AS are reduced to 1.39 *in.*, 0.58g and 13.7 *kips*, respectively. The response of 3SFS with the viscous damper (PS) is also calculated to demonstrate the role of NSD in the AS. Although the deformations are reduced with the addition of viscous damper, the acceleration and the base shear of the assembly will significantly shoot up due to the damper force, as shown in Figure 5.28(b,c), 5.29 and Table 5.2. The peak deformation, acceleration and base shear of the PS are 1.93 *in.*, 0.73g and 22.4 *kips*. Clearly, by adding the NSD along with the damper, the base shear and accelerations can be reduced. Assembly force-deformation loops of all the four systems, shown in Figure 5.29, confirms that by adding NSD and damper to the bilinear inelastic structure, the displacement, acceleration and base shear can be reduced.

Table 5.2 and Figure 5.30 summarizes the peak response characteristics of all the four systems for four ground motions at higher PGA values so that the primary structure will yield. The key observations are:

1. Due to the presence of NSD, base shear of the NS and AS is consistently reduced up to 35% compared to the BS in the mild yielding cases. In the heavy yielding cases, the base shear in the assembly will be similar to the BS because of the stiffening. However, the structure can be prevented from collapse due to the high stiffness.

2. The addition of a viscous damper (PS) reduces the deformation of the assembly by more than 30% but the reduction in base shear less than 10%. In the case of Kobe ground motion, the base shear in PS has increased by 23%.

3. By adding the viscous damper in conjunction with NSD, the displacements, accelerations and base shears can be consistently reduced by more than 20%.

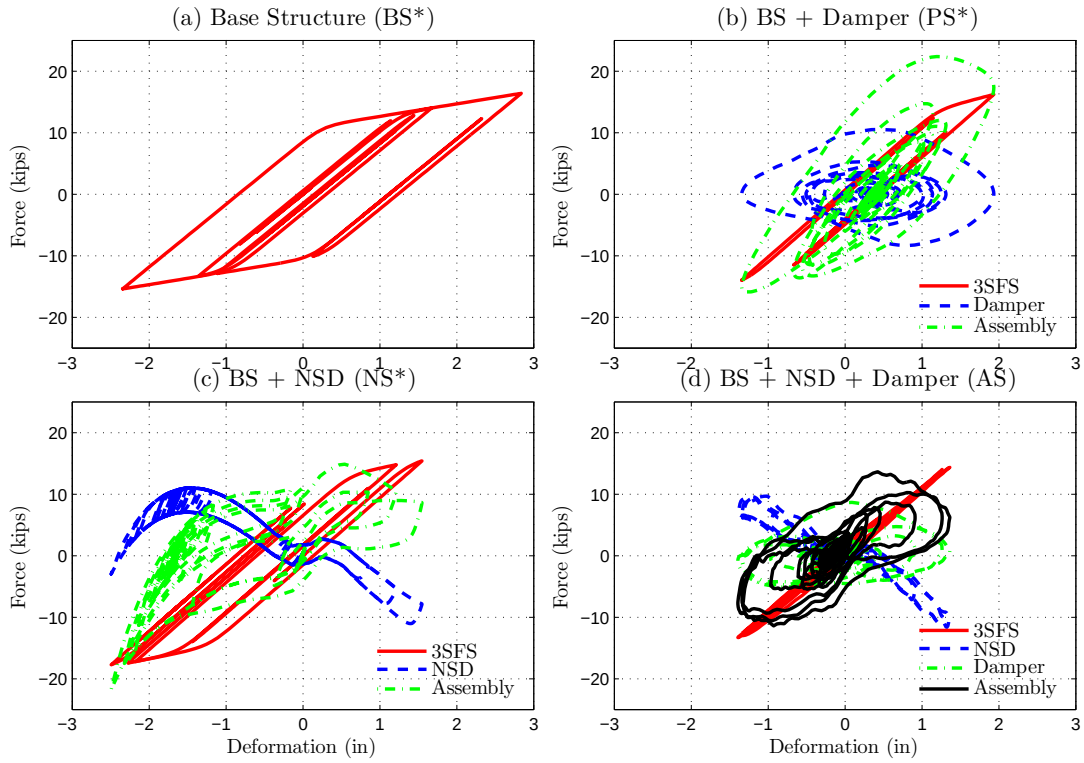

Figure 5.27 : F-D behavior of BS, PS, NS and AS with components (Kobe GM; PGA=0.65g)

4. Permanent drift in the assembly after the ground motion is equal to the plastic deformation in the primary structure if the plastic-deformation is less than simulated yield displacement. If the plastic deformation in primary structure is larger than the simulated yield-displacement then the permanent drift in the assembly will be higher than the plastic deformation but the drift in excess of plastic-deformation is recoverable.

5. The residual drift in AS is comparable with that of BS and PS. It should be noted that in the case of BS and PS the 3SFS is yielding in both the directions, so some of the plastic deformation is recovered. In the case of 3SFS and NSD

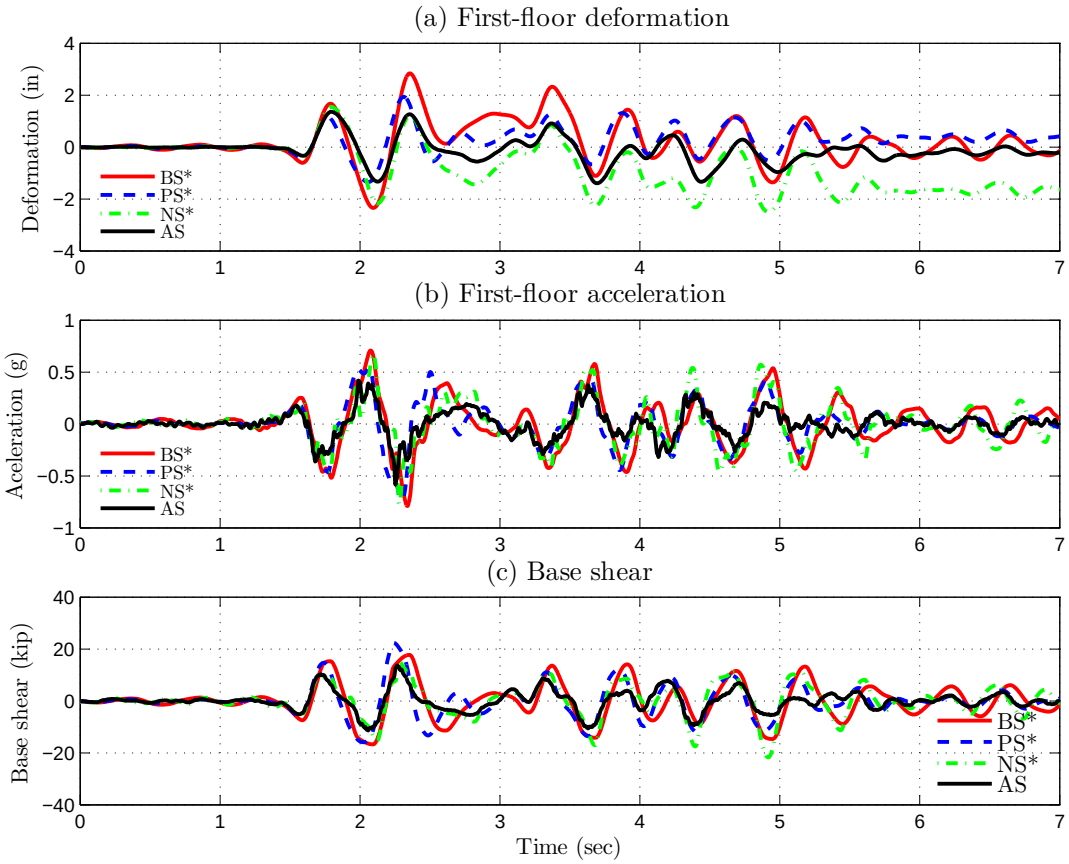

Figure 5.28 : Comparison of first-floor displacement, acceleration and base-shear (Kobe GM; PGA=0.65g)

assembly, since the force-deformation behavior of NSD is very asymmetric, the assembly has the tendency to remain in the region in which it has yielded first. However, simulation studies with a symmetric force-deformation of NSD have shown that the assembly can yield in both sides during the same ground motion (presented in chapter 2)

Table 5.2 : Summary of the peak responses from the shake table tests [Yielding-tests]

Sl. no.	Ground motion	Sys.	PGA (g)	First-floor response		Permanent drift			Base shear (kip)
				Deform. (in)	Accel. (g)	Tot.	Recov.	Resid.	
1		BS*	0.65	2.84	0.79	0.05	-	0.05	17.72
2	Kobe,	PS*	0.65	1.93 (32%)	0.73 (7%)	0.36	-	0.36	22.36 (-26%)
3	1995	NS*	0.65	2.49 (12%)	0.77 (2%)	1.67	0.80	0.87	21.74 (-23%)
4		AS	0.65	1.39 (51%)	0.58 (26%)	0.17	0.00	0.17	13.65 (23%)
5		BS	0.75	1.92	0.56	0.20	-	0.20	15.89
6	Pacoima,	PS*	0.81	1.16 (40%)	0.49 (13%)	0.00	-	0.00	14.47 (9%)
7	1997	NS	0.81	2.83 (-47%)	0.46 (18%)	2.11	0.97	1.14	14.45 (9%)
8		AS	0.75	1.65 (14%)	0.37 (35%)	0.32	0.12	0.20	10.10 (36%)
9		BS	0.68	1.29	0.47	0.00	-	0.00	13.37
10	Sylmar,	PS*	0.68	0.87 (32%)	0.38 (19%)	0.02	-	0.02	11.78 (12%)
11	1994	NS	0.63	1.71 (-32%)	0.34 (27%)	0.91	0.58	0.33	9.08 (32%)
12		AS	0.63	1.18 (8%)	0.34 (28%)	0.10	0.00	0.10	8.55 (36%)
13		BS	0.44	1.72	0.50	0.03	-	0.03	15.91
14	Newhall,	PS*	0.48	1.16 (33%)	0.44 (13%)	0.00	-	0.00	14.56 (8%)
15	1994	NS	0.48	1.36 (21%)	0.44 (12%)	0.43	0.30	0.13	10.02 (37%)
16		AS	0.44	1.30 (24%)	0.39 (22%)	0.16	0.00	0.16	10.71 (33%)

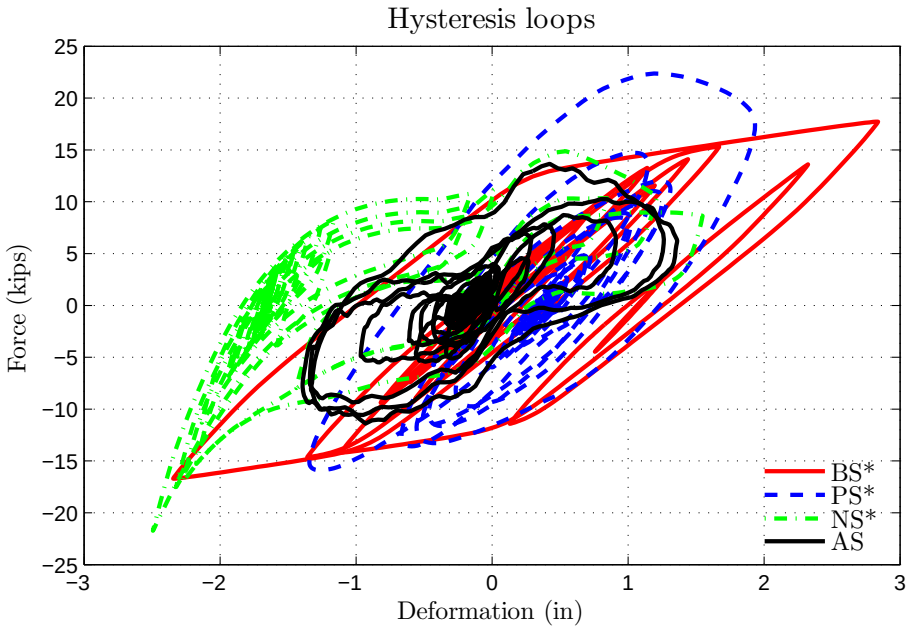

Figure 5.29 : Comparison of assembly forces in SDOF structure (Kobe GM; PGA=0.65g)

5.3 Summary

In this chapter, the concept of "apparent weakening" is analyzed in elastic and yielding structures. Comprehensive experimental and simulation studies have been carried on SDOF-3SFS yielding structure, to study the behavior of bilinear inelastic structure and NSD assembly during severe ground motions. Shake table studies carried on a SDOF-3SFS with the NSDs and damper installed in the first floor (AS) show that by adding NSD to the elastic structure, a bilinear elastic system can be emulated and as a result the base shear demands on the main structure during strong earthquakes can be reduced by 30%. The peak acceleration experienced by the structure is also reduced by more than 20%. However, the peak displacement of the NSD and structure assembly is increased due to the reduction in stiffness induced by the NSD.

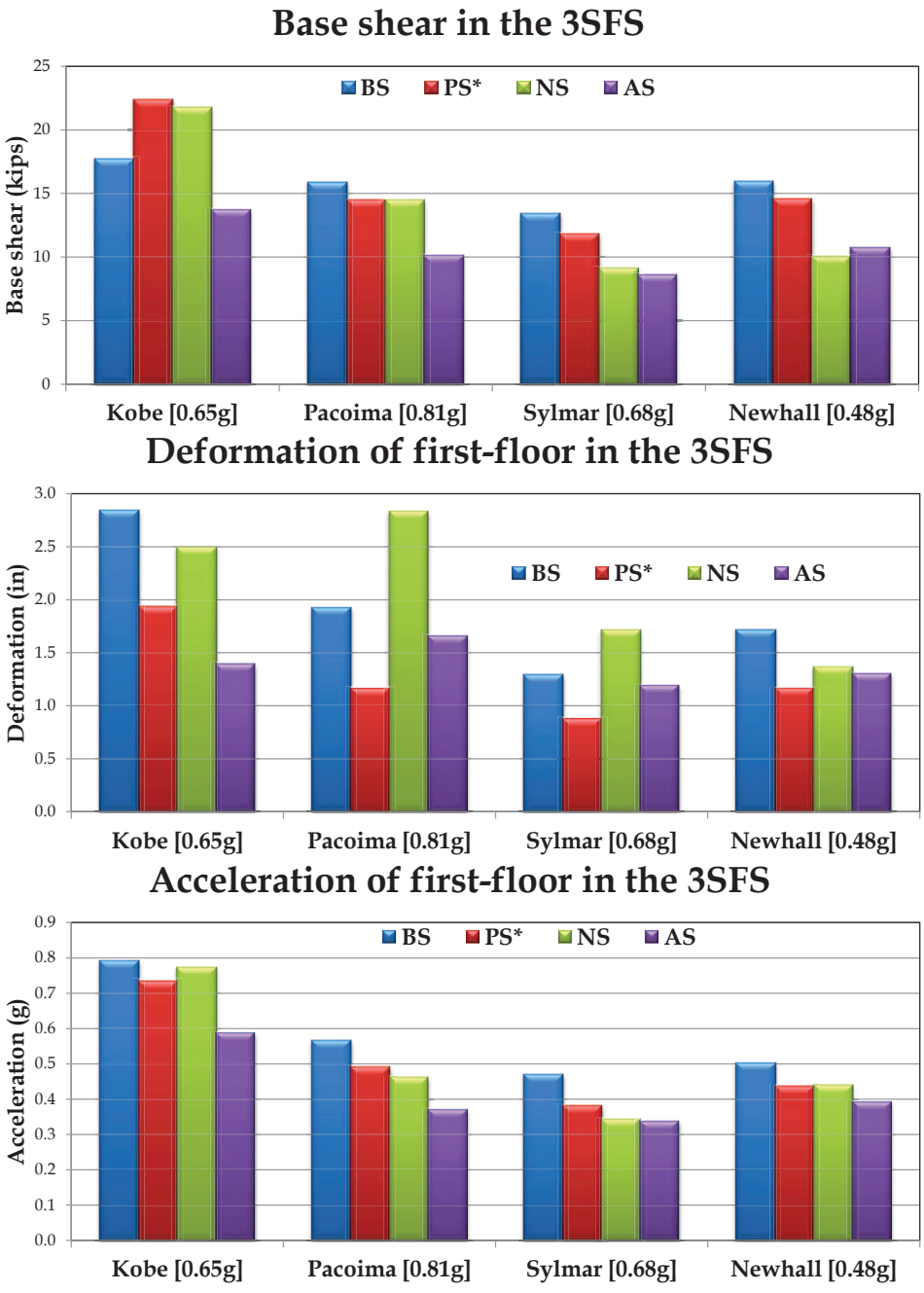

Figure 5.30 : Summary of peak responses in yielding systems

These increased deformations are controlled by adding a viscous damper. Consistent response reductions are observed for a suite of ground motions by the addition of the viscous fluid damper. The observed experimental behavior can be reproduced by the presented analytical models at the component level and also for the structure and device assembly.

It has been shown through numerical studies that the addition of viscous damper will reduce the peak deformation by more than 20% but the structure will experience almost the same acceleration and base shear as the uncontrolled structure. The NSD in conjunction with a viscous damper is capable of simultaneously reducing the base shear, the acceleration and the displacement of the structure.

With the addition of NSD to the bilinear inelastic structure, the base shear and accelerations of the assembly are reduced by more than 30% for ground motions in which there is mild yielding in the primary structure. For more severe ground motions, the deformations of the assembly will be larger than the stiffening point of NSD; resulting in very high assembly stiffness, thereby increase in base shear and accelerations of the assembly. However, the high stiffness of the assembly will prevent the structure from collapsing. In the case where there is heavy yielding in the primary structure, the permanent drift in the assembly is larger than the plastic deformation in the primary structure. The permanent drift in excess of the plastic-deformation in the primary structure can be completely recovered by disengaging the NSD from the primary structure. It has also been demonstrated that the stiffening in NSD will prevent the structure from collapsing. Analogous to the inelastic design, the acceleration and base shear and deformation of the structure and NSD assembly can be reduced by more than 20% for moderate ground motions and the collapse of structure can be prevented for severe ground motions. Additionally, part of the inelastic excursions

incurred after a severe ground motion can be recovered by disconnecting the NSD.

Chapter 6

Apparent-Weakening in MDOF Structures

Experimental studies presented in previous chapter have confirmed that by adding the NSD to a SDOF system, the acceleration and base shear of the structure can be reduced significantly at the expense of increased deformations. The excessive deformations caused due to the reduction in "apparent stiffness" can be contained by adding a passive damper. So far, the focus and the application of NSD has only been on the response reduction of that story in which the NSD is installed. The impact of adding NSDs in one floor and multiple floors is the focus of study in this chapter. Because of the involved dynamics in the case of MDOF structures, the behavior of NSD in multi-story frames is studied in two different sections. First, the experimental results of 3SFS with NSDs in the first floor is studied to analyze the effect of NSDs on upper stories. Later, simulation studies on an inelastic nine-story multistoried shear building to demonstrate the effectiveness of placing NSDs and dampers at multiple locations along the height of the building is demonstrated [162].

The results reported in this chapter have demonstrated that by placing a NSD in a particular story the superstructure above that storey can be isolated from the effects of ground motion. Since the energy from ground motion is transmitted from bottom to top, the NSDs in the bottom floors will undergo large deformations. However, due to the reduction in assembly stiffness with the addition of NSDs, the bottom floors will undergo large deformations. To overcome this, a generalized scheme to incorporate NSDs with different properties is proposed in this study. To highlight the

advantages of using NSDs and dampers in multiple stories, the response is compared with a passively controlled system and the uncontrolled primary structure for six standard ground motions. Large base deformations and permanent drifts which is common in base-isolating the structural systems are overcome by using NSDs in multiple stories, since the isolation is achieved over the height of the building and not confined to the base: referred as distributed isolation. It has been shown through the simulation studies that by placing the NSDs in the lower story's the acceleration of the superstructure and base shear can be reduced significantly without affecting the drifts.

Rest of the chapter is organized as follows: First the shake table results on 3SFS (without braces in the moment frame) with NSDs in the first floor are presented for moderate ground motions in section-6.1 and for severe ground motions in section-6.2. A nine-story 1:3 scale frame used to demonstrate the concept of distributed isolation is presented in section-6.3. Simulation results on the nine-story frame depicting the isolation capabilities of NSD and an optimization scheme to distribute isolation over the height of bottom few floors are presented in section-6.4 for a suite of ground motions.

6.1 Unbraced 3SFS Response to moderate ground motion

The beams in the 3SFS were yielding after the specimen is subjected to severe ground motion and to replace these beams, the whole structure has to be disassembled. Since it involves a great deal of money and time in order to do multiple yielding tests, the experimental tests were only performed on the 3SFS and NSD assembly. As mentioned earlier, to justify the importance of NSD, response of four systems have to be compared. So, the responses of 3SFS and 3SFS with damper have to be

simulated using the analytical models. To ensure the consistency in modeling, first, the analytical models for the components developed in chapter 4 from first-principles and the unknown parameters in the models are obtained by calibrating with the experimental results of 3SFS and NSD assembly. Using the analytical models, the predicted behavior of the assembly is compared and they are in good agreement.

Elevation, actual photograph and the schematic of the 3SFS is shown in Figure 6.1; the elements in the schematic are color coded. In this section, experimental results of two tests (1) 3SFS, NSDs and damper assembly (AS) for Pacoima ground motion with a PGA of 0.62g and (2) 3SFS and NSDs assembly (NS) for Pacoima ground motion with a PGA of 0.78g are presented. Experimental results are compared with the simulation results to demonstrate the accuracy of analytical models used. Also, response of four different systems: (1) 3SFS or the base structure (BS); (2) 3SFS and NSD assembly (NS); (3) 3SFS, NSD and damper assembly (AS); (4) 3SFS and damper (PS) are generated using the analytical models and compared to highlight the advantages of apparent-weakening in multi-story building.

First, the impact of NSD in 3SFS for moderate ground motions is analyzed. Force-deformation (F-D) plots of all the three floors comparing the experimental and simulations results for Pacoima ground motion [PGA=0.62g] are separately shown in Figure 6.2. The force-deformation behavior of all the components (3SFS, NSD-East, NSD-West and damper) in the first floor is shown in Figure 6.3. From Figure 6.2(a), the overall behavior in the experiments and simulations of first-floor is similar but the maximum deformation in the experiments is 0.23 *in.* more than the simulations. This is due to the variable friction loop observed in the components, shown in Figure 6.3(b,c). The F-D behavior of 3SFS measured using load-cells, shown in Figure 6.3(a) has confirmed that the structure remains elastic. The F-D behavior of the

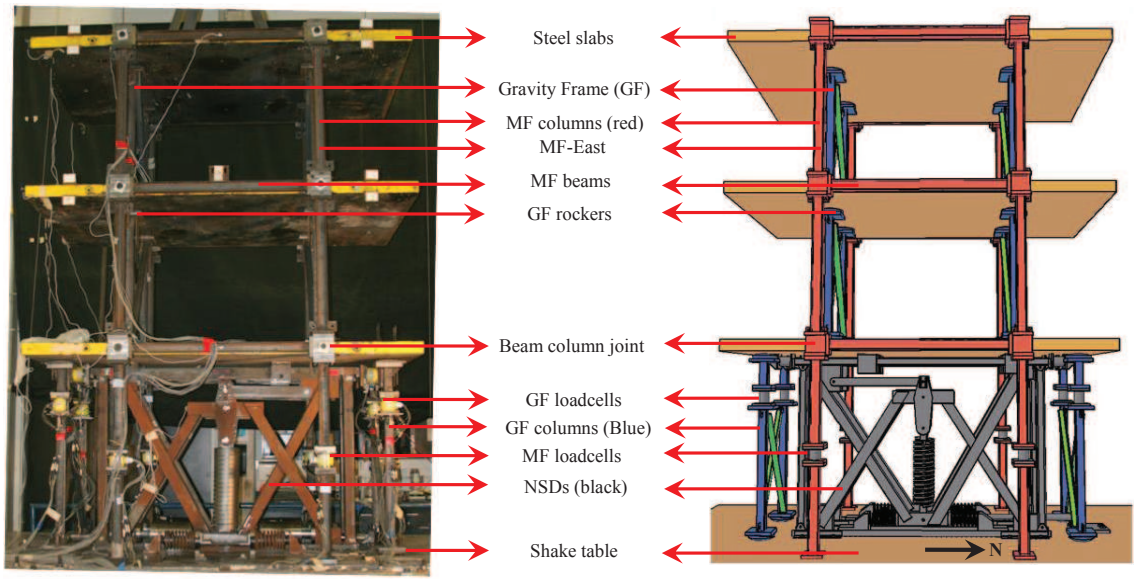

Figure 6.1 : Schematic diagram and picture of unbraced 3SFS

damper measured using the uni-axial load cell is also in close agreement with the predicted behavior. As mentioned previously, the F-D behavior of the second and third floors, shown in Figure 6.2(b,c), is very noisy because the force in these storys is calculated using the accelerations of the steel slabs, however the average slope of the experimental results is closely matching with the simulation results. Figure 6.2,6.3 confirm that the analytical models used for the components can be used to capture the experimentally observed behavior of the assembly reasonably well.

The time-history response of first floor deformation, acceleration and base shear are compared in Figure 6.4. The F-D behavior of assembly and components in AS are shown separately for simulations and experiments in Figure 6.5. The comparisons of the results from shake-table tests and predicted results from the analytical models are in very good agreement.

Using the ground acceleration and the shake-table rocking data measured during

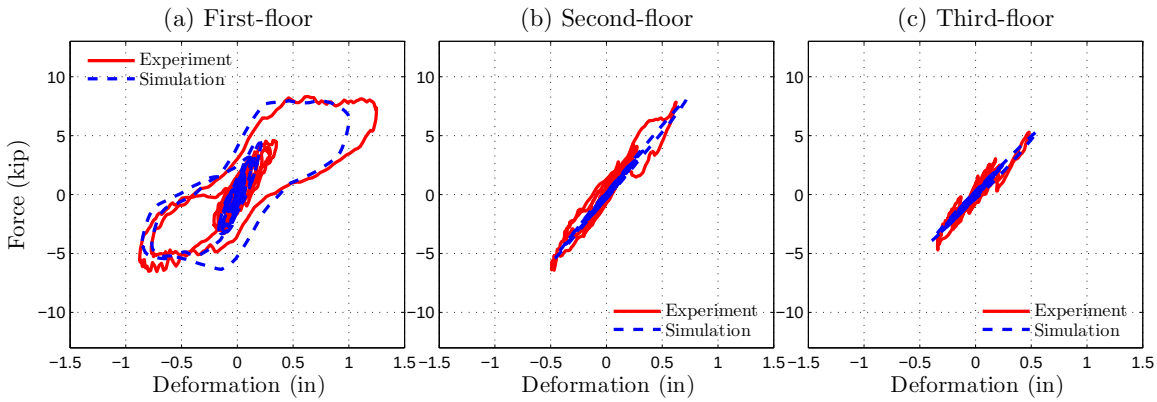

Figure 6.2 : F-D behavior of individual floor in AS for Pacoima ground motion (PGA=0.62g)

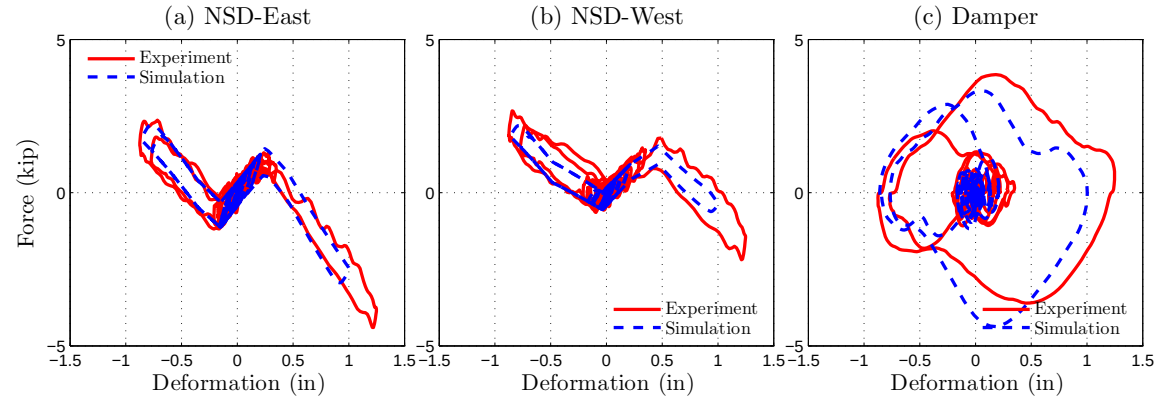

Figure 6.3 : F-D behavior of NSD-East, NSD-West and damper in AS for Pacoima ground motion (PGA=0.62g)

the shake-table test, the behavior of BS, PS and NS is predicted and the F-D behavior of all the four systems is shown in Figure 6.6. F-D behavior of the first-floor in all the four systems are compared in Figure 6.7. First floor displacement, acceleration and base shear of all the four systems is compared in Figure 6.8. The superscript-"*" in Figure 6.6-6.9 indicates that the results are obtained using the simulations. Figure 6.6 shows that the first and second floors of BS will yield for the Pacoima

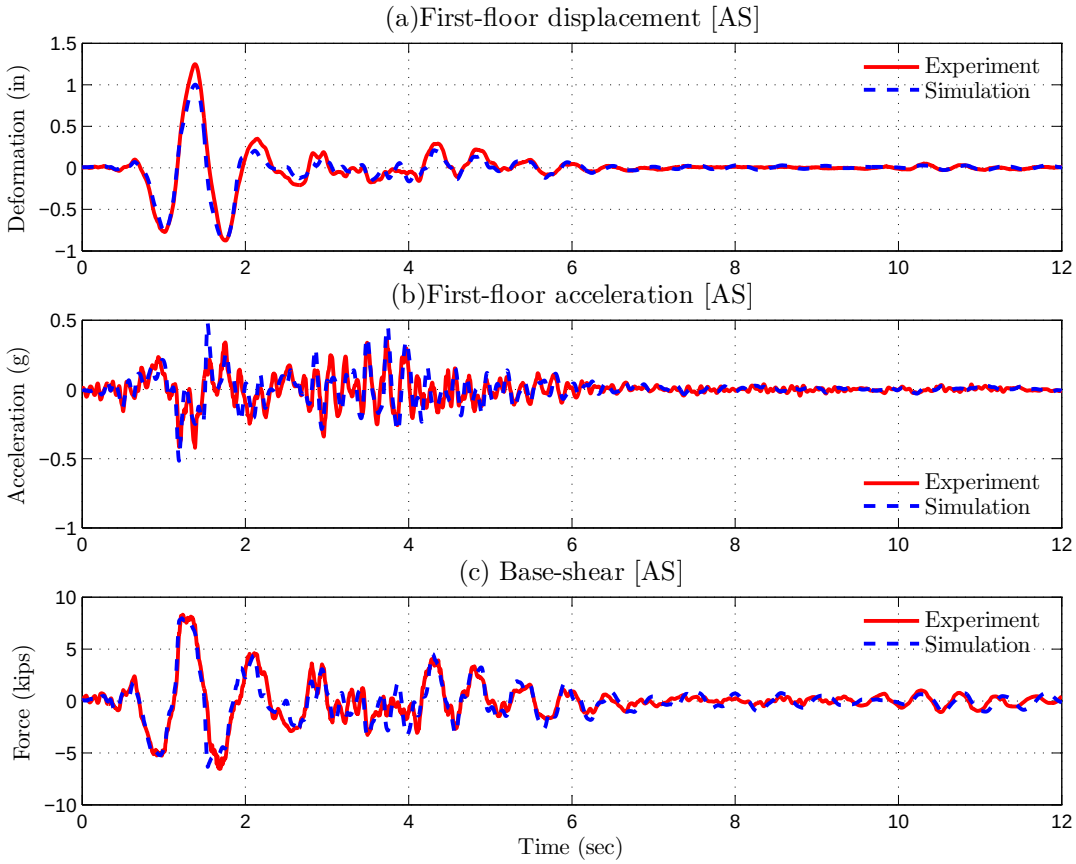

Figure 6.4 : First floor response and base shear of AS (Pacoima GM; PGA=0.62g)

ground motion at a PGA of 0.62g. By adding damper to the base structure (PS), the input energy transferred to the second and third floors is reduced but the base shear experience by the first floor is same as in the BS, shown in Figure 6.6,6.7. If NSDs are connected in the first-floor instead of damper, shown as NS in Figure 6.6, the response of second and third floors and the base shear is reduced more than the BS and PS cases. However, the reduction in base-shear occurs at the expense of excessive displacement (50% more deformation in the first story compared to BS) due to the reduction in stiffness with the addition of NSD. By adding NSDs along with the damper, the inter-story response of the all the three floors are significantly

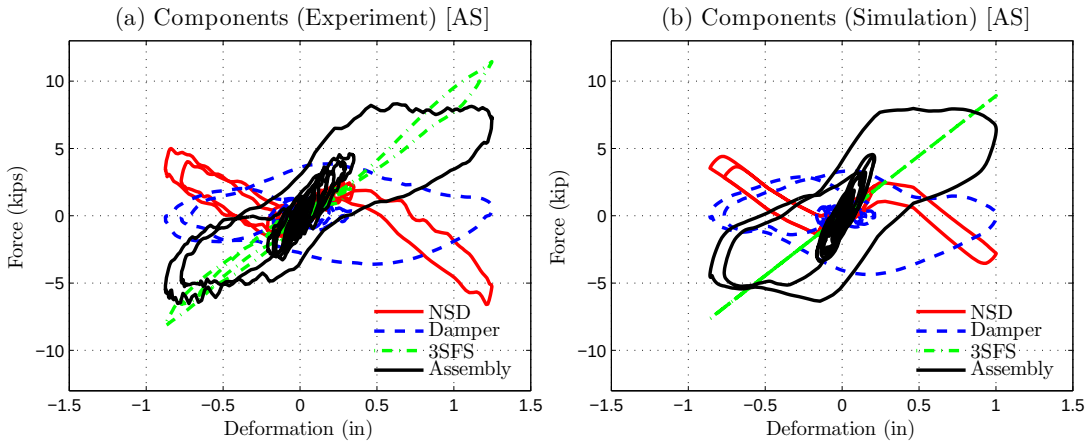

Figure 6.5 : Comparison of F-D behavior of AS with components (Pacoima GM, PHA=0.62g)

reduced compared to BS, PS and NS, as shown in Figure 6.6,6.7,6.8.

The profile of maximum inter-story deformation, maximum floor displacement with respect to the shake-table and the maximum floor acceleration of all the three floors are shown in Figure 6.9. The inter-story deformation of the NS and AS is significantly reduced with the addition of NSDs in the second and third floor, shown in Figure 6.9(a). The relative deformation and acceleration of the first floor has increased with the addition of NSDs but the displacement and acceleration has increased marginally over the other two storys. As a result, the roof acceleration of AS is 30% less than BS, and the acceleration of NS is 15% smaller than the BS, shown in Figure 6.9(c). The roof displacement of AS is 30% less than the BS and 10% less than the NS. Although the inter-story drift in the first story of NS is 40% more than the other three systems, the roof deformation of NS is 15% less than the BS. Next, the behavior of NS and AS is analyzed for more sever ground motion [Pacoima ground motion with PGA of 0.78g].

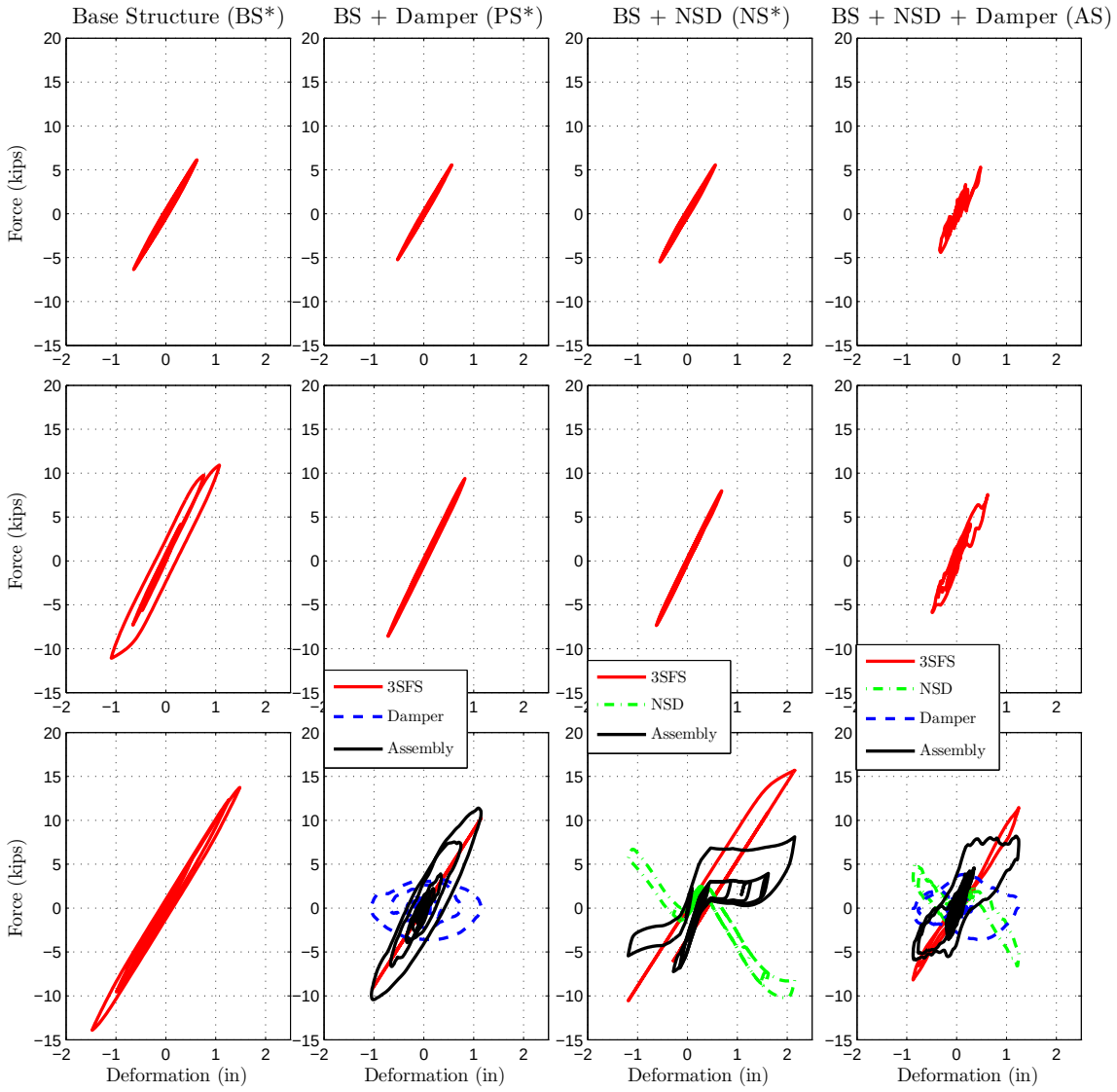

Figure 6.6 : F-D behavior of all the floors in AS, BS, PS and AS with components (Pacoima; PGA=0.62g)

6.2 Unbraced 3SFS Response to severe ground motion

Shake-table test is performed on the 3SFS and NSDs assembly (NS) and the observed response of NS and components is compared with simulation results in Figure 6.10-

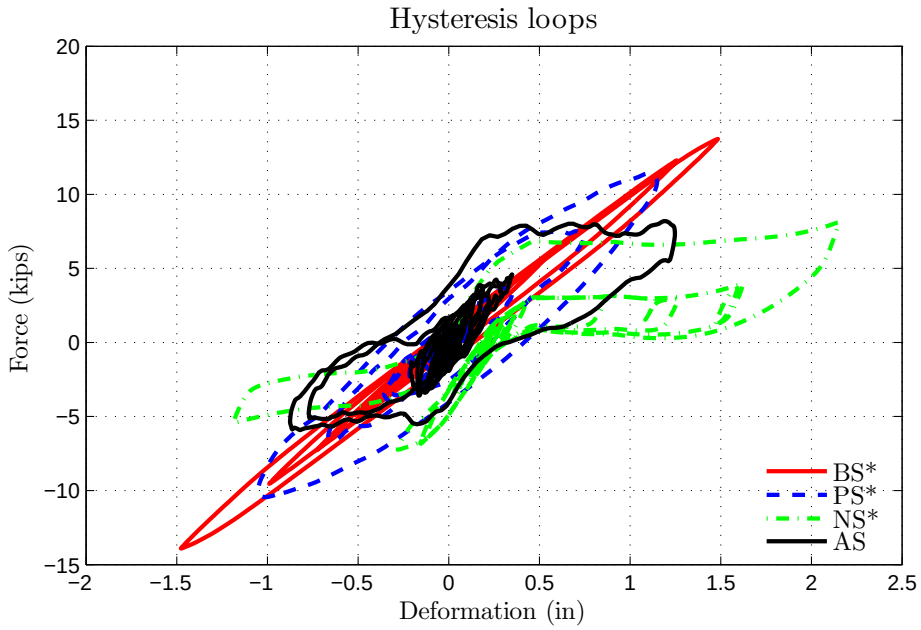

Figure 6.7 : Comparison of F-D behavior of all the systems in first-floor (Pacoima; PGA=0.62g)

6.13. Force-deformation (F-D) plots of all the three floors comparing the experimental and simulations results are separately shown in Figure 6.10. The force-deformation behavior of all the components (NSD-East and NSD-West) in the first floor is shown in Figure 6.11. Similar to the results in Figure 6.2, the overall behavior in the experiments and simulations of first-floor, shown in Figure 6.10, is very similar. The first floor deformation, acceleration and base shear is shown in Figure 6.12. The F-D behavior of assembly and components in NS are shown separately for simulations and experiments in Figure 6.13.

The first-floor has deformed in the negative direction first with mild yielding and then it yielded in the positive direction (plastic deformation of more than 1 *in.*) as shown in Figure 6.13. Due to the permanent drift in the first-floor, there is slight rigid body rotation in the second and third floor, as a result, the F-D plots appear

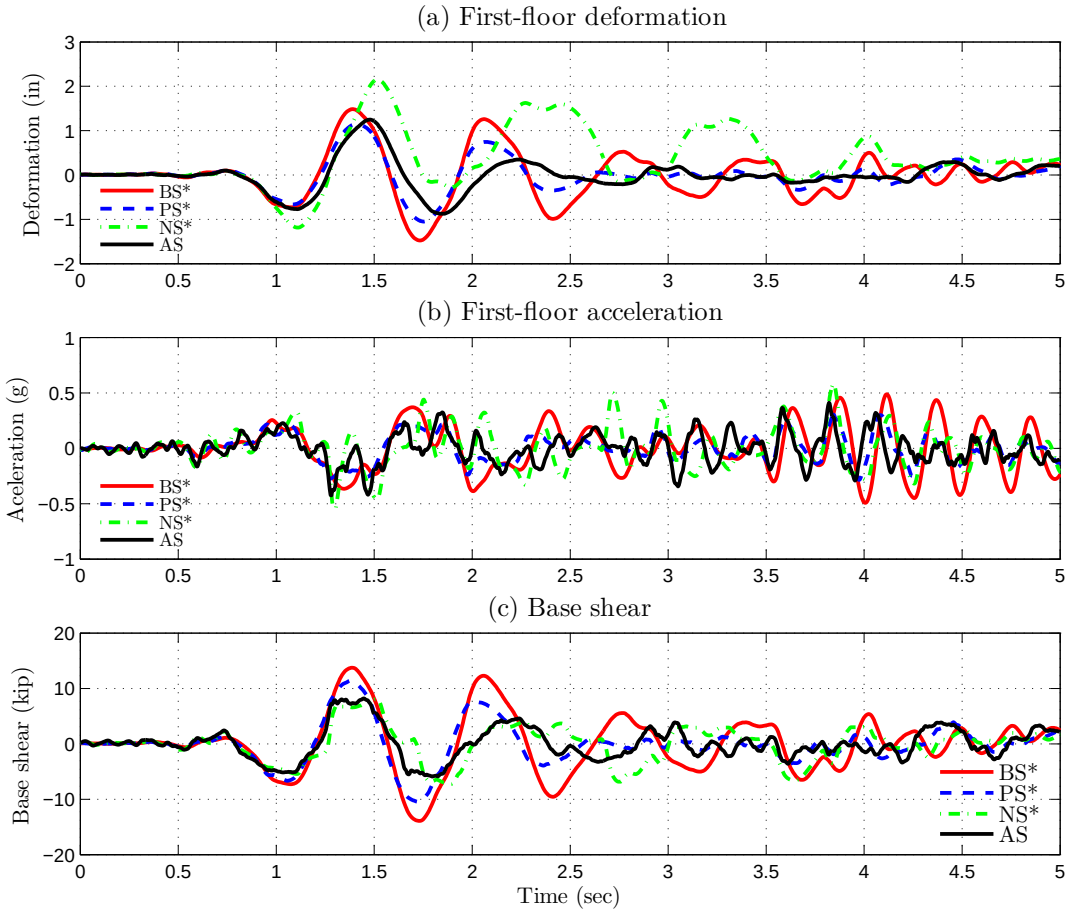

Figure 6.8 : Comparison of the time-history of first floor response in all systems (Pacoima; PGA=0.62g)

to have a permanent drift of 0.23 in. as shown in Figure 6.10(b,c). The measured and simulated F-D behavior of NSD-east and NSD-west are shown in 6.11 and it is clear from these plots that the NSDs enter the stiffening region. The stiffness of the assembly in the first floor reduces from 0.35 *in.* till 2 *in.* and beyond 2 *in.* it increases again. Overall, from Figure 6.10-6.13, the analytical models used were able to capture the observed experimental behavior reasonably well even when the primary structure has yielded significantly.

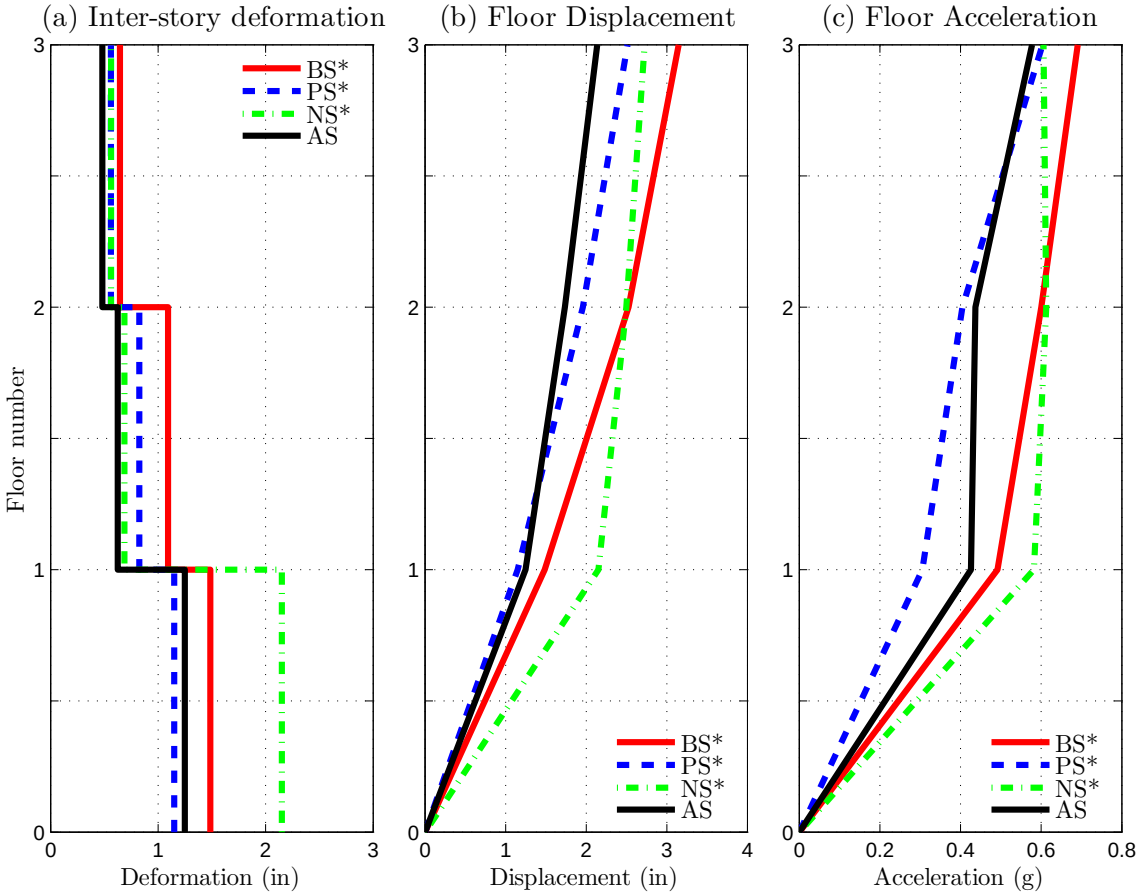

Figure 6.9 : Comparison of response profile of all the systems in unbraced 3SFS (Pacoima; PGA=0.62g)

Using the ground acceleration and the shake-table rocking data measured during the shake-table test, the behavior of BS, PS and AS is predicted and the F-D behavior of all the four systems is shown separately in Figure 6.14. First-floor F-D behavior of all the four systems is compared in Figure 6.15, first floor displacement, acceleration and base shear is compared in Figure 6.16. Time-history trace of the roof displacement and acceleration of all the four systems is compared in Figure 6.17.

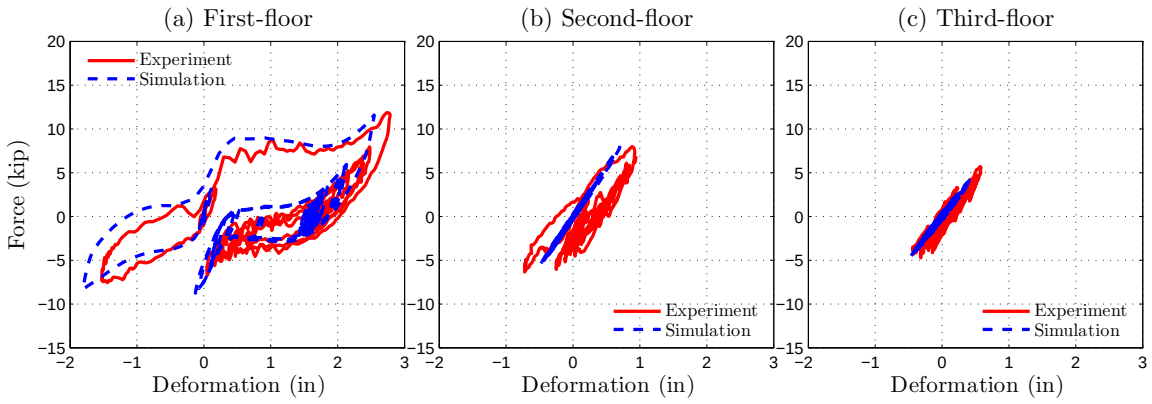

Figure 6.10 : F-D behavior of individual floor in NS for Pacoima ground motion (PGA=0.78g)

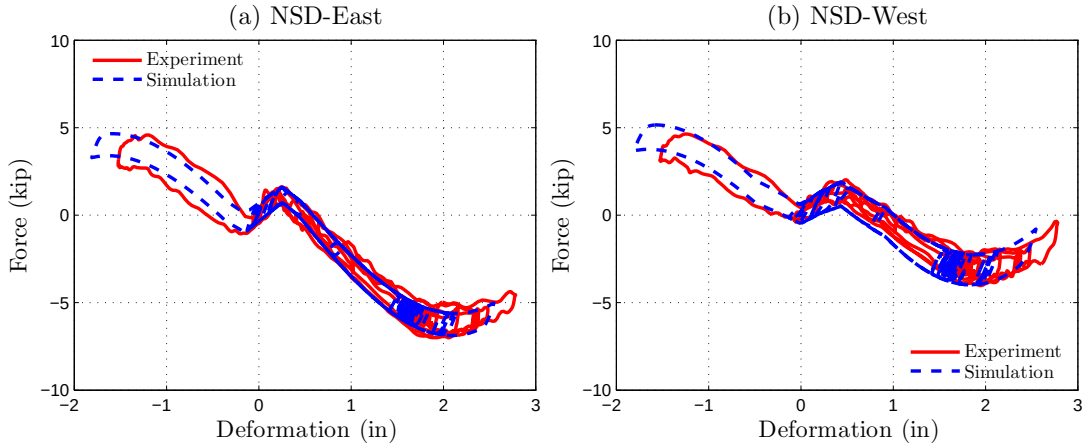

Figure 6.11 : F-D behavior of NSD-East and NSD-West in NS for Pacoima ground motion (PGA=0.78g)

Figure 6.14 shows that the first and second floors of BS will yield for the Pacoima ground motion at a PGA of 0.78g. With the addition of damper to the base structure (PS), the deformation in the first floor is reduced but the input energy transferred to the second and third floors is not reduced as a result the second floor has yielded, shown in Figure 6.14. Also, the base shear in PS is same as BS, shown in Figure

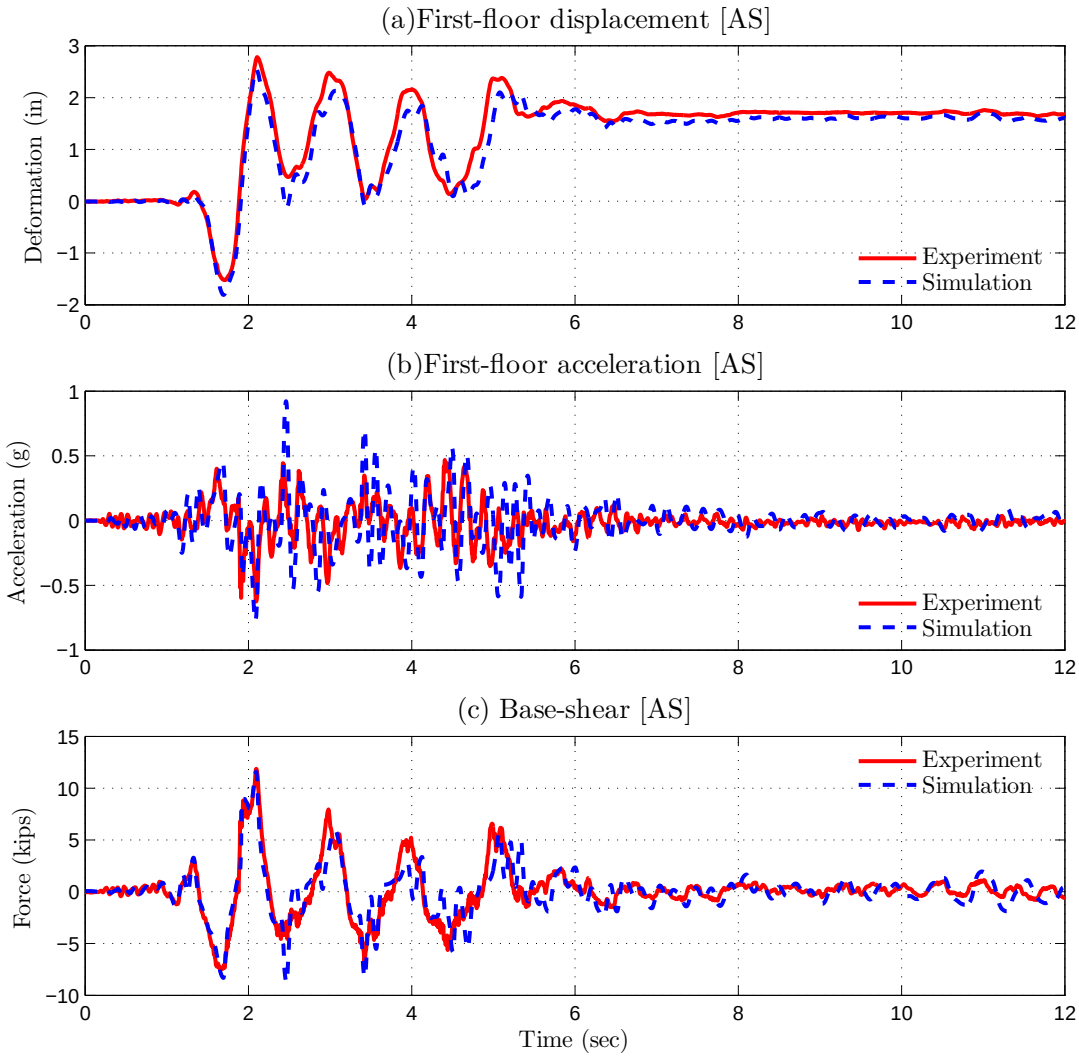

Figure 6.12 : First floor response and base shear of NS (Pacoima GM; PGA=0.78g)

6.16. If NSDs are connected in the first-floor instead of damper, shown as NS in Figure 6.14, the response of second and third floors and the base shear is reduced more than the BS and PS cases and they remain elastic. The base shear of NS is reduced by more than 20% compared to BS and PS, shown in Figure 6.16. However, the reduction in base-shear occurs at the expense of large first-floor deformation (20%

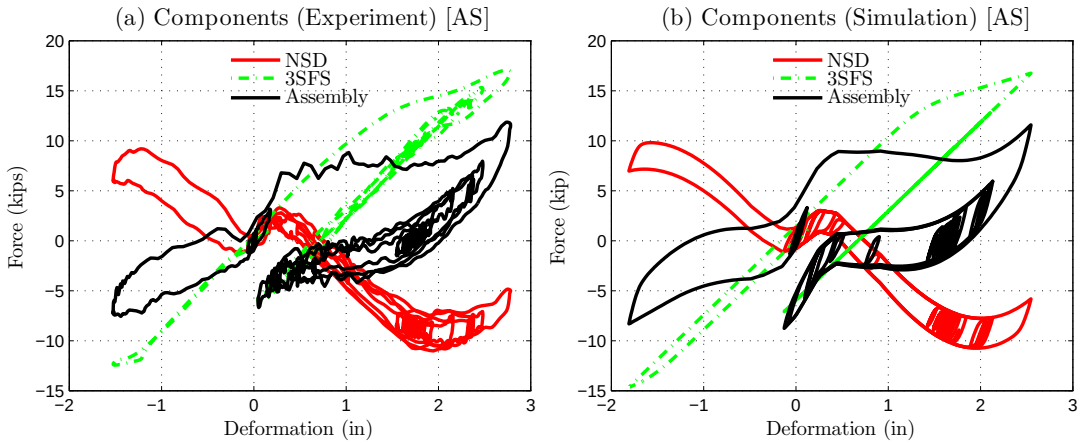

Figure 6.13 : Comparison of F-D behavior of NS with components (Pacoima GM, PHA=0.78g)

more deformation in the first story compared to BS) due to the reduction in stiffness with the addition of NSD, shown in Figure 6.15. By adding NSDs along with the damper, the inter-story response of the all the three floors are significantly reduced compared to BS, PS and NS, as shown in Figure 6.14 and Figure 6.17.

The profile of maximum inter-story deformation, maximum floor displacement with respect to the shake-table and the maximum floor acceleration of all the three floors are shown in Figure 6.18 for Pacoima ground motion with PGA of 0.78g. The inter-story deformation of the NS and AS in the second and third floor is 30% less than the BS and PS due to the addition of NSDs, shown in Figure 6.18(a). The relative deformation and acceleration of the first floor has increased with the addition of just the NSDs, shown as NS in Figure 6.18(b,c), but the displacement and acceleration of the other two floors has not increased because the NSDs will prevent the transfer of input energy to the higher floors. As a result, the roof acceleration of NS is 20% less than BS and PS. By adding viscous damper along with the NSDs, all the responses i.e.,

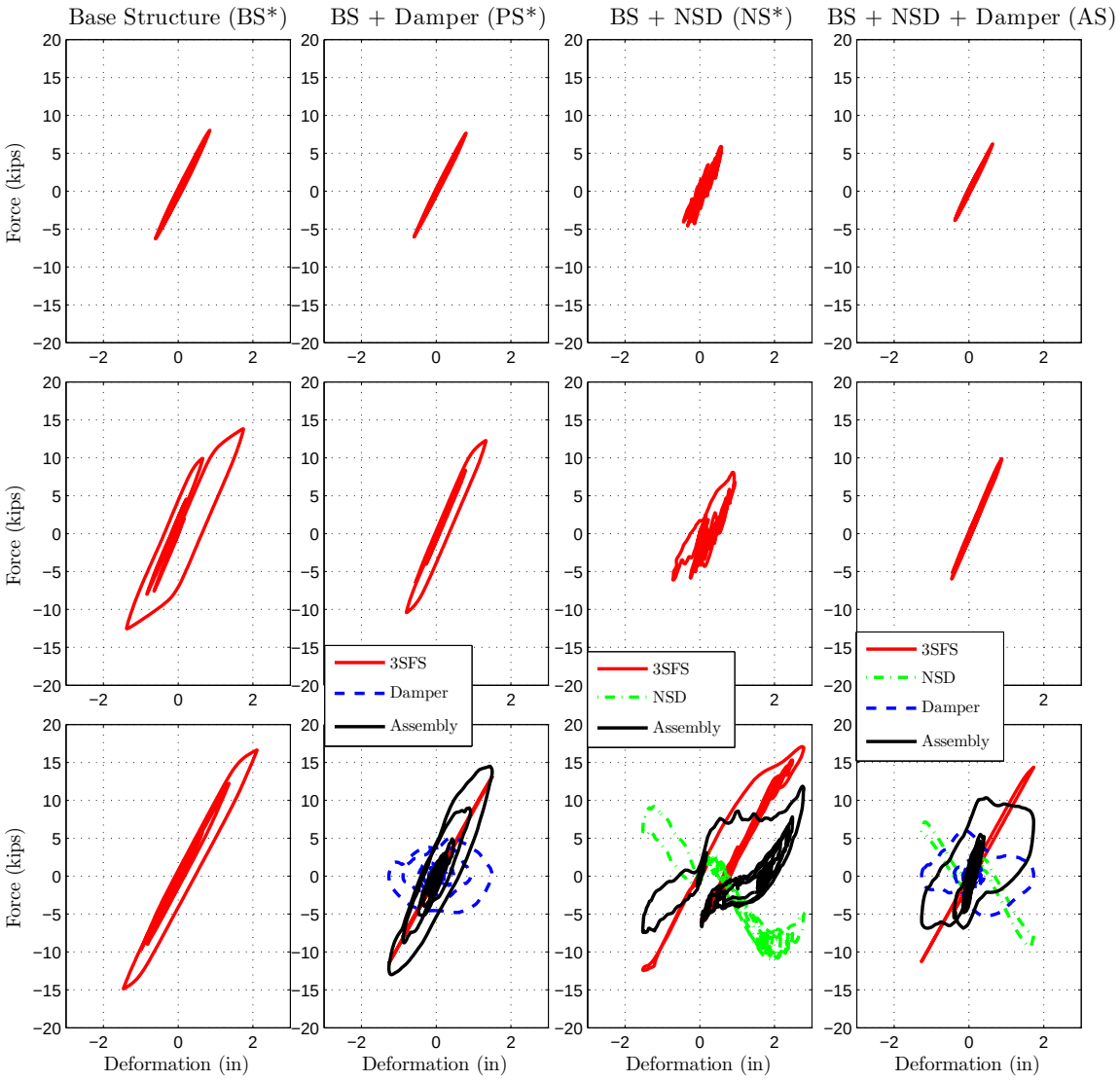

Figure 6.14 : F-D behavior of all the floors in AS, BS, PS and AS with components (Pacoima; PGA=0.78g)

the deformation in the first-floor, base shear, roof displacement and roof acceleration will be reduced compared to the other three systems, shown in Figure 6.18(a,b,c). Essentially, in the case of NS and AS, the NSDs are preventing the transmission of the input energy from the shake-table motion to the second and third floors by

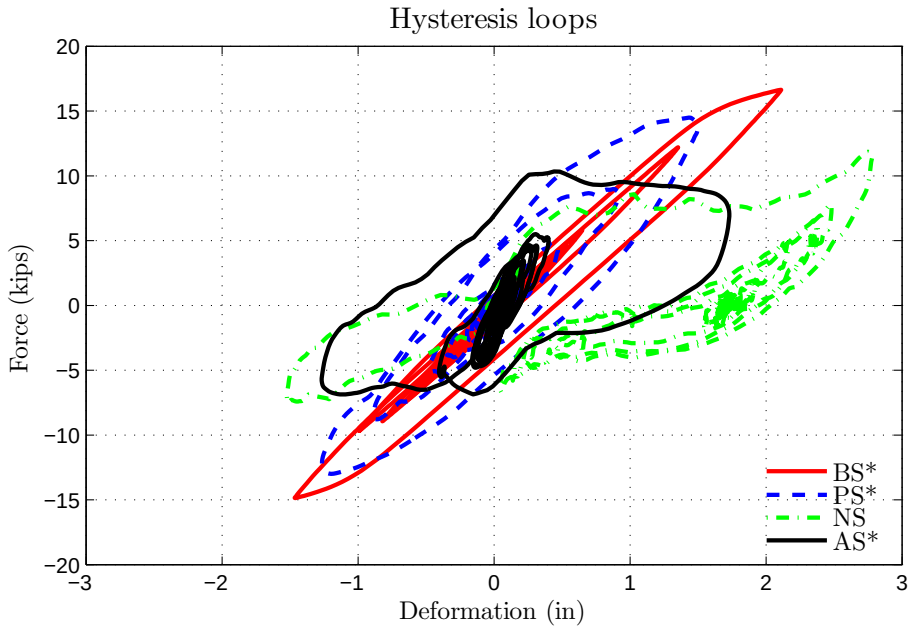

Figure 6.15 : Comparison of F-D behavior of all the systems in first-floor (Pacoima; PGA=0.78g)

absorbing all the energy and viscous damper is dissipating the absorbed energy. The viscous damper in the AS will also prevent the excessive deformation caused due to the reduction in stiffness. The peak response characteristics of all the four systems are summarized in Table 6.1 and also shown as bar-graphs in Figure 6.19 for three ground motions. The results are summarized below:

1. Addition of NSD in the first-floor will prevent the transfer of input energy from the ground motion to the second and third floors. Consequently, the inter-story deformation of the higher floors is significantly reduced, shown in Figure 6.19.

2. Addition of damper can control the deformations at the installation level, but the structure experiences same level of base-shear and the second and third floors will undergo the same level of inter-story deformations similar to the

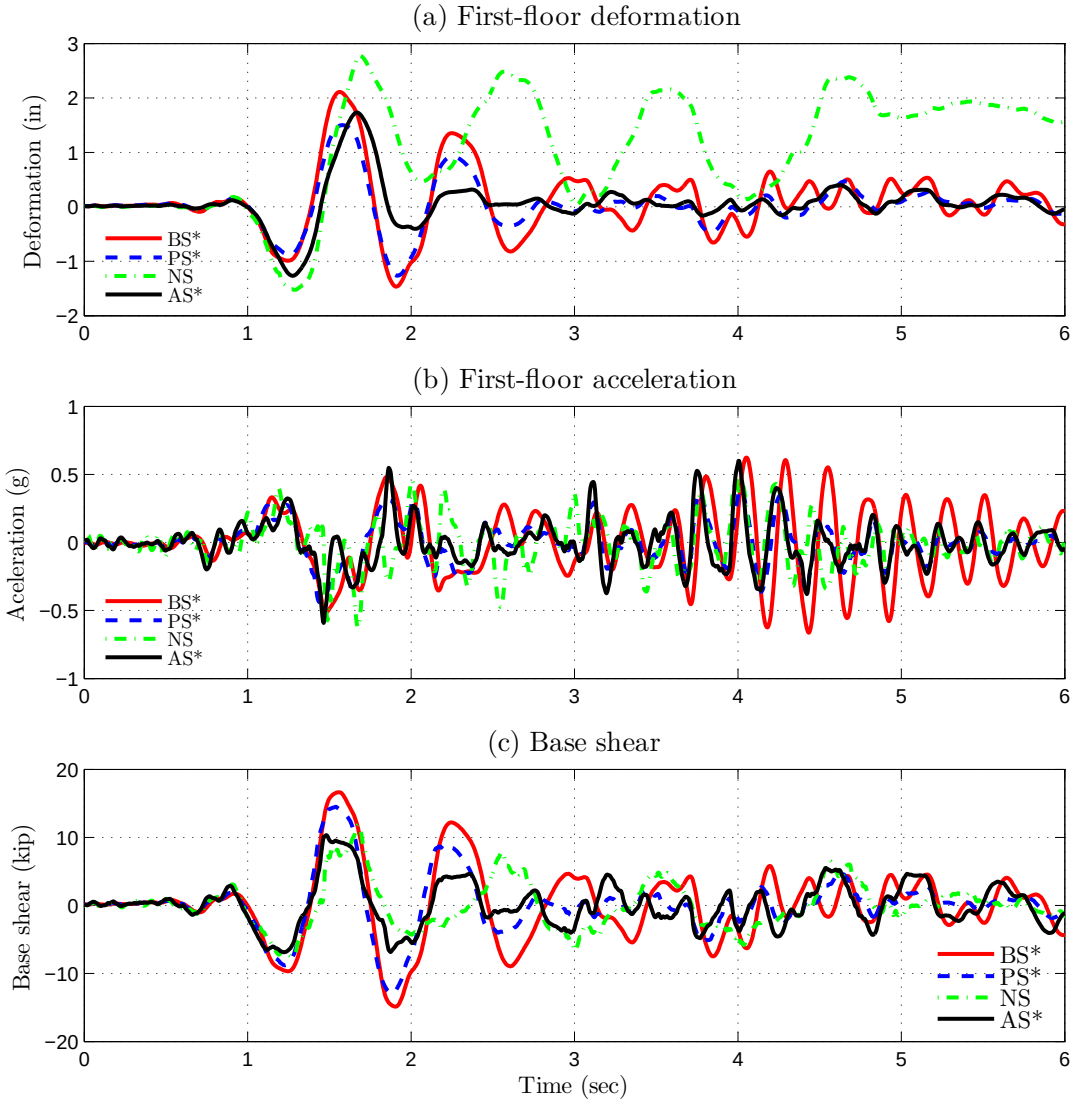

Figure 6.16 : Comparison of the time-history of first floor response in all systems (Pacoima; PGA=0.78g)

uncontrolled structure.

3. By incorporating NSDs and damper together in the structure, all the response characteristics can be consistently reduced.

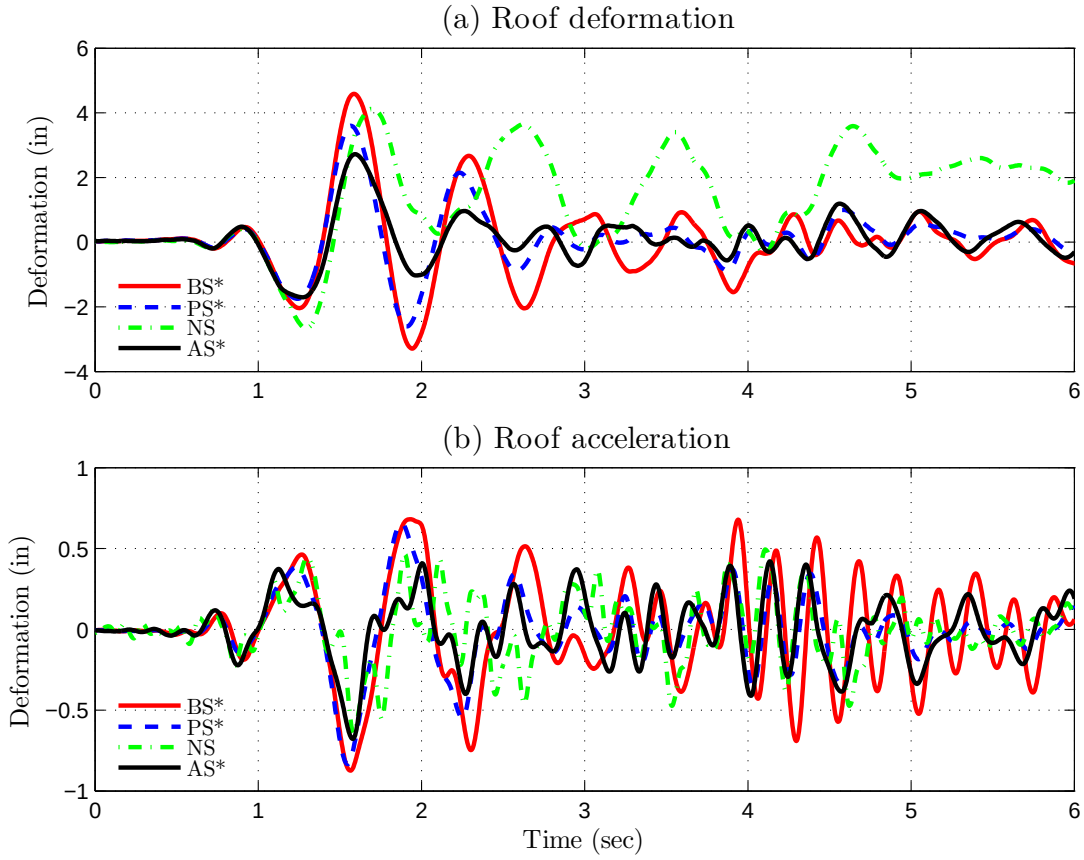

Figure 6.17 : F-D behavior of all the systems and components shown separately (Pacoima; PGA=0.78g)

6.3 Analytical modeling of nine-story frame

The advantages of installing NSDs and supplemental dampers in multiple stories is demonstrated through simulation studies on a nine-story, one-bay shear building [163]. The story stiffness is assumed to be bilinear inelastic, inherent viscous damping of 1% is assumed for each story. Damping coefficient is calculated using the elastic stiffness of the structure, and maintained constant throughout the inelastic regime. Three dimensional drawing of the shear building with the NSDs installed in the walls at each story level is shown in Figure 6.20(left). Schematic diagram showing the

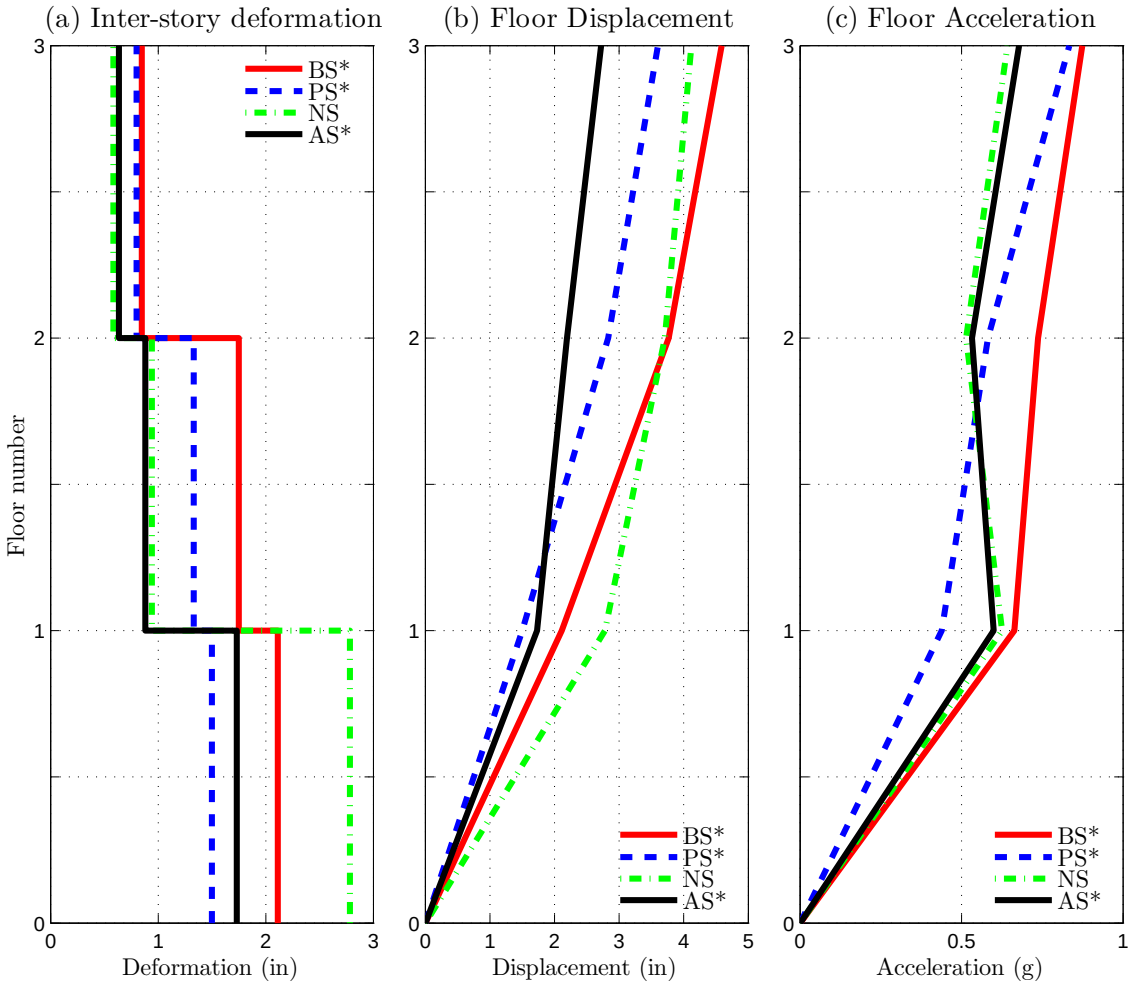

Figure 6.18 : Comparison of response profile of all the systems in unbraced 3SFS (Pacoima; PGA=0.78g)

equivalent components in each story, i.e. bilinear inelastic columns, supplemental passive damper and NSD is shown in Figure 6.20(Right). When connected, the NSDs will only transmit lateral forces and the device is self-contained in the vertical

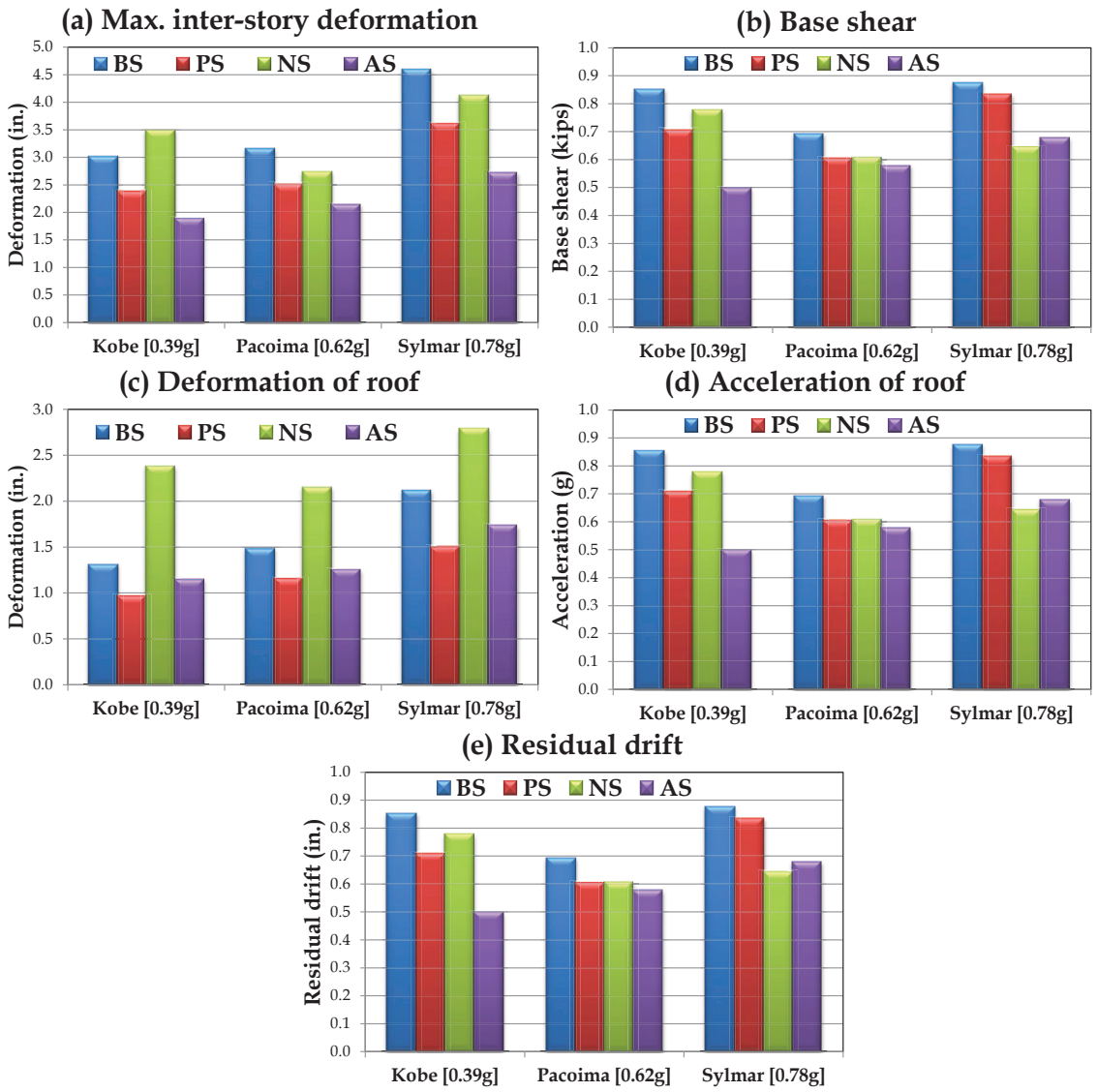

Figure 6.19 : Bar graphs summarizing the shake-table results of unbraced 3SFS

direction. The governing equation for the i^{th} floor is given by:

$$m_i\ddot{u}_i + F_{si}\left(u_{di}\right) + F_{NSDi}\left(u_{di}\right) + c_i\left(\dot{u}_{di}\right) - F_{si+1}\left(u_{di+1}\right) - F_{NSDi}\left(u_{di+1}\right) - c_{i+1}\left(\dot{u}_{di+1}\right) = 0 \tag{6.1}$$

Table 6.1 : Summary of the peak responses from the shake table tests [Elastic-tests]

Sl. no.	Ground motion	System	Cmd. PGA (g)	First-floor response		Base shear (kip)	
				Deform. (in)	Accel. (g)		
1	Kobe (Elastic) PGA:0.39g	BS*	1.31	3.00	0.85	0.68	12.60
2		PS*	0.96(27%)	2.38(21%)	0.71(17%)	0.25	9.73(23%)
3		NS*	2.38(-81%)	3.48(-16%)	0.78(9%)	0.55	14.3(-14%)
4		AS	1.15(12%)	1.88(37%)	0.50(42%)	0.18	7.61(40%)
5	Pacoima (Elastic) PGA:0.62g	BS*	1.49	3.15	0.69	0.34	13.91
6		PS*	1.15(23%)	2.51(20%)	0.60(13%)	0.14	11.40(18%)
7		NS*	2.15(-45%)	2.73(13%)	0.61(12%)	0.31	8.12(42%)
8		AS	1.25(16%)	2.14(32%)	0.58(16%)	0.12	8.20(41%)
9	Pacoima (Yielding) PGA:0.78g	BS*	2.11	4.59	0.87	0.47	16.63
10		PS*	1.50(29%)	3.60(22%)	0.83(5%)	0.23	14.49(13%)
11		NS	2.78(-32%)	4.12(10%)	0.64(26%)	0.60	11.86(29%)
12		AS*	1.73(18%)	2.72(41%)	0.68(22%)	0.07	10.34(38%)

where, subscripts *i, i+1, i-1* stands for the story number. m_i is the mass of i^{th} floor. $u_{ri} = u_i - u_{i-1}$, is the inter-story deformation of the i^{th} floor. u_i, $\dot{u}_i$ and $\ddot{u}_i$ are the displacement, velocity and acceleration of the i^{th} floor, respectively. F_{si} is the force exerted by the bilinear inelastic columns in the i^{th} floor and it is calculated using Sivaselvan-Reinhorn (SR) model [152]. The inelastic column force is given by

$$F_{si}\left(u_{di}\right) = \alpha_{si} K_{si} u_{di} + \left(1 - \alpha_{si}\right) K_{si} u_{syi} z_{si} \tag{6.2}$$

$$\left(\frac{dz_{si}}{du_{di}}\right) = \frac{1}{u_{syi}}\left(1 - |z_{si}|^{\eta_{si}}\left(\gamma_{si}\mathrm{sgn}\left(z_{si} \times du_{di}\right) + \beta_{si}\right)\right) \tag{6.3}$$

K_{si} is the initial elastic stiffness of the floor, α_{si} is the post-yielding stiffness ratio, u_{syi} is the yield displacement. The parameters η_{si}, γ_{si}, and β_{si} are the constants in Sivaselvan-Reinhorn model for i^{th} story. The tangential stiffness of the hysteretic part

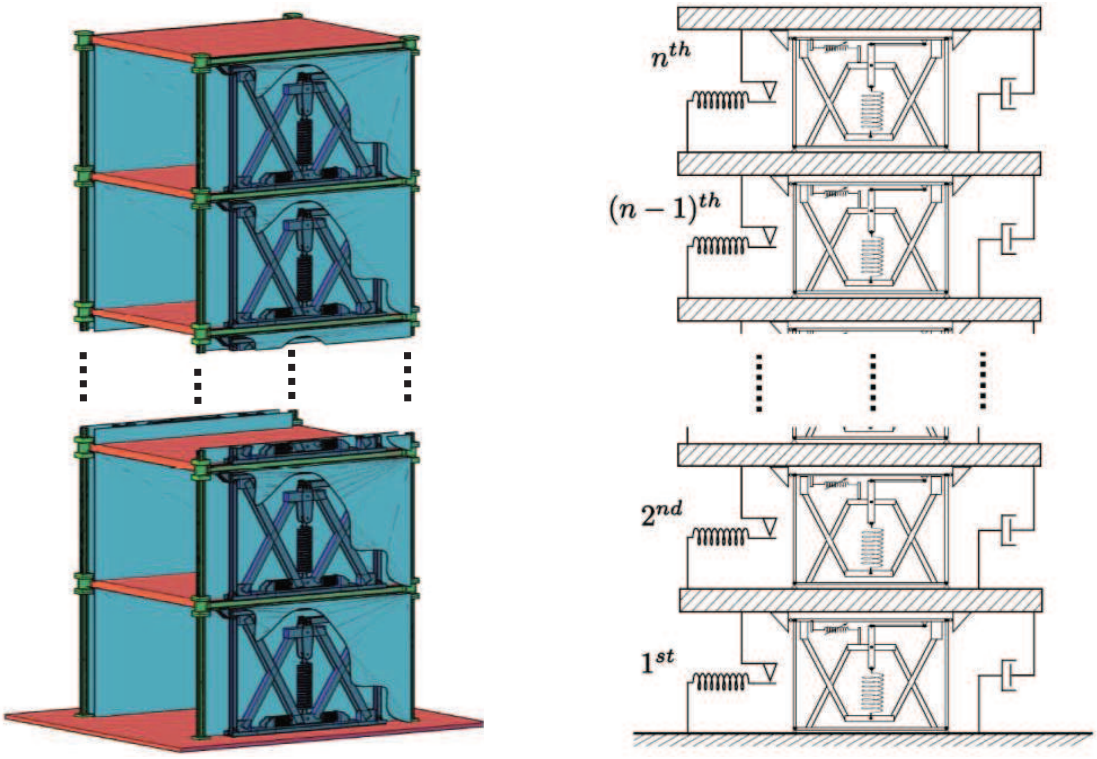

Figure 6.20 : Schematic diagram of multi-story building with NSDs in every floor

is proportional to dz_{si}/du_{di}. The tangent stiffness of the system, K_{tsi}, can be then be represented by Eq. 6.4, which shows low stiffness after yielding ($z \longrightarrow 1$):

$$K_{tsi} = K_{si}\left(\alpha_{si} + (1-\alpha_{si})\left(1 - |z_{si}|^{\eta_{si}}\left(\gamma_{si}\mathrm{sgn}\left(z_{si} \times du_{di}\right) + \beta_{si}\right)\right)\right) \tag{6.4}$$

Mass, elastic-stiffness, yield displacement, damping values and the values of the SR model in the individual floor are obtained from the 3SFS presented in 4. The damping term consists of two components as shown in Eq. 6.5

$$F_{Di} = c_i\left(\dot{u}_i - \dot{u}_{i+1}\right) = 2\left(\xi_i + \xi_{sdi}\right)\sqrt{K_{si}m_i}\left(\dot{u}_i - \dot{u}_{i+1}\right) \tag{6.5}$$

ξ_i is the inherent damping ratio of the i^{th} floor and ξ_{sdi} is the damping ratio of the supplemental damper added along with the NSD. In this study ξ_i =1% is used based on the experimental observations and ξ_{sdi}=20% (initial) is adopted based on the results presented in chapter 2. The force exerted by the NSD, F_{NSDi} is given in Eq. 6.6 (also presented in Eq. 3.10).

$$F_{NSDi} = -\left(\frac{P_{in} + K_s l_p}{l_s} - K_s\right)\left(\frac{l_1}{l_2}\right)\left(2 + \frac{l_2}{l_1} + \frac{l_p + l_1}{\sqrt{l_2^2 - u_{di}^2}}\right) u + K_g\left(u_{di}\right) u_{di} \quad (6.6)$$

The values of the parameters used for the simulations study are: P_{in}=8 *kips*; K_s=1.6 *kip/in*; l_p=30 *in*; l_1=10 *in*; l_2=5 *in* and K_g has bilinear elastic behavior with initial stiffness of 5.9 *kip/in* and the stiffness becomes 0.15 *kip/in* for deformations larger than 0.3 *in*. K_g represents the behavior of gap-spring assembly; a two spring assembly connected in series to achieve zero stiffness in NSD for $|u| < u'_y$.

The height of each floor is 60 *in*. and the weight of each floor is 8.9 *kips*. The first three natural time-periods of the structure are 1.75 *sec*, 0.59 *sec* and 0.36 *sec*. Two NSDs are incorporated in each floor. Force deformation behavior the bilinear inelastic system (calculated using Eq. 6.2), supplemental viscous damper (calculated using Eq. 6.5), the NSD force (calculated using Eq. 6.6) and the assembly is shown in Figure 6.21. All the simulation results on nine-story frame are normalized and represented in dimensionless terms: force terms are normalized with respect to the yield force of the columns, F_y, floor displacement and inter-story deformations are normalized with respect to the yield displacement, u_y, of the columns.

The governing equation for the entire structure subjected to a ground motion with

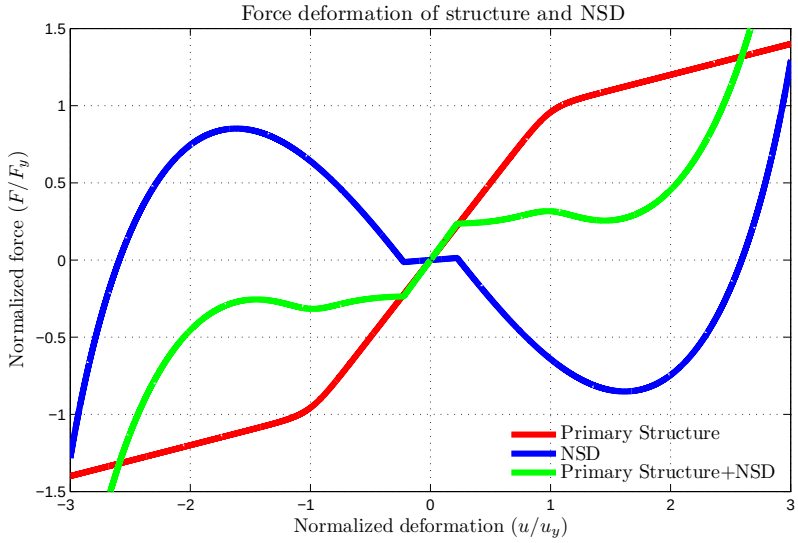

Figure 6.21 : Schematic F-D plots depicting the strength reduction factor

acceleration $\ddot{u}_g(t)$ is given by

$$\mathbf{M}\ddot{\mathbf{u}}_\mathbf{r}(t) + \mathbf{C}\dot{\mathbf{u}}_\mathbf{r}(t) + \mathbf{F_s}\left(\mathbf{u_r}\right) + \mathbf{F_{NSD}}\left(\mathbf{u_r}\right) = -\mathbf{M}\mathbf{I}\ddot{u}_g(t) \tag{6.7}$$

where, $\mathbf{M}$ and $\mathbf{C}$ are the mass and damping matrices of the structure. $\mathbf{u_r}(t)$, $\dot{\mathbf{u}}_\mathbf{r}(t)$ and $\ddot{\mathbf{u}}_\mathbf{r}(t)$ are the displacement, velocity and acceleration vectors containing the floor response at each story with respect to the ground. $\mathbf{F_s}$ and $\mathbf{F_{NSD}}$ are the force vectors consisting of the nonlinear forces exerted on each mass due to the nonlinear stiffness of the structure and the NSD, respectively. $\mathbf{I}$ is the influence coefficient vector for ground acceleration. Two other force terms will be used in the simulation studies presented in the next section; F_i refers to assembly shear-force in the i^{th} story and F_b refers to the base shear (foundation force) of the structure. Using the analytical models described in this section, simulation studies demonstrating the advantages of using NSDs in multiple stories is demonstrated next.

The properties of NSD have to be chosen such that the strength reduction factor of bilinear structure and NSD assembly should comply with the values described in ASCE-07. The properties of the elastic structure, bilinear inelastic structure and assembly are shown in Figure 6.22. The strength reduction factor of the test frame used in this study, $R_{oy} = F_o/F_y$, is 1.25, but the suggested strength reduction factor in the design codes is 4. F_o is the maximum force in the elastic system for the suite of the ground motions used in this study and F_y is the yield force of the three-story structure. Since the columns of the test frame are conservative, the NSD is added to the system so that a strength reduction factor of 4 is achieved without altering the structure properties. After adding the NSD the strength reduction factor of the assembly, $R_{yy'} = F_y/F'_y$=4. The strength reduction factor $R_{yy'}$ should not be greater than 4 due to safety considerations. F'_y is the apparent-yield-strength (force in the NSD and structure assembly at u'_y). Hence, the NSD and structure assembly has a strength reduction factor, $R_{oy'} = F_o/F'_y$ of 5.

The ground movement during an earthquake will transmit energy to the structure. The peak response of the superstructure depends on the amount of energy transmitted from the ground motion. The impact of reducing the accelerations by adding the NSD is justified based on the amount on input energy transmitted to the structure. Using the governing equation developed in Eq. 6.7, the energy equation for the structure will be [3]

$$\underbrace{\frac{1}{2}\dot{\mathbf{u}}_\mathbf{r}^T\mathbf{M}\dot{\mathbf{u}}_\mathbf{r}}_{\text{Kinetic energy}} + \underbrace{\int_0^t (\dot{\mathbf{u}}_r\mathbf{C})\, d\dot{\mathbf{u}}_r}_{\text{Damper dissipated energy}} + \underbrace{\int_0^t \mathbf{F_{NSD}}^T d\mathbf{u_r}}_{\text{Work done by NSD}} = \underbrace{\int_0^t \left[\sum_{i=1}^{n}(\ddot{u}_i^T m_i)\right] du_g}_{\text{Input energy}} \tag{6.8}$$

In Eq. 6.8, the term on the right hand side represents the input energy transmitted to the structure due to the ground motion; it depends on the ground displacement,

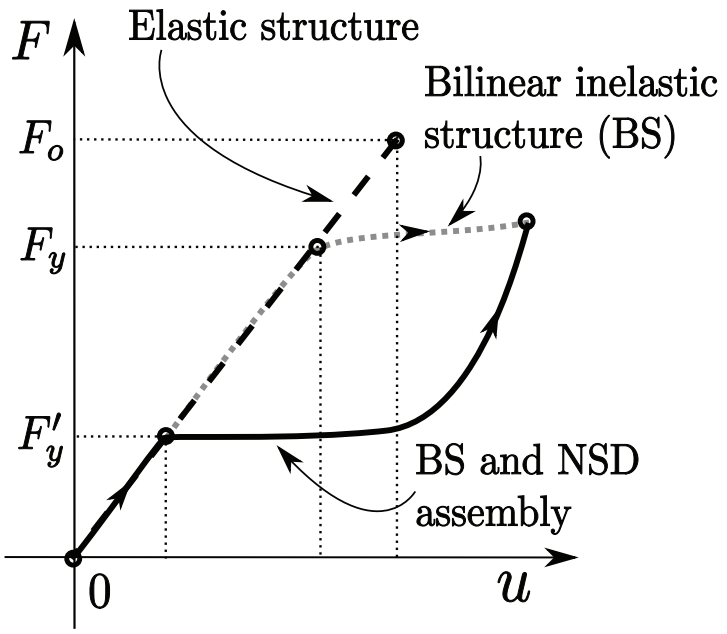

Figure 6.22 : Schematic F-D plots depicting the strength reduction factor

u_g, and the acceleration of individual floor, $\ddot{u}_i$. There is an additional term on the left hand side due to the addition of NSDs; work done by the NSD. Since the NSD exhibits nonlinear elastic behavior, the total work done by the NSD will be zero after the ground motion if there is no permanent deformation in the primary structure. By comparing the response of a structure and NSD assembly with an uncontrolled structure; since the ground displacement remains the same for both the structures, reducing the acceleration of the structure is equivalent to reducing the amount of energy transmitted. This is further justified through simulation studies in the next section.

6.4 Vertically distributed isolation

To justify the addition of NSDs and also to highlight the role of NSDs, the response of three systems is compared in this study: base structure or primary structure (BS); primary structure with dampers or passively controlled system (PS); primary structure with NSDs and dampers or adaptive system (AS). As explained in the previous sections, adding the NSDs will reduce the acceleration of superstructure or in other words, the amount of energy transmitted to the super structure is decreased. The added supplemental damper will contain the excessive interstory deformations caused due to the reduction in the assembly stiffness. In the previous section, experimental results are presented with NSDs in the first floor of 3SFS. To exemplify the isolation attributes possessed by the NSD, the response of nine-story structure with a NSD and damper in the third-floor (randomly chosen) is analyzed next.

Nine-story structure (BS), nine-story structure with viscous damper in the third floor (PS-3) and nine-story structure with NSDs and viscous damper in the third floor (AS-3) are subjected to three cycles of sinusoidal ground motion. The time period of the input ground motion is equal to the fundamental period of the structure. The peak inter-story deformation, u_{di}, of all the floors is compared in Figure 6.23(a) for BS, PS-3 and AS-3. Inter-story deformations are normalized with the yield displacement of the floor-columns, u_y; so, $u_{di}/u_y > 1$ infers that the floor has undergone inelastic deformation. The floor displacement with respect to the ground is shown in Figure 6.23(b) and the floor acceleration is shown in Figure 6.23(c).

The force-deformation behavior of the three systems in third-floor is shown in Figure 6.24 and the response of the roof displacement, acceleration and base shear are shown in Figure 6.25. A vertical line is shown in Figure 6.25 at 5.75 sec marking the stop time of external input. From Figure 6.23-6.25, it is clear that the addition of

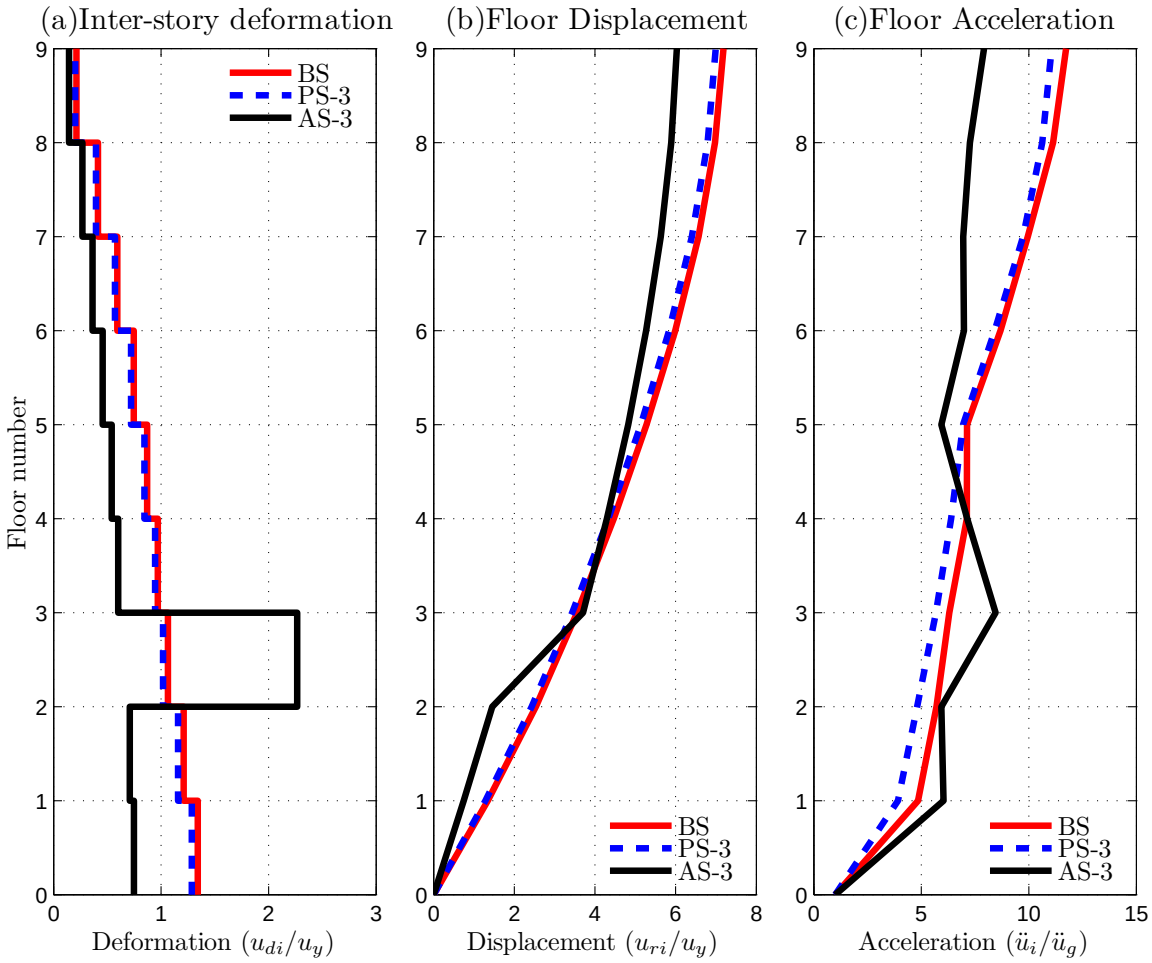

Figure 6.23 : Comparison of the maximum response profile of the structure for periodic input. In AS-3, NSD and damper is placed in the third floor.

damper in the third-floor (PS-3) resulted in very little reduction of the peak response characteristics. By adding two NSDs in the third floor along with the damper (AS-3), the response of the structure both above and below the third-floor is significantly reduced. For the AS-3, inter-story deformation in the first story and base shear (shown in Figure 6.25) is reduced by 50%, roof displacement is reduced by 15% and

the roof acceleration (shown in Figure 6.25) is reduced by 30% compared to the BS and PS-3. Columns in all the floors of AS-3 remained elastic, except third floor, but the first three floors in BS and PS-3 have yielded. The reduction in response achieved in AS-3 is mainly attributed to two factors:

1. The energy transmitted to the floors four through nine is reduced due to the reduction in assembly stiffness of the third-floor. As explained previously in section-2, once the NSD engages, the assembly stiffness reduces and as a result the forces transferred to the floors above the third floor will be reduced.

2. By incorporating NSD, resonance in AS-3 can be avoided. Since the excitation frequency is matching with the natural frequency of BS and PS-3, they will resonate resulting in large deformations and accelerations. Whereas in the AS-3, after the NSDs are engaged (inter-story deformation of third floor exceeds the "apparent yield-displacement", u'_y, of the NSDs), due to the bilinear-elastic behavior of the NSD and structure assembly, the natural frequency of the assembly changes and the assembly is prevented from resonating.

It is clear from Figure 6.23-6.25 that the addition of NSD in a particular floor results in reduction of the response of the floors above that floor. Although the response of the superstructure and substructure of the third-floor in AS-3 is reduced, the third floor has undergone deformations twice that of BS and PS-3 due to the reduction in assembly stiffness. Also, the third floor in AS-3 has undergone large permanent drift where as the other systems remained elastic, shown in Figure 6.24. Although a passive damper is present in the third floor of AS-3 along with the NSDs, it is not enough to prevent the primary structure from undergoing inelastic deformations. Subsequent sections in this chapter discuss various approaches to prevent these large

localized deformations.

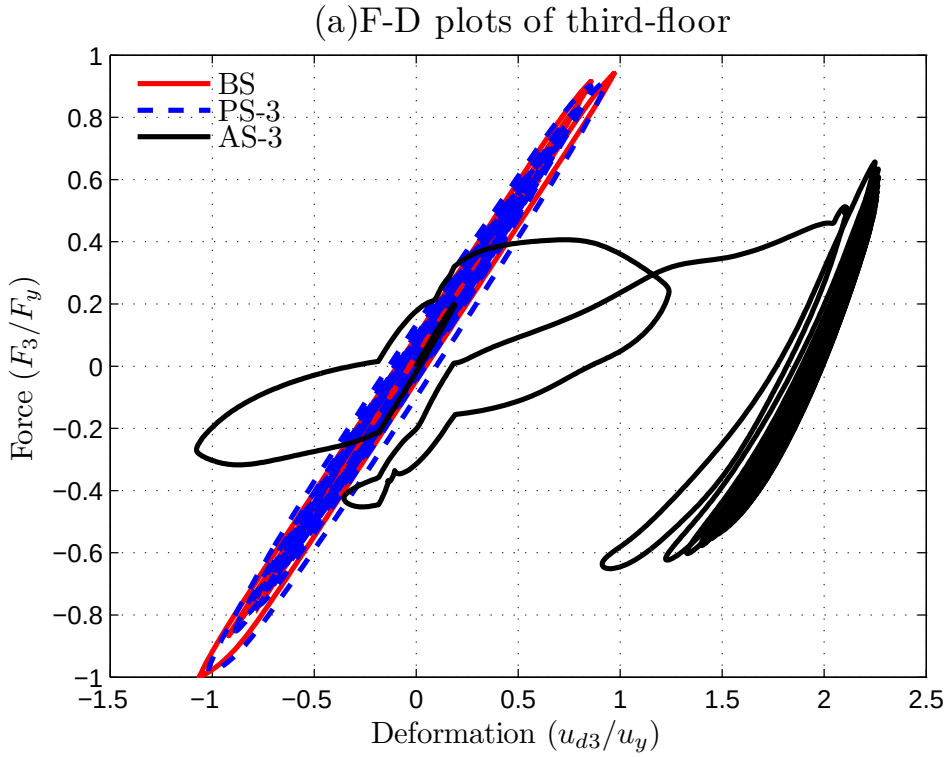

Figure 6.24 : Comparison roof acceleration and base shear experienced by the BS, PS-3 and AS-3 for periodic input. In the case of AS-3, NSD and damper are placed in the third-floor and only damper in the case of PS-3.

Further, two NSDs and a viscous damper are placed in every floor for AS and a damper is placed in every floor for PS. The peak inter-story deformation, floor displacement and floor acceleration are shown in Figure 6.26. The force-deformation behavior of the three systems in first-floor is shown in Figure 6.27, response of the roof acceleration and base shear are shown in Figure 6.28. Adding viscous dampers in all the floors to the primary structure (PS) will result in the reduction of inter-story deformation of first floor by 35%, roof deformation by 20% and roof acceleration by 35% compared to BS (shown in Figure 6.26), but the base shear of the structure is

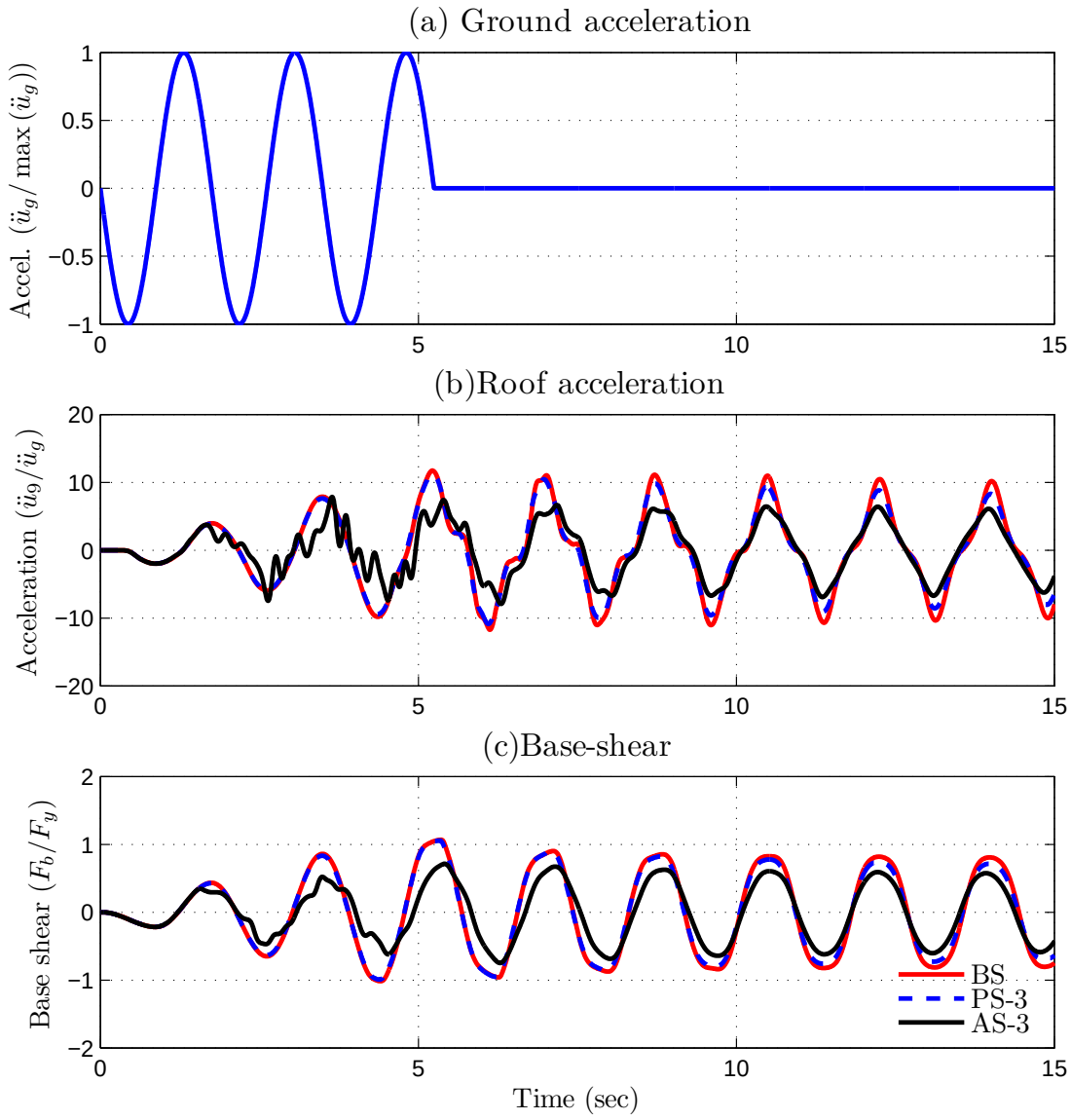

Figure 6.25 : F-D behavior of third-floor for periodic input. In the case of AS-3, NSD and damper are placed in the third-floor and only damper in the case of PS-3.

same as the BS, shown in Figure 6.28(c). With the addition of NSDs in every floor (AS), all the responses are further reduced by 20% and the base shear is also reduced by more than 50%. The reduction in response is again due to the reduction in the force transmitted to the superstructure due to the addition of NSDs and avoiding the

resonance state. Unlike the results with NSDs only in third-floor (shown in Figure 6.23-6.25), by adding NSDs in all the floors, the response is consistently reduced in all the floors without any excessive localized deformations.

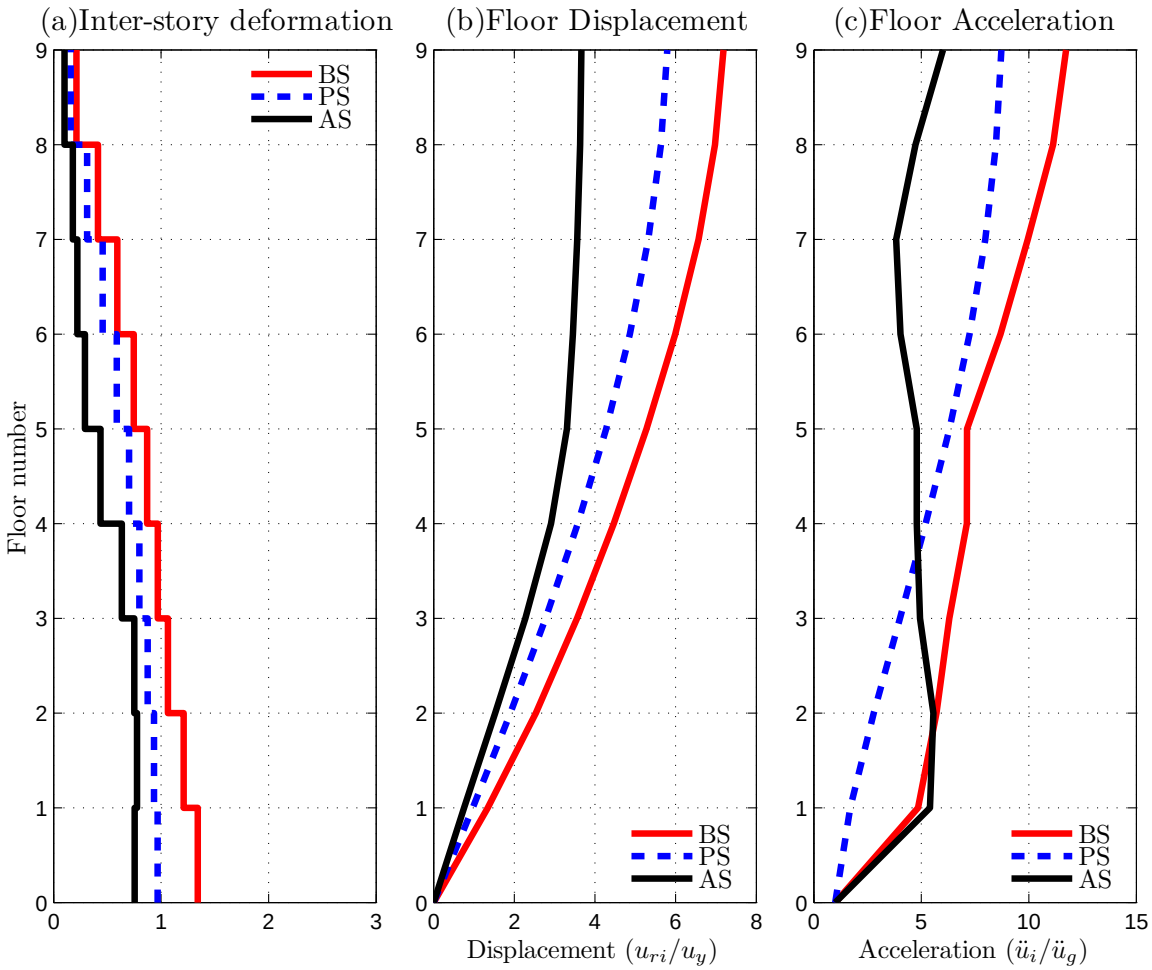

Figure 6.26 : Comparison of the maximum response profile of the structure for periodic input. In AS-3, NSD and damper is placed in the third floor.

Preliminary analysis has revealed that even with the NSDs and dampers in every floor (AS), large inter-story deformations in the bottom three floors is common for six

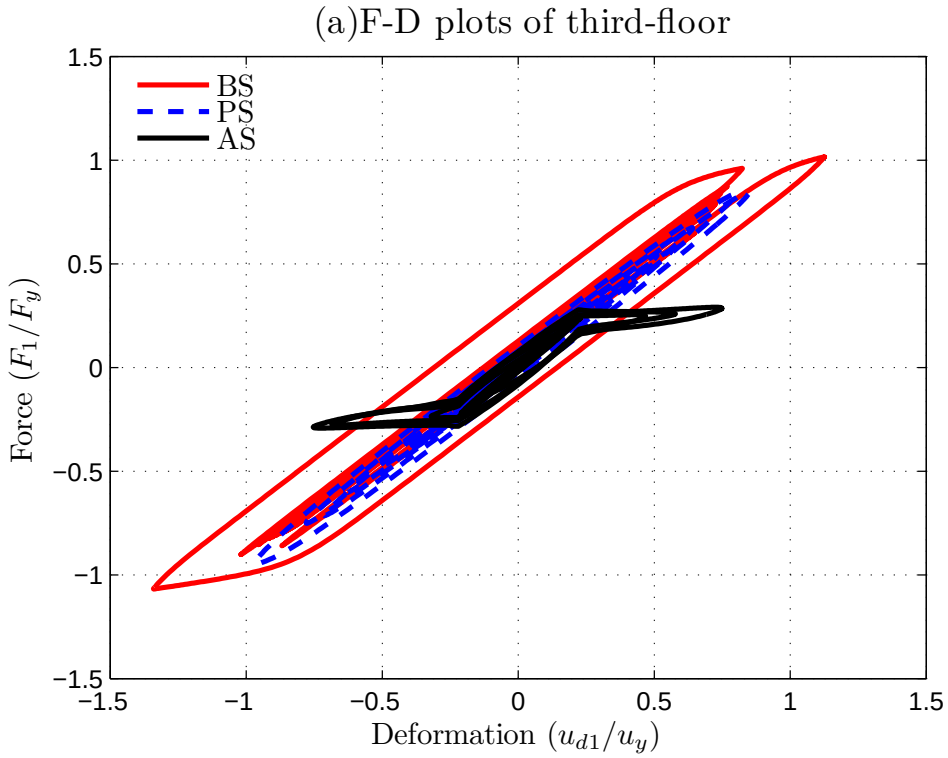

Figure 6.27 : Comparison roof acceleration and base shear experienced by the BS, PS and AS for periodic input. In the case of AS, NSDs with dampers are placed in all the floors and dampers are placed in the case of PS.

ground motions used in this study. The peak interstory deformation, floor displacement and floor acceleration are shown in Figure 6.29 for Kobe-JMA (NS component) ground motion with PGA of 0.84g. From Figure 6.29, although the floor accelerations and floor displacements of AS are substantially reduced, the inter-story deformation in the first floor is very high (u_{di}/u_y=1.65). This is due to the fact that during a ground motion, the forces are transmitted from bottom to top in multi-story structure, so the bottom stories always yield first. Since the magnitude of all the ground motions used in this study is high, the columns in first floor have yielded significantly in all the test cases.

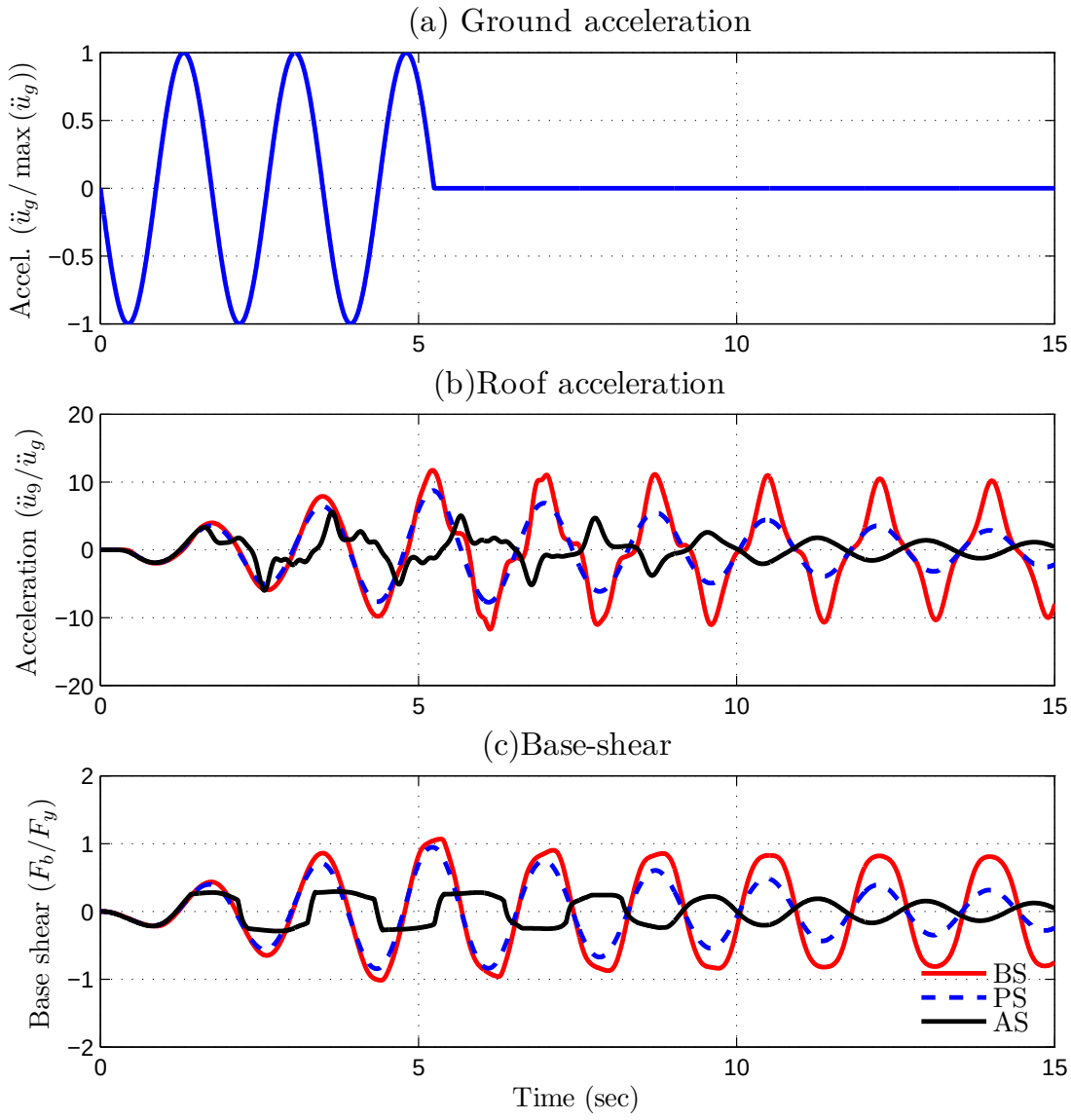

Figure 6.28 : F-D behavior of first-floor for periodic input. In the case of AS, NSD and damper are placed in all floors and only damper in the case of PS.

However, the results presented in Figure 6.23-6.25 are an exception because of the time-period of the input ground motion. If the time-period of the ground input is large (greater than or equal to the fundamental period of the structure), then all the NSDs in the higher floors also engage as a result the response reduction is achieved

over multiple floors. For short period pulses like the ground motion data, only the NSDs in the first-floor engage as a result the columns in the first floor will always undergo large inelastic deformation. To overcome this limitation, the properties of NSDs in different floors are modified such that NSDs in all the floors engage to prevent excessive inter-story deformation in the first-floor.

"Apparent yield-displacement", u'_y, of NSDs in different stories is modified to achieve the desired objective. Using an optimization algorithm, the desired set of apparent yield-displacements of NSDs in all the floors is calculated by minimizing the peak responses of all the floors. Constrained nonlinear optimization algorithm is used to find the optimal NSD properties. The objective function is a weighted sum of individual story drifts and story acceleration as shown in Eq. 6.9.

$$\Pi = \sum_{i=1}^{9} \left(\lambda_d |u_{di}| + \lambda_a |\ddot{u}_i|\right) \tag{6.9}$$

λ_d and λ_a the weighting functions used in calculating the objective function. The goal of optimization is to minimize Π, subject to the constraints that the strength reduction factor of individual story R'_{yyi} should be less than 4, shown in Eq. 6.10.

$$\underbrace{\min}_{\ddot{u}_g} \quad \Pi\left(\ddot{u}_g\right) \tag{6.10}$$

$$\text{subject} \quad R_{yy'_i} \leq 4 \tag{6.11}$$

The damper properties remain unchanged i.e., viscous damper with 20% damping ratio. Response of the structure with different NSD properties in every floor is referred as AS-optimal.

Since the primary structure is inelastic system and the NSD is nonlinear, the op-

Table 6.2 : Summary of the peak responses from the shake table tests [Yielding-tests]

Floor No.	Kobe	Sylmar	Newhall	Chi-Chi	Rinaldi	Erzikan
1	1.00	1.00	1.00	1.00	1.00	1.00
2	0.86	0.76	0.83	1.00	0.75	0.94
3	0.79	0.71	0.67	0.93	0.60	0.90
4	0.71	0.67	0.67	0.86	0.55	0.90
5	0.71	0.71	0.67	1.04	0.50	0.90
6	0.71	0.71	0.67	1.07	0.50	0.90

timization problem is nonconvex and will have no unique solution. For each ground motion, several solutions were obtained from the optimization tool (MATLAB, *fmincon* [164]) by changing the starting seed. The solutions that follow a certain trend are picked as the acceptable solutions. Obtaining a generalized solution given the structure properties and design ground motion will be the focus of future study.

The optimal NSD parameters obtained from the optimization has revealed that the u'_y of the second floor should be lower than the u'_y of first floor so that NSDs in both the floors will engage at the same time and prevent excessive deformation in the first-floor. By extending this idea to higher floors, u'_y should decrease from bottom floor to top floor. The values of u'_y in AS-optimal are listed in Table 6.2 for six ground motions; values are normalized with the first-floor u'_y. It should be noted that there are multiple solutions to the optimization problem and the results that suit the general pattern are chosen and reported in this study. After the NSDs in the bottom five floors are engaged the upper four floors have undergone very little deformation so the u'_y of floors six to nine have no impact on the overall behavior.

The peak inter-story deformation of all the floors is compared in Figure 6.29(a) for BS, PS, AS and AS-optimal for Kobe-NS ground motion [PGA=0.84g]. The floor

displacement with respect to the ground is shown in Figure 6.29(b) and the floor acceleration is shown in Figure 6.29(c). The force-deformation behavior of BS, PS and AS-optimal in first-floor is shown in Figure 6.30 and the response of the roof displacement, acceleration and base shear are shown in Figure 6.31. It is clear from the response profiles in Figure 6.29(a) that the peak inter-story deformation of all the floors is reduced in the case of AS-optimal. The floor deformation of the roof is reduced by more than 15%, the roof acceleration is reduced by 30% and base shear is reduced by more than 30% compared to BS and PS, shown in Figure 6.29-6.31 and Table 6.3. In the case of inter-story deformation and floor acceleration the achieved reduction in all the floors should also be a criterion. To take this into account the average of response in all the floors is calculated and used as a performance index. The profiles of story drift, story acceleration and inter-story deformation of the nine-story frame for all the six ground motions comparing the BS, PS and AS-optimal are shown in Figure 6.32, 6.33 and 6.34, respectively. Bar-graphs summarizing the results from all the six ground motions are shown in Figure 6.35 and tabulated in Table 6.3. AS in Figures 6.32-6.35 and Table 6.3 refers to AS-optimal.

The story drift profiles shown in Figure 6.32, confirms that the addition of dampers (BS and AS-optimal) will reduce the story drifts compared to BS. With the addition of NSDs in all the floors along with dampers, the drift is localized to the first three or four floors and the higher stories undergo rigid body motion, from Figure 6.32 and Figure 6.34. The inter-story deformation in the bottom three floors of NS is higher than the PS in case of Chi-Chi and Rinaldi ground motions, but is consistently less than the BS by more than 20%. Although the inter-story drifts of AS-optimal is higher than PS for few ground motions, the average drift is less than PS, shown in Figure 6.35 and the Table 6.3. This shows that the inter-story deformation is localized

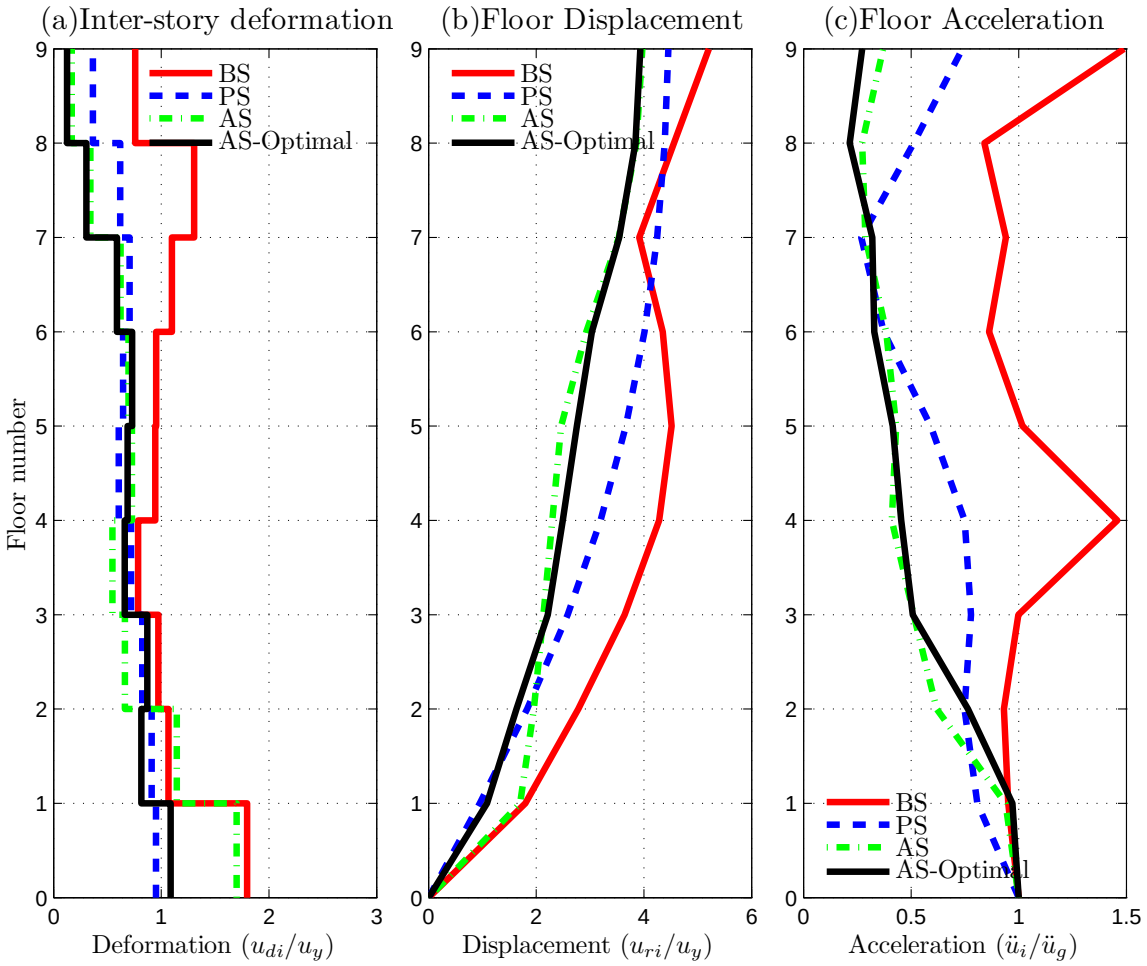

Figure 6.29 : Comparison of the maximum response profile of the structure for Kobe-NS ground motion [PGA=0.84g])

in the bottom floors, essentially isolating the higher floors. The acceleration profiles shown in Figure 6.33 for all the ground motions shows the acceleration reductions in all the floors. The bar-graphs shown in Figure 6.35 and the Table 6.3 can be summarized as follows:

1. The floor acceleration, roof displacement and base shear of AS-optimal is con-

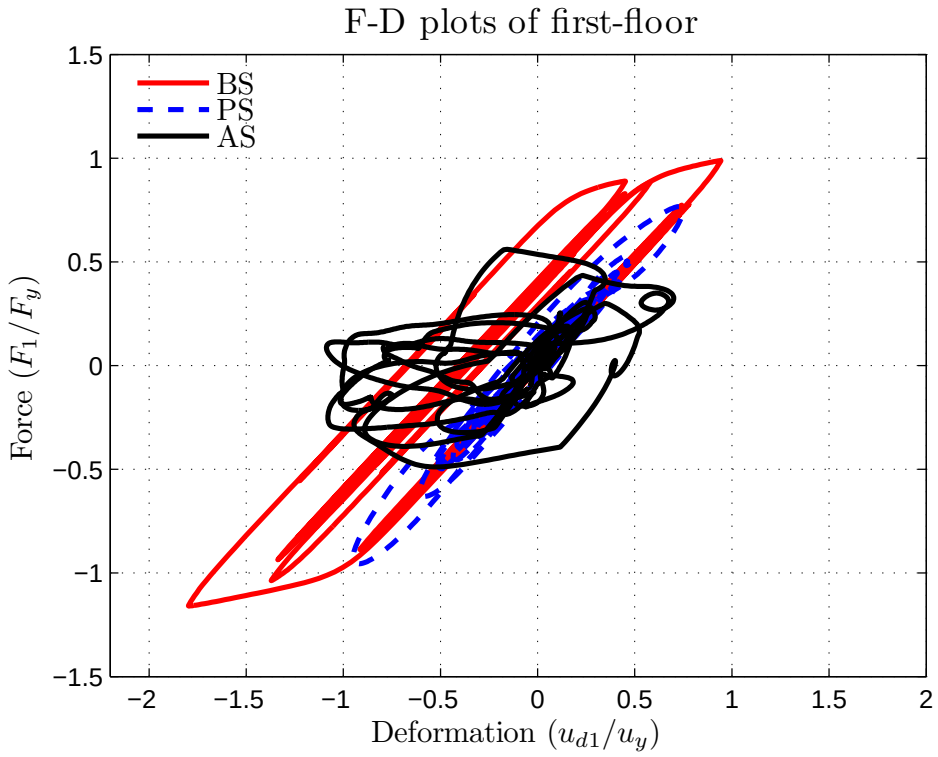

Figure 6.30 : F-D behavior of the 1st floor in BS, PS and AS-optimal for Kobe-NS ground motion [PGA=0.84g]

sistently less than BS and PS by more than 20% for all the ground motions.

2. Peak inter-story deformation of AS-optimal for some ground motions is higher than PS but it always less than BS. Although the maximum inter-story deformation of AS-optimal, which generally occurs in the bottom three floors, is larger than PS, it should be noted that the inter-story deformation in all other floors is less than BS and PS.

3. Adding the NSDs will result in consistent reduction of floor accelerations, floor deformations of all the floors (average values in Table 6.3 and Figure 6.35) and base shear as compared to BS.

Table 6.3 : Summary of the peak responses from the shake table tests [Yielding-tests]

Sl. no.	Ground motion	System	PGA (g)	Drift u_9/H	Inter-defor u_{di}/u_y		Accel. $\ddot{u}_i/\ddot{u}_g$		Base shear F_b/F_y
					Max.	Mean	Max.	Mean	
1	Kobe-NS,1995	BS	0.84	1.30	1.80	1.08	1.49	1.05	1.16
2		PS	0.84	1.11(14)	0.95(47)	0.70(34)	0.74(50)	0.62(41)	0.96(18)
3		AS	0.84	0.93(29)	1.07(41)	0.54(50)	0.35(77)	0.39(63)	0.56(52)
4	Erzikan-NS (1992)	BS	0.36	1.66	1.24	0.84	1.72	1.09	1.05
5		PS	0.36	1.41(15)	0.93(25)	0.67(20)	1.07(38)	0.73(33)	0.92(13)
6		AS	0.36	1.19(28)	0.87(30)	0.60(29)	0.64(63)	0.58(47)	0.34(68)
7	Rinaldi-FN (1994)	BS	0.63	1.55	1.77	1.11	1.72	1.10	1.15
8		PS	0.63	1.35(13)	1.09(38)	0.82(26)	0.96(44)	0.72(35)	1.05(9)
9		AS	0.63	1.40(10)	1.62(8)	0.76(31)	0.26(85)	0.34(69)	0.50(56)
10	Newhall-FN (1994)	BS	0.55	1.37	1.25	0.91	1.93	1.39	1.05
11		PS	0.55	1.02(26)	1.01(19)	0.65(28)	0.96(50)	0.82(41)	1.00(5)
12		AS	0.55	1.24(10)	1.35(-8)	0.74(19)	0.34(83)	0.45(67)	0.54(48)
13	Chi-Chi NS (1999)	BS	0.20	1.83	1.86	0.88	2.09	1.51	1.17
14		PS	0.20	1.59(13)	1.21(35)	0.71(19)	1.33(37)	1.08(29)	1.05(11)
15		AS	0.20	1.31(28)	1.88(-1)	0.88(-1)	0.83(60)	0.66(56)	0.59(49)
16	Sylmar-FN (1994)	BS	0.61	1.98	1.39	0.99	1.48	1.05	1.08
17		PS	0.61	1.77(10)	1.10(21)	0.80(19)	0.65(56)	0.52(51)	1.04(3)
18		AS	0.61	1.07(46)	1.18(15)	0.59(40)	0.24(84)	0.31(71)	0.45(58)

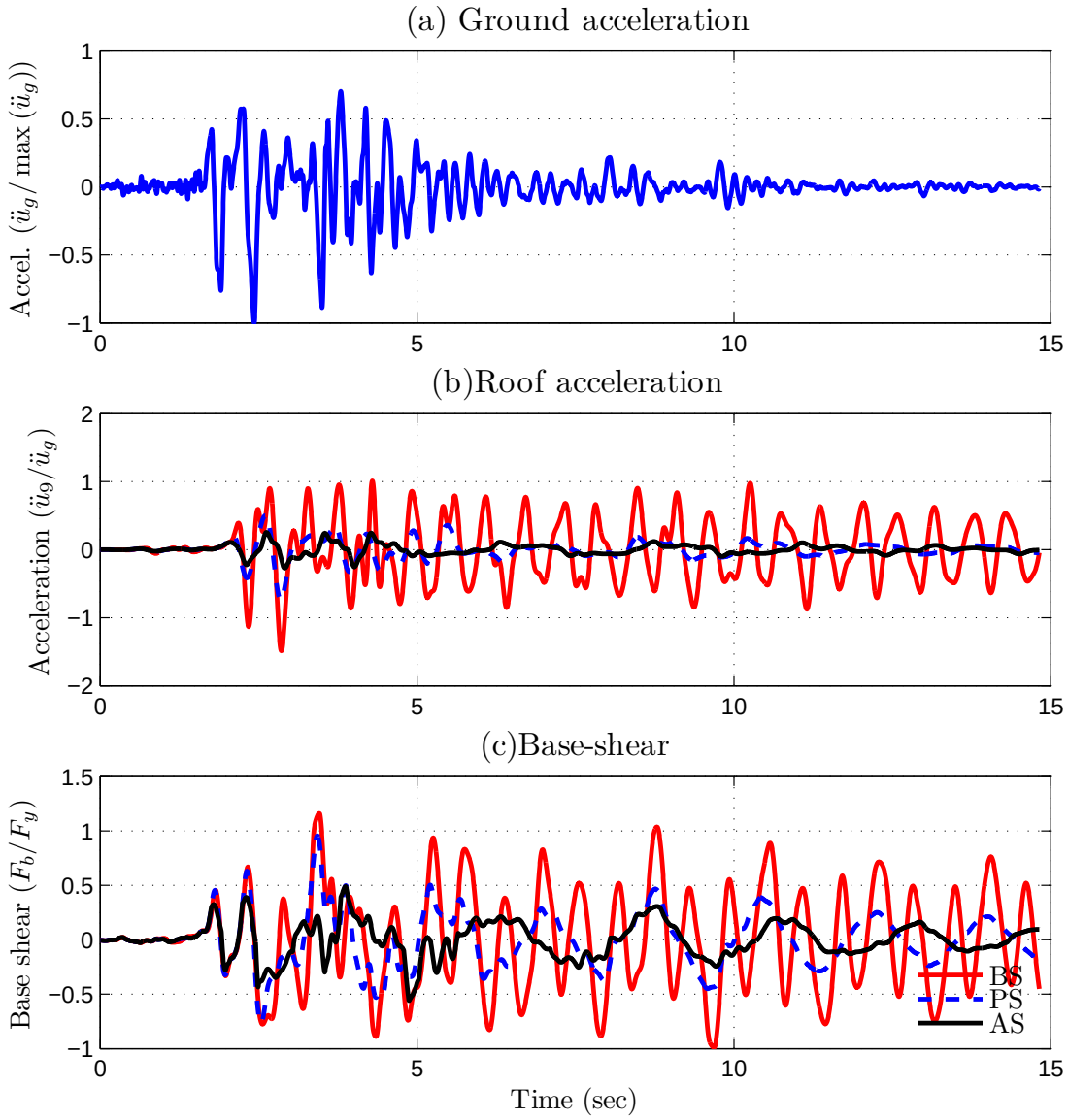

Figure 6.31 : Comparison of roof acceleration and base shear experienced by the BS, PS and AS-optimal for Kobe-NS ground motion [PGA=0.84g]

6.5 Summary

In this chapter, the advantages of using NSDs in multi-story structures are demonstrated through experimental and simulation studies. Shake-table studies have been

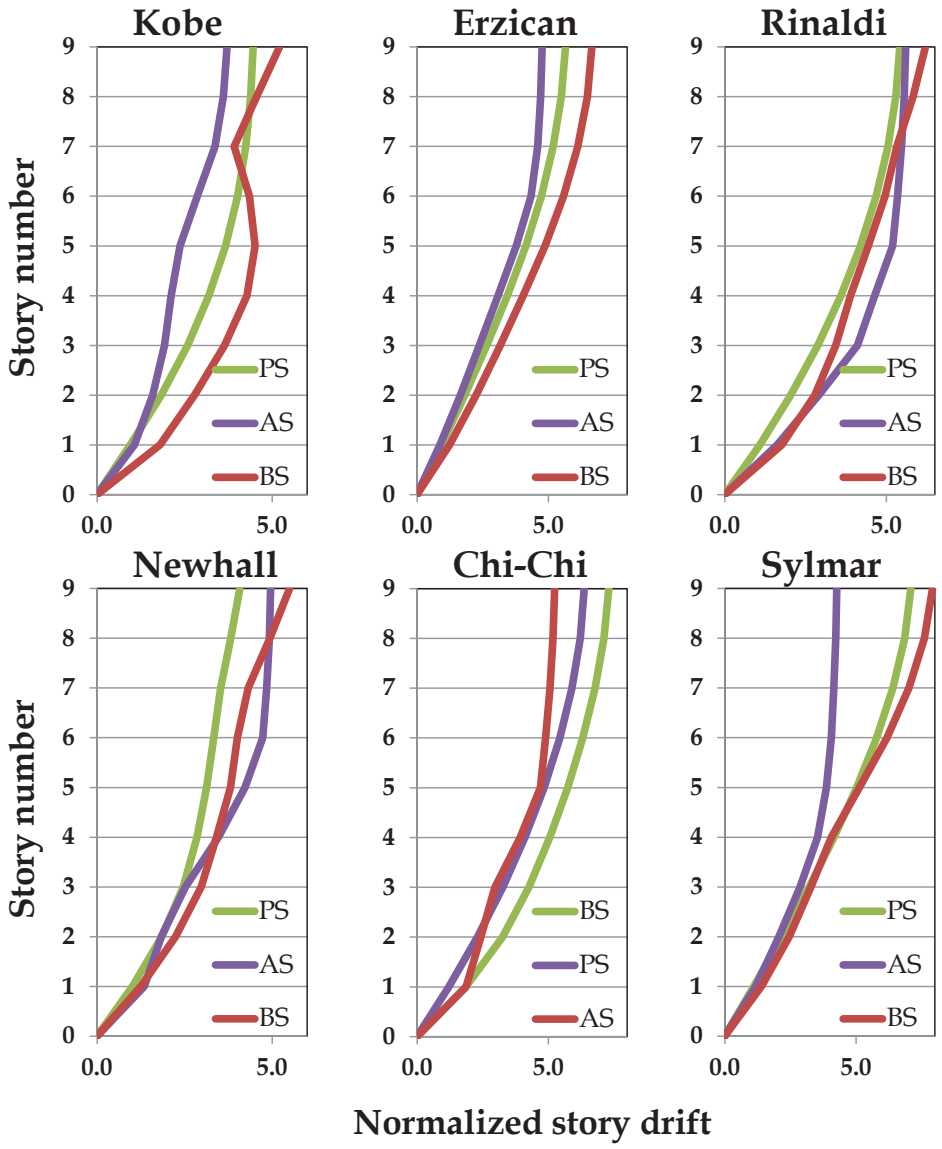

Figure 6.32 : Comparison of the story drift profiles of BS, PS and AS

performed on three-story fixed base structure with two NSDs and a viscous damper in the first floor. Experimental results have proved that the addition of NSDs in the first-floor will screen the input energy transmitted to the super structure. However, the first-floor is subjected to large inter-story deformation due to the reduction in

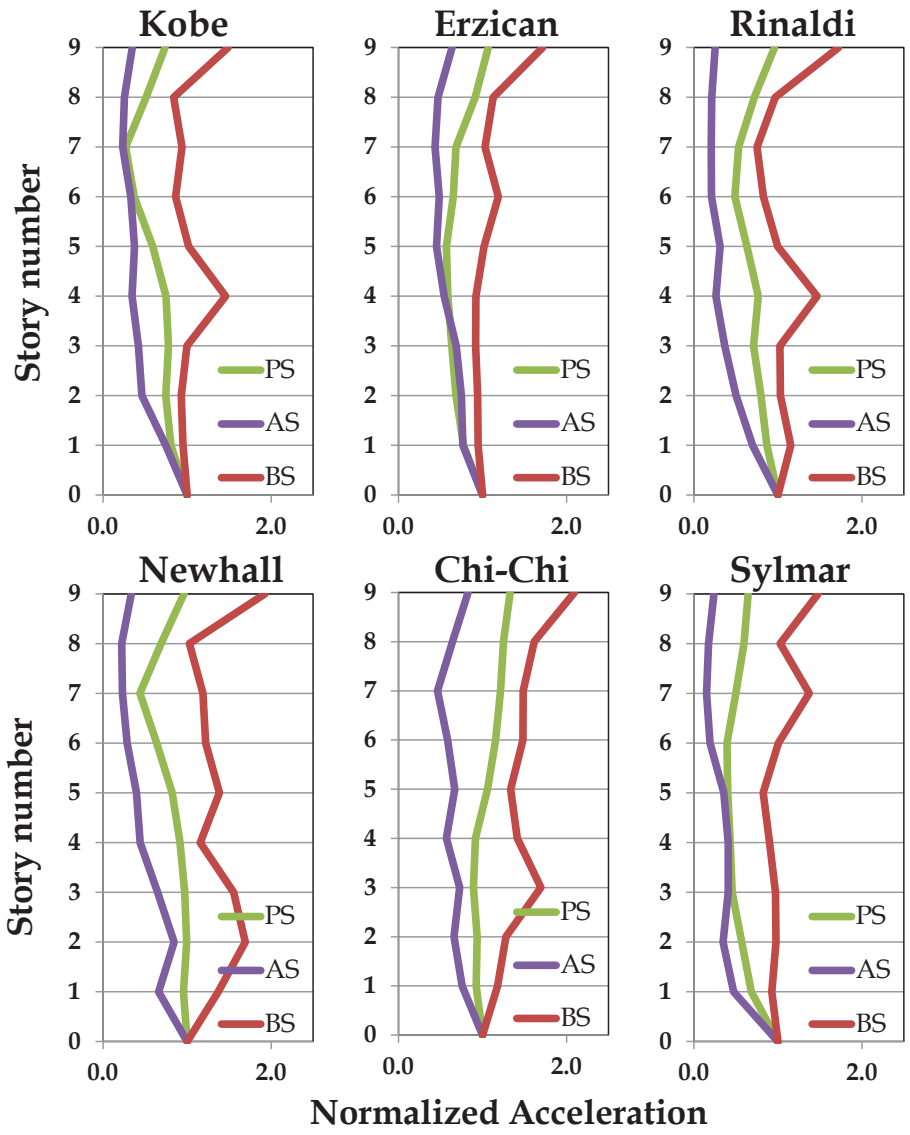

Figure 6.33 : Comparison of the story acceleration profiles of BS, PS and AS

stiffness with the addition of NSDs. By adding a viscous damper along with the NSDs, the deformations can be contained without increasing the base shear and roof accelerations.

Experimental results on the unbraced 3SFS have confirmed that the inter-story de-

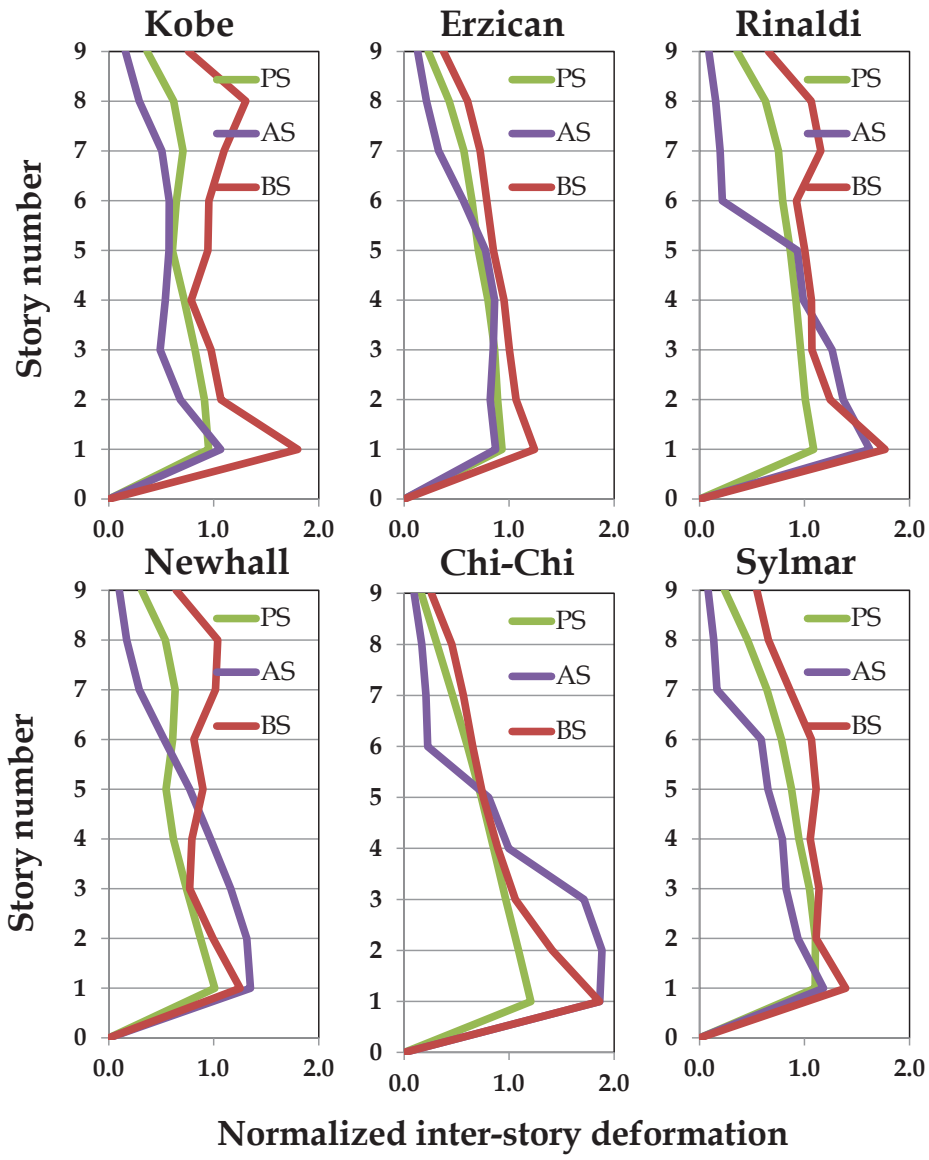

Figure 6.34 : Comparison of the inter-story deformation profiles of BS, PS and AS

formations, roof accelerations and base shear of the AS will be consistently reduced by more than 15%, 20% and 40%, respectively, compared to the BS, PS. NSDs are capable of absorbing most of the input energy and dissipate it through the viscous damper thus preventing the structural and non-structural components of the super-structure

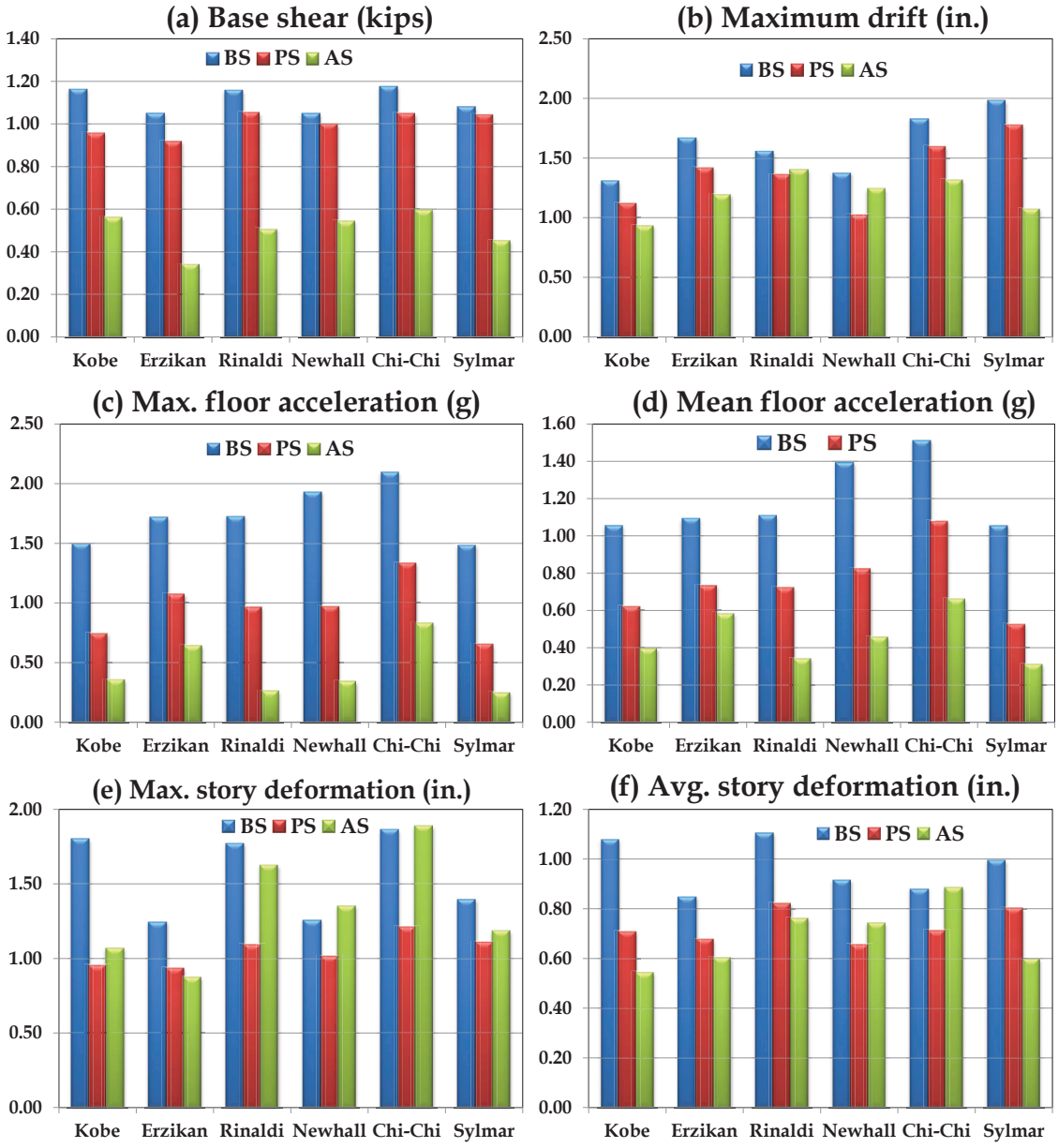

Figure 6.35 : Bar graphs summarizing the normalized response of Bs, PS and AS for six ground motions

from experiencing large accelerations and preserve the integrity of the structure. Also, the huge reductions in base shear will avoid the large foundation forces experienced otherwise. Generic numerical models are also developed and calibrated to replicate

the experimental results at component level and assembly level. These models can be used to study the sensitivity of the design parameters for the structure and the NSD. Given the nonlinear behavior of the components and the complexity of the assembly, the close agreement between the experimental results and the analytical predictions shows that developed models are representative of the actual structures.

Comprehensive simulation studies have also been carried on 1:3 scale nine-story yielding structure, to analyze the role of NSDs in multistory buildings and also to find the desired configuration of NSDs to achieve response reduction during severe ground motions. Results presented herein have confirmed that the addition of NSD in a particular story will prevent the transfer of the input energy from ground motion to the super structure and also the resonance state of the primary structure can be avoided. However, the inter-story deformations in the installed floor will be significantly larger compared to uncontrolled structure. These excessive localized deformations can be prevented by placing NSDs (having different properties) in multiple stories and letting them engage at the same time.

An optimization study has been carried to find the desired properties of NSD as a function of the story height for six ground motions. The "apparent yield-displacement" of the NSDs should decrease from bottom to top to prevent large inelastic deformations in the first story. The optimal properties of NSDs for a given structure and a target response reduction can be calculated based on the site specific spectra. Response has demonstrated that the base shear and maximum floor accelerations of the AS-optimal is reduced by more than 40% and 20%, respectively for all the ground motions tested. In all the test cases, the top four floors of the nine-story frame have undergone very little deformation confirming that the input energy is dissipated in the bottom five floors, unlike the base-isolation system where all the deformations

and energy dissipation occurs at the base of structure. This study has revealed that installing NSDs and dampers in multiple stories can overcome some of the limitations posed by the passive control devices and base-isolation systems. However, from the practical point of view, the proposed approach and the NSD needs to be enhanced further because they are sensitive to the design ground motion, the estimated force-deformation behavior and the excessive permanent deformations observed for severe ground motions. In the next chapter, two semi-active mechanisms are proposed for the NSD to address the issues pertaining to assembly drifts and also to improve the performance of NSD.

Chapter 7

Semi-active Negative Stiffness Device

So far, the importance and application of NSD in "apparent-weakening" of structures is studied in SDOF elastic, inelastic and MDOF structures. Results from the shake-table studies on three-story frame structure has confirmed the idea and also uncovered the issues pertaining to the large permanent-drifts and the sensitivity of NSD properties. The NSD discussed so far is a passive device and exhibits a definite F-D behavior based on the installed configuration. In this chapter we seek to develop a semi-active NSD (SA-NSD) to overcome the limitations of the passive NSD.

Two issues with the passive NSD as detailed in chapter 2 and chapter 5 are:

- To achieve zero assembly stiffness beyond apparent yield displacement (u'_y)
- To avoid large permanent drifts in the structure and NSD assembly when the base structure undergoes significant yielding.

Both the issues can only be addressed by changing the properties of NSD in real-time using a local feedback and is not feasible through a passive system.

Two semi-active mechanisms are proposed in this chapter to address each of the above mentioned issues. The underlying principle in both the approaches is to change the lever-ratio of NSD by moving the pin connecting the pivot plate and lever-arm, shown in Figure 3.1. Moving the point-B will change the F-D behavior of NSD. Exploiting this feature the desired force displacement behavior of the assembly can be tuned by moving the pin at point-B in real-time. Two different objectives can be

achieved by moving the point-B: first objective is to move the point-B such that a prescribed force-displacement behavior of the NSD is obtained and the second objective is to reset the zero of the NSD when the primary structure yields to prevent the large assembly drifts.

The rest of the chapter is organized as follows: the details pertaining to the development and implementation of SA-NSD is presented in section-7.1. Analytical models for the proposed SA-NSD and the advantages of both the semi-active devices are presented through numerical studies in section-7.2. Simulation results on a SDOF system with the proposed SA-NSD are compared with the passive NSD in section-7.3. The proposed idea and the simulation results are summarized in section-7.4.

7.1 Semi-active NSD

In the passive NSD, the pin at point-B is held fixed in the middle of a vertical slotted hole but in the semi-active NSD the pin is moved in the slot. The two semi-active approaches proposed based on the shape of the slotted holes

- Arc slotted hole (shown in Figure 7.1)
- Linear slotted hole (shown in Figure 7.2)

The lever-arm is axially rigid and there is no friction in the pin at point-B, so by moving the pin, the pivot plate rotates such that the lever-arm is always perpendicular to the slotted hole. Arc type slotted hole is designed to change the lever arm and consequently the force exerted by NSD without changing the zero position of the NSD. This is achieved if the radius of the arc is equal to the lever arm length, l_{lv}. In the case of SA-NSD with a vertical slotted hole, zero of the NSD is also drifted when the point-B is moved in the vertical slotted hole. The pivot-plate rotates and positions itself

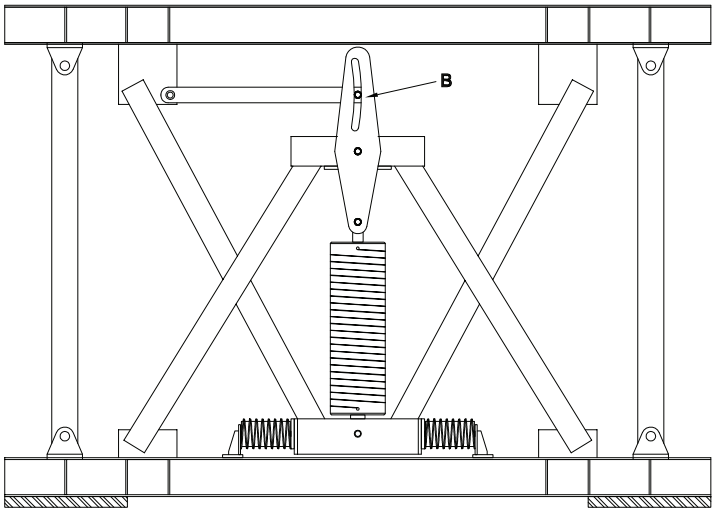

Figure 7.1 : Semi-active NSD with an arc slotted hole to move pin at point-B

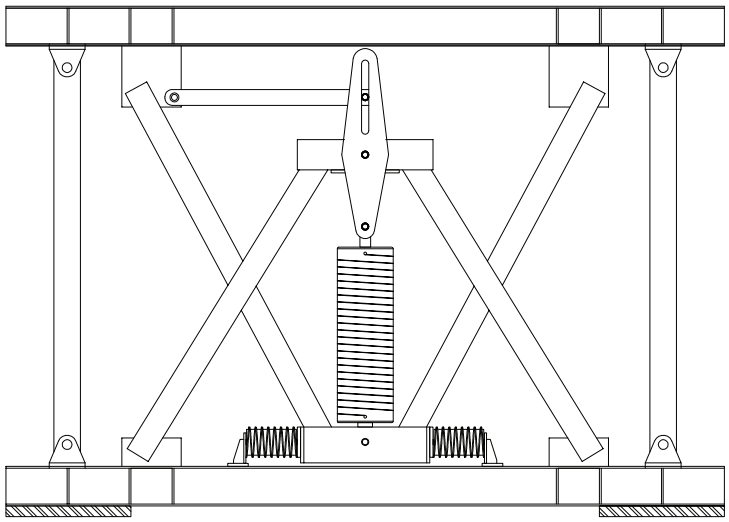

Figure 7.2 : Semi-active NSD with a vertical slotted hole to move pin at point-B

such that the lever-arm is perpendicular to the slotted hole. As a result, pivot plate and compressed spring will have an initial rotation in the undeformed configuration.

In passive NSD, the pin at point-B is fixed using the interface plates as shown in Figure 3.1, but in the case of SA-NSD to control the vertical position in slotted hole an external actuator is needed. In this study a passive hydraulic actuator is proposed to adjust the pin at point-B. The hydraulic device uses local displacement of NSD as the feedback and moves the pin at point-B to get the desired force deformation behavior. The hydraulic double acting cylinder proposed for the SA-NSD is explained next.

The pin at point-B is directly connected to the clevis of a piston-rod as shown in Figure 7.3 and 7.4. The other end of piston is connected to the piston that separates the cylinder into two halves filled with fluid. The other end of the hydraulic device is connected to the pin at point-D (top of precompressed spring) as shown in Figure 7.3. Each half has an opening that in turn is connected to a cylinder, through a pipe, that is placed horizontally on the bottom chevron seat. Both the pipes connected to the cylinder has a valve that is regulated by a mechanical switch. Two square plates are welded on either side of pivot plate. The horizontal cylinders has a piston facing the square steel plate, shown in Figure 7.4. When the pivot plates rotate the square plates rotate along with the pivot plate and touch one of the horizontal cylinder.

Initial configuration of the hydraulic setup is shown in Figure 7.4. As the structure starts moving either to the left or right the ceiling of the NSD moves with the structure. Since the connecting-arm is connected to the ceiling of the NSD, it moves in the same direction as the structure's displacement. As the connecting-arm moves, the pivot-plate rotates about the pin at point-C. Initially the two valves in the pipes connecting the horizontal and vertical cylinders are closed, this way there is no move-

ment of fluid in the cylinders. As the lever-arm rotates beyond certain displacement, the square plate touches the piston of horizontal cylinder, the mechanical switch gets activated and the valves open. For any further displacement beyond the yield point the piston of the horizontal cylinder pushes the fluid into the vertical cylinder which will in turn move the piston in vertical cylinder thereby moving the pin at point-B. Local feedback signal is used to regulate the valves and achieve the desired behavior of NSD. The advantages of each SA-NSD is detailed in the next section.

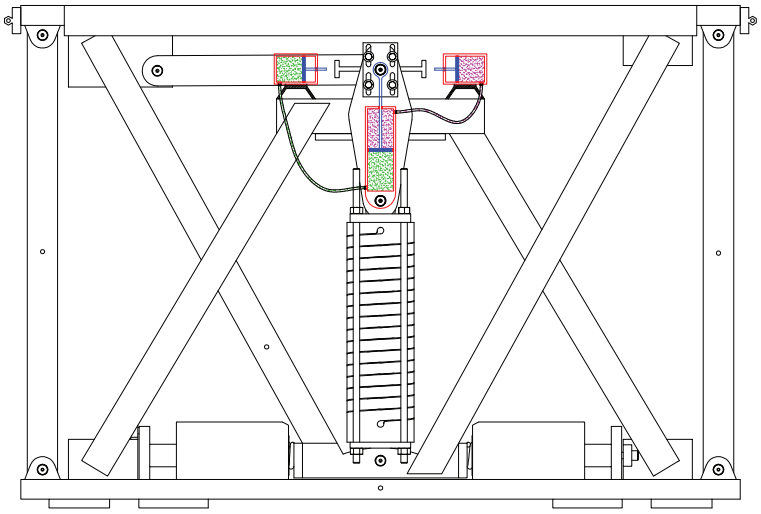

Figure 7.3 : Semi-active NSD with a hydraulic device to move pin at point-B

7.2 Behavior of semi-active NSD

The point "B" is displaced initially so the lever-arm, pivot plate and compressed spring will have an initial rotation as shown in 7.5. Let the vertical offset of the point-B from its nominal position be $\delta(t)$ then the length of the lever length $l_2 = l_2' - \delta(t)$. Where, l_2' is the undisplaced length of the pivot plate. Length of compressed spring in vertical position is l_p. The stiffness of pre-compressed spring is K_{sc} and the preload

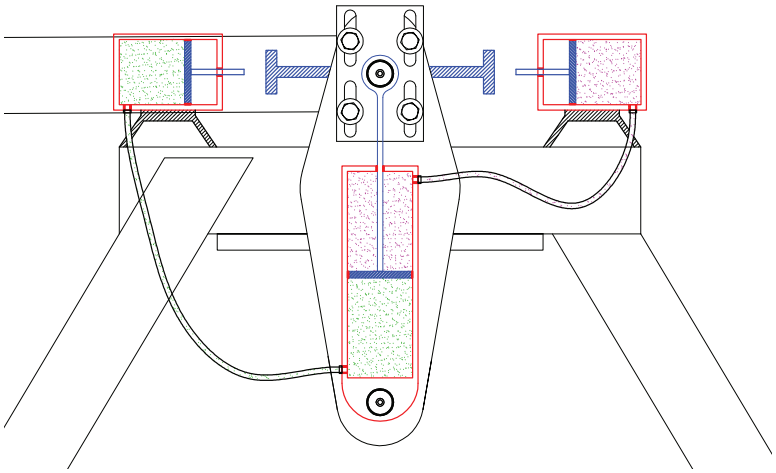

Figure 7.4 : Semi-active NSD with a hydraulic device to move pin at point-B

in the spring is P_{in}. The governing equation of NSD for SA-NSD with arc slotted hole (SA1) and the NSD with vertical slotted hole (SA2) are different. For SA1, they are same as the equation presented in 3.4-3.10, but the lever-length is replaced by $l_2 = l_2' - \delta(t)$. For the SA2, because of the initial deformation, the displacements of point-B and point-D will change.

Initial horizontal deformation of point-B is u_0' and point-D is u_{D0}. The displacements u_0' and u_{D0} are always in opposite direction. The length of the other end of lever remain constant, l_1. Initial Deformation, u_0', u_{D0} initial rotation θ_{lv0} are calculated from the vertical displacement of point-B ($\delta(t)$). The rotation of pivot-plate and the precompressed spring are given by Eq. 7.1 and 7.2

$$\psi = \sin^{-1}\left(\frac{u_0' + u}{l_2}\right) \tag{7.1}$$

$$\theta = \tan^{-1}\left(\frac{\left[(u_0' + u)\,\frac{l_1}{l_2}\right]}{\left[l_p + l_1\,(1 - \cos(\psi)) + h'\right]}\right) \tag{7.2}$$

Rest of the equations will be the same as the ones listed in Eq. 3.6-3.10.

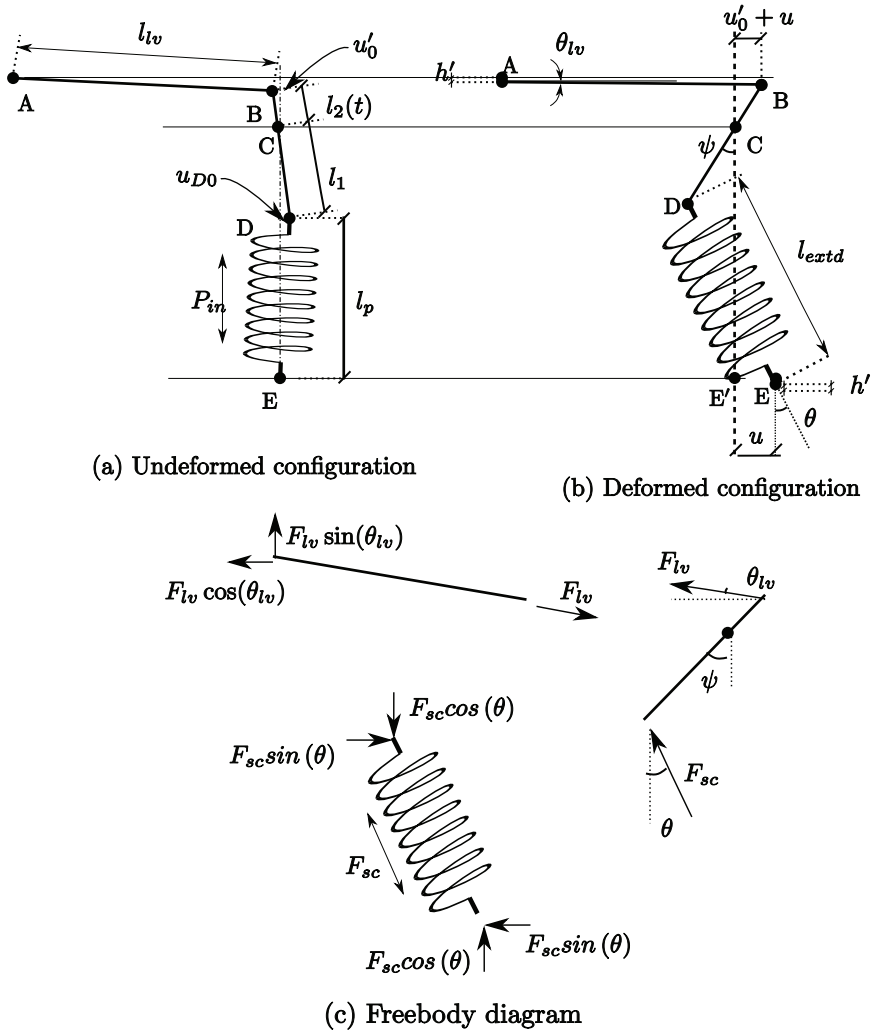

Figure 7.5 : Undeformed shape, deformed shape and free body diagram of semi-active NSD with an initial offset in point-"B"

7.2.1 Semi-active NSD with arc-shape slotted hole

To simulate "apparent-weakening" in elastic systems, the following factors need to be considered in designing the NSD: apparent-yield displacement, stiffness of assembly

beyond apparent-yield displacement and the stiffening point. Apparent yield displacement depends only on the properties of gap spring assembly (GSA). The post-yielding (apparent-yielding) stiffness of assembly and the stiffening point depends only on the stiffness and preload in the precompressed spring. Any desired set of values can be obtained by adjusting the properties of precompressed spring. In the case of bilinear inelastic systems, design of NSD get complicated because of multiple constraints. Desired F-D behavior for the inelastic structure and NSD assembly should have the following attributes, with reference to Figure 7.6,

1. The stiffness of the NSD-assembly between 0.25 $in.$ and 1 $in.$ should be as close to zero as possible (region enclosed in black bounding box)

2. Negative effective-stiffness of the NSD-assembly that occurs beyond 1 $in.$ should be avoided (region enclosed in magenta bounding box)

3. Stiffening that occurs in the NSD should be high to prevent the structure from collapsing (region to the right of cyan line)

The first condition can be easily satisfied by choosing appropriate NSD properties and lever-arm length but the other two criteria will be violated for this length. From Figure 7.6, the properties of passive NSD are chosen such that the stiffness of the assembly should be zero but the effective stiffness of the assembly beyond 1 $in.$ is negative. So, the objective of semi-active NSD is to satisfy all the three criteria. This is achieved by changing the lever arm length of the NSD. An actuator is assumed to move the pin at point-B that connects the connecting-arm and lever-arm. The pivot is moved on a curved groove to retain the zero-position of the NSD. Radius of curvature of the groove is equal to the length of the connecting-arm. By moving the pin at point-B, there will be two implications in the force exerted by the NSD

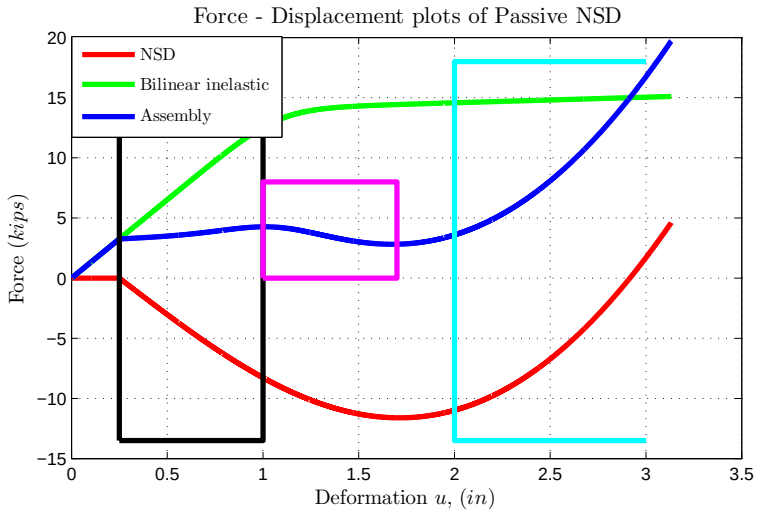

Figure 7.6 : Force deformation of assembly with passive NSD

1. Length of the effective lever-arm l_2 will change

2. Force exerted by the NSD on structure is reduced by increasing or decreasing the angle θ_{lv}.

Force-deformation behavior of the NSD and bilinear inelastic structure assembly for different lever-ratios is shown in Figure 7.7. Also shown in Figure 7.7 is the desired window for the F-D behavior of assembly. The bottom line of the window is the target force deformation behavior. Once the target is fixed, the difference of the F-D behavior of assembly with each lever-ratio and the target is calculated as shown in Figure 7.8. The difference in force between the horizontal broken black line and the various passive NSD force-displacement plots (shown in Figure 7.7) are shown in Figure 7.8. In Figure 7.8, the displacement at which each of these curves cross the zero line is picked and lever-ratios corresponding to these points are used as a reference to develop the switching pattern for point-B.

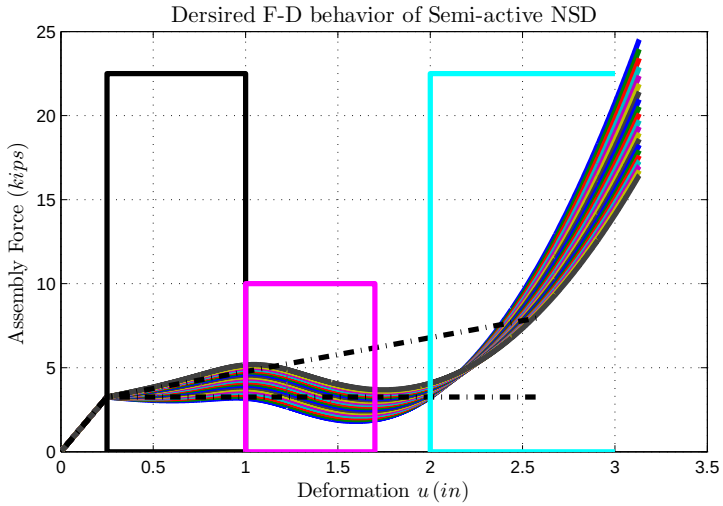

Figure 7.7 : F-D behavior of NSD and structure assembly with different lever-ratios

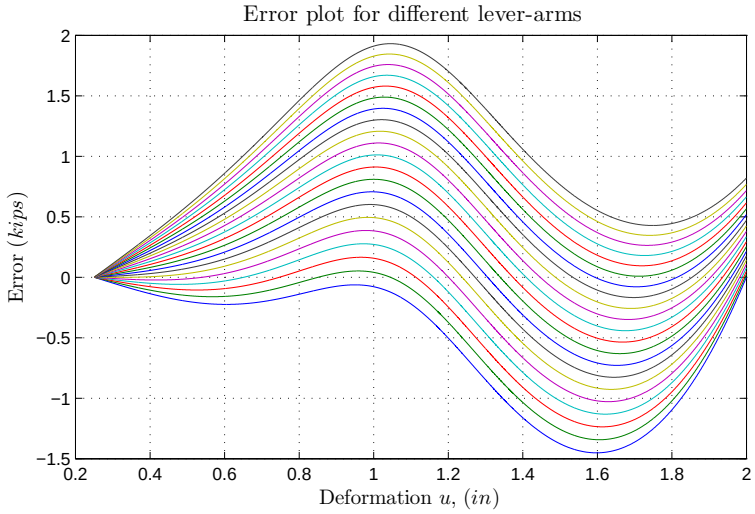

Figure 7.8 : Error in the force of NSD with respect to the target F-D behavior

Variation of lever arm length with displacement for this method is shown in Figure 7.9. The optimal switching condition is such that the error should be zero for all the displacements. Lever-arm lengths corresponding to a set of discrete displacement values, to achieve optimal switching condition, are shown in Figure 7.9. It is clear

from Figure 7.9 that, to achieve optimal performance, switching is nonlinear. Till $0.53''$ the effective lever-arm length is kept as constant at $6.2''$ and for displacements higher than $2''$ it is kept constant at $6.05''$. F-D behavior of SA-NSD assembly is compared with passive NSD assembly in Figure 7.10.

It is clear from the F-D plot of the assembly that the stiffness is almost zero from $0.25''$ till $2''$ and the effective negative stiffness is totally avoided and the desired stiffening is also achieved. Improved performance of the SA-NSD over the passive NSD is shown in the hysteresis plots in Figure 7.10.

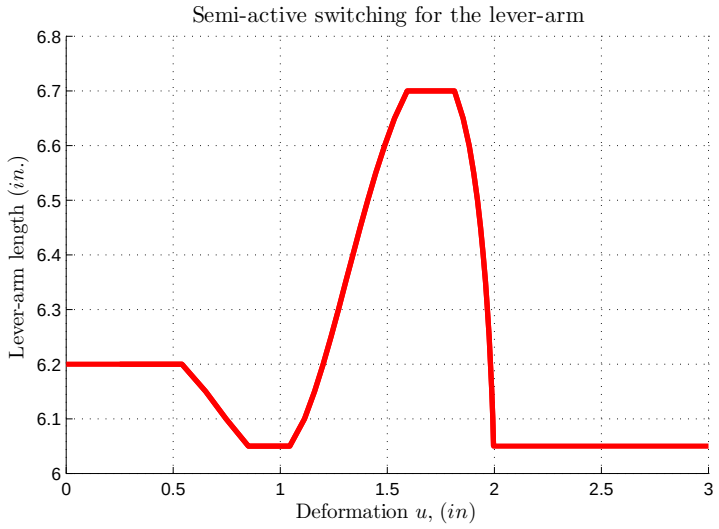

Figure 7.9 : Displacement of point-B to achieve the desired F-D behavior of assembly

7.2.2 Semi-active NSD with vertical slotted hole

By moving point-B in a vertical slotted hole, the zero position of the NSD will be shifted. Since the lever-arm is axially rigid, by moving the pin upwards the pivot plate will rotate in anti-clockwise direction. Due to the rotation of pivot-plate the point-D (shown in Figure 7.5) will move towards the right and the precompressed spring will

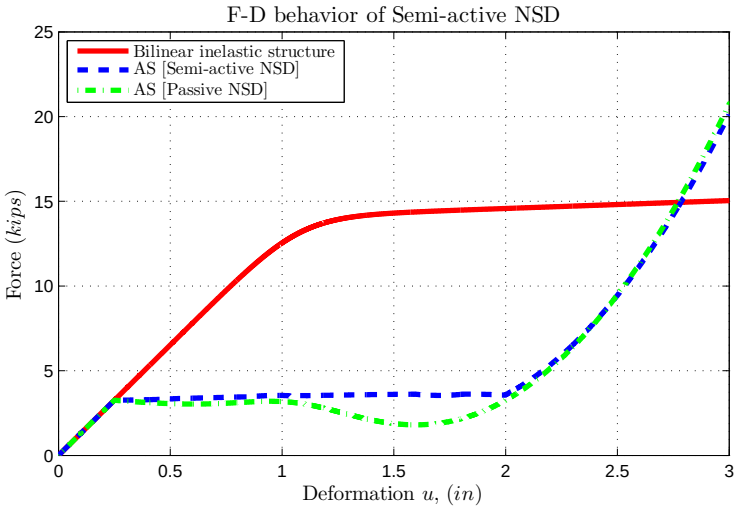

Figure 7.10 : Comparison of the F-D behavior of passive and semi-active NSD

exert a force on the structure. For the NSD configuration shown in Figure 7.2, by moving the pin upwards (negative direction) the zero of the device shifts to the right and vice-versa. The force-deformation behavior of SA-NSD for one *in*. deformation of point-B in positive (downward) and negative direction is shown in Figure 7.11 without the gap spring assembly (GSA) and is shown in Figure 7.12 with GSA. The stiffness of the semi-active and passive NSDs are the same for small deformations, but the peak deformation of semi-active NSD is 10% less than the passive NSD due to the rotation of the lever-arm. The point-B is moved using the double-acting hydraulic device and similar mechanism should be adapted to move the GSA. The GSA is deigned for the initial configuration of the passive NSD, so if the GSA is not transformed along with point-B the F-D behavior of the SA-NSD will be asymmetric. To avoid this, the double acting hydraulic device is also connected to the GSAs. The idea of moving the point-B to change the zero position of NSD is called resetting method. The advantages of using resetting method in a SDOF structure is demonstrated through

simulation results next.

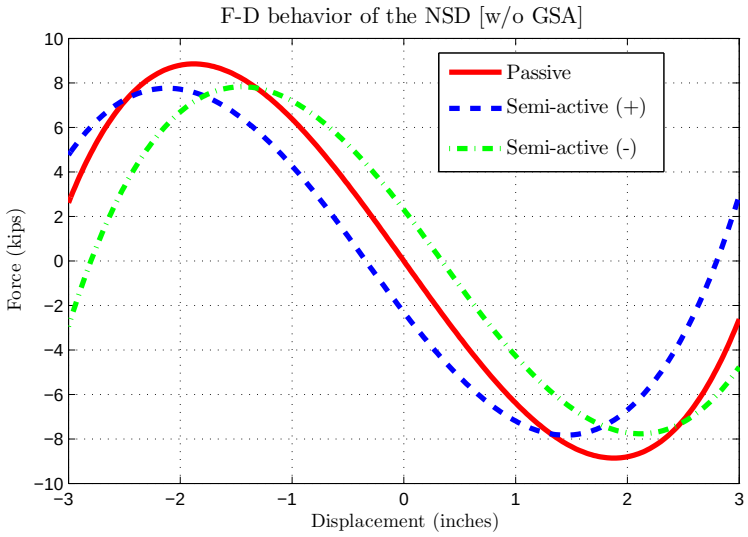

Figure 7.11 : Force deformation behavior of semi-active NSD without GSA

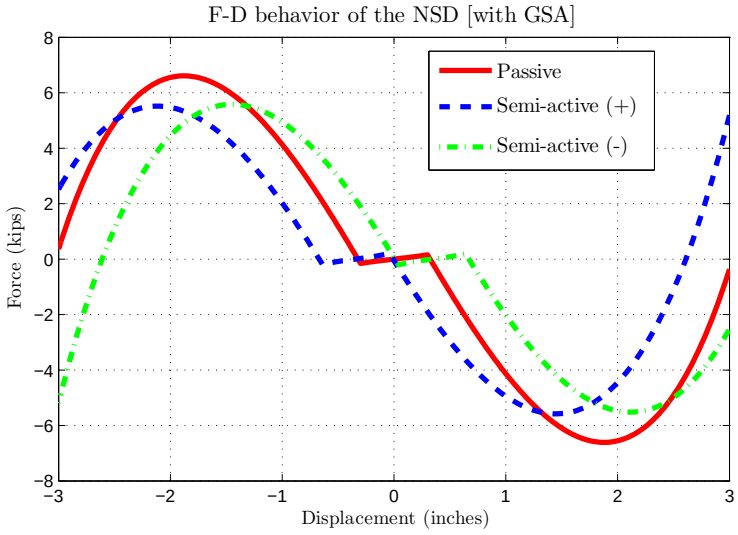

Figure 7.12 : Force deformation behavior of semi-active NSD with GSA

7.3 Simulation Results

From the experimental studies on 3SFS and the simulation studies it has been found that the permanent deformation in the structure and NSD assembly is significantly large compared to the inelastic deformation in the primary structure. The semi-active NSD with vertical slotted hole is developed to address this issue. The assembly drift in bilinear inelastic structure with NSD is grouped into two categories, described in section-5.2: (1) mild-yielding (inelastic deformation in the structure is less than u'_y) (2) heavy yielding structure (inelastic deformation in the structure is larger than u'_y). For mild yielding structures, the assembly drift is same as the inelastic deformation in the primary structure, but in the heavy yielding case, assembly drift is two times the inelastic deformation in the primary structure. Although these permanent drifts can be recovered after a seismic event using a slotted hole connection, the drift will be an issue if the ground motion has multiple pulses or in the case of after-shocks.

The semi-active mechanism (SA2) presented in the previous section is used to overcome the large assembly drifts. Next step is to find algorithm to move the point-B. Two criteria has to be considered in adapting the SA-NSD; the first is to find the instance at which the zero position of SA-NSD need to be shifted and the second is to find the distance by which it has to be shifted. Since the objective of SA-NSD is to reduce the large permanent drifts the zero position of NSD is shifted every time the structure undergoes inelastic deformation. The amount by which the zero position of the NSD shift is dependent on the inelastic deformation in the primary structure. Since the assembly drift is same as the inelastic deformation in the primary structure in the case of mild-yielding structure, there is no need to shift the zero position. For heavy yielding structure, say, the inelastic deformation in the structure is u_{id} and u'_y is the apparent yield displacement of the structure then the zero position, u_{zo}, of the

SA-NSD is shifted by a minimum distance of $u_{zo} - u'_y$. For ground motion in which the primary structure yield multiple times in both the directions, the distance by which the zero-position of SA-NSD is displaced will be large. To over come this, the shift in zero-position is set equal to the inelastic deformation in primary structure.

To demonstrate the superior performance of SA-NSD over the passive NSD, simulation results on a SDOF bilinear inelastic structure are presented next. The properties of the SDOF structure used in the simulation study is detailed in section-2.5. Three different systems are compared in the results presented: (1) bilinear inelastic structure (base structure) (2) base structure with passive NSD (3) base structure with semi-active NSD. Five cycles of sinusoidal input with amplitude of 0.16 g and frequency equal to the natural frequency of the structure is used as ground acceleration, shown in Figure 7.13(a). The displacement and acceleration of the structure is compared in Figure 7.13(b,c) for all the three systems. The force deformation behavior of all the three systems is compared in Figure 7.14. The F-D behavior of the assembly with components are shown in Figure 7.15 for passive NSD and in Figure 7.16 for SA-NSD. For the first cycle of input the behavior of passive NSD and SA-NSD are same because the primary structure remained elastic. The response remain the same for the half cycle but the primary structure undergoes inelastic deformation in the second-half of second cycle as a result the response changes beyond 1.6 *sec*, shown in Figure 7.13(b),7.14. After the primary structure yield, in the case of assembly with SA-NSD, the zero-position of the NSD is reset to match the yield displacement as a result the deformation of the structure is significantly reduced compared to the case with passive NSD, shown in Figure 7.14. The reduction in maximum assembly shear and acceleration is the same in the case of both passive and semi-active NSD but the inelastic deformation and assembly drift in the assembly is reduced by more than

70%.

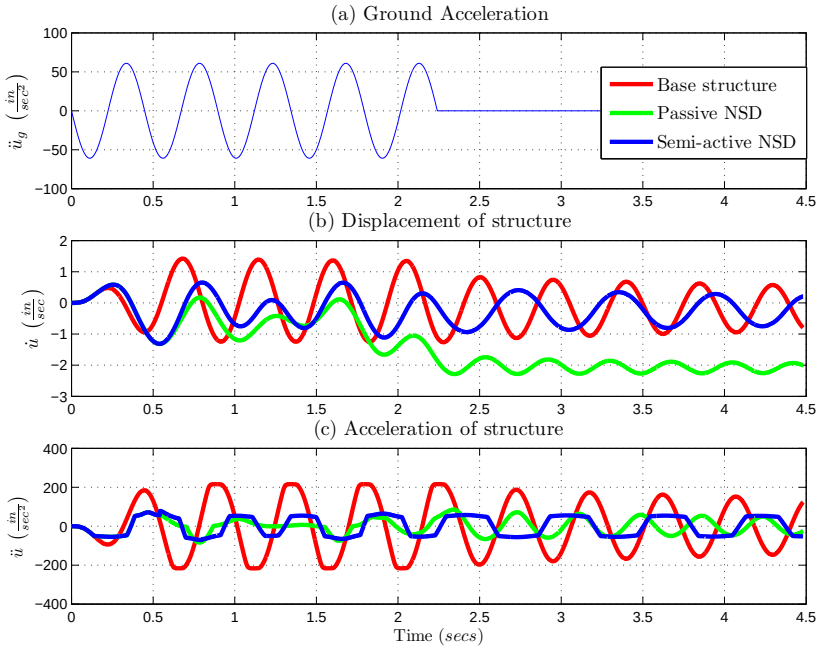

Figure 7.13 : Response comparison of structure with passive and semi-active NSD

7.4 Summary

In this chapter, two novel semi-active approaches are proposed for the NSD to improve the performance of bilinear inelastic structure and NSD assembly. Double-acting hydraulic device is adapted to move the pin connecting the pivot plate and lever arm. In the first approach, the pin is moved in a arc shaped slotted hole. By doing this in real-time any desired force-deformation of the assembly can be achieved. This approach will help fine-tune the F-D behavior of assembly and also to easily accommodate the change in structure properties.

In the second approach, the pin is moved in a vertical slotted hole as a result the zero-position of the NSD will be shifted based on the direction in which the pin is

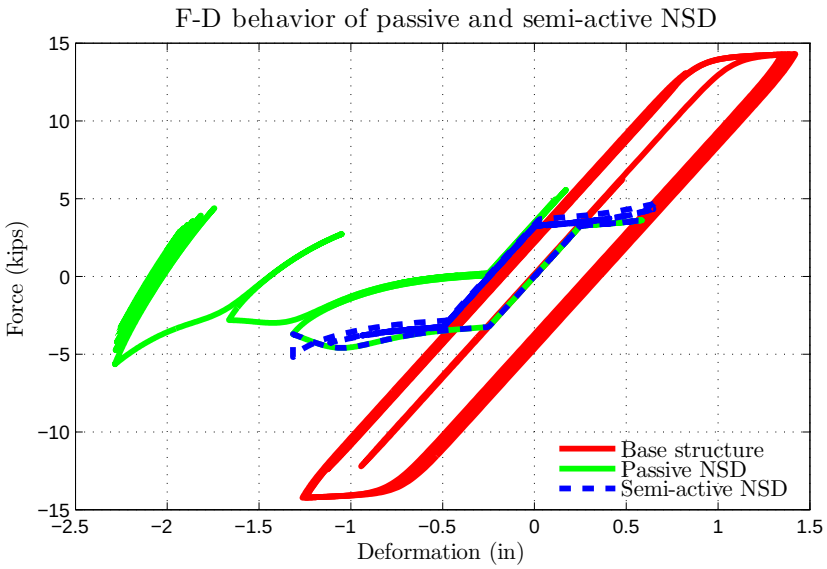

Figure 7.14 : Comparison of the F-D behavior of structure with passive and semi-active NSD

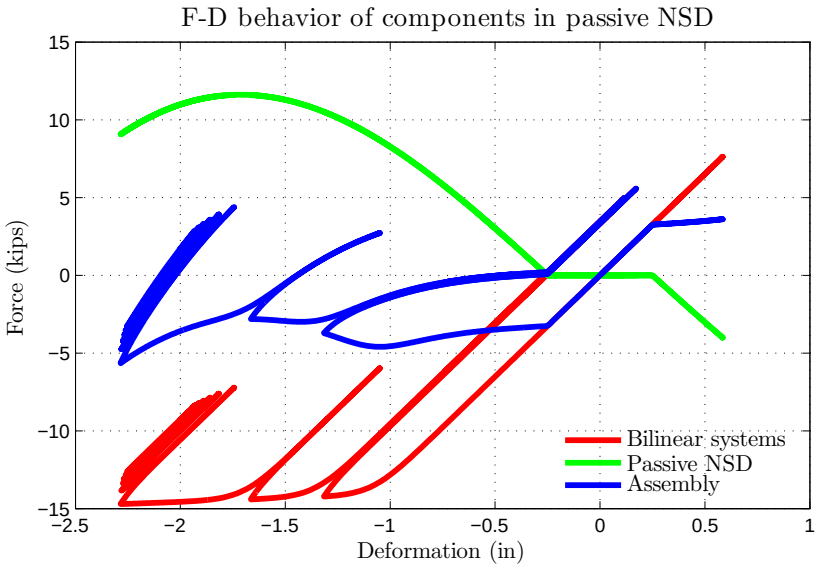

Figure 7.15 : F-D behavior of components in AS with passive NSD

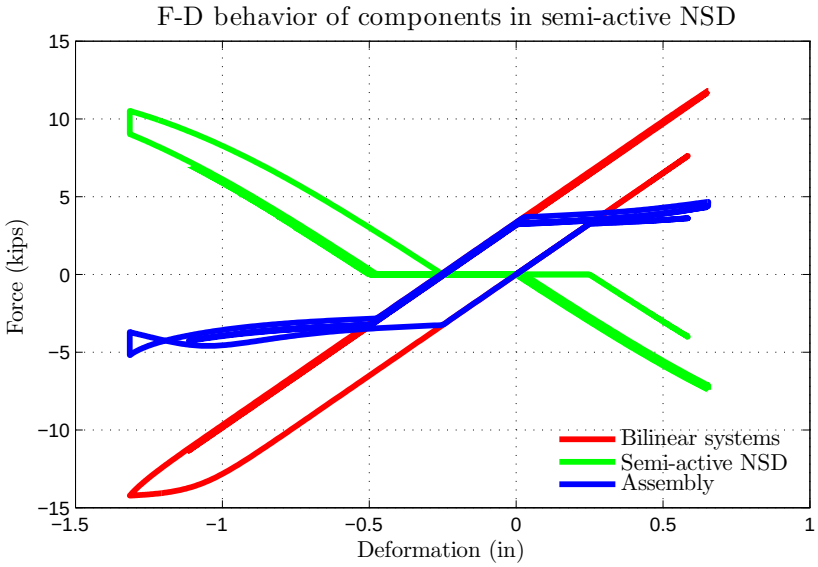

Figure 7.16 : F-D behavior of components in AS with semi-active NSD

moved. The objective of this approach is to overcome the large assembly drifts which are common using a passive NSD. The position of pin is moved every time the primary structure undergo inelastic deformation. The amount by which the zero position of the NSD need to be shifted is dependent on the inelastic deformation in the primary structure. The shift in zero-position of SA-NSD is equal to the inelastic deformation in primary structure. Simulation studies on a SDOF inelastic structure have confirmed that the deformation of the assembly is significantly reduced compared to the case with passive NSD. The reduction in maximum assembly shear and acceleration is same in the case of both passive and semi-active NSD but the inelastic deformation and assembly drift is reduced by more than 70%.

Chapter 8

Adaptive-Length Pendulum (ALP) Tuned Mass Damper (TMD)

The second contribution of this research is in developing a novel passive and adaptive-passive pendulum dampers to control the response of structures. Similar to the NSDs, the objective of the TMD is to mitigate the response of structures, however the working principle of the TMD is quite different from NSD. More details pertaining to the working principle and development of the TMD are given in the forthcoming sections.

The TMD developed in this study is a pendulum damper capable of adjusting the pendulum length in real-time using a shape memory alloy (SMA) wire actuator. Using an instantaneous frequency tracking algorithm, the dominant frequency of the structure can be tracked from a local feedback signal, then the length of pendulum is adjusted to match the dominant frequency. Before explaining the working principle and the experimental results of the developed STMD in detail a brief introduction on the TMDs is given in the next section.

8.1 Tuned Mass Dampers

The tuned mass damper (TMD) is a passive energy-absorbing system [165] consisting of a secondary mass, a spring, and a viscous damper attached to a primary system to reduce undesirable vibrations. The TMD has many advantages compared with other passive damping devices: reliability, efficiency, and low maintenance cost to name

few. Hence in recent years it has been widely used in civil engineering structures [166, 167]. Many researchers have studied the advantages and effectiveness of TMD and have proposed various schemes to improve their robustness and reliability. Most often, in a structure, the first vibrational frequency and mode of the primary system plays a dominant role in the dynamic response. To be effective TMD must remain tuned to the first mode frequency of the original primary system [165].

However, as it is well known, the TMD is very sensitive to even a small change in the tuning, which can be disadvantageous. The use of more than one TMD i.e. multiple TMD (MTMD) [56, 168, 169] with different dynamic characteristics to improve the robustness has been proposed. However, like a single TMD, MTMDs are not robust under variations in both the primary structures natural frequencies and the damping ratio. The use of an active TMD (ATMD) provides one possibility to overcome these drawbacks [170, 171]. ATMD and active mass dampers (AMD) have also been developed and implemented widely for applications in response control [5, 170, 171] of buildings and bridges. ATMD can be more robust to tuning error with the appropriate use of feedback and can be effective in reducing response, but with associated need for application of active forces and substantial power requirement to operate. Semi-active control of TMD [58, 121, 129, 130] and smart tuned liquid column STLD [172] offer an attractive alternative to provide a comparable performance with an order of magnitude less power requirement [129, 131].

The smart TMDs (STMD) and smart MTMDs, developed by Nagarajaiah and coworkers [129, 130], is capable of continuously varying its stiffness and re-tuning its frequency due to real time control, and is robust to changes in building stiffness and damping [114]. In comparison, the passive TMD can only be tuned to the first mode frequency of the building. The building fundamental frequency can change due to

damage or other reasons. The STMDs developed by Nagarajaiah [114] overcomes the limitations of the TMD (i.e. detuning) by retuning the frequency in real time and requires an order of magnitude less power [129, 131]. Due to the shift in paradigm from passive control to adaptive control, smart tuned mass dampers (STMDs) have received considerable attention for vibration control in tall buildings and bridges. STMDs are superior to tuned mass dampers (TMDs) in reducing the response of the primary structure. Unlike TMDs, STMDs are capable of accommodating the changes in primary structure properties, due to damage or deterioration, by tuning in real time based on a local feedback.

STMD can be tuned to the first mode of the primary system or the dominant response frequency (close to a selected mode–usually the first mode), at which the primary system is responding [129], or can be tuned to the dominant excitation frequency [130]. In this study, TMD is tuned to the dominant frequency, at which the primary system is responding, by tracking it using the displacement response of the building. ALP-STMD performance in the presence of real-time primary system stiffness change is studied by Contreras et al. [173].

8.2 Adaptive-passive TMD (APTMD) and Adaptive TMD

The concept of APTMDs and adaptive-TMDs was first introduced by Nagarajaiah [114]. APTMD is a TMD in which a tuning parameter such as frequency is adjusted passively based on some local mechanical feedback (displacement, velocity, rotation, etc.), but without associated sensing and computer feedback needed in a STMD. In adaptive-TMD the tuning parameter is adjusted in real-time using the local mechanical feedback. Also, the concept of adaptive-TMD is further developed in this study and a mechanism to practically implement this method is presented. Systems

with semiactive variable stiffness devices and TMD/APTMD are linear time varying systems (LTV); hence, algorithms are needed for their identification and control. Recently, Nagarajaiah and his coworkers have developed instantaneous frequency tracking control algorithms [114]. In this experimental study, short time fourier transform (STFT) is used for tracking instantaneous frequency from the measured displacement signal.

In this thesis, the development of a new STMD to reduce the vibrations of structures is presented. The new STMD is an adaptive length pendulum (ALP) damper. The length of the pendulum is varied in real time to match the dominant frequency of the structure. A mechanism is developed using shape memory alloy (SMA) actuator, and pulley system to change the length in real time using a DC power supply. The length of the pendulum is adjusted, using a battery, to match the instantaneous frequency calculated using STFT algorithm. Experimental studies are carried on a two-storey scaled model building with ALP-STMD to validate its effectiveness.

This chapter is organized as follows: Section 8.3 presents the STFT time frequency technique. Section 8.4 details the experimental setup and working principle of the proposed ALP-STMD. Section 8.5 contains the experimental results for forced vibration, for free vibration and for non-stationary input (sine-sweep). Experimental results are summarized in section 8.6.

8.3 Real Time Tuning of Adaptive Length Pendulum (ALP) STMD using STFT Control Algorithm

The instantaneous natural frequency of the pendulum, ω, is given by

$$\omega = \sqrt{\frac{g}{L}} \tag{8.1}$$

where, g is acceleration due to gravity, and L is the length of the pendulum. If the length of the pendulum is varied in real time, so does its instantaneous frequency. Pendulum length is adjusted using SMA wire actuator. Thus, the name adaptive length pendulum - smart tuned mass damper (ALP-STMD) and adaptive passive tuned mass damper (APTMD) depending on whether length is controlled in real-time or adjusted passively using mechanical feedback.

8.3.1 STFT control algorithm for real time tuning of ALP-STMD

The fourier transform (FT) of a signal $s(t)$ is given by $s(\omega) = \frac{1}{\sqrt{2\pi}} \int s(t) e^{-j\omega t} dt$. The short-time fourier transform (STFT), the first tool devised for analyzing a signal in both time and frequency, is based on FT of a short portion of signal $s_h(\tau)$ sampled by a moving window $h(\tau - t)$ [174]. The running time is τ and the fixed time is t. Since the time interval is short compared to the whole signal, this process is called the STFT.

$$S_t(\omega) = \frac{1}{\sqrt{2\pi}} \int_{-\infty}^{\infty} s_h(\tau) e^{-j\omega\tau} d\tau \tag{8.2}$$

where $s_h(\tau)$ is defined as follows:

$$s_h(\tau) = s(\tau) h(\tau - t) \tag{8.3}$$

in which $h(\tau - t)$ is an appropriately chosen window function that emphasizes the signal around the time t, and is a function $\tau - t$, i.e., $s_h(\tau) = s(\tau)$ for τ near t and $s_h(\tau) = 0$ for τ far away from t. Considering this signal as a function of τ, the spectrum can be calculated. Since the window has been chosen to emphasize the signal at t, the spectrum will emphasize the frequencies at that time and hence give an indication of the frequencies at that time. In particular, the spectrum is,

$$S_t(\omega) = \frac{1}{\sqrt{2\pi}} \int_{-\infty}^{\infty} s_h(\tau) h(\tau - t) e^{-j\omega\tau} d\tau \tag{8.4}$$

which is the short-time Fourier transform (STFT). The STFT control algorithm [114] is adopted to re-tune the ALP-STMD. STFT controller is effective in both mono-component harmonic excitations, as well as in multicomponent non-stationary earthquake excitations. The instantaneous frequency is identified based on STFT algorithm [114, 175, 176]. The STFT algorithm developed to choose the length of the ALP-STMD is as follows:

1. A moving window is chosen to determine the STFT dominant frequency from the top floor displacement feedback.

2. The dominant frequency, f_d , in each window is identified.

3. If the dominant frequency, f_d, is in the range $0.7f_{p1} < f_d < 1.3f_{p1}$, then $f_{STMD} = f_d$, else go to next step.

4. Set f_{STMD} to the optimum value of f_{TMD}.

Once the dominant instantaneous frequency at which the system is responding is identified, the length of the ALP-STMD is changed to tune to the dominant frequency and maximize the response reduction.

8.4 Experimental Setup

8.4.1 Description of actual structure

A prototype two-storey shear frame is used in this work, with aluminium flats as columns and 0.25 in × 1.5 in steel flats as slabs, as shown in Figure 8.1. The frame is fastened on a shaking table such that the direction of ground motion will cause only in plane motion in the shear frame. The displacement of the frame at floor level is measured using a laser displacement sensor. ALP-STMD is placed on the second-floor. All the results presented in this study are carried with the ALP-STMD at the second-floor level.

Shape memory alloy wire is used to change the length of pendulum in real time. SMAs are smart materials which have the ability to return to a predetermined shape when heated. When an SMA is below its transformation temperature, it has a very low yield strength and can be deformed quite easily upon the application of load. However, when the material is heated above its transformation temperature, it undergoes a change in crystal structure which causes it to return to its original shape. The most common shape memory material, an alloy of nickel and titanium called Nitinol, is used in this experiment. This particular alloy has long fatigue life and high corrosion resistance. Nitinol also has high electrical resistivity which enables it to be actuated electrically by Joule heating. Nitinol SMA wire actuator of 0.010 mm diameter and a transition temperature of 90^o C is used in this research. Preliminary tests indicate 0.69 A current is required to raise the temperature of SMA wire beyond the transition temperature.

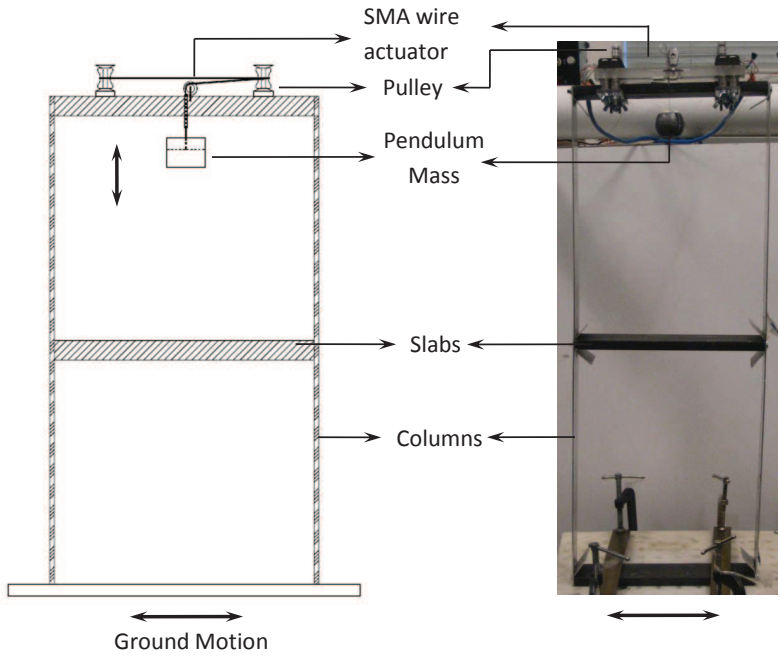

Figure 8.1 : Elevation of two-storey frame. *Left*: Schematic representation. *Right*: Actual setup.

8.4.2 ALP-STMD mechanism

Two rows of pulleys are placed at a spacing of 13 *cm*, aligned in parallel, on the second-floor slab as shown in Figure 8.2. Each pulley is made of steel bearing and it is held intact on the screw using aluminium holders. A provision is made to apply voltage to any of the pulleys independently as shown in Figure 8.2 (bottom). SMA wire is coiled around the pulleys in each row, alternatingly, as shown in Figure 8.2. One end of the SMA wire is fixed and the other end is connected to a mass weighing 8 *oz*. The mass is suspended over a pulley as shown in Figures 8.1, 8.2. Change in overhang length of pendulum can be achieved in two ways:

1. *Changing the current in SMA wire*: By choosing any two specific pulleys, assuming the length of SMA wire coiled between these two pulleys (L_0) produces

enough elongation, changing the amount of current in L_0 will result in a variable length pendulum. In this experimental study, an input current of 0.69 A will result in maximum contraction of the SMA wire and the pendulum mass comes all the way up and sits against the ceiling, this configuration has zero pendulum length and is considered as original structure, shown in Figure 8.3(left). By reducing the amount of current the length of pendulum starts increasing and when there is no current in the wire longest pendulum length is achieved, shown in Figure 8.3(right).

2. *Changing the effective length of SMA wire*: Alternative way to achieve this variable pendulum length is by keeping the current constant and changing the pulleys through which the current is sent. By choosing different pulleys, effective current carrying length of the SMA wire is changed. One limitation of this approach is that it cannot be used to achieve any desired length of pendulum. Only some discrete lengths are achievable, depending on the number of pulleys used in the setup.

The choice of the mechanism depends on many factors like availability of the desired relays to regulate the current, constant-current power supply source and ease of implementation. In this work the first approach is used. Whole length of coiled SMA wire is used and the current through the SMA wire is regulated in real time using a electronic-relay and dSPACE data-acquisition board.

8.5 Experimental Results

As a proof of concept, in this work, the effectiveness of the proposed ALP-STMD is demonstrated for three different input conditions:

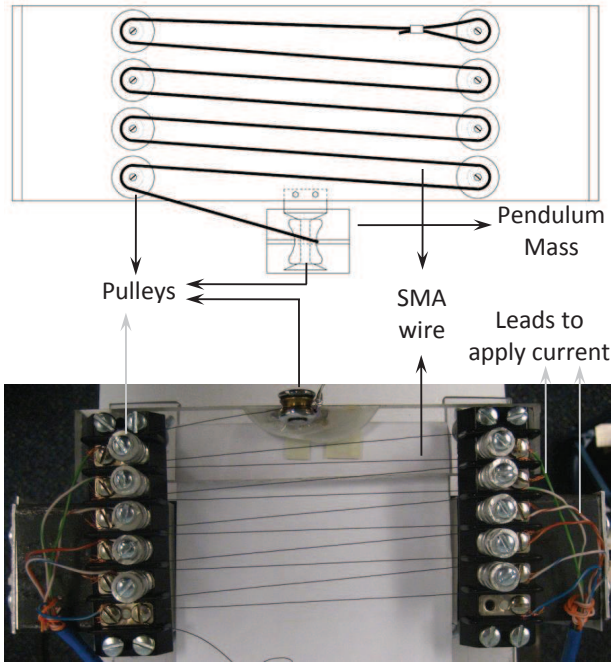

Figure 8.2 : Top view depicting the mechanism to change the length of pendulum in real time. *Top*: Schematic representation. *Bottom*: Actual setup.

1. Steady state response reduction

2. Faster decay of free vibration and

3. Real time response control for a non-stationary input

Displacement response is measured at both first and second-floor level using a laser displacement sensor.

8.5.1 System identification

Using the chirp signal as input and the displacement as output, frequency response functions (FRFs) obtained for the first and second-floor are shown in Figure 8.4. First and second natural frequencies are at 2.341 Hz and 7.09 Hz respectively. The tuning

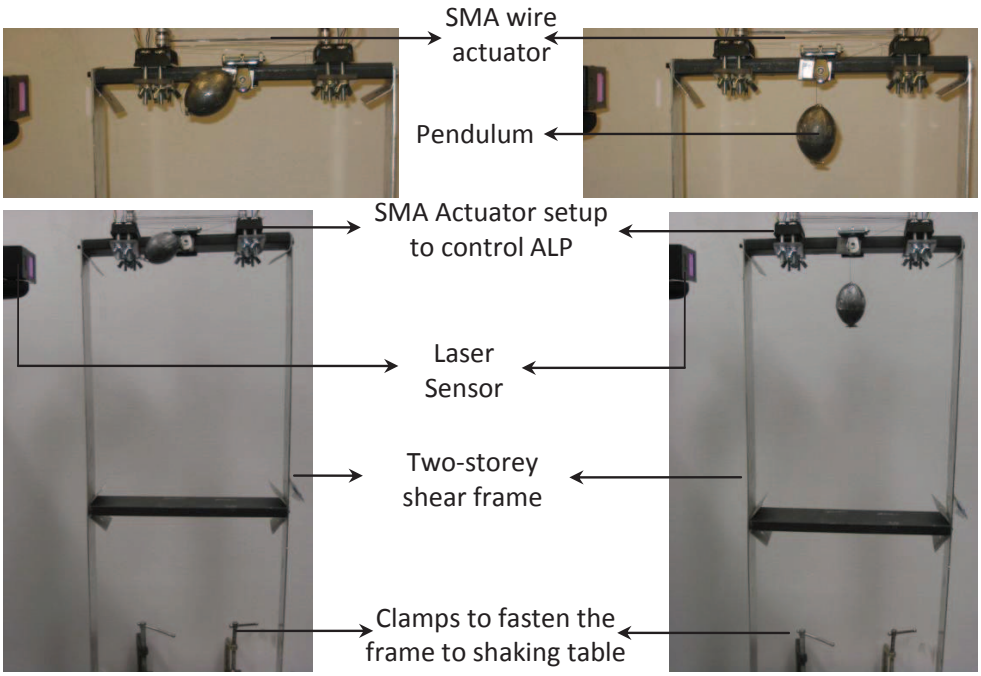

Figure 8.3 : Experimental setup (Elevation of two storey frame): *Left* - Maximum current is sent in the SMA wire and in this position TMD is not engaged; *Left* - Current in the SMA is reduced resulting in a smart pendulum damper

length of pendulum corresponding to each of these frequencies is 4.53 cm and 0.5 cm, respectively. Total length of SMA wire is adjusted such that when there is no current in the SMA wire the overhang length, or the length of the pendulum, is close to 4.53 cm, this configuration will be called as first-mode controlled APTMD from here on. When a current of 0.69 A is applied to the SMA wire the mass will be held all the way up against the ceiling and this is regarded as the original structure (or no TMD). By reducing the current in SMA to 0.51 A the length of the overhang will be 0.5 cm and this is regarded as second-mode controlled APTMD.

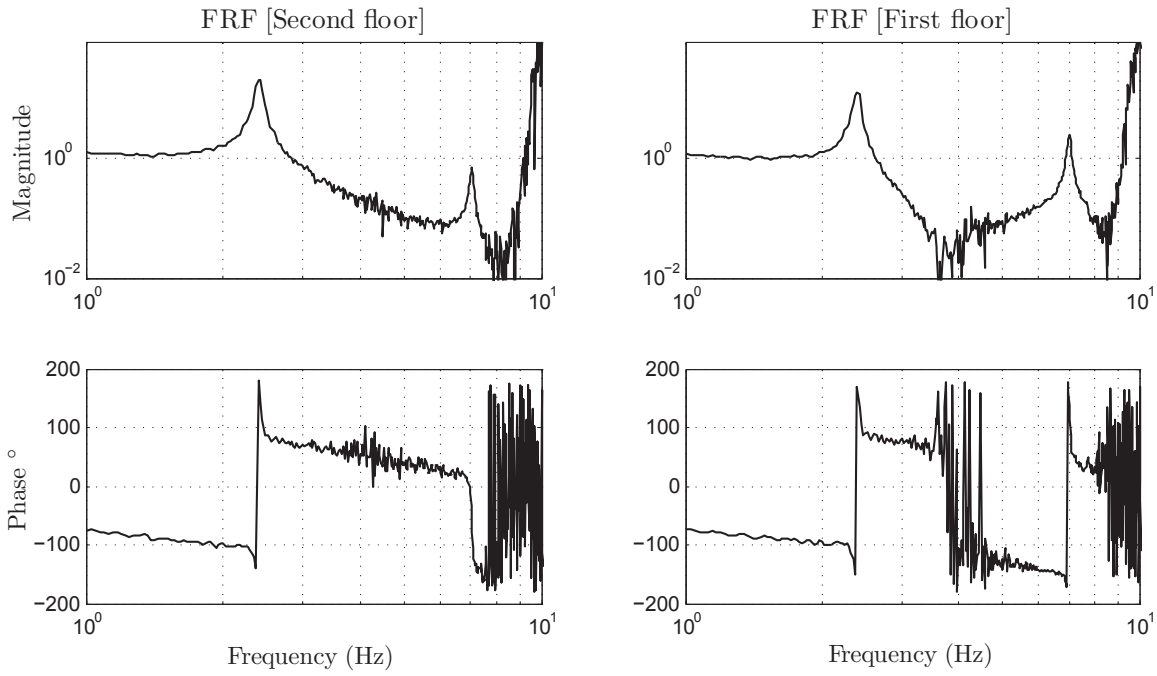

Figure 8.4 : Frequency response function (FRF) of original structure. *Left*: FRF from input to second-floor displacement. *Right*: FRF from input to first-floor displacement

8.5.2 Frequency domain results

All the three configurations, described in section 8.5.1, are subjected to the chirp signal and the FRF magnitude obtained for first and second-floor displacement is shown in Figure 8.5. In Figure 8.5(left) the FRF magnitude of the structure with first-mode controlled APTMD at fundamental frequency (2.341 Hz) is close to 0; where as, the original structure is 12.5 and 21.5 in the first and second floors, respectively. This shows that, when the length of pendulum is tuned with the first-mode the pendulum damper absorbs all the energy corresponding to that frequency. Similarly, from Figure 8.5(right) it can be seen that the FRF magnitude at the first-floor with the second-mode controlled APTMD is 60 % of the original structure.

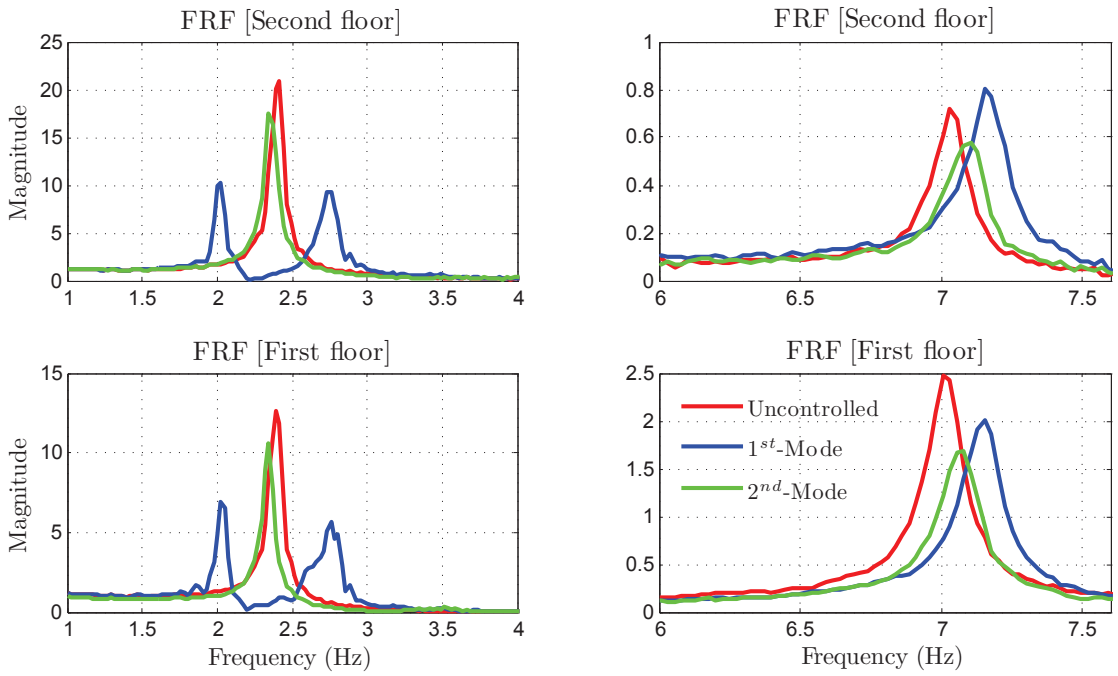

Figure 8.5 : Comparing the FRF magnitude from input to displacement output *Top*: FRF from input to second-floor displacement. *Bottom*: FRF from input to first-floor displacement

8.5.3 Time domain results

Steady state response reduction:

To examine the effectiveness of ALP-STMD as a vibration absorber, two-storey frame is subjected to sinusoidal ground motion and allowed to achieve steady state. After the frame reached the steady state, the pendulum damper is engaged with first-mode length and second-mode length in two different cases; these responses are in turn compared with uncontrolled case.

The second-floor and the first-floor displacement responses when the frame is subjected to sinusoidal excitation at first natural frequency are shown in Figure 8.6(top and middle). ALP-STMD is engaged after 45 seconds as shown in Figure 8.6(bottom).

Since the tuning frequency of the first-mode controlled ALP-STMD and the excitation frequency are matching it gives the optimal control performance. Although there is reduction in response with the second-mode controlled ALP-STMD it is not as effective as the first-mode controlled ALP-STMD, because it is in off-tuned state. This is clear from both the first-floor and second-floor displacement response in Figure 8.6. Similarly, for sinusoidal ground motion at second natural frequency, second-floor and the first-floor displacements are shown in Figure 8.7(top and middle) for all the three configurations and the corresponding plot depicting current variation in ALP-STMD is shown in Figure 8.7(bottom).

It is evident from the Figures 8.6-8.7 that when the excitation frequency matches with the frequency corresponding to the pendulum length substantial reduction in the displacement responses are achieved; this is called tuning condition. Off-tuned reductions have also been observed but they are not as effective as they are in the tuned case. In the tuned-condition the higher percentage reduction in floor displacements is achieved at the second-floor when the structure is subjected to harmonic excitation at first natural frequency, shown in Figure 8.6(top). When the structure is excited at second natural frequency, higher percentage reduction is achieved in the first-floor, shown in Figure 8.7(middle).

Free vibration:

To verify that the ALP-STMD increases the damping of the structure, the two-storey frame is subjected to sinusoidal ground motion, once it reaches the steady state the externally excitation is stopped and it is allowed to vibrate freely until the oscillations die out. At the same instant, when the external excitation is stopped, the ALP-STMD is engaged with first-mode length and second-mode length in two different cases;

these responses are in turn compared with free-vibration results of the uncontrolled structure.

The structure is excited at first natural frequency to reach the steady state and after stopping the excitation, the free vibration displacements of second-floor and the first-floor for all the three configurations are shown in Figure 8.8(top and middle) and the corresponding plot depicting the current variation in ALP-STMDs is shown in Figure 8.8(bottom). Similarly, for the free vibration after exciting the structure at second natural frequency free vibration displacements of second-floor and the first-floor are shown in Figure 8.9(top and middle) and the corresponding plots depicting the current in ALP-STMDs is shown in Figure 8.9(bottom). It is clear from free vibration results that the ALP-STMD increases the damping properties of the structure both in the tuned and off-tuned conditions but the reductions will be slightly higher in the tuned case, shown in Figures 8.8(top) and 8.9(middle).

Non-stationary input:

To show the capability of ALP-STMD to adapt in real time, modified chirp signal is used as ground motion, shown in Figure 8.10(top), to excite both first and second modes of the two-storey frame. Response of the uncontrolled structure is compared with a APTMD tuned to first-mode and an ALP-STMD which is capable of changing the length of pendulum in real-time by tracking the instantaneous dominant-frequency of the structure. Instantaneous frequency of the structure is found by applying STFT algorithm on the second-floor displacement signal.

It can be seen that the input chirp signal has two different amplitudes, at high frequencies larger amplitude is chosen because the higher modes need a large amount of energy to excite. In the APTMD the current is kept constant at 0 A, shown

in Figure 8.10(bottom). In ALP-STMD, before exerting the ground motion on the structure the current in ALP-STMD is 0.69 A (uncontrolled state), then the current is reduced to 0 A after 5 seconds because the instantaneous frequency of structure is close to first natural frequency. Then the length of the pendulum is changed from first mode length to second mode length at 55 seconds by increasing the current in SMA to 0.51 A, shown in Figure 8.10(bottom).

Response of all the three structures is shown in Figure 8.10(middle). Since both the APTMD and ALP-STMD are in tuned-condition from 5 seconds to 55 seconds the large peak observed in the uncontrolled structure at 25 seconds is avoided, shown in Figure 8.10(middle). At 110 seconds, in Figure 8.10(middle), since the APTMD is off-tuned it has higher response compared to ALP-STMD; but, it is still significantly lower than the uncontrolled structure. It is evident from the Figure 8.10 that the ALP-STMD will have all the advantages of passive TMD and additionally, the length of the pendulum can be adjusted in real time resulting in a reduced structural response. Exact trend is observed in the FRF plots shown in Figure 8.11. Both ALP-STMD and APTMD have very low magnitude at first natural frequency, shown in Figure 8.11(left) but ALP-STMD has 50 % less magnitude at second natural frequency, shown in Figure 8.11(right).

8.6 Summary

In this chapter, a novel method to control the response of structural system using adaptive length pendulum smart tuned mass damper (ALP-STMD) is presented. A mechanism to achieve the variable pendulum length is developed using shape memory alloy wire actuator. The effectiveness of the developed ALP-STMDs has been verified through experimental studies. STFT algorithm is used to find the instantaneous

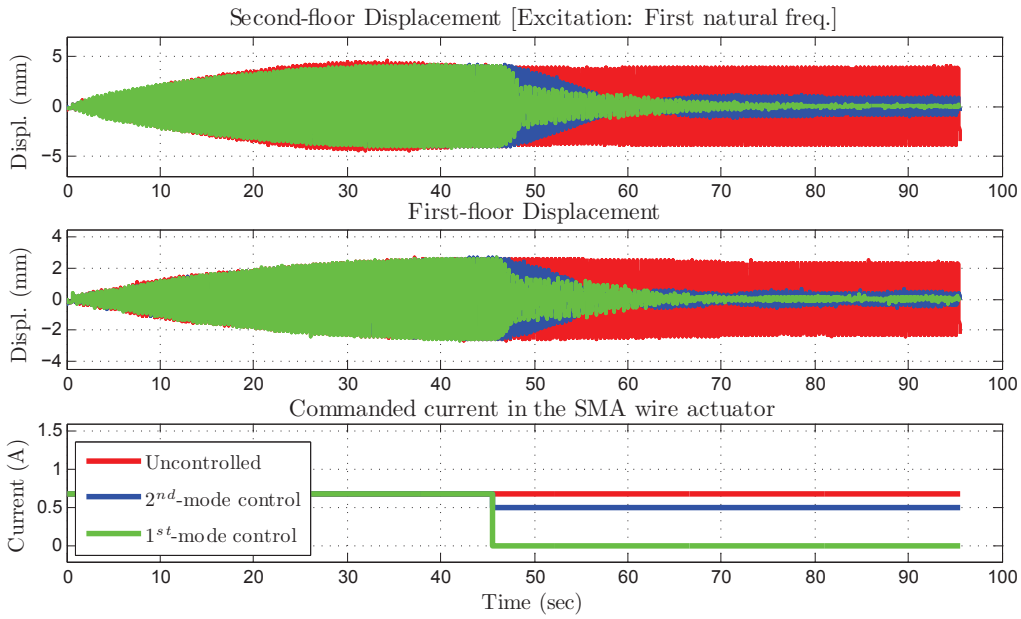

Figure 8.6 : Response of structure for sinusoidal excitation, excited at first natural frequency

frequency of the structure. ALP-STMD acts as a vibration absorber and since the length is tuned to match the instantaneous frequency all the vibrations pertaining to the dominant frequency are absorbed. The performance of the ALP-STMD is verified for forced vibration (stationary and non-stationary) and free vibration. It has been found that the novel ALP-STMD developed in this study is capable of absorbing all the energy pertaining to the tuned-frequency of the system.

APTMD, wherein, the length is adjusted passively (offline) is an ALP-TMD in which the frequency is adjusted by changing the length of pendulum passively without any associated sensing and computer feedback signal. The new ALP-STMD and the APTMD proposed in this study have a great promise for practical implementation.

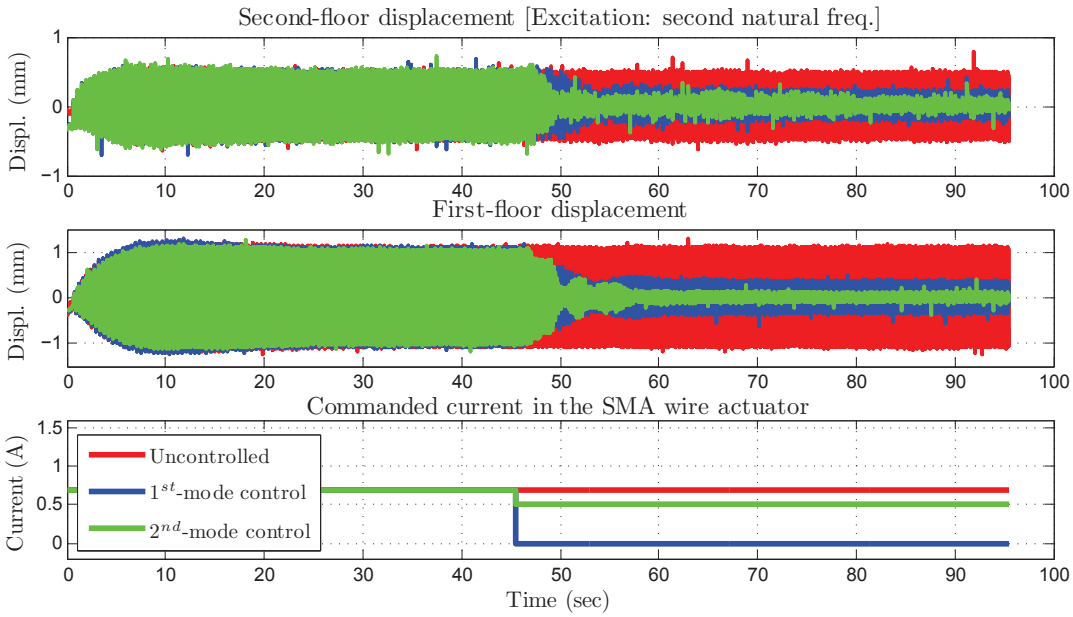

Figure 8.7 : Response of structure for sinusoidal excitation, excited at second natural frequency

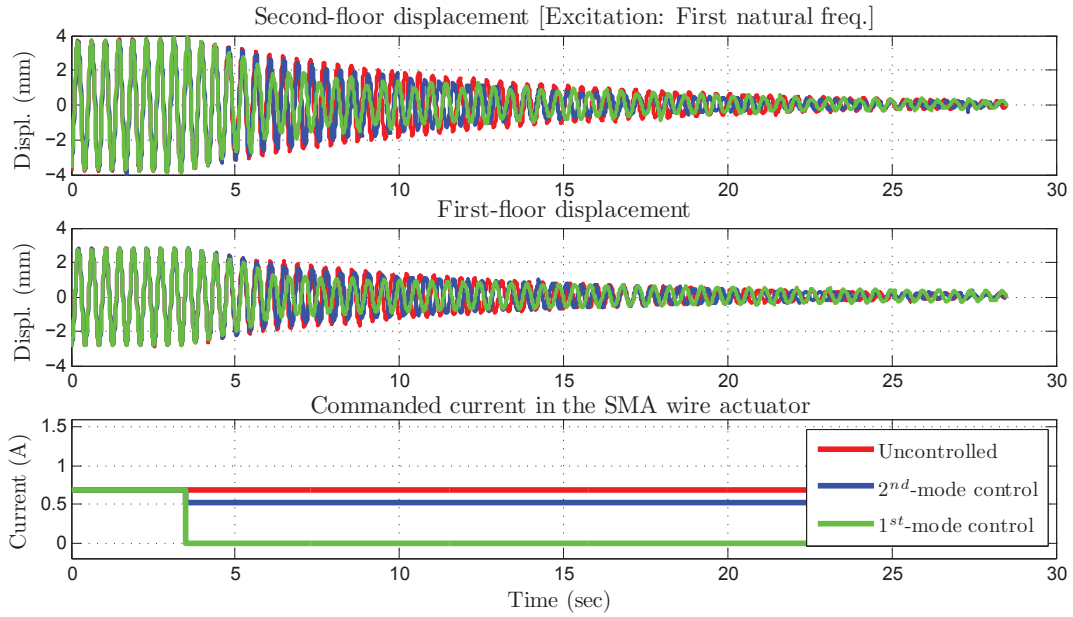

Figure 8.8 : Free vibration response of structure, after exciting system at first natural frequency up to 3 seconds

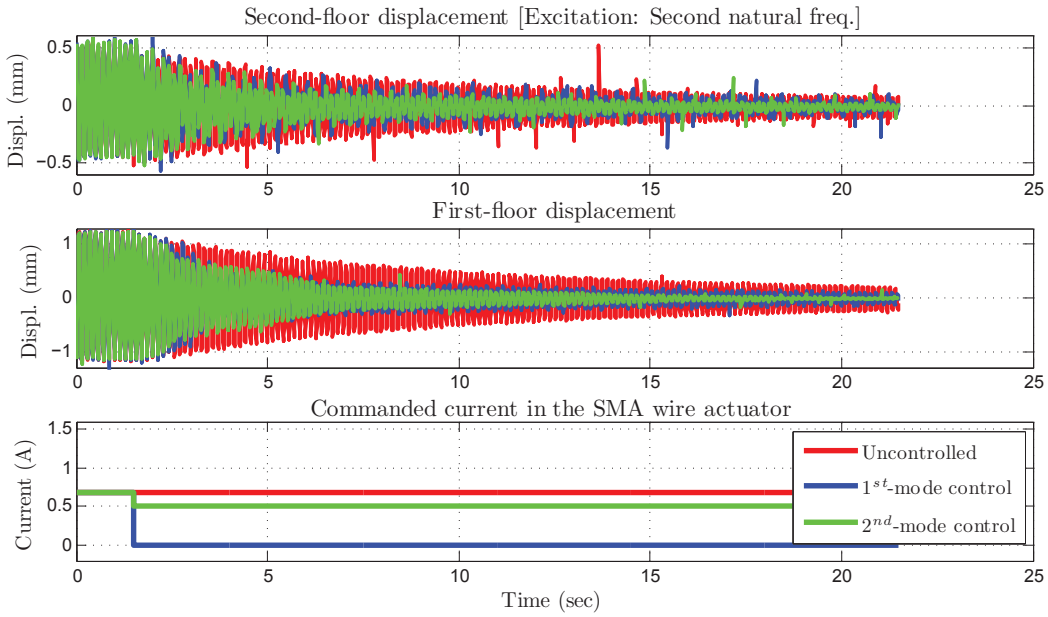

Figure 8.9 : Free vibration response of structure, after exciting system at second natural frequency up to 2 seconds

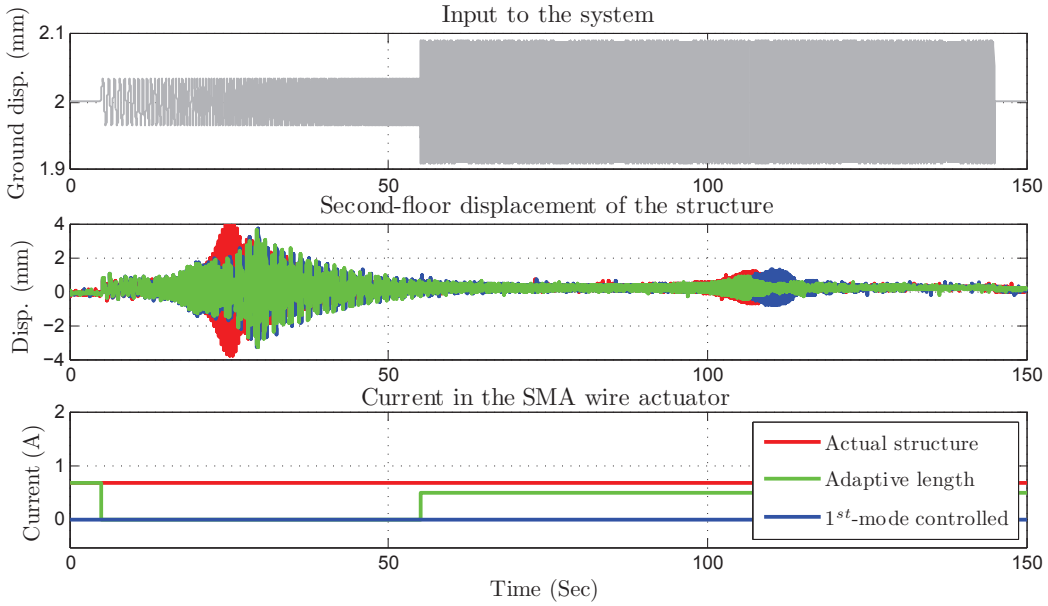

Figure 8.10 : Response of structure, excited using sine-sweep input and displacement measured at second-floor

5

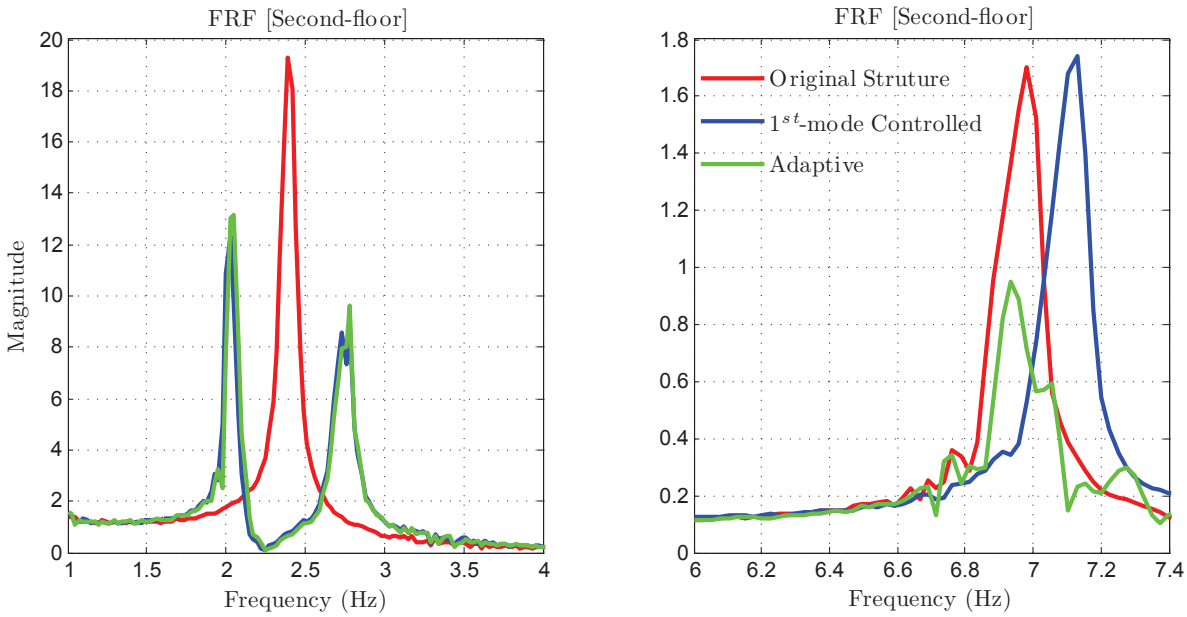

Figure 8.11 : FRF magnitude from input to second-floor displacement, for sine-sweep excitation

Chapter 9

Linear Parameter Varying Gain-Scheduled Controller

Primary focus of this thesis is to develop novel devices to control the response of structures. Since the developed devices are passive and adaptive-passive, control algorithms are not needed to operate these devices. In the case of active control systems, control algorithms play a vital role in the operation. To this end, a novel adaptive control approach to compensate hysteresis in variable-stiffness system is presented in this chapter.

Hysteresis is a very common phenomenon observed in many electromechanical, structural and material systems at macro-, meso-, micro- and nano-scales. Examples of such systems are gear systems, vibrating systems with umbilicals and smart materials like piezoceramic materials, magnetostrictive materials, electro-active polymers, electro-rheological and magneto-rheological fluids [177]. Applications of these smart materials has been growing at a very fast rate in the last decade [178, 179, 180]. However, the hysteresis behavior hinders the ability to exploit the unique properties possessed by these materials such as solid state actuation. This is due to the fact that uncompensated hysteresis can cause a number of undesirable effects including poor performance, steady-state errors, limit cycle behavior and in some cases loss of stability [181, 182, 183].

The most widely accepted approach for control of hysteretic systems is by using inverse compensation in conjunction with a linear controller [184, 185]. The basic idea

of inverse compensation is to use the exact or approximate inverse hysteresis models to cancel the effects of the hysteresis nonlinearity [186]. The dynamics of a plant is represented as a linear term and nonlinear hysteretic term, the controller is designed for the linear part and the nonlinear term in the plant is canceled using the inverse mathematical model [185, 187]. Two well explored and tested examples of inverse compensation are piezoceramic sensors, actuators and magneto rheological dampers [5, 188, 189]. Although the inverse compensation is simple and easy to implement it is effective only if the hysteretic system is either in the beginning or end of a complex system. If the nonlinearity is sandwiched between two dynamic blocks then adaptive inversion methods have to be used [187, 190]. Even with these adaptive inversion schemes this approach suffers from few limitations: the mathematical models assume that the systems with hysteresis have piecewise linear behavior, but this assumption is not true in case of many practical systems. Online adaptive inverse schemes are computationally intensive and also sensitive to experimental errors [189].

A conservative way of compensating hysteresis is by linearizing the hysteresis curve over a range of displacements, resulting in a set of parameter (equivalent stiffness) values over which robust stability and performance must be achieved [191, 192]. Then, a single robust linear time invariant controller can be designed to stabilize the system over a given range of parameter (equivalent stiffness) values. Tradeoff between the range of parameter variation and tracking performance of the closed-loop system limits this approach [193]. Pasala [192] demonstrated through experimental studies that the robust controller can compensate hysteresis in tracking periodic signals. Reported experimental results on thunder-actuator confirmed that repetitive control using a linear time invariant controller is effective for various frequency ranges and tracking amplitudes [192].

A significantly less-conservative approach would be to design a time-varying controller expressed explicitly as a function of system parameters, also called as gain-scheduled (GS) controller [194]. Formulation of feedback control problem as a set of linear matrix inequalities is a significant leap to achieve this objective [195, 196, 197, 198]. Due to the advent of powerful polynomial time computational algorithms, like interior point algorithms, the computational time for calculating controllers has decreased substantially [89].

Previously, Zhang *et al.*[191] have proposed an approach to design a gain-scheduled controller based on the tangential stiffness of vibration isolation system with hysteresis. They assumed that the bounds of parameters are known beforehand and designed two fixed controllers for the plant at the minimum and maximum values of the parameter (tangential stiffness). Then the controller at every instant is calculated by linearly interpolating between the controllers designed for the limiting parameter values. The designed controller is based on constant Lyapunov function which assumes that the parameter variation rate is arbitrarily fast. Such a controller will not be effective for systems with variable stiffness hysteresis properties, which is described in detail next.

Variable stiffness hysteretic systems, shown in Figure 9.1, comprise of a time-varying linear stiffness (slow varying parameter) and stiffness of the friction-hysteresis (fast varying parameter). In this study, both the parameters are considered separately and parameter dependent Lyapunov function is used in designing the gain-scheduled controller. Controller as an explicit function of parameters is calculated from the parameter dependent Lyapunov matrices using projection method. Since the parameter-variation-rate bounds have to be specified for both the parameters separately the designed GS controller will be able to accommodate the different rates

of variation and will be sensitive to even the small variations of the slow-varying parameter which is not possible using the controller proposed by Zhang *et al.*[191]. Both the parameters defined in this study can be calculated in real-time from the measured sensor output. The control objective in this study is to track a reference signal.

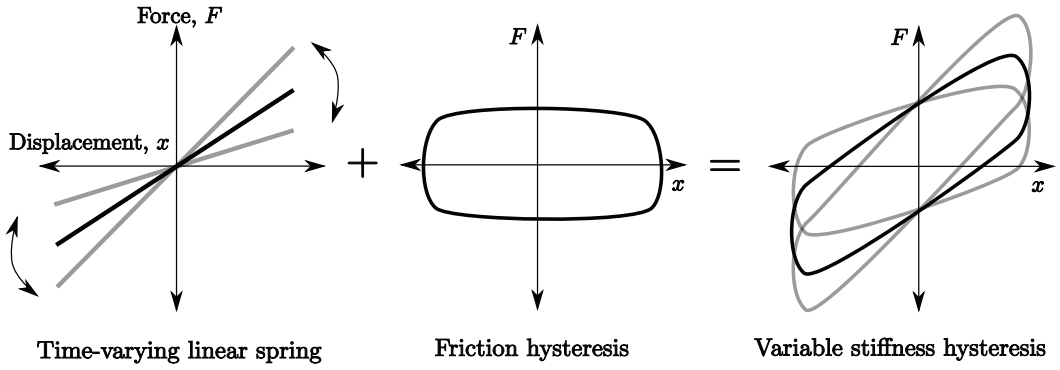

Figure 9.1 : Schematic diagram showing the variable stiffness hysteresis characteristics of SAIVS device [combination of linear time-varying spring and a friction hysteresis]

Using the experimental data, a nonlinear hysteretic model is developed for SAIVS system (Bouc-Wen model). Bou-Wen model, consisting of variable stiffness and hysteresis terms, is represented as a quasi linear parameter varying (LPV) system. GS controller is constructed from the parameter dependent Lyapunov matrices, which are obtained as optimal solutions of linear matrix inequalities (LMIs) that ensures the feasibility solution for closed loop system performance. To demonstrate the effectiveness of proposed gain-scheduled controller, the tracking response results are compared with a fixed robust $\mathcal{H}_\infty$-controller that is designed assuming the parameter variation as an uncertainty.

This chapter is organized as follows: section 9.1,9.2 contains the description of

the SAIVS device, experimental setup and analytical Bou-Wen model for the SAIVS system. Section 9.3 consists of the new formulation showing the representation of Bou-Wen model as a quasi-LPV system. Section 9.4 details the design of gain-scheduled controller using LMI approach. Control objectives, constraints and and closed-loop performance of the fixed robust $\mathcal{H}_\infty$ controller and LPV-GS controller are also presented in section 9.4. Section 9.5 presents the tracking results from the numerical studies performed on the SAIVS system. Finally, the results are summarized in section 9.6.

9.1 SAIVS system

SAIVS system is a spring-mass system where the spring is replaced by SAIVS device [116, 117, 199]. Readers should pay attention to the two different terms used in this chapter: SAIVS-device and SAIVS-system. SAIVS-device is a device which is equivalent to a parallel combination of spring and a friction damper whereas the SAIVS-system is a series connection of SAIVS-device, mass and an actuator. Schematic diagram of SAIVS system is shown in Figure 9.2 and the experimental setup of the SAIVS system is shown in Figure 9.3 (inset of Figure 9.3 shows the schematic diagram of SAIVS-device). A rectangular steel frame is supported on four linear bearings and it is connected to the Modal-50 shaker (actuator) to actuate the frame along "X" direction. The ends of SAIVS device are connected to the frame (joint-2) and the servo-motor (joint-1) such that the stiffness of the SAIVS device can be changed in real-time using the servo-motor; the connection is detailed in the later part of this section. Modal-50 shaker is used as an actuator to exert the control force on the frame. Displacement of the frame along "X"-direction is measured using linear varying displacement transducer (LVDT). The dynamic equation of motion for the SAIVS

system can be written as

$$m\ddot{x} + F_s(t) + F_d(\dot{x}) = F_{ctr}(t) + v(t) \tag{9.1}$$

where $F_{ctr}(t)$ is the force exerted by Modal-50 shaker, $v(t)$ is the external disturbance on the mass, m is total mass of rectangular frame. F_s is the force exerted due to spring deformation and F_d is due to the friction in the elements. Total force $F_s + F_d$ can be measured using the load-cell placed in series between the rectangular frame and the Modal-50 shaker, shown in Figure 9.3.

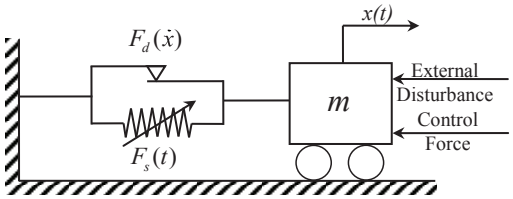

Figure 9.2 : Schematic diagram of the SAIVS system depicted as a combination of variable linear-stiffness element and nonlinear hysteresis element

9.2 SAIVS Device

The SAIVS device was developed originally by Nagarajaiah and coworkers [116, 129, 199]. Schematic of the SAIVS device is shown in the inset of Figure 9.3. The SAIVS device can vary the stiffness continuously and smoothly. The device is controlled by an electric DC servo motor and a controller. The stiffness of the device is a function of its position. The SAIVS device consists of four springs arranged in a rhombus configuration as shown in Figure 9.3. Each spring is located at an angle θ

to the guiding rail (rod that is passing through joint-3 and joint-4). Each of the four springs is supported on the inside by two telescoping tubes, which allow extension and compression of the springs and prevent them from buckling. As shown in Figure 9.3, joint-1 is fixed in the "X"direction and free to move in "Y"-direction. Joint-1 is connected to a LVDT to measure the displacement, $y_L(t)$, in the "Y"-direction. Joint 2 is free to move in "X" and "Y" direction. Joints 3 and 4 can move in "X"-direction only. At any instant the angle θ can be calculated from the voltage reading in the LVDT using Eq. 9.2 [116, 199].

$$\theta(t) = \sin^{-1}\left(c_0 - \frac{y_L(t)}{L_s}\right) \tag{9.2}$$

where, y_L is the LVDT reading, c_0 is a constant and L_s $(4\ in)$ is the length of each spring. Joint-2 is connected to the mass "m". Motion of joint-2 in the "X"-direction is governed by the Modal-50 shaker, but in the "Y"-direction it is allowed to move freely. Force exerted by the SAIVS device on the mass is measured using the load-cell.

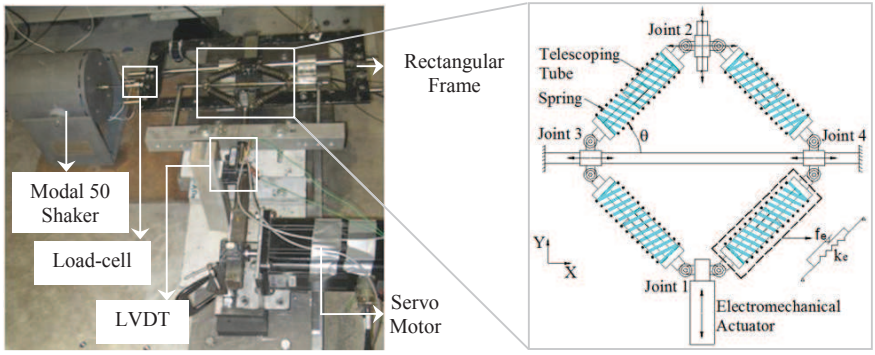

Figure 9.3 : Experimental setup of SAIVS system [Inset: Schematic diagram of the SAIVS device]

9.2.1 Analytical Model for the SAIVS Device

Four springs, shown in Figure 9.3, of SAIVS are modeled as stiffness elements. Each spring element in the device forms an angle θ to the horizontal. This time varying angle $\theta(t)$ is computed using the device position in the "Y"-direction, which can be calculated by measuring the displacement using LVDT attached to joint 1. The device also possesses hysteretic damping because of friction in the telescoping tubes and joints. For more elaborate study on the analytical modeling of SAIVS device, readers are referred to Nagarajaiah *et al.*[117]. So, for any specific position, the restoring force, F_r (measured using the load-cell), in the SAIVS device can be written as

$$F_r\left(t,\dot{x}\right) = F_s\left(t\right) + F_d\left(\dot{x},t\right) \tag{9.3}$$

where, F_s is the restoring force due to the deformation of linear spring, F_d due to the friction in the elements. x, $\dot{x}$ are the relative displacement and relative velocity, respectively, between joints 2 and 1 in the "X"-direction. The spring force, F_s at joint 2 in the "X"-direction is

$$F_s\left(t\right) = K_e \cos^2(\theta(t))x \tag{9.4}$$

where K_e is the stiffness of single spring. The force F_d is given by

$$F_d\left(\dot{x},t\right) = \alpha_f' \cos(\theta(t))z(\dot{x}) \tag{9.5}$$

where α_f' is a constant and z is evolutionary variable [152, 200, 201, 202]. Evolutionary variable (Bouc-Wen model) is dependent on the displacement and is given by

$$\frac{dz}{dx} = \left(\frac{1}{Y} - \frac{|z|^2}{Y}\left(\gamma sgn(\dot{x}z) + \eta\right)\right) \tag{9.6}$$

For the SAIVS device developed, magnitude of F_d is four times smaller than F_s and moreover the variation in $\cos(\theta(t))$ is less than 10% about the mean value. So Eq. 9.5 is further simplified by assuming, $\alpha_f = \alpha'_f \cos(\theta_0)$. Consequently,

$$F_d(\dot{x}) = \alpha_f z(\dot{x}) \tag{9.7}$$

This assumption is essential in order to represent the Bou-Wen model as a simple LPV system from the implementation point of view [197].

9.2.2 Experimental results

SAIVS system experimental setup is developed in structural dynamics lab at Rice University. The measured mass, m, is 10 lbs, stiffness, K_e of each spring is 39 lb/in and the remaining parameters are estimated using an optimization algorithm. $\alpha_f = 1.15$, $\eta = 0.1$, $\gamma_f = 0.9$ and $Y = 0.02in$. Comparison of the analytical hysteresis loops and the experimental hysteresis loops shown in Figure 9.4 and Figure 9.5 indicate good agreement. A series of tests are performed to characterize the dynamic behavior of the device. Two signals are commanded from the data acquisition board: command signal to exert the external force on mass (excitation) and a command signal to change the stiffness of the SAIVS device (switching pattern). The system is subjected to harmonic excitation, using the Model-50 shaker, at an amplitude of 0.25 inches and frequency of 1 Hz in all the tests. Different switching patterns have been tested experimentally for this harmonic excitation input. Experimental loops and predicted analytical loops are shown in Figure 9.4 and Figure 9.5 for two switching patterns: low frequency sinusoidal switching and square switching respectively. Since the frequency of sinusoidal switching (0.325 Hz) is smaller compared to the excitation frequency (1

Hz), the stiffness variation is slow relative to excitation and the hysteresis loops with different linear-stiffness can be seen in Figure 9.4.

The hysteretic behavior due to friction in the telescoping tubes and other connections is evident in both the experimental force-displacement loops. In the experimental plots, the displacement (x-axis) data is measured using the LVDT and the force (y-axis) data is measured using the load-cell.

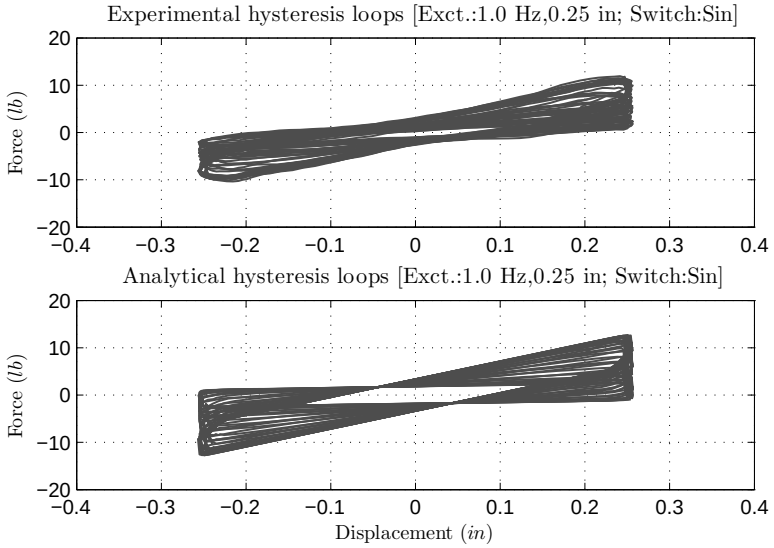

Figure 9.4 : Comparison of the experimental and analytical hysteresis loops of SAIVS system. Stiffness of the SAIVS device is changed using a sinusoidal wave of 0.325 Hz frequency

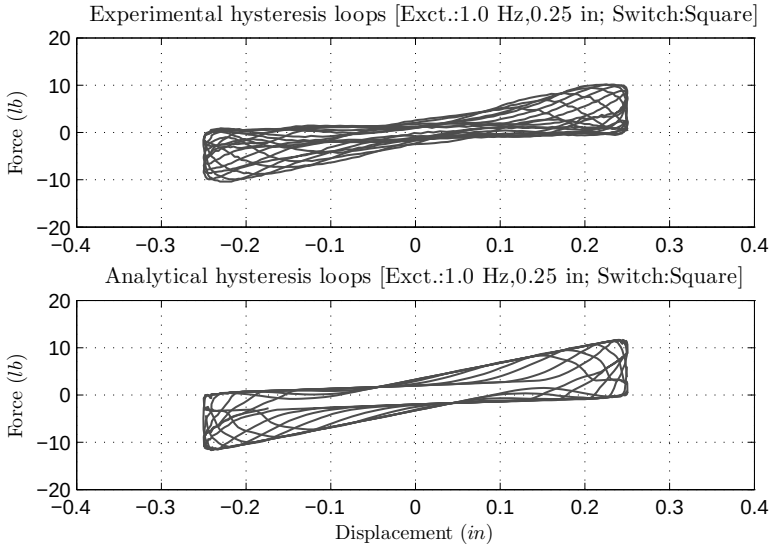

Figure 9.5 : Comparison of the experimental and analytical hysteresis loops of SAIVS system. Stiffness of the SAIVS device is changed using a square wave of 1 Hz frequency

9.3 LPV formulation of the SAIVS system

Equation of motion given in Eq. 9.1 can be represented in state space form by assuming $X_1 = x$ and $X_2 = \dot{x}$ as the two states,

$$\dot{X}_1 = X_2 \tag{9.8}$$

$$\dot{X}_2 = -\frac{K_e cos^2(\theta)}{m} X_1 - \frac{\alpha_f z}{m} + \frac{F_{ctr}}{m} \tag{9.9}$$

Augmenting the system order by assuming $X_3 = -\frac{\alpha_f}{m} z$ will result in a state space realization that is uncontrollable. So, the following term is chosen as the third state

[189]:

$$X_3 = -\frac{\alpha_f}{m} z + \frac{F_{ctr}}{m} \tag{9.10}$$

$$\dot{X}_3 = -\frac{\alpha_f}{m}\frac{\rho_2}{Y} X_2 + \frac{\dot{F}_{ctr}}{m} \tag{9.11}$$

$$\frac{\rho_2}{Y} X_2 = \dot{z} \tag{9.12}$$

The state space representation of approximated SAIVS system as a controllable quasi-LPV system is shown below

$$\begin{bmatrix} \dot{X}_1 \\ \dot{X}_2 \\ \dot{X}_3 \end{bmatrix} = \begin{bmatrix} 0 & 1 & 0 \\ -\frac{K_e \rho_1}{m} & 0 & 1 \\ 0 & -\frac{\alpha_f}{m}\frac{\rho_2}{Y} & 0 \end{bmatrix} \times \begin{bmatrix} X_1 \\ X_2 \\ X_3 \end{bmatrix} + \begin{bmatrix} 0 \\ 0 \\ \frac{1}{m} \end{bmatrix} \times \dot{F}_{ctr} \tag{9.13}$$

$$y = \begin{bmatrix} 1 & 0 & 0 \end{bmatrix} \times \begin{bmatrix} X_1 & X_2 & X_3 \end{bmatrix}^T \tag{9.14}$$

where,

$$\rho_1 = \cos^2(\theta) \tag{9.15}$$

$$\rho_2 = \left(1 - \gamma sign\left(\dot{x}\right) z|z| - \eta z^2\right) \tag{9.16}$$

Since the parameter ρ_2 is state dependent the representation in Eq. 9.13 is called quasi-LPV system. Designed controller is scheduled based on the parameters ρ_1 and ρ_2. Parameter ρ_1 is representative of the linear time-varying stiffness of the spring. Parameter ρ_2 is proportional to the instantaneous stiffness of the friction assembly (compare Eq. 9.6 and Eq. 9.16). At any instant, $\rho_1(t)$ is calculated from $y_L(t)$ using

Eq. 9.2 and Eq. 9.15. ρ_2 is calculated from the load-cell data, F_r, in the following steps:

1. Since $\theta(t)$ is known, $F_s(t)$ is calculated using Eq. 9.4
2. F_d is calculated from F_r and $F_s(t)$ using Eq. 9.3
3. The change of F_d with respect to x is calculated $\left(\frac{dF_d}{dx}\right)$
4. From Eq. 9.7, $\frac{dF_d}{dx} = \alpha_f \frac{dz}{dx}$, $\frac{dz}{dx}$ is calculated
5. ρ_2 is obtained from $\frac{dz}{dx}$ by multiplying with Y

It should be noted that the control force on the right hand side of Eq. 9.13 has a time derivative. Gain scheduled controller is designed for system in Eq. 9.13 so, when the controller is implemented experimentally an integration-operator, $1/s$, has to be added to the plant and the equivalent closed loop system can be visualized as the one shown in Figure 9.6.

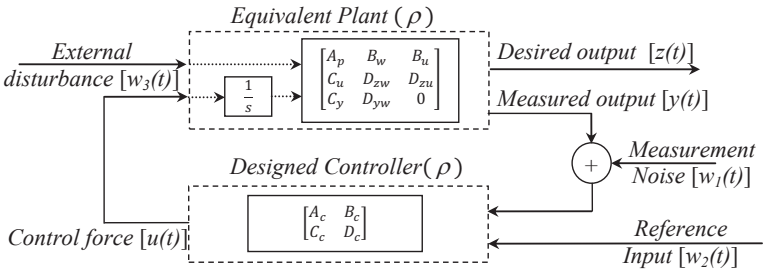

Figure 9.6 : Equivalent closed loop system

9.4 Controller design

Designing a gain scheduled controller for a generalized LPV plant is detailed in this section. It is assumed that the parameter and the parameter-rate is bounded and is known beforehand. Consider a generalized LPV plant:

$$\dot{X} = A_p(\rho)X + B_w(\rho)w + B_u(\rho)u \tag{9.17}$$

$$z = C_z(\rho)X + D_{zw}(\rho)w + D_{zu}(\rho)u \tag{9.18}$$

$$y = C_y(\rho)X + D_{yw}(\rho)w \tag{9.19}$$

where, X is the internal states of the plant, w is the external disturbance, u is the control force, z is the desired output and y is the measured output shown in Figure 9.6. $A_p \in \mathbb{R}^{n_s \times n_s}$, $B_w \in \mathbb{R}^{n_s \times n_d}$, $B_u \in \mathbb{R}^{n_s \times n_u}$, $C_z \in \mathbb{R}^{n_e \times n_s}$, $D_{zw} \in \mathbb{R}^{n_e \times n_d}$, $D_{zu} \in \mathbb{R}^{n_e \times n_u}$, $C_y \in \mathbb{R}^{n_y \times n_s}$ and $D_{yw} \in \mathbb{R}^{n_y \times n_d}$ and time varying parameter $\rho := \begin{pmatrix} \rho_1 & \rho_2 \end{pmatrix}^T$. n_s is number of states, n_d is number of exogenous inputs, n_u is number of outputs from the controller (Control force), n_e is number of desired outputs, n_y is number of measured outputs fed to the controller. Full order LPV gain-scheduled output-feedback controller is assumed to be of form

$$\dot{X}_c = A_c(\rho, \dot{\rho})X_c + B_c(\rho, \dot{\rho})y \tag{9.20}$$

$$u = C_c(\rho, \dot{\rho})X_c + D_c(\rho, \dot{\rho})y \tag{9.21}$$

where, X_c is the states of the controller, $A_c \in \mathbb{R}^{n_s \times n_s}$, $B_c \in \mathbb{R}^{n_s \times n_y}$, $C_c \in \mathbb{R}^{n_u \times n_s}$ and $D_c \in \mathbb{R}^{n_u \times n_y}$. Controller, $\begin{bmatrix} A_c & B_c \\ C_c & D_c \end{bmatrix}$, that satisfies the closed-loop $\mathcal{L}_2$ bound, $\frac{\int_0^t z^T z \, d\tau}{\int_0^t w^T w \, d\tau} \leq \gamma^2$, $\forall t \geq 0$ exist if there exists parameter dependent Lyapunov matrices

$P(\rho)$ and $Q(\rho)$ such that for all pairs of $(\rho, \dot{\rho})$ satisfy the following infinite-dimensional linear matrix inequalities [197]:

$$\left[\begin{array}{cc|c} \mathcal{N}_{P_1}^T & \mathcal{N}_{P_2}^T & 0 \\ \hline 0 & 0 & I \end{array}\right] \left[\begin{array}{cc|c} \hat{P} & PB_w & C_z^T \\ B_w^T P & -\gamma I & D_{zw}^T \\ \hline C_z & D_{zw} & -\gamma I \end{array}\right] \left[\begin{array}{cc|c} \mathcal{N}_{P_1} & 0 \\ \mathcal{N}_{P_2} & 0 \\ \hline 0 & I \end{array}\right] < 0 \tag{9.22}$$

$$\left[\begin{array}{cc|c} \mathcal{N}_{Q_1}^T & \mathcal{N}_{Q_2}^T & 0 \\ \hline 0 & 0 & I \end{array}\right] \left[\begin{array}{cc|c} \hat{Q} & QC_z^T & B_w \\ C_z Q & -\gamma I & D_{zw} \\ \hline B_w^T & D_{zw}^T & -\gamma I \end{array}\right] \left[\begin{array}{cc|c} \mathcal{N}_{Q_1} & 0 \\ \mathcal{N}_{Q_2} & 0 \\ \hline 0 & I \end{array}\right] < 0 \tag{9.23}$$

$$\left[\begin{array}{c|c} P & I \\ \hline I & Q \end{array}\right] > 0 \tag{9.24}$$

where, $\hat{P} = \dot{P} + PA_p + A_p^T P$, $\hat{Q} = -\dot{Q} + QA_p^T + A_p Q$, $\begin{bmatrix} \mathcal{N}_{P_1} \\ \mathcal{N}_{P_2} \end{bmatrix} \in null\left(\begin{bmatrix} C_y & D_{yw} \end{bmatrix}\right)$ and $\begin{bmatrix} \mathcal{N}_{Q_1} \\ \mathcal{N}_{Q_2} \end{bmatrix} \in null\left(\begin{bmatrix} B_y^T & D_{zu}^T \end{bmatrix}\right)$. Aforementioned infinite-dimensional problem is reduced to a finite dimensional problem by gridding the parameter space and ensuring that Eq. 9.22-Eq. 9.24 are valid at all the grid points.

9.4.1 Controller construction using projections method

The controller matrices can be calculated based on the obtained parameter dependent Lyapunov matrices ($P(\rho)$ and $Q(\rho)$) using the following projections method [197]. D_{zu} and D_{yw} have to be full-column and full-row rank respectively to apply this method.

First step is to calculate the matrix D_c such that

$$\sigma_{\max}\left(D_{zw} + D_{zu}D_cD_{yw}\right) < \gamma \tag{9.25}$$

where $\sigma_{\max}$ is the spectral norm. Then, calculate D_{cl}, $\hat{B}_c$, $\hat{C}_c$ and $\hat{A}_c$ using the following equations

$$D_{cl} = D_{zw} + D_{zu}D_cD_{yw} \tag{9.26}$$

$$\begin{bmatrix} 0 & D_{yw} & 0 \\ D_{yw}^T & -\gamma I & D_{cl}^T \\ 0 & D_{cl} & -\gamma I \end{bmatrix} \begin{bmatrix} \hat{B}_c^{\,T} \\ \star \end{bmatrix} = - \begin{bmatrix} C_y \\ B_w^T P \\ C_z + D_{zu}D_cC_y \end{bmatrix} \tag{9.27}$$

$$\begin{bmatrix} 0 & D_{zu}^T & 0 \\ D_{zu}^T & -\gamma I & D_{cl} \\ 0 & D_{cl}^T & -\gamma I \end{bmatrix} \begin{bmatrix} \hat{C}_c \\ \star \end{bmatrix} = - \begin{bmatrix} B_u^T \\ C_zQ \\ \left(B_w + B_uD_cD_{yw}\right)^T \end{bmatrix} \tag{9.28}$$

$$\begin{aligned} \hat{A}_c \;=\; & -\left(A_p + B_uD_cC_y\right) + \begin{bmatrix} PB_w + \hat{B}_cD_{yw} & \left(C_z + D_{zu}D_CC_u\right)^T \end{bmatrix} \\ & \cdot \begin{bmatrix} -\gamma I & D_{cl}^T \\ D_{cl} & -\gamma I \end{bmatrix}^{-1} \begin{bmatrix} \left(B_w + B_uD_cD_{yw}\right)^T \\ C_zQ + D_{zu}\hat{C}_c \end{bmatrix} \end{aligned} \tag{9.29}$$

Using the variables calculated from (9.26-9.29), the controller state space matrices A_c, B_c and C_c can be calculated using the following equations

$$A_c = N^{-1}\left(\hat{A}_c - P\left(A_p - B_uD_cC_y\right)Q - \hat{B}_cC_yQ - PB_u\hat{C}_c\right)M^{-T} \tag{9.30}$$

$$B_c = N^{-1}\left(\hat{B}_c - PB_uD_c\right) \tag{9.31}$$

$$C_c = \left(\hat{C}_c - D_c C_y Q\right) M^{-T} \tag{9.32}$$

where, N and M are calculated based on the guidelines suggested by Apkarian and Adams [197] from the practical implementation point of view. Assuming $P = P(\rho)$ and $Q = Q_0$ where Q_0 is constant (independent of parameter). N and M can be obtained from P and Q using the following selection, $N := I - P(\rho)Q_0$ and $M := I$. Parameter dependent Lyapunov matrices assumed in this study are of the following form:

$$P(\rho) = P_0 + P_1\rho_1 + P_2\rho_2 \tag{9.33}$$

$$Q(\rho) = Q_0 \tag{9.34}$$

where, P_0, P_1, P_2 are Q_0 are constant matrices that ensure the stability of the closed-loop system and also result in optimal $\mathcal{H}_\infty$-norm of the closed-loop system. These matrices are calculated from (9.22-9.24).

9.4.2 Control Objectives and Constraints

The main objective of designed closed loop system is to track the commanded input. Numerically, the performance objective is specified in terms of the ratio of induced $\mathcal{L}_2$ norm. Optimal controller is obtained by minimizing the energy-to-energy norm from disturbance signal to the error signal. Additional specifications includes:

1. **Control constraint:** Assuming there is actuator saturation, control effort exerted should be limited and should not exceed a predefined value. In this case $|F_{ctr}| < 4\ lb$

2. **Performance objectives:** Settling and overshoot have to be minimized. This is governed by the choice of frequency dependent weighting functions or penalty

functions.

3. **Noise rejection:** Impact of measurement noise on the desired objective has to be minimized.

4. **Robustness specifications**: Stability and tracking performance of closed-loop system has to be ensured for different switching cases of SAIVS

To find the optimal controller, $\mathcal{H}_\infty$-norm of the closed-loop system, specified as a ratio of induced $\mathcal{L}_2$ norms of weighted desired-outputs to the exogenous inputs, has to be minimized [203, 204]. To design a fixed and robust $\mathcal{H}_\infty$ controller, only the nominal plant is used [205]. Robust-$\mathcal{H}_\infty$ controller will be referred as just $\mathcal{H}_\infty$ controller from hereon. LPV gain scheduled controller is calculated for the SAIVS system using the approach proposed by Apkarian and Adams [197]. First, parameter dependent Lyapunov matrices that minimize the $\mathcal{H}_\infty$-norm of the closed loop systems are calculated then the state space matrices of the controller are calculated using Eq. 9.30-Eq. 9.32.

Block diagram of the closed-loop LPV-GS controller with all the interconnections is shown in Figure 9.7. To design the LPV-GS plant state space equations have to be augmented by incorporating the other exogenous inputs, measurement noise ($n(t)$, $h(t)$ and $j(t)$) and reference signal ($r(t)$), and the frequency dependent weights, W_e, W_u, W_j, W_h, W_n, W_r and W_x, as shown in Figure 9.7. For the analytical model calculated in previous section, fixed robust $\mathcal{H}_\infty$ controller is designed by choosing nominal values for the parameters ρ_1 and ρ_2 and the parameter variation is represented as an uncertainty.

$r(t)$ is the reference displacement to be tracked. $n(t)$, $h(t)$ and $j(t)$ are the experimental noise signals in measuring x, y_L and F_d respectively. $W_n(s)$ is the weight

function for measurement noise of x, $W_h(s)$ is the weight function for measurement noise of y_L, $W_j(s)$ is the weight function for measurement noise of F_d, $W_r(s)$ is the weight function for reference input, $W_u(s)$ is the weight function for control input, $W_e(s)$ is the weight function for tracking error and $W_x(s)$ is the weight function for the plant output. $z_1 = W_x x$ is the weighted output, $z_3 = W_e e$ is the weighted error signal and $z_2 = W_u \dot{F}_{ctr}$ is the weighted control force. S and R in Figure 9.7 represents the blocks to calculate the parameters ρ_1 (using Eq. 9.2 and Eq. 9.15) and ρ_2 (using Eq. 9.4, Eq. 9.3, Eq. 9.6 and Eq. 9.16) from the measured experimental data. The exogenous inputs acting on the system are $[r(t), n(t), h(t), j(t)]^T$ and the desired outputs to be minimized are $[z_1(t), z_2(t), z_3(t)]^T$. Frequency dependent weights are chosen to reflect the performance objectives and control constraints [206, 207]. W_p should have a pure integrator in it but to avoid the computational problems in finding the controller in MATLAB [208] $W_p = \frac{1}{s+0.0001}$ is chosen.

The Bouc-Wen model, representing friction, in Eq. 9.6, is highly nonlinear and represents a stiff-differential equation. For this reason the closed-loop response of the hysteretic system is calculated using adaptive, variable time-step solvers. Since these solvers are not supported in the data-acquisition system used in the experimental setup, described in section 9.2.2, the developed controller could not be implemented experimentally. Only the numerical results are presented from hereon.

9.4.3 Closed-loop performance

To show the effectiveness of LPV GS controller, bode plots of closed-loop transfer function (for a set of frozen parameter values) from reference-signal to output $x(t)$ for a closed loop system with fixed robust $\mathcal{H}_\infty$ controller (designed for nominal plant) and LPV-GS controller at various parameter grid points are shown in Figure 9.8 and

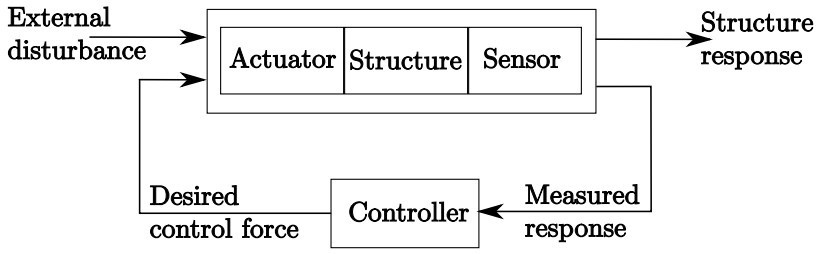

Figure 9.7 : Augmented closed loop block diagram with detailed interconnections for LPV-GS Controller

Figure 9.9 respectively. ρ_1 has grid points at [0.15 0.3 0.45 0.6] and ρ_2 has grid points at [0.1 0.5 0.9 1.3 1.7]. Ideal Bode plot for tracking control should have a flat end at 0 dB for low frequencies and should roll off with a steep slope at high frequencies to have good noise rejection attributes. The frequency dependent weights are chosen in such a way that this objective is achieved.

Results shown in Figure 9.8 and Figure 9.9 are for a set of frozen parameter values. These plots do not depict the behavior of the system for time-varying parameters. From the plots shown in Figure 9.8 it can be seen that fixed-$\mathcal{H}_\infty$ controller is effective only when the uncertain plant parameters are close to the nominal plant parameters. Magnitude of the closed-loop system with $\mathcal{H}_\infty$ controller varies from -50 dB to 25 dB and the phase fluctuates between -180° and 180° for frequencies less than 10 rad/sec. Where as in the case of LPV-GS controller, shown in Figure 9.9, the performance of the closed-loop system is very consistent and the Bode plots for all the sets of parameters have a flat end till 20 rad/sec frequency. This shows the effectiveness of the gain-scheduled controller.

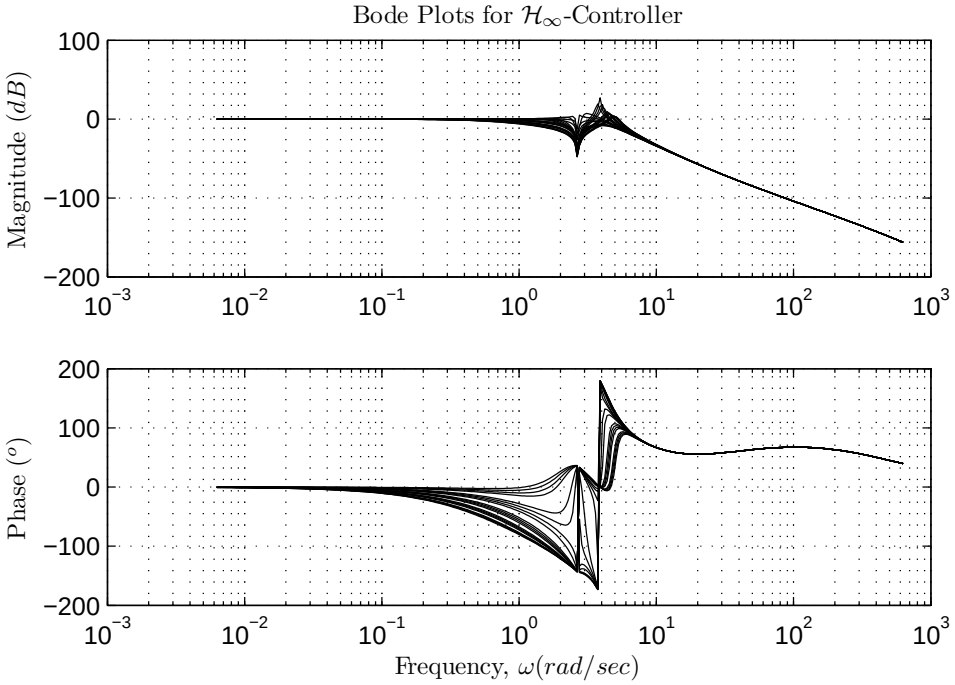

Figure 9.8 : Frozen parameter bode plots of $\mathcal{H}_\infty$-controller: Transfer function from reference to output

9.5 Simulation results

The key difference between the robust $\mathcal{H}_\infty$ controller and the LPV-GS controller is that the $\mathcal{H}_\infty$ controller will not be able to adapt to the change in system properties. Closed-loop system with $\mathcal{H}_\infty$ controller will be stable only for small parameter variations around the nominal plant parameters. Whereas the LPV-GS controller is consistently effective for all the parameter variations by taking into account the change in system properties and accommodating into the controller in real time. To emphasize more on this point, the performance of both the controllers for ramp SAIVS switching and three pulses of square wave tracking input is calculated. Tracking performance of both the controllers is shown in Figure 9.10. In case of $\mathcal{H}_\infty$ controller

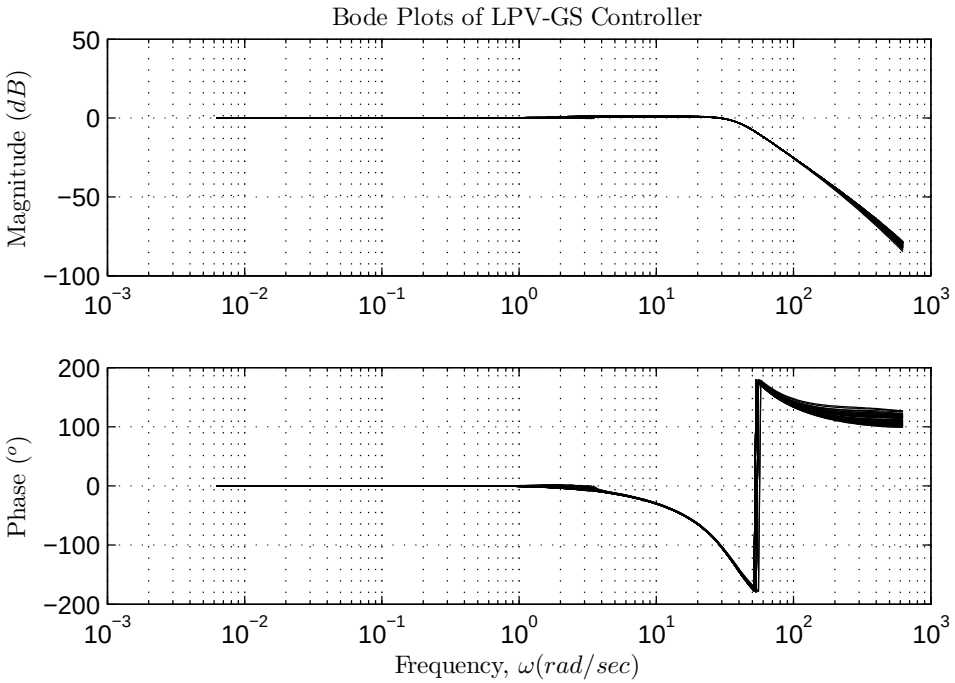

Figure 9.9 : Frozen parameter bode plots of LPV-GS controller: Transfer function from reference to output

response, the performance keeps deteriorating for the subsequent cycles unlike the LVS-GS response which is consistent. Since the $\mathcal{H}_\infty$ controller is designed for the parameters at $t = 0$, as the system parameters drift away from the nominal plant the performance of the closed-loop system with $\mathcal{H}_\infty$ controller deteriorates. This is more evident from the tracking error plot shown in Figure 9.11(top). Control force exerted by the actuator is shown in Figure 9.11(bottom). For further variation in the linear stiffness of the SAIVS device, beyond 900 *sec*, the closed-loop system with $\mathcal{H}_\infty$ controller becomes unstable for subsequent cycles. It should be noted that the actual force rate calculated from the LPV-GS controller is $\dot{F}_{ctr}$ from which the control force F_{ctr} is obtained.

Linear stiffness of the SAIVS device is decreased from 11.4 lb/in to 4.7 lb/in in 900 seconds using the servo-motor. Change in SAIVS angle, θ, is shown in Figure 9.12(top,left) and Figure 9.13(top,left) for systems with $\mathcal{H}_\infty$ controller and LPV-GS controller respectively. Parameter-ρ_1, calculated using θ, is shown in Figure 9.12(top,right) and Figure 9.13(top,right). Frictional force measured is shown in Figure 9.12(bottom,left) and Figure 9.13(bottom,left) for systems with $\mathcal{H}_\infty$ controller and LPV-GS controller respectively. Parameter-ρ_2 calculated is shown in Figure 9.12(bottom,right) and Figure 9.13(bottom,right). For the same desired tracking reference signal and ρ_1, the frictional force, F_d (consequently, ρ_2) is quite different for closed-loop system with $\mathcal{H}_\infty$ controller and LPV-GS controller. This is due to the difference in the working principle of the controllers. Since the LPV-GS controller is scheduled based on the parameter ρ_2, the control input is dependent on the time-history data of ρ_2 and vice-versa. Whereas in the case of $\mathcal{H}_\infty$ controller control input is only influenced by the tracking error.

Hysteresis loops of closed loop systems are shown in Figure 9.14. From Figure 9.14 it can be clearly seen that LPV-GS controller is very effective in controlling systems with variable hysteresis. Since the linear stiffness of the system is dropping the hysteresis loops in Figure 9.14 are tilting in the clockwise direction. Hysteresis loops of closed-loop system with $\mathcal{H}_\infty$ controller are wider because of the high overshoot. The key observations that can be made from the Figure 9.10 through Figure 9.14 are listed below

1. LPV-GS controller has smaller settling time and overshoot compared to $\mathcal{H}_\infty$ controller.

2. Performance of closed-loop system with $\mathcal{H}_\infty$ controller is sensitive to system

parameters, unlike the LPV GS controller.

3. LPV-GS controller is capable of handling the change in system parameters by updating the controller.

4. $\mathcal{H}_\infty$ controller becomes unstable for large variations in linear stiffness of the SAIVS device.

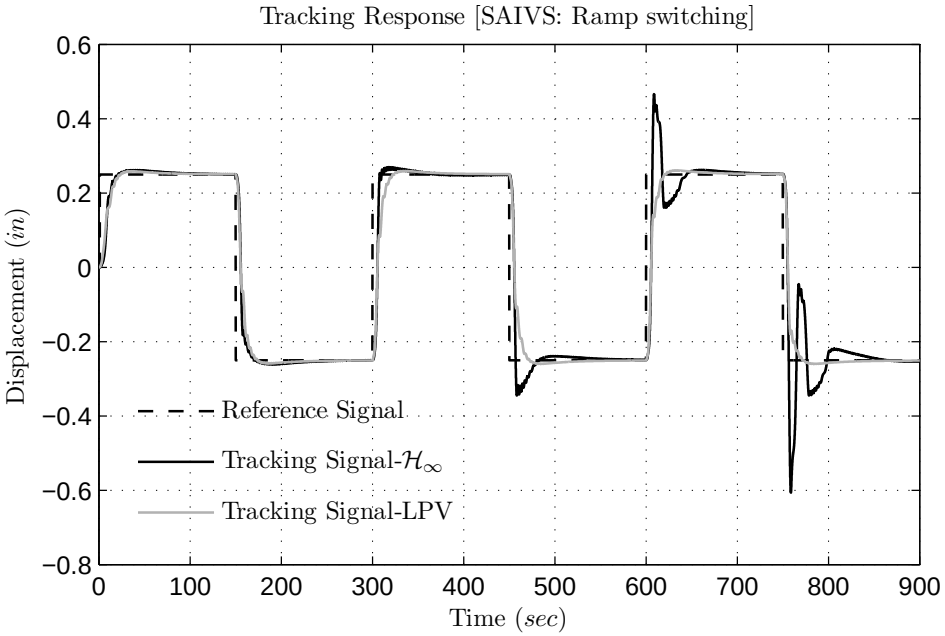

Figure 9.10 : Tracking response of closed loop SAIVS system to step input using LPV-GS controller and $\mathcal{H}_\infty$ controller in presence of ramp SAIVS switching

9.6 Summary

In this study, hysteretic system with variable stiffness hysteresis is represented as a quasi-linear parameter varying system. A gain scheduled controller is designed for

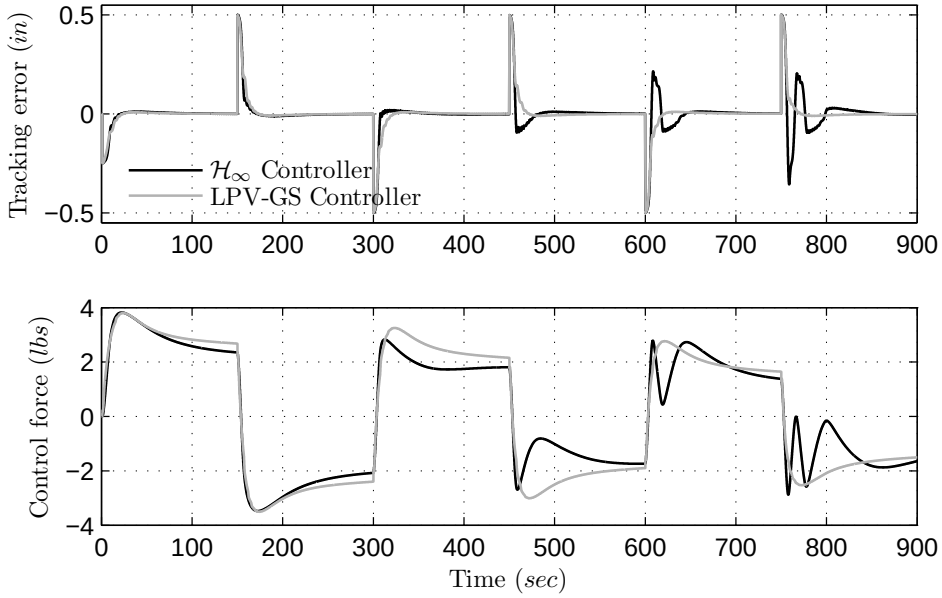

Figure 9.11 : Comparison of (a) Tracking error of closed loop SAIVS system (b) Control effort exerted by the actuator, using LPV-GS controller and $\mathcal{H}_\infty$ controller in presence of ramp SAIVS switching

the quasi-LPV system using LMI approach. Designed controller is scheduled based on two parameters: linear time-varying stiffness (slow varying parameter) and the stiffness of friction hysteresis (fast varying parameter). Gain-scheduled controller is constructed from the parameter dependent Lyapunov matrices, which are obtained as optimal solutions of linear matrix inequalities that ensures the feasibility solution for closed loop system performance.

To show the effectiveness of the proposed controller numerical studies are carried out comparing the proposed controller with fixed robust $\mathcal{H}_\infty$ controller. Tracking performance of the system using both the controllers is verified for different switching cases and for different amplitudes of tracking displacements. Superior performance of the LPV-GS over the robust $\mathcal{H}_\infty$ controller in different displacement ranges is

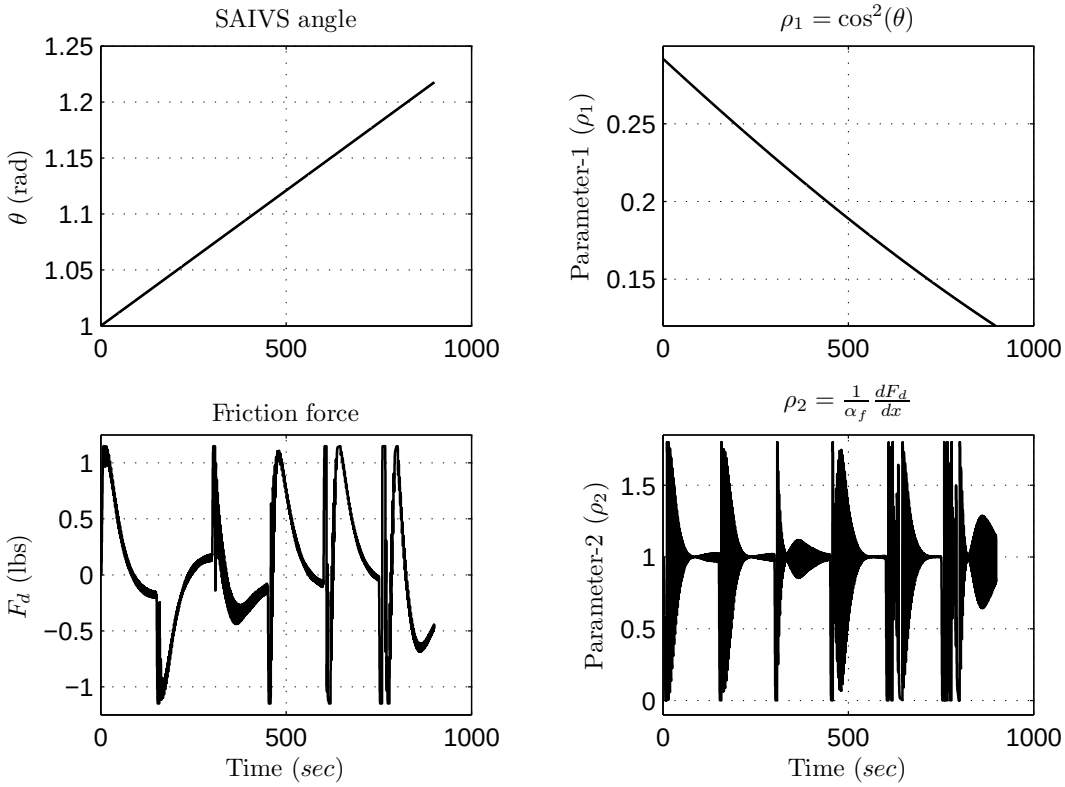

Figure 9.12 : Parameter variation in closed-loop tracking using $\mathcal{H}_\infty$ controller in presence of ramp SAIVS switching. (Top,left): SAIVS angle, θ; (Top,right):ρ_1; (Bottom,left):Friction force, F_d; (Bottom,right):ρ_2

clearly evident from the reported results. Robust $\mathcal{H}_\infty$ controller is effective only when the system parameters are in the vicinity of the nominal plant parameters for which the controller is designed. The LPV-GS controller is capable of adapting to the parameter changes and is effective over the entire range of parameter variations. For large parameter variations, the robust $\mathcal{H}_\infty$ controller becomes unstable whereas the LPV-GS will ensure stability and guarantee the desired closed-loop performance.

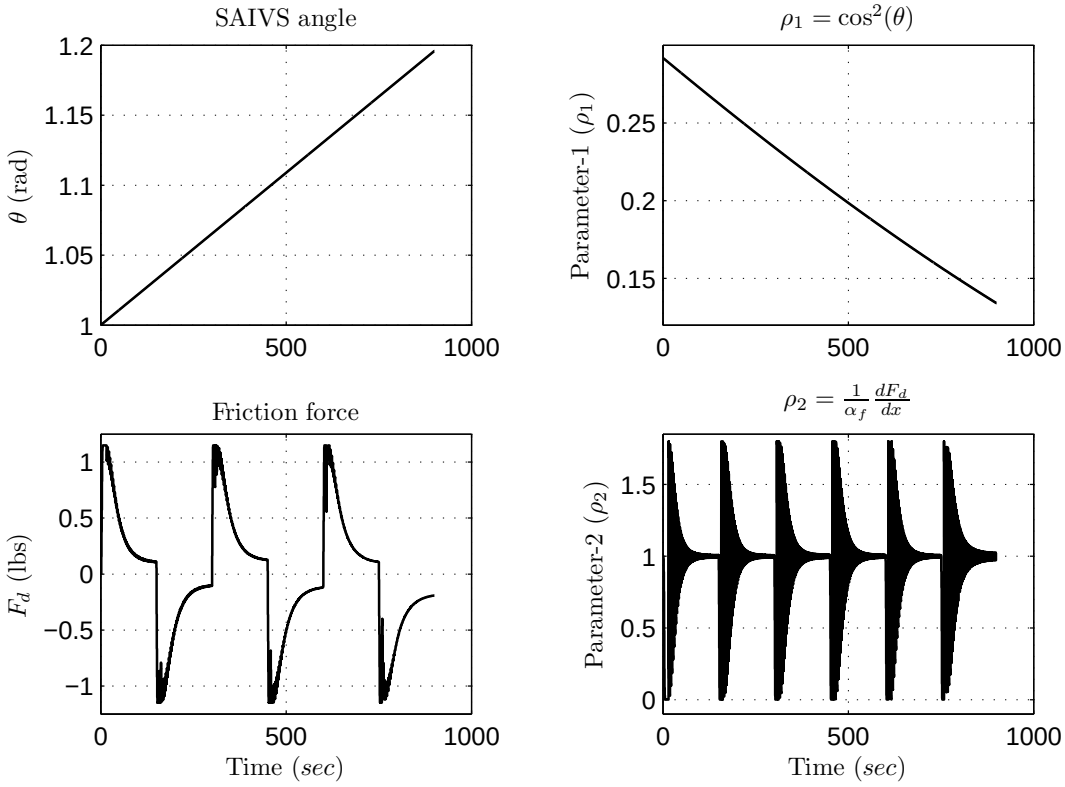

Figure 9.13 : Parameter variation in closed-loop tracking using LPV-GS controller in presence of ramp SAIVS switching. (Top,left): SAIVS angle, θ; (Top,right):ρ_1; (Bottom,left):Friction force, F_d; (Bottom,right):ρ_2

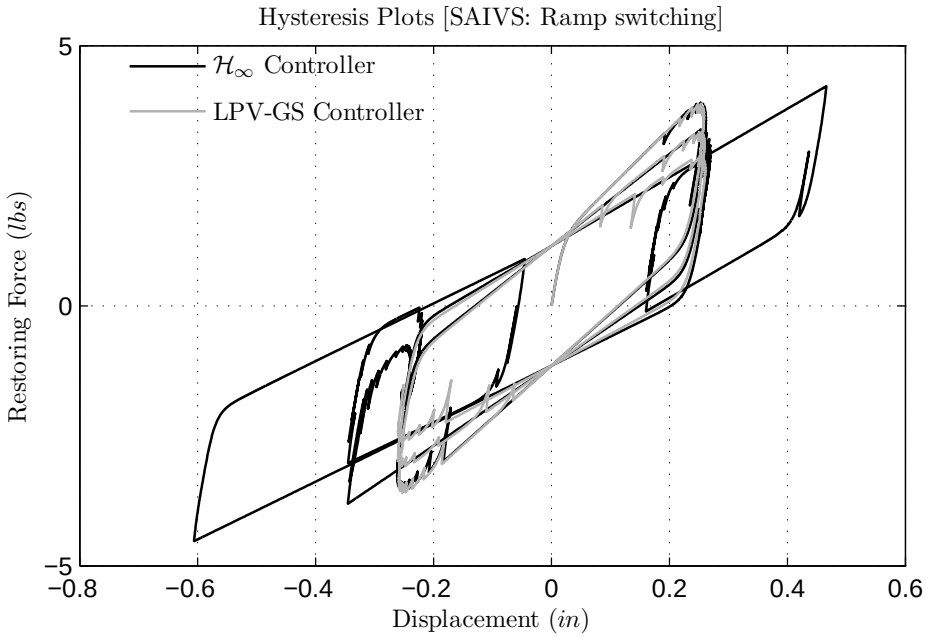

Figure 9.14 : Comparison of hysteresis loops of step input tracking response in LPV-GS controller and $\mathcal{H}_\infty$ controller in presence of ramp SAIVS switching

Chapter 10

Conclusions

For a new concept to get accepted and materialize in the structural engineering community, implementation-lag is about two to three decades. Complexity of the control device and uncertainty over its reliable in-situ performance plays a major role in getting an approval from the practicing engineers. Taking these factors into consideration, in this research, we attempted to develop novel adaptive control devices and new control strategies to mitigate the excessive structural responses during strong earthquake motions. The key emphasis is on developing an adaptive control device capable of being implemented in a real-life structure. The key contributions of this study are summarized next.

10.1 "Apparent weakening" in elastic SDOF structure

Comprehensive experimental and simulation studies have been carried on SDOF-3SFS structure, to study the behavior in elastic structure and negative stiffness device (NSD) assembly for a suite of ground motions. Five ground motions are used for shake table tests and seven ground motion are used for simulation studies; the ground motions chosen are representative of both near-fault and far-field earthquakes. Shake table studies carried on a SDOF-3SFS with the NSDs and damper installed in the first floor (AS) show that by adding NSD to the elastic structure, a bilinear elastic system can be emulated and as a result the base shear demands on the main structure during

strong earthquakes can be reduced by 30%. The peak acceleration experienced by the structure is also reduced by more than 20%. However, the peak displacement of the NSD and structure assembly is increased due to the reduction in stiffness induced by the NSD. These increased deformations are controlled by adding a viscous damper. Consistent response reductions are observed for a suite of ground motions by the addition of the viscous fluid damper. The observed experimental behavior can be reproduced by the presented analytical models at the component level and also for the structure and device assembly.

It has been shown through the numerical studies that the addition of viscous damper will reduce the peak deformation by more than 20% but the structure will experience almost the same acceleration and base shear as the uncontrolled structure. The NSD in conjunction with a viscous damper is capable of simultaneously reducing the base shear, the acceleration and the displacement of the structure.

10.2 "Apparent weakening" in yielding SDOF structure

With the addition of NSD to the bilinear inelastic structure, the base shear and accelerations of the assembly are reduced by more than 30% for ground motions in which there is mild yielding in the primary structure. For more severe ground motions, the deformations of the assembly will be larger than the stiffening point of NSD; resulting in very high assembly stiffness thereby increase in base shear and accelerations of the assembly. However, the high stiffness of the assembly will prevent the structure from collapsing. In the case where there is heavy yielding in the primary structure, the permanent drift in the assembly is larger than the plastic deformation in the primary structure. The permanent drift in excess of the plastic-deformation in the primary structure can be completely recovered by disengaging the NSD from the primary

structure. It has also been demonstrated that the stiffening in NSD will prevent the structure from collapsing. Analogous to the inelastic design, the acceleration and base shear and deformation of the structure and NSD assembly can be reduced by more than 20% for moderate ground motions and the collapse of structure can be prevented for severe ground motions. Additionally, part of the inelastic excursions incurred after a severe ground motion can be recovered by disconnecting the NSD.

10.3 Distributed isolation in MDOF structure using NSD

The advantages of using NSDs in multi-story structures are demonstrated through experimental and simulation studies. Shake-table studies performed on three-story fixed base structure have proved that the addition of NSDs in the first-floor will screen the input energy transmitted to the super structure. Experimental results on the unbraced 3SFS have confirmed that the inter-story deformations, roof accelerations and base shear of the AS will be consistently reduced by more than 15%, 20% and 40%, respectively, compared to the primary structure (BS) and primary structure with passive damper (PS). NSDs are capable of preventing the transmission of input energy thus preventing the structural and non-structural components of the super-structure from experiencing large accelerations and preserve the integrity of the structure.

Also, reductions more than 30% in base shear will avoid the large foundation forces experienced otherwise. Generic numerical models are also developed and calibrated to replicate the experimental results at component level and assembly level. These models can be used to study the sensitivity of the design parameters for the structure and the NSD. Given the nonlinear behavior of the components and the complexity of the assembly, the close agreement between the experimental results and the analytical predictions shows that developed models are representative of the actual structures.

Comprehensive simulation studies carried on 1:3 scale nine-story yielding structure, demonstrated the role of NSDs in multistory buildings and also to find the desired configuration of NSDs to achieve response reduction during severe ground motions. Addition of NSD in a particular story will prevent the transfer of the input energy from ground motion to the super structure and also the resonance state of the primary structure can be avoided. However, the inter-story deformations in the installed floor will be significantly larger compared to uncontrolled structure. These excessive localized deformations can be prevented by placing NSDs (having different properties) in multiple stories and letting them engage at the same time. The "apparent yield-displacement" of the NSDs should decrease from bottom to top to prevent large inelastic deformations in the first story. The optimal properties of NSDs for a given structure and a target response reduction can be calculated based on the site specific spectra. Numerical studies have demonstrated that the base shear and maximum floor accelerations of the AS with optimal NSD properties are reduced by more than 40% and 20%, respectively for all the ground motions tested. In all the test cases, the top four floors of the nine-story frame have undergone very little deformation confirming that the input energy is dissipated in the bottom five floors, unlike the base-isolation system where all the deformations and energy dissipation occurs at the base of structure.

10.4 Semi-active Negative Stiffness Device

This study has revealed that installing NSDs and dampers in multiple stories can overcome some of the limitations posed by the passive control devices and base-isolation systems. However, from the practical point of view, the proposed approach and the NSD needs to be enhanced further because they are sensitive to the design ground

motion, the estimated force-deformation behavior and the excessive permanent deformations observed for severe ground motions. Two semi-active mechanisms are proposed for the NSD to address the issues pertaining to assembly drifts and also to improve the performance of NSD.

Double-acting hydraulic device is adapted to move the pin connecting the pivot plate and lever arm. In the first approach, the pin is moved in a arc shaped slotted hole. By doing this in real-time, any desired force-deformation of the assembly can be achieved. This approach will help fine-tune the F-D behavior of assembly and also to easily accommodate the change in structure properties.

In the second approach, the pin is moved in a vertical slotted hole; as a result the zero-position of the NSD will be shifted based on the direction in which the pin is moved. The objective of this approach is to overcome the large assembly drifts which are common using a passive NSD. The position of pin is moved every time the primary structure undergo inelastic deformation. The amount by which the zero position of the NSD shift depends on the inelastic deformation in the primary structure. The shift in zero-position of SA-NSD is equal to the inelastic deformation in primary structure. Simulation studies on a SDOF inelastic structure have confirmed that the deformation of the assembly is significantly reduced compared to the case with passive NSD. The reduction in maximum assembly shear and acceleration is same in the case of both passive and semi-active NSD but the inelastic deformation and assembly drift in the assembly is reduced by more than 70%.

10.5 Adaptive length pendulum smart tuned mass damper

Tuned mass dampers received a lot attention since the opening of Taipei 101 in 2004 [5]. Simplicity, low-cost and ease of installation makes them an effective option for

response attenuation in building. The second component in this thesis is development of a novel adaptive-length pendulum (ALP) smart tuned mass damper (STMD) and to verify it experimentally. ALP-STMD is a semi-active control device capable of accommodating the changes in primary structure properties, due to damage or deterioration, by tuning in real time based on a local feedback. Length of the pendulum is adjusted in real time using a shape memory alloy (SMA) wire actuator. Using an instantaneous frequency tracking algorithm, the dominant frequency of the structure can be tracked from a local feedback signal, then the length of pendulum is adjusted to match the dominant frequency. Effectiveness of the proposed ALP-STMD mechanism is verified experimentally on a prototype two-storey shear frame. Experimental studies have confirmed that the ALP-STMD absorbs most of the input energy associated in the vicinity of tuned frequency of the pendulum damper. The storey-displacements are reduced by 80% when subjected to forced excitation (harmonic and chirp-signal) and a faster decay rate during free vibration.

10.6 Linear parameter varying gain-scheduled controller

The third component of this thesis is to develop control algorithms to compensate hysteresis in hysteretic systems. The algorithms developed in this thesis are applicable for hysteretic systems with multiple hysteretic parameters (could be a combination of fast and slow varying parameters). A systematic approach has also been developed to model the hysteresis and to design a gain-scheduled controller for tracking applications. The proposed methods are implemented on a SAIVS (semi-active independently variable stiffness) system that exhibits hysteresis. SAIVS system with variable stiffness and hysteresis is represented as a quasi linear parameter varying (LPV) system. Gain scheduled (GS) controller is constructed from the parameter de-

pendent Lyapunov matrices, which are obtained as optimal solutions of linear matrix inequalities (LMIs) that ensure the feasibility solution for closed loop system performance. The effectiveness of the proposed method is demonstrated using numerical simulations.

The proposed method is implemented on a spring-mass system which consists of a semi-active independently variable stiffness (SAIVS) device that exhibits hysteresis and precisely controllable stiffness change in real-time. SAIVS system with variable stiffness hysteresis is represented as quasi linear parameter varying (LPV) system with two parameters: linear time-varying stiffness (parameter with slow variation rate) and stiffness of the friction-hysteresis (parameter with high variation rate). The proposed LPV-GS controller can accommodate both slow and fast varying parameters that was not feasible with the controllers proposed in prior studies. Effectiveness of the proposed controller is demonstrated by comparing the results with a fixed robust $\mathcal{H}_\infty$ controller that assumes the parameter variation as an uncertainty. Performance of both the controllers is verified for varying stiffness hysteresis of SAIVS device and for different ranges of tracking displacements. Superior performance of the LPV-GS over the robust $\mathcal{H}_\infty$ controller is demonstrated from the results presented in this study. LPV-GS controller is capable of adapting to any parameter changes whereas the $\mathcal{H}_\infty$ controller is effective only when the system parameters are in the vicinity of the nominal plant parameters for which the controller is designed. Robust $\mathcal{H}_\infty$ controller becomes unstable under large parameter variations but the LPV-GS will ensure stability and guarantee the desired closed-loop performance.

Chapter 11

Future Study and Recommendations

Since both the NSD and ALP-STMD developed and tested in this thesis are new and still in their infancy, there are some issues in both the devices that needs further exploration. These issues that still needs to be addressed in the future study are presented in this section. Towards the end of this chapter few recommendations are provided for further research based on some of the observations during the shake table studies on NSD.

11.1 Negative Stiffness Device and Adaptive System

The force-deformation loops of NSD-East are asymmetric due to the tolerances the crept in during the installation of GSAs in the NSD. The mechanism used for the GSA needs to modified to avoid any such asymmetries, as it would effect the performance of the structure and NSD assembly in yielding systems. Another possible factor for the asymmetry is the difference in stiffness of the two legs in each chevron brace the NSD. For the devices tested in this study, one leg of the chevron brace has a tubular cross section and the other leg has two rectangular flats. Any possible asymmetry in the behavior of NSD caused due to this differential stiffness can be avoided by making both the legs from elements with same cross-section.

The advantages of adding hydraulic devices and displacement sensors to change the force-displacement behavior of NSD in real-time is demonstrated through numer-

ical studies. Incorporating these features in the NSDs will certainly overcome the large assembly drifts observed in primary structure that undergoes heavy yielding during severe ground motions.

To achieve vertical-distributed-isolation, NSDs with different apparent yield displacements are used in each story, along the height of the structure, to achieve uniform response reduction. The search space used for optimization is only dependent on one optimization variable (apparent yield displacement). By considering the initial stiffness, stiffening displacement, and stiffness beyond the stiffening point of each NSD as optimization variables there is scope for achieving more reduction in response.

From the implementation point of view, there are three things that needs to changed

1. End angle assembly needs to be incorporated into the NSD so that the NSD can be easily bolted to the structure.

2. Providing a provision to allow the NSD to move out of plane in case if the ground motion is perpendicular to the plane of NSD.

3. Packaging the whole NSD to be able to install in moment frames with different height.

11.2 Adaptive Length Pendulum Damper

STMD is effective at the location where the displacement is maximum. Since the STMD developed in this study is tested on a prototype two story structure, placing it on the roof will give maximum response reduction. For a multi-story structure in which multiple modes can get excited in different directions, for the best performance

STMDs should be placed at multiple locations. The potential of using multiple ALP-STMDs need to be explored and verified experimentally.

11.3 Shake Table Testing of Adaptive System

The mass of shake table is two times the mass of the 3SFS. Since the mass of super structure (3SFS) is comparable with the shake table mass, there will be a lot of interaction between the actuator and structure. As a mandatary routine procedure, the shake table was tuned for 3SFS at the very beginning of the tests. However, when the NSD is connected, because of the change in super structure properties (stiffness), the shake table gets off-tuned as a result the observed acceleration of the structure is different from the commanded acceleration. It is recommended to use the large pool of recorded experimental data to study the actuator-structure interaction in nonlinear systems.

Appendix A

Component Drawings of 3SFS

Table A.1 : List of components, dimensions and the location

Components	Elements	Location	Section (in)	Dim. (in)	Figures
Slabs	Steel plates	Floor level	steel plates	3.5x117.5x78.75	A.2
Moment frame	Columns	1^{st} floor	S3x5.7	57	A.5,A.16
		2^{nd} & 3^{rd} floor	S3x5.7	38.25	A.6,A.14
	Beams	all the floors	S3x5.7	51	A.7,A.13
	Braces	2^{nd} & 3^{rd} floors	C3x4.1	65	A.8
	Load-cells	1^{st} floor	-	6x6x5.5	A.5,A.15
	Beam-column block	Beam, column and slab connection	-	6x6x7	A.10,A.13
Gravity frame	Columns-1	All floors	S3x5.7	39.5	A.12
	Columns-2	1^{st} floor	S3x5.7	13.25	A.5
	Rockers	either ends of columns	-	8x8x1.5	A.11,A.12
	Braces	all floors	L2x2x0.25	51.3	A.8
	Load-cells	1^{st} floor	-	6x6x5.5	A.11

The hole pattern on the base plate, top view, front view and side view are shown in A.1, A.2, A.3 and A.4, respectively.

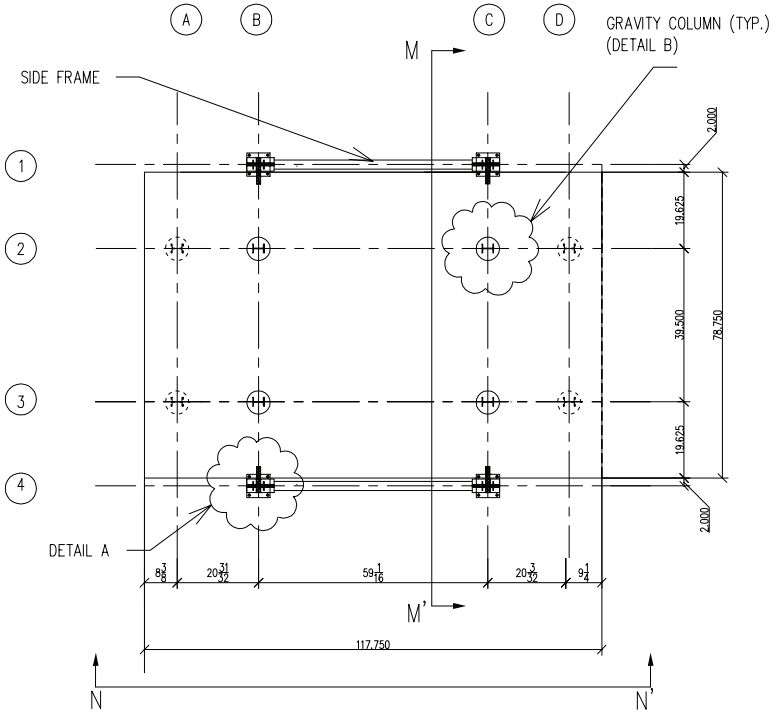

Figure A.2 : Top view of 3SFS

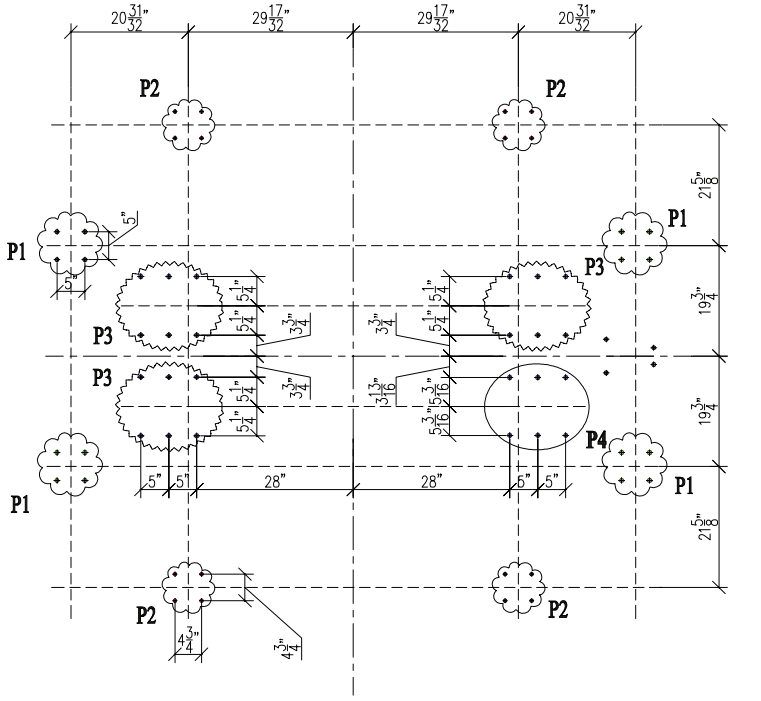

P1: Gravity columns 1/2"ø threaded	**P2**: Moment frame columns 5/8"ø threaded	**P3**: NSD connection 3/4"ø threaded	**P4**: NSD connection 3/4"ø threaded	**P5**: Damper connection 3/4"ø threaded

Figure A.1 : Foot print of hole pattern on the shake table base-plate

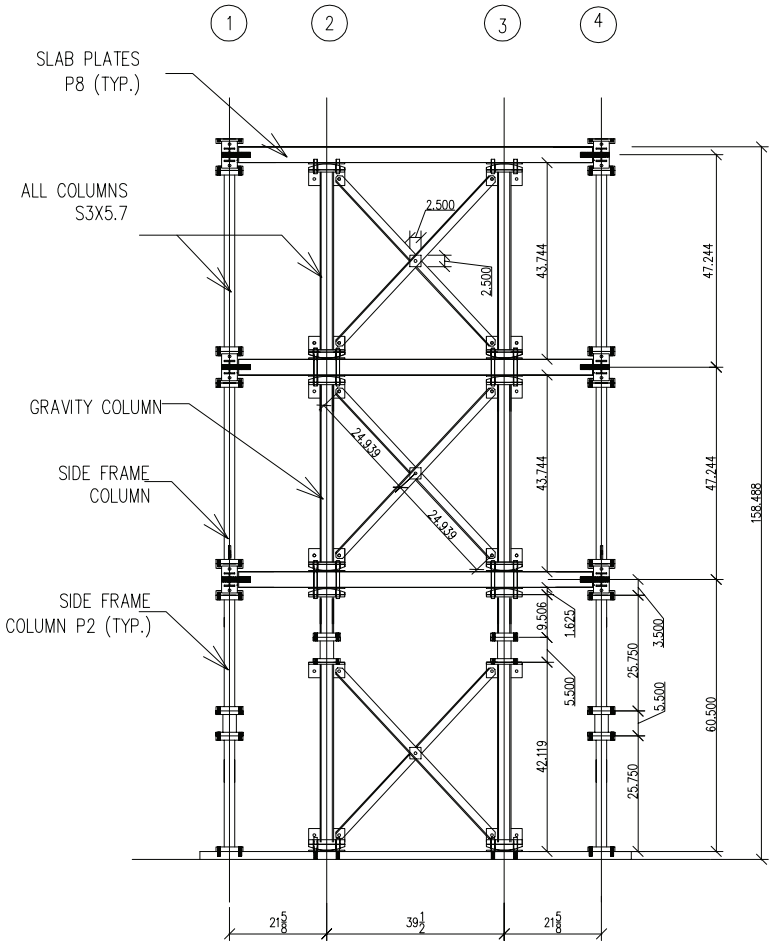

Figure A.4 : Side view of 3SFS

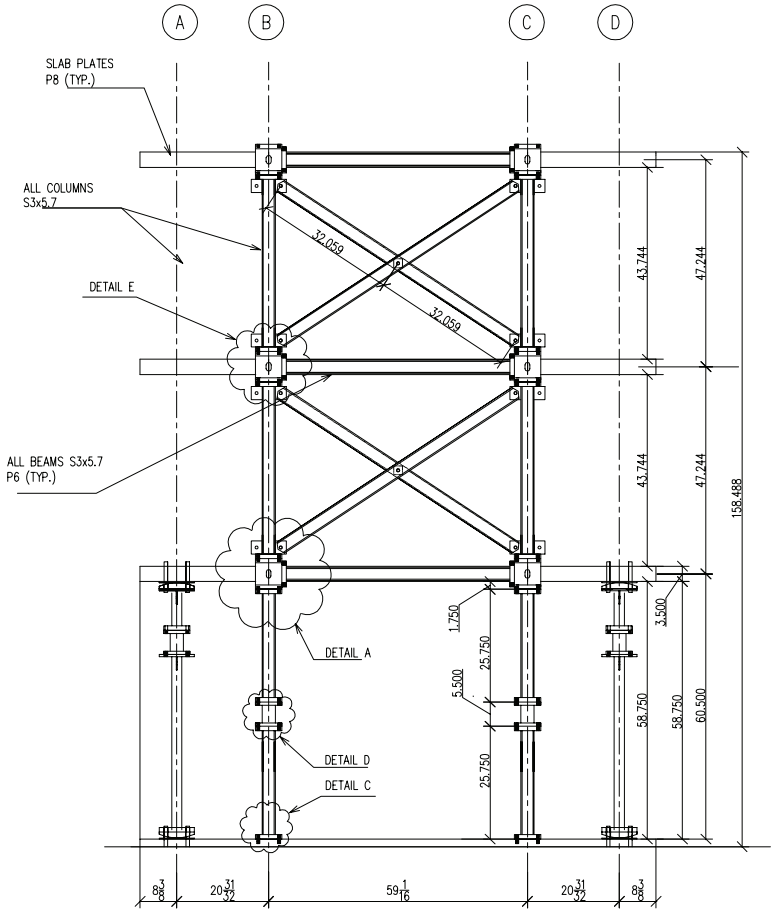

Figure A.3 : Front view of 3SFS

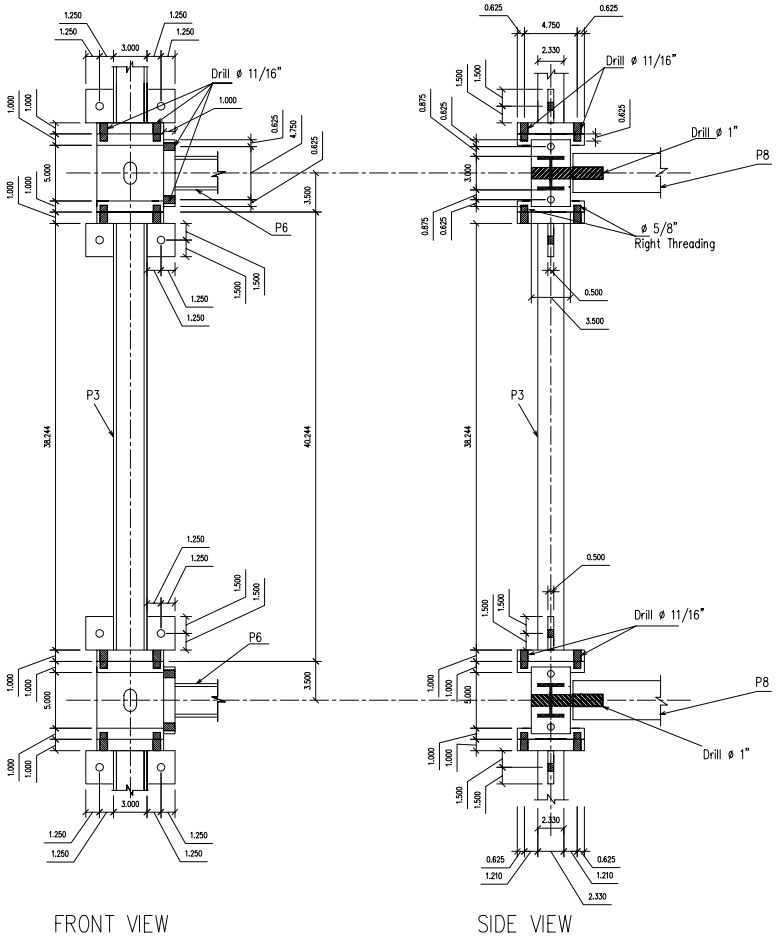

Figure A.6 : Moment frame columns in the second and third floor

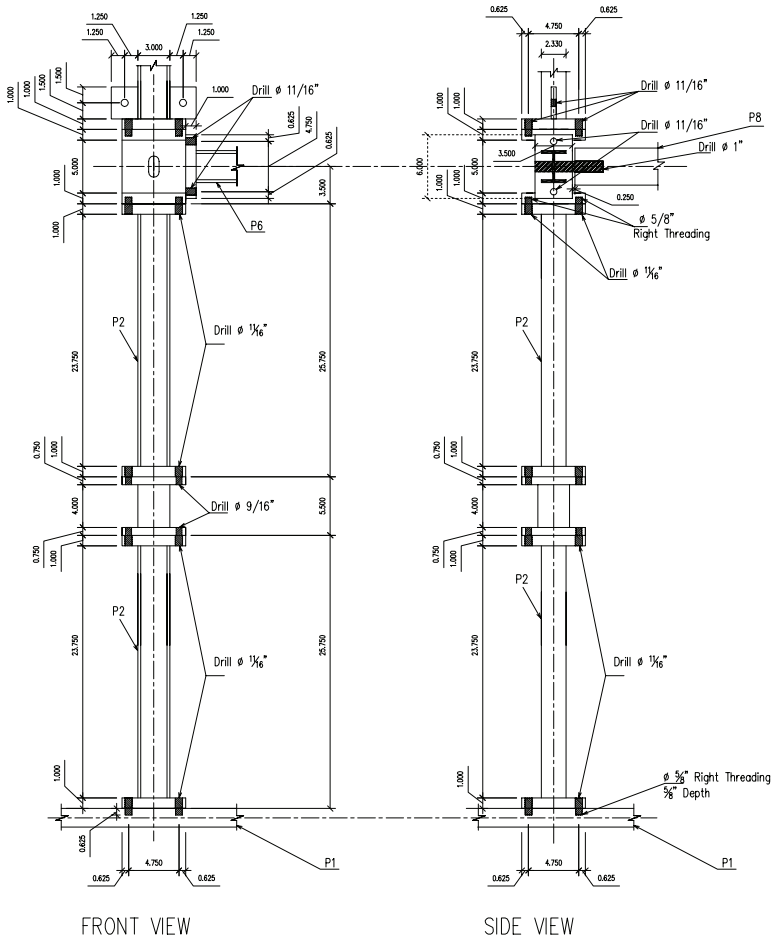

Figure A.5 : Moment frame columns in the first floor

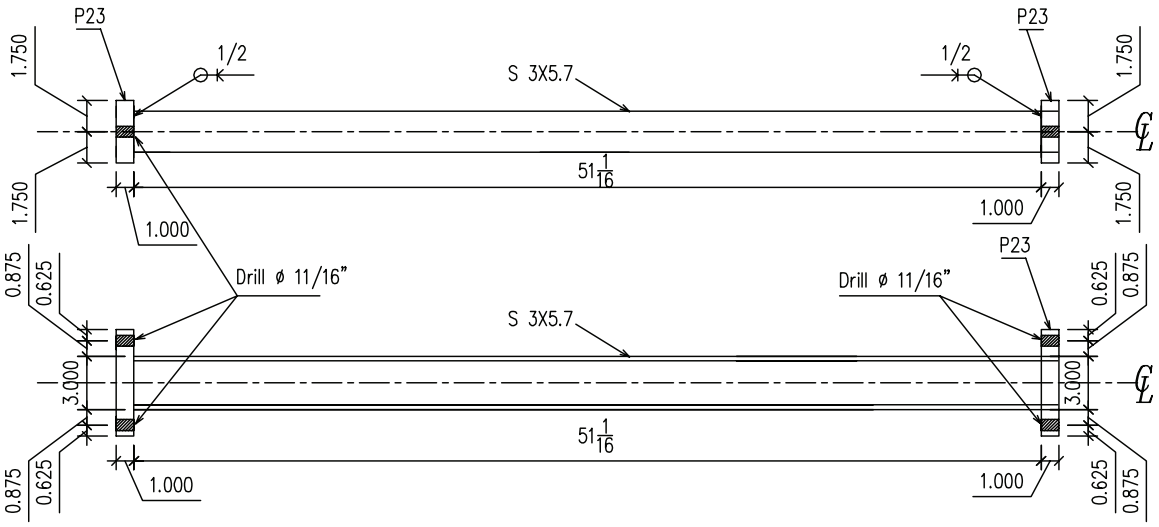

Figure A.7 : Moment frame beams of the 3SFS

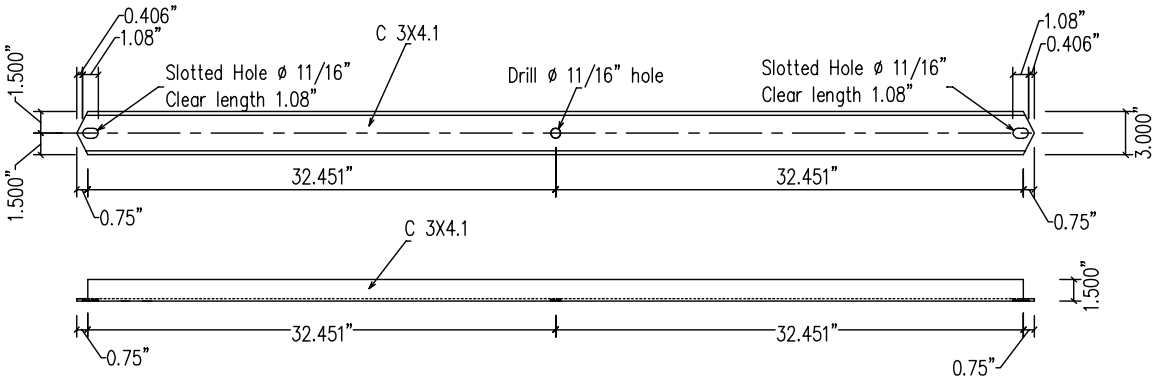

Figure A.8 : Moment frame braces in the second and third floor of 3SFS

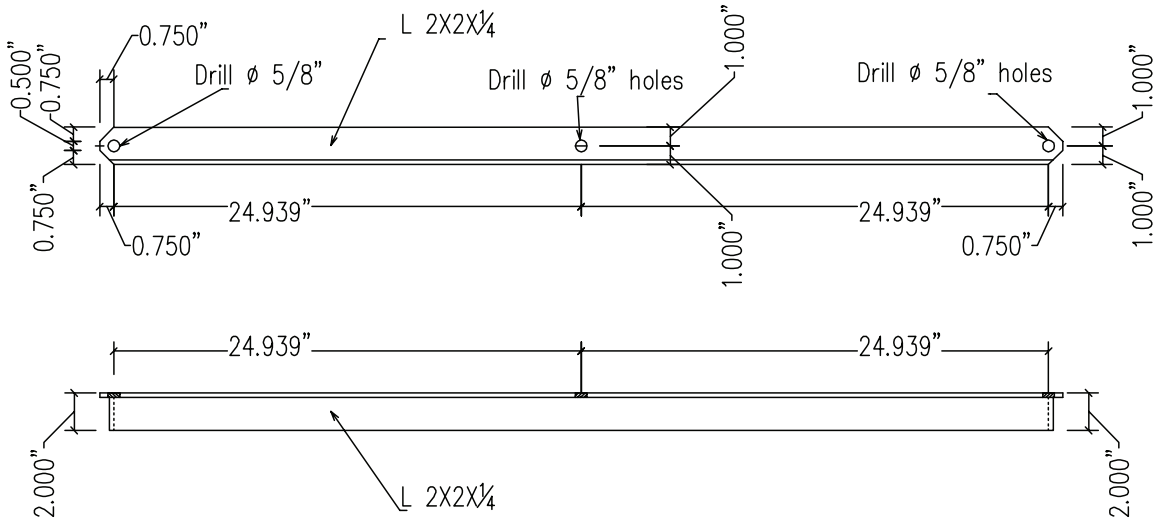

Figure A.9 : Gravity frame braces of 3SFS

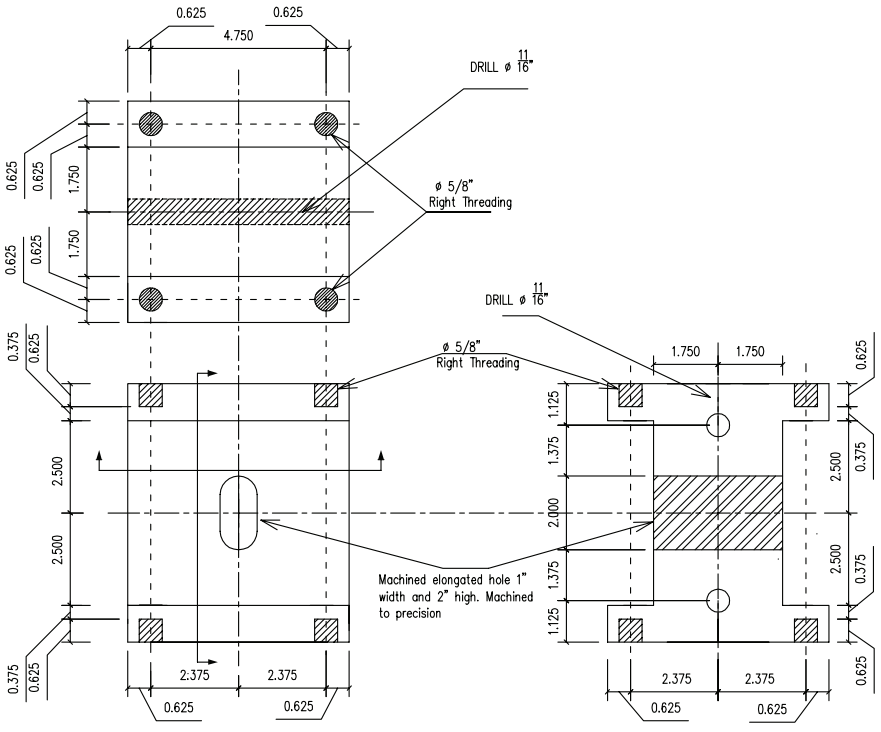

Figure A.10 : Beam column block of the moment-frame

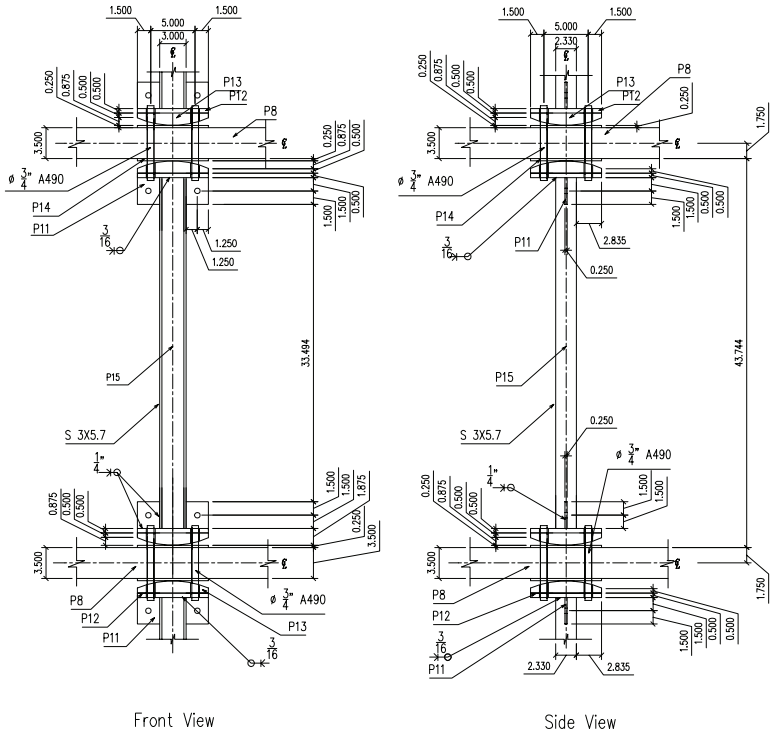

Figure A.12 : Gravity frame columns in the second and third floor

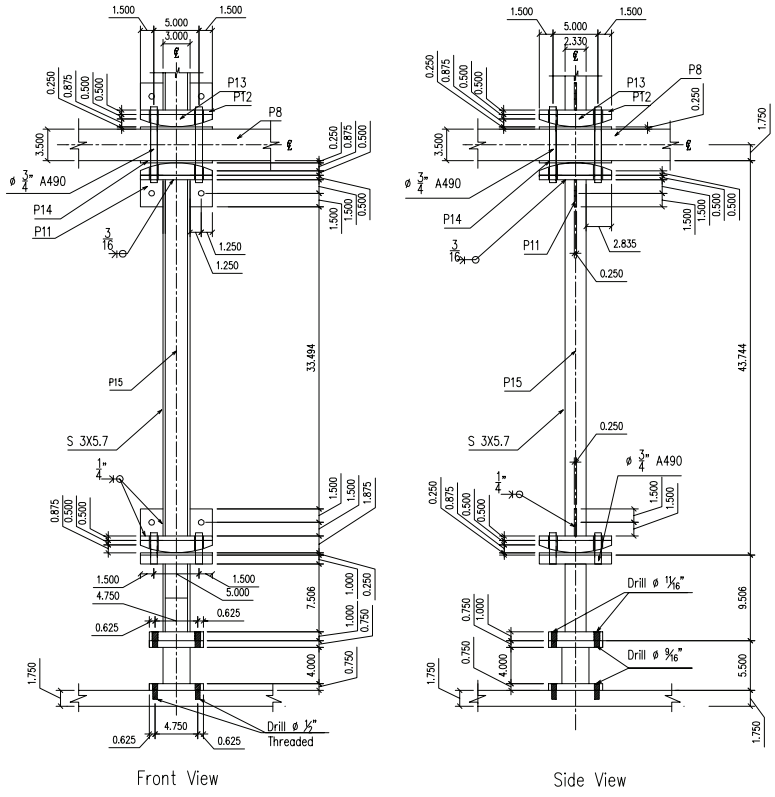

Figure A.11 : Gravity frame columns in the first floor

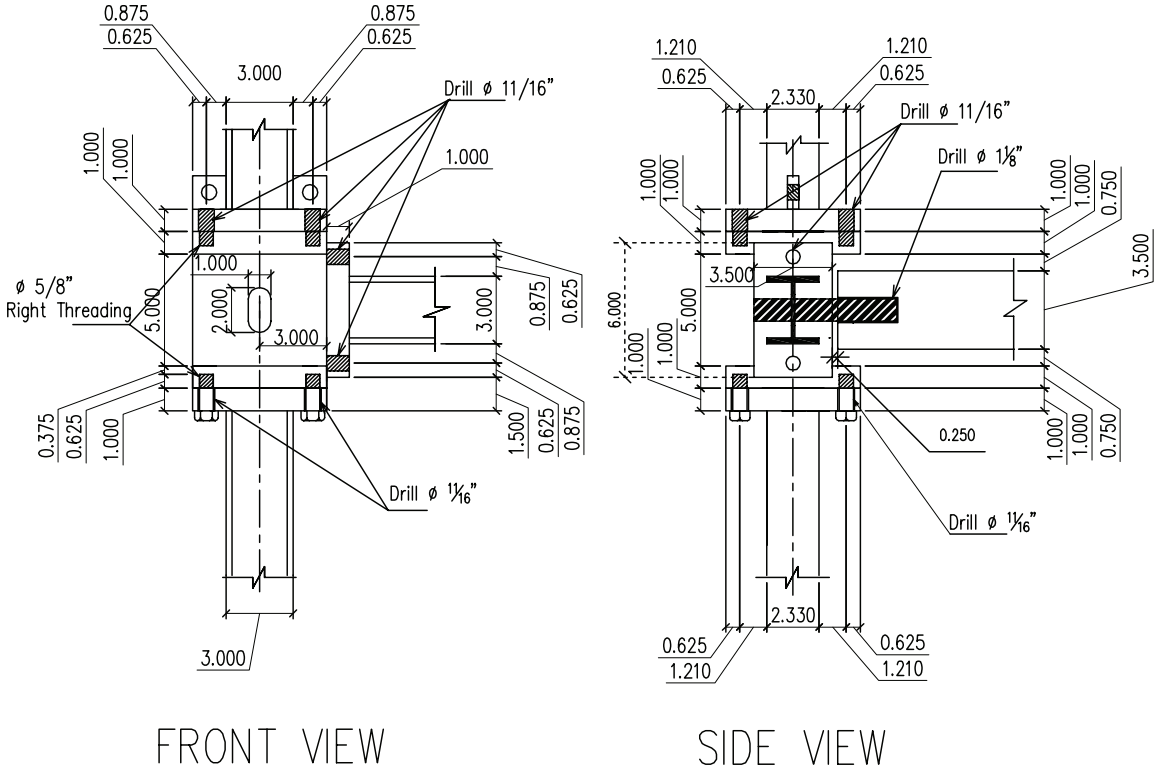

Figure A.13 : Detail-A of moment frame columns

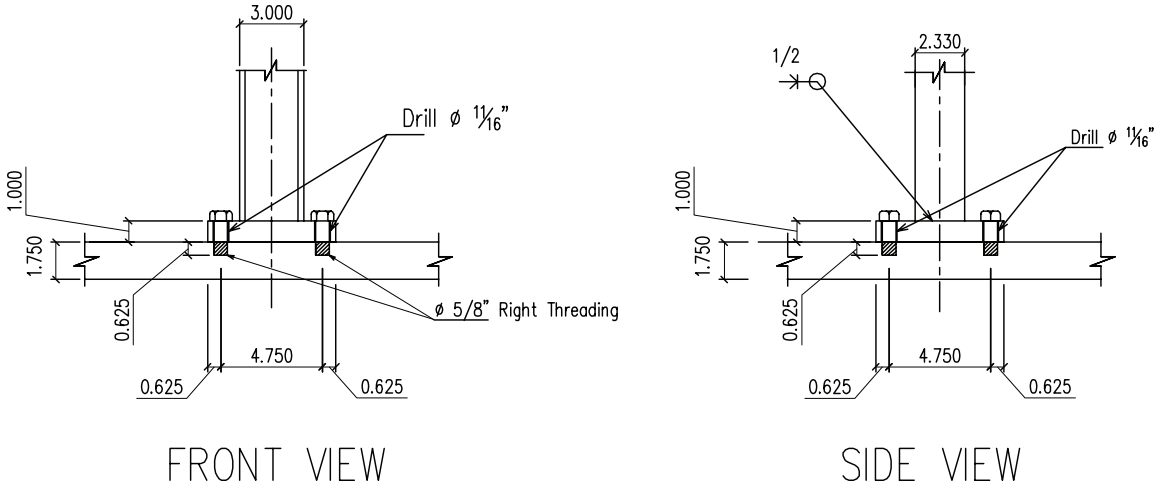

Figure A.14 : Detail-C of moment frame columns

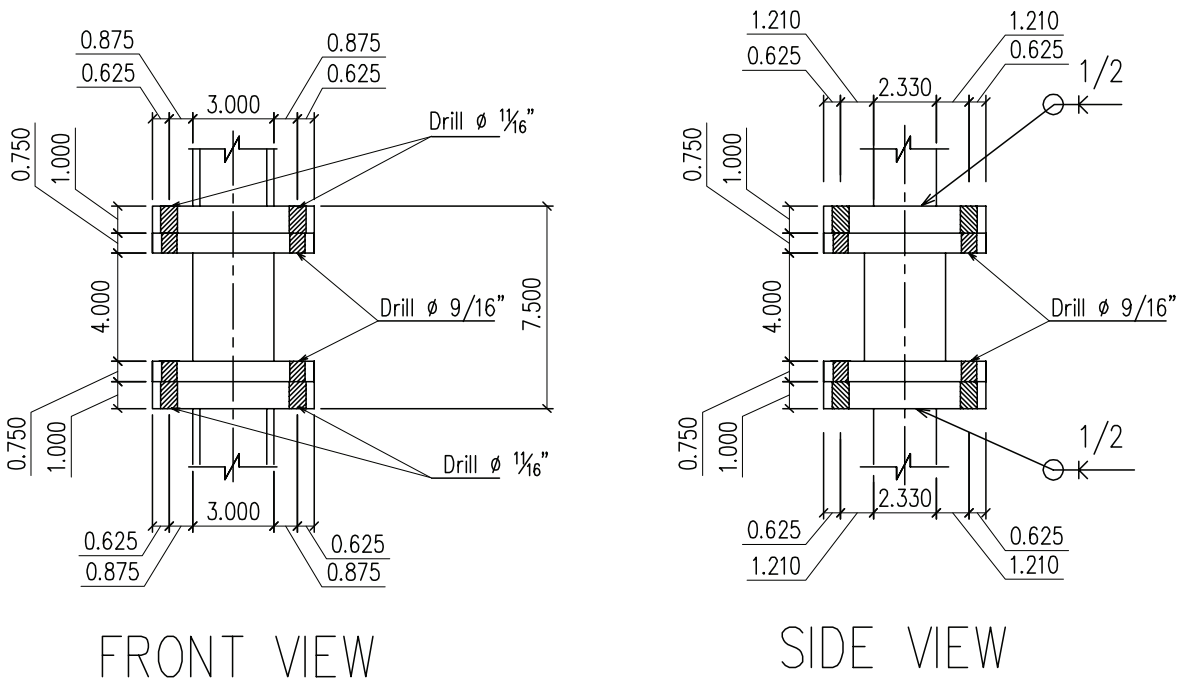

Figure A.15 : Detail-D of moment frame columns

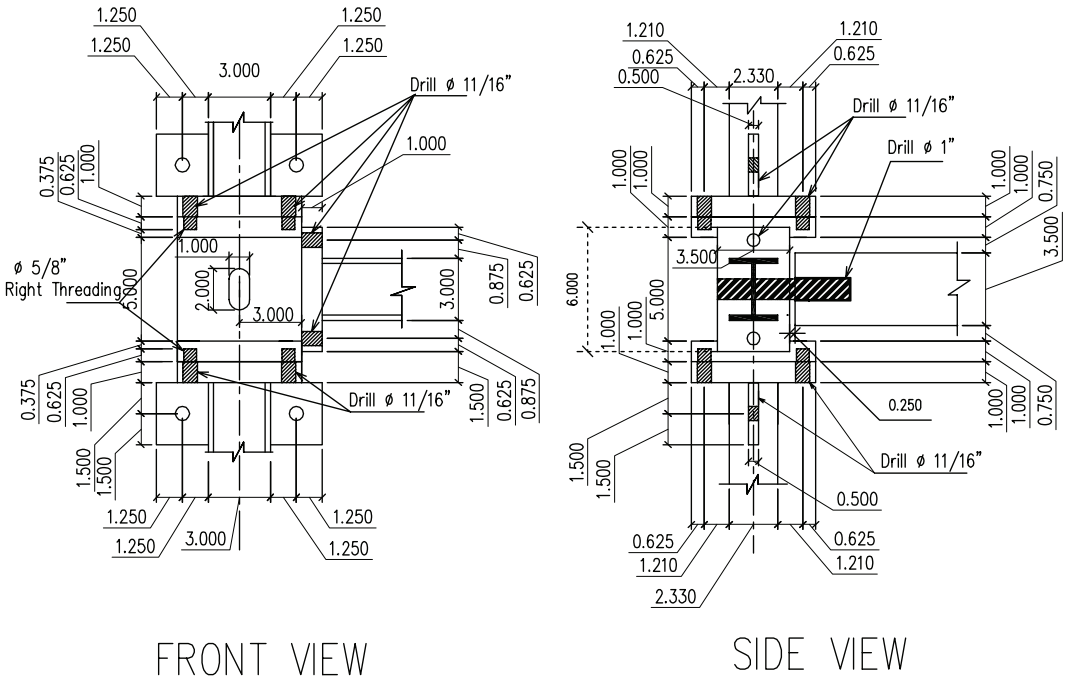

Figure A.16 : Detail-E of moment frame columns

Bibliography

[1] "USGS: Largest and deadliest earthquakes by year." http://earthquake.usgs.gov/earthquakes/eqarchives/year/byyear.php.

[2] "Preventing earthquake disasters: The grand challenge in earthquake engineering: A research agenda for the network for earthquake engineering simulation (NEES)." http://www.nap.edu/openbook.php?record_id=10799&page=156.

[3] A. K. Chopra, *Dynamics of structures: Theory and applications to earthquake engineering*. Prentice-Hall international series in civil engineering and engineering mechanics, Pearson/Prentice Hall, 2007.

[4] G. W. Housner, L. A. Bergman, T. K. Caughey, A. G. Chassiakos, R. O. Claus, S. F. Masri, R. E. Skelton, T. T. Soong, B. F. Spencer, and J. T. P. Yao, "Structural control: past, present, and future," *Journal of Engineering Mechanics*, vol. 123, pp. 897–971, 1997.

[5] B. F. Spencer and S. Nagarajaiah, "State of the art of structural control," *Journal of Structural Engineering, ASCE*, vol. 129, no. 7, pp. 845–856, 2003.

[6] S. Nagarajaiah and S. Narasimhan, "Smart base-isolated benchmark building. part ii: phase i sample controllers for linear isolation systems," *Structural Control and Health Monitoring*, vol. 13, no. 2-3, pp. 589–604, 2006.

[7] "Whats happened to seismic isolation of buildings in the u.s.?."

http://www.structuremag.org/article.aspx?articleID=1404.

[8] J. M. Kelly, "Aseismic base isolation: its history and prospects," in *Proceedings of First World Congress on Joints and Bearings*, vol. 1, pp. 549–586, 1981.

[9] J. M. Kelly, "Aseismic base isolation: review and bibliography," *Soil Dynamics and Earthquake Engineering*, vol. 5, no. 3, pp. 202–216, 1986.

[10] I. G. Buckle and R. L. Mayes, "Seismic isolation: History, application, and performance—a world view," *Earthquake Spectra*, vol. 6, no. 2, pp. 161–201, 1990.

[11] T. T. Soong and M. C. Constantinou, *Passive and active structural vibration control in civil engineering.* Courses and lectures - International Centre for Mechanical Sciences, Springer-Verlag, 1994.

[12] W. H. Robinson, "Lead-rubber hysteretic bearings suitable for protecting structures during earthquakes," *Earthquake Engineering & Structural Dynamics*, vol. 10, no. 4, pp. 593–604, 1982.

[13] S. Nagarajaiah and S. Narasimhan, "Smart base-isolated benchmark building. part ii: phase i sample controllers for linear isolation systems," *Structural Control and Health Monitoring*, vol. 13, no. 2-3, pp. 589–604, 2006.

[14] S. Sahasrabudhe and S. Nagarajaiah, "Experimental study of sliding base-isolated buildings with magnetorheological dampers in near-fault earthquakes," *Journal of Structural Engineering, ASCE*, vol. 131, no. 7, pp. 1025–1034, 2005.

[15] S. Narasimhan, S. Nagarajaiah, E. A. Johnson, and H. P. Gavin, "Smart base-isolated benchmark building. part i: problem definition," *Structural Control*

and Health Monitoring, vol. 13, no. 2-3, pp. 573–588, 2006.

[16] S. Nagarajaiah and K. Ferrell, "Stability of elastomeric seismic isolation bearings," *Journal of Structural Engineering*, vol. 125, no. 9, pp. 946–954, 1999.

[17] T. Sasaki and K. Kashiyama, "Spherical sliding bearing," January 1996.

[18] S. Nagarajaiah and M. C. Reinhorn, "A. M."and Constantinou, "Experimental study of sliding isolated structures with uplift restraint," *Journal of Structural Engineering*, vol. 118, no. 6, pp. 1666–1682, 1992.

[19] V. A. Zayas, S. S. Low, and S. A. Mahin, "A simple pendulum technique for achieving seismic isolation," *Earthquake Spectra*, vol. 6, no. 2, pp. 317–333, 1990.

[20] D. M. Fenz and M. C. Constantinou, "Spherical sliding isolation bearings with adaptive behavior: Theory," *Earthquake Engineering & Structural Dynamics*, vol. 37, no. 2, pp. 163–183, 2008.

[21] D. M. Fenz and M. C. Constantinou, "Spherical sliding isolation bearings with adaptive behavior: Experimental verification," *Earthquake Engineering & Structural Dynamics*, vol. 37, no. 2, pp. 185–205, 2007.

[22] S. Nagarajaiah, A. M. Reinhorn, and M. C. Constantinou, "Nonlinear dynamic analysis of 3d base-isolated structures," *Journal of Structural Engineering, ASCE*, vol. 117, no. 7, pp. 2035–2054, 1991.

[23] T. T. Soong and G. F. Dargush, *Passive energy dissipation systems in structural engineering*. Wiley, 1997.

[24] M. C. Constantinou, T. T. Soong, and G. F. Dargush, *Passive energy dissipation systems for structural design and retrofit.* NCEER Monograph Series, Multidisciplinary Center for Earthquake Engineering Research, 1998.

[25] R. I. Skinner, J. M. Kelly, and A. J. Heine, "Hysteretic dampers for earthquake-resistant structures," *Earthquake Engineering & Structural Dynamics*, vol. 3, no. 3, pp. 287–296, 1974.

[26] J. M. Kelly, R. I. Skinner, and A. J. Heine, "Hysteretic dampers for earthquake-resistant structures," *New Zealand Society for Earthquake Engineering*, vol. 5, no. 3, pp. 63–88, 1972.

[27] T. Sakurai, K. Shibata, S. Watanabe, A. Endoh, K. Yamada, N. Tanaka, and H. Kobayashi, "Application of joint damper to thermal power plant buildings," in *Proceedings of 10th World Conference in Earthquake Engineering*, vol. 7, pp. 4149–4154, 1992.

[28] I. D. Aiken and J. M. Kelly, "Comparative study of four passive energy dissipation systems," *New Zealand National Society for Earthquake Engineering*, vol. 25, no. 3, pp. 175–192, 1992.

[29] A. S. Whittaker, V. V. Bertero, C. L. Thompson, and L. J. Alonso, "Seismic testing of steel plate energy dissipation devices," *Earthquake Spectra*, vol. 7, no. 4, pp. 563–604, 1991.

[30] K. C. Tsai, H. W. Chen, C. P. Hong, and Y. F. Su, "Design of steel triangular plate energy absorbers for seismic-resistant construction," *Earthquake Spectra*, vol. 9, no. 3, pp. 505–528, 1993.

[31] T. T. Soong, "Experimental simulation of degrading structures through active control," *Earthquake Engineering & Structural Dynamics*, vol. 27, no. 2, pp. 143–154, 1998.

[32] A. S. Pall and C. Marsh, "Seismic response of friction damped braced frames," *Journal of the Structural Division*, vol. 108, pp. 1313–1323, June 1982.

[33] A. Filiatrault and S. Cherry, "Performance evaluation of friction damped braced steel frames under simulated earthquake loads," *Earthquake Spectra*, vol. 3, no. 1, pp. 57–78, 1987.

[34] D. K. Nims, P. J. Richter, and R. E. Bachman, "The use of the energy dissipating restraint for seismic hazard mitigation," *Earthquake Spectra*, vol. 9, no. 3, pp. 467–489, 1993.

[35] M. C. Constantinou and M. D. Symans, "Experimental study of seismic response of buildings with supplemental fluid dampers," *The Structural Design of Tall Buildings*, vol. 2, no. 2, pp. 93–132, 1993.

[36] I. D. Aiken, D. K. Nims, A. S. Whittaker, and J. M. Kelly, "Testing of passive energy dissipation systems," *Earthquake Spectra*, vol. 9, no. 3, pp. 335–370, 1993.

[37] T. F. FitzGerald, T. Anagnos, M. Goodson, and T. Zsutty, "Slotted bolted connections in aseismic design for concentrically braced connections," *Earthquake Spectra*, vol. 5, no. 2, pp. 383–391, 1989.

[38] A. M. Reinhorn and C. Li, "Experimental and analytical investigation of seismic retrofit of structures with supplemental damping: Part. ii friction dampers," Technical Report 95-0009, NCEER, 1995.

[39] N. Makris and M. C. Constantinou, "Viscous dampers: Testing, modeling and application in vibration and seismic isolation," Technical Report 95-0028, NCEER, 1990.

[40] M. D. Symans and M. C. Constantinou, "Seismic testing of a building structure with a semi-active fluid damper control system," *Earthquake Engineering and Structural Dynamics*, vol. 26, no. 7, pp. 759–777, 1997.

[41] F. Arima, M. Miyazaki, T. "H.", and Y. Yamazaki, "A study on building with large damping using viscous damping walls," in *Proceedings of 9th World Conference in Earthquake Engineering*, vol. 5, pp. 821–826, 1988.

[42] E. J. Nielsen, M. L. Lai, T. T. Soong, and J. M. Kelly, "Viscoelastic damper overview for seismic and wind applications," vol. 2720, pp. 138–144, SPIE, 1996.

[43] K. Chang, T. T. Soong, S. T. Oh, and M. L. Lai, "Seismic response of a 2/5 scale steel structure with added viscoelastic dampers," Technical Report 91-0012, NCEER, 1991.

[44] T. Fujita, "Seismic isolation and response control for nuclear and non-nuclear structures," 1991.

[45] G. Tsiatas and K. Daly, "Controlling vibrations with combination viscous/friction mechanisms," in *Proceedings of First World Conference on Structural Control*, vol. 1, 1994.

[46] A. M. Reinhorn and C. Li, "Experimental and analytical investigation of seismic retrofit of structures with supplemental damping: Part. iii viscous walls," Technical Report 95-0013, NCEER, 1995.

[47] W. S. Pong, C. S. Tsai, and G. C. Lee, "Seismic performance of high-rise building frames with added energy-absorbing devices," Technical Report 94-0016, NCEER, 1994.

[48] H. J. Pradlwarter, G. I. Schueller, and U. Dorka, "Reliability of MDOF-systems with hysteretic devices," *Engineering Structures*, vol. 20, no. 8, pp. 685–691, 1998.

[49] J. P. DenHartog, *Mechanical Vibrations*. New York: McGraw-Hill, 4th ed., 1956.

[50] R. Villaverde and L. A. Koyama, "Damped resonant appendages to increase inherent damping in buildings," *Earthquake Engineering & Structural Dynamics*, vol. 22, no. 6, pp. 491–507, 1993.

[51] S. Nagarajaiah, D. T. R. Pasala, and C. Huang, "Smart TMD: Adaptive length pendulum dampers," in *Proceedings of the* 5^{th} *world conference on structural control and health monitoring*, vol. CDROM, July 2010.

[52] A. J. Clark, "Multiple passive tuned mass damper for reducing earthquake induced building motion," in *Proceedings of 9th World Conference in Earthquake Engineering*, vol. 5, pp. 779–784, 1988.

[53] T. Igusa and K. Xu, "Vibration control using multiple tuned mass dampers," *Journal of Sound and Vibration*, vol. 175, pp. 491–503, Aug. 1994.

[54] H. Yamaguchi and N. Harnpornchai, "Fundamental characteristics of multiple tuned mass dampers for suppressing harmonically forced oscillations," *Earthquake Engineering & Structural Dynamics*, vol. 22, no. 1, pp. 51–62, 1993.

[55] M. Setareh, "Use of the doubly-tuned mass dampers for passive vibration control," in *Proceedings of First World Conference in Earthquake Engineering*, vol. 1, 1994.

[56] A. Kareem and S. Kline, "Performance of multiple mass dampers under random loading," *Journal of Structural Engineering*, vol. 121, pp. 348–361, Feb. 1995.

[57] L. M. Sun, *Semi-analytical modeling ofthe tuned liquid damper with emphasis on damping of liquid sloshing.* PhD thesis, University of Tokyo, Tokyo, Tokyo, Japan, 1991.

[58] J. Q. Sun, M. R. Jolly, and M. A. Norris, "Passive, adaptive and active tuned vibration absorbers – a survey," *Journal of Mechanical Design*, vol. 117, no. B, pp. 234–242, 1995.

[59] F. Welt and V. J. Modi, "Vibration damping through liquid sloshing, part 2: Experimental results," *Journal of Vibration and Acoustics*, vol. 114, no. 1, pp. 17–23, 1992.

[60] H. F. Bauer, "Oscillations of immiscible liquids in a rectangular container: A new damper for excited structures," *Journal of Sound and Vibration*, vol. 93, no. 1, pp. 117–133, 1984.

[61] Y. Fujino, B. M. Pacheco, P. Chaiseri, and L. M. Sun, "Parametric studies on tuned liquid damper (TLD) using circular containers by free oscillation experiments," *Structural Engineering/Earthquake Engineering*, vol. 5, no. 2, pp. 381–391, 1988.

[62] Y. L. Xu, K. C. S. Kwok, and B. Samali, "Control of wind-induced tall building

vibration by tuned mass dampers," *Journal of Wind Engineering and Industrial Aerodynamics*, vol. 40, no. 1, pp. 1 – 32, 1992.

[63] Y. Nakamura, H. Watanabe, and S. Kawamata, "Seismic response of structures by accelerated liquid mass damper," in *Proceedings of 9th World Conference in Earthquake Engineering*, vol. 5, pp. 785–790, 1988.

[64] T. Kobori, M. Takahashi, T. Nasu, N. Niwa, and K. Ogasawara, "Seismic response controlled structure with active variable stiffness system," *Earthquake Engineering and Structural Dynamics*, vol. 22, no. 11, pp. 925–941, 1993.

[65] T. Kobori, N. Koshika, N. Yamada, and Y. Ikeda, "Seismic response controlled structure with active mass driver system. part 1: Design," *Earthquake Engineering & Structural Dynamics*, vol. 20, pp. 133–139, 1991.

[66] T. Kobori, "Past, present and future in seismic response control in civil engineering structures," in *Proceedings of 3rd World Conference in Structural Control*, pp. 9–14, 2003.

[67] A. M. Reinhorn, T. T. Soong, R. C. Lin, M. A. Riley, Y. P. Wang, S. Aizawa, and M. Higashino, "Active bracing system: A full scale implementation of active control," Technical Report 92-0020, NCEER, 1992.

[68] R. Betti and G. F. Panariello, "Active tendon control systems for structures subjected to multiple support excitation," *Smart Materials and Structures*, vol. 4, no. 3, p. 153, 1995.

[69] C. Goong, C. Guanrong, and H. Shih-Hsun, *Linear Stochastic Control Systems*. CRC Press, 1995.

[70] G. N. Saridis, *Stochastic processes, estimation, and control : the entropy approach*. New York, NY [u.a.]: Wiley, 1995.

[71] R. E. Skelton, *Dynamic systems control: linear systems analysis and synthesis*. Wiley, 1988.

[72] J. C. Doyle, K. Glover, P. P. Khargonekar, and B. A. Francis, "State-space solutions to standard $\mathcal{H}_2$ and $\mathcal{H}_\infty$ control problems," *IEEE Transactions on Automatic Control*, vol. 34, 1989.

[73] B. F. Spencer, J. Suhardjo, and M. K. Sain, "Frequency domain optimal control strategies for aseismic protection," *Journal of Engineering Mechanics*, vol. 120, no. 1, pp. 135–158, 1994.

[74] R. E. Skelton, "Control of state and input covariances for dynamic systems," in *Decision and Control, 1988., Proceedings of the 27th IEEE Conference on*, vol. 3, pp. 1902 –1907, 1988.

[75] B. F. Spencer, T. L. Timlin, M. K. Sain, and S. J. Dyke, "Series solution of a class of nonlinear optimal regulators," *Journal of Optimization Theory and Applications*, vol. 91, pp. 321–345, Nov. 1996.

[76] B. F. Spencer and L. A. Bergman, "On the numerical solution of the fokker-planck equation for nonlinear stochastic systems," *Nonlinear Dynamics*, vol. 4, pp. 357–372, 1993.

[77] G. Kreisselmeier and K. Narendra, "Stable model reference adaptive control in the presence of bounded disturbances," *Automatic Control, IEEE Transactions on*, vol. 27, no. 6, pp. 1169 – 1175, 1982.

[78] R. E. Skelton and D. H. Owens, *Model error concepts and compensation*. Published for the International Federation of Automatic Control by Pergamon Press, 1986.

[79] S. Mukhopadhyay and K. S. Narendra, "Disturbance rejection in nonlinear systems using neural networks," *Neural Networks, IEEE Transactions on*, vol. 4, pp. 63 –72, Jan. 1993.

[80] K. S. Narendra and K. Parthasarathy, "Identification and control of dynamical systems using neural networks," *Neural Networks, IEEE Transactions on*, vol. 1, pp. 4 –27, Mar. 1990.

[81] S. Kumpati, Narendra, and O. Romeo, *Advances in Adaptive Control*. 1991.

[82] S. Suresh, S. Narasimhan, and S. Nagarajaiah, "Direct adaptive neural controller for the active control of earthquake-excited nonlinear base-isolated buildings," *Structural Control and Health Monitoring*, vol. 19, no. 3, pp. 370–384, 2012.

[83] S. Narasimhan, S. Suresh, S. Nagarajaiah, and N. Sundararajan, "On-line learning failure-tolerant neural-aided controller for earthquake excited structures," *Journal of Engineering Mechanics*, vol. 134, no. 3, pp. 258–268, 2008.

[84] V. I. Utkin, "Variable structure systems with sliding modes," *IEEE Transactions on Automatic Control*, vol. 22, no. 2, pp. 212–222, 1977.

[85] J. J. E. Slotine, "Sliding controller design for non-linear systems," *International Journal of Control*, vol. 40, no. 2, pp. 421–434, 1984.

[86] J. N. Yang, J. C. Wu, A. K. Agrawal, and S. Y. Hsu, "Sliding mode control with compensator for wind and seismic response control," *Earthquake Engineering & Structural Dynamics*, vol. 26, no. 11, pp. 1137–1156, 1997.

[87] J. N. Yang, J. Kim, and A. K. Agrawal, "Resetting semiactive stiffness damper for seismic response control," *Journal of Structural Engineering, ASCE*, vol. 126, no. 12, pp. 1427–1433, 2000.

[88] A. F. Hotz and R. E. Skelton, "Controller design for robust stability and performance," in *American Control Conference, 1986*, pp. 1813 –1817, 1986.

[89] R. E. Skelton, T. Iwasaki, and K. M. Grigoriadis, *A Unified Algebraic Approach to Linear Control Design*. CRC Press, 1998.

[90] K. M. Grigoriadis, G. Zhu, and R. E. Skelton, "Optimal redesign of linear systems," *Journal of Dynamic Systems, Measurement, and Control*, vol. 118, no. 3, p. 598, 1996.

[91] K. Nonami, H. Nishimura, and H. Tian, "$\mathcal{H}_\infty/\mu$ control-based frequency-shaped sliding mode control for flexible structures," in *Proceedings of First World Conference on Structural Control*, pp. 110–119, 1994.

[92] H. Nishimura, K. Nonami, and O. Nakada, "$\mathcal{H}_\infty$ control with pole assignment for building-like structure by using active dynamic vibration absorber," in *Proceedings of First World Conference on Structural Control*, pp. 73–82, 1994.

[93] T. T. Soong and A. M. Reinhorn, "An overview of active and hybrid structural control research in the u.s.," *The Structural Design of Tall Buildings*, vol. 2, no. 3, pp. 193–209, 1993.

[94] G. J. Lee-Glauser, G. Ahmadi, and L. G. Horta, "Integrated passive/active vibration absorber for multistory buildings," *Journal of Structural Engineering*, vol. 123, no. 4, pp. 499–504, 1997.

[95] K. Tanida, "Active control of bridge towers during erection," in *Proceedings of Third Colloquim on Vibration Control of Structures*, pp. 173–184, 1995.

[96] Y. Koike, T. Murata, K. Tanida, T. Kobori, K. Ishii, and Y. Takenaka, "Development of v-shaped hybrid mass damper and its application to high-rise buildings," in *Proceedings of First World Conference on Structural Control*, pp. 3–12, 1994.

[97] S. Yamazaki, N. Nagata, and H. Abiru, "Tuned active dampers installed in the minato mirai (mm) 21 landmark tower in yokohama," *Journal of Wind Engineering and Industrial Aerodynamics*, vol. 43, no. 13, pp. 1937 – 1948, 1992.

[98] S. Yamazaki, N. Nagata, and H. Abiru, "Full scale investigation of performance of tuned active dampers installed in landmark tower in yokohama," in *Proceedings of International Wind Engineering Conference*, pp. 1631–1642, 1995.

[99] T. Kobori, "Future direction on research and development of seismic-response-controlled structures," *Computer-Aided Civil and Infrastructure Engineering*, vol. 11, no. 5, pp. 297–304, 1996.

[100] S. Ohrui, T. Kabori, M. Sakomoto, K. Koshika, I. Nishimura, K. Sasaki, A. Kondo, and Fukushima, "Development of active-passive composite tuned mass damper and an application to a highrise building," in *Proceedings of First World Conference on Structural Control*, pp. 100–109, 1994.

[101] H. Iemura and K. Izuno, "Development of the self-oscillating TMD and shaking table tests," in *Proceedings of First World Conference on Structural Control*, pp. 42–51, 1994.

[102] S. Otsuka, I. Shimoda, N. Kawai, K. Inaba, I. Kurimoto, K. Yasui, and M. Mochimaru, "Development and verification of activepassive mass damper," in *Proceedings of First World Conference on Structural Control*, pp. 72–79, 1994.

[103] W. Cheng, W. Qu, and A. Li, "Hybrid vibration control of nanjing TV tower under wind excitation," in *Proceedings of First World Conference on Structural Control*, pp. 32–41, 1994.

[104] E. Y. Cheng and P. Tian, "Generalized optimal active and hybrid control for seismic structures," in *Proceedings of First World Conference on Structural Control*, pp. 21–30, 1994.

[105] A. M. Reinhorn, T. T. Soong, and C. V. Wen, "Base-isolated structures with active control," in *Proceedings of ASME Pressure Vessels and Piping Conference*, pp. 413–420, 1987.

[106] W. E. Schmitendorf, F. Jabbari, and J. N. Yang, "Robust control techniques for buildings under earthquake excitation," *Earthquake Engineering & Structural Dynamics*, vol. 23, no. 5, pp. 539–552, 1994.

[107] J. M. Kelly, G. Leitmann, and A. G. Soldatos, "Robust control of base-isolated structures under earthquake excitation," *Journal of Optimization Theory and Applications*, vol. 53, pp. 159–180, 1987.

[108] K. Yoshida and T. Watanabe, "Robust control of structural vibrations using active dynamic vibration absorber systems," in *Proceedings of First World Conference on Structural Control*, pp. 53–62, 1994.

[109] A. M. Reinhorn and M. A. Riley, "Control of bridge vibrations with hybrid devices," in *Proceedings of First World Conference on Structural Control*, pp. 50–59, 1994.

[110] Q. Feng, M. Shinozuka, and S. Fujii, "Friction-controllable sliding isolated systems," *Journal of Engineering Mechanics*, vol. 119, no. 9, pp. 1845–1864, 1993.

[111] J. N. Yang, J. C. Wu, A. M. Reinhorn, M. A. Riley, W. E. Schmitendorf, and E. Jabbari, "Experimental verifications of $\mathcal{H}_\infty$ and sliding mode control for seismic-excited buildings," in *Proceedings of First World Conference on Structural Control*, pp. 63–72, 1994.

[112] S. Nagarajaiah and A. M. Reinhorn, "Applicability of pseudo-force method to highly nonlinear dynamic problems," in *Proceedings of Structures Congress*, pp. 165–172, ASCE, 1994.

[113] J. Rodellar, A. H. Barbat, and N. Molinares, "Response analysis of buildings with a new nonlinear base isolation system," in *Proceedings of First World Conference on Structural Control*, pp. 31–40, 1994.

[114] S. Nagarajaiah, "Adaptive passive, semiactive, smart tuned mass dampers: identification and control using empirical mode decomposition, hilbert transform, and short-term fourier transform," *Structural Control and Health Monitoring*, vol. 16, no. 7-8, pp. 800–841, 2009.

[115] B. F. Spencer and M. K. Sain, "Controlling buildings: a new frontier in feedback," *Control Systems, IEEE*, vol. 17, pp. 19 –35, Dec. 1997.

[116] S. Nagarajaiah and D. Mate, "Semi-active control of continuously variable stiffness system," in *Proceeding of Second World Conference on Structural Control*, vol. 1, pp. 397–406, July 1998.

[117] S. Nagarajaiah and S. Sahasrabudhe, "Seismic response control of smart sliding isolated buildings using variable stiffness systems: experimental and numerical study," *Earthquake Engineering & Structural Dynamics*, vol. 35, no. 2, pp. 177–197, 2006.

[118] M. Q. Feng and M. Shinozuka, "Use of a variable damper for hybrid control of bridge response under earthquake," in *Proceedings of U.S. National Workshop on Structural Control Research*, USC Publication, 1990.

[119] M. Shinozuka, M. C. Constantinou, and R. Ghanem, "Passive and active fluid dampers in structural applications," in *Proceedings of U.S./China/Japan Workshop on Structural Control*, pp. 507–516, 1992.

[120] R. L. Sack and W. Patten, "Semiactive hydraulic structural control," in *Proceedings of International Workshop on Structural Control*, pp. 417–431, 1993.

[121] D. Hrovat, P. Barak, and M. Rabins, "Semi-active versus passive or active tuned mass dampers for structural control," *Journal of Engineering Mechanics*, vol. 109, no. 3, p. 691, 1983.

[122] W. N. Patten, Q. He, C. C. Kuo, L. Liu, and R. L. Sack, "Seismic structural control via hydraulic semi-active vibration dampers," in *Proceedings of First World Conference on Structural Control*, pp. 83–89, 1994.

[123] Z. Akbay and H. M. Aktan, "Actively regulated friction slip devices," in *Proceedings of Sixth Canadian Conference on Earthquake Engineering*, pp. 367–374, 1991.

[124] S. Kannan, H. M. Uras, and H. M. Aktan, "Active control of building seismic response by energy dissipation," *Earthquake Engineering & Structural Dynamics*, vol. 24, no. 5, pp. 747–759, 1995.

[125] D. J. Dowdell and S. Cherry, "Structural control using semiactive friction dampers," in *Proceedings, First World Conference on Structural Control*, pp. 59–68, 1994.

[126] S. Cherry, "Research on friction damping at the university of british columbia," in *Proceedings, Internatinal Workshop on Structural Control*, pp. 84–91, 1994.

[127] J. Y. K. Lou, L. D. Lutes, and J. J. Li, "Active tuned liquid damper for structural control," in *Proceedings, First World Conference on Structural Control*, pp. 70–78, 1994.

[128] M. A. Haroun, J. A. Pires, and A. Won, "Active orifice control in hybrid liquid column dampers," in *Proceedings, First World Conference on Structural Control*, pp. 69–78, 1994.

[129] S. Nagarajaiah and N. Varadarajan, "Short time fourier transform algorithm for wind response control of buildings with variable stiffness TMD," *Engineering Structures*, vol. 27, no. 3, pp. 431–441, 2005.

[130] S. Nagarajaiah and E. Sonmez, "Structures with semiactive variable stiffness single/multiple tuned mass dampers," *Journal of Structural Engineering*, vol. 133, no. 1, pp. 67–77, 2007.

[131] N. Varadarajan and S. Nagarajaiah, "Wind response control of building with variable stiffness tuned mass damper using empirical mode decomposition/hilbert transform," *Journal of Engineering Mechanics*, vol. 130, no. 4, pp. 451–458, 2004.

[132] R. C. Ehrgott and S. F. Masri, "Experimental characterization of an electrorheological material subjected to oscillatory shear strains," *Journal of Vibration and Acoustics*, vol. 116, no. 1, pp. 53–60, 1994.

[133] H. P. Gavin, Y. D. Hose, and R. D. Hanson, "Design and control of electrorheological dampers," in *Proceedings, First World Conference on Structural Control*, pp. 83–92, 1994.

[134] G. Leitmann and E. Reithmeier, "Semiactive control of a vibrating system by means of electrorheological fluids," *Dynamics and Control*, vol. 3, pp. 7–33, 1993.

[135] F. Gordaninejad, A. Rau, and R. Bindu, "Vibration control of structures using hybrid electrorheological-viscous fluid dampers," in *Proceedings, First World Conference on Structural Control*, pp. 41–49, 1994.

[136] S. F. Masri, S. Chavakula, and T. K. Caughey, "Control of intelligent nonlinear adaptive systems under earthquake excitation," *Journal of Structural Control*, vol. 1, no. 1-2, pp. 23–38, 1994.

[137] J. D. Carlson and B. F. Spencer, "Magneto-rheological fluid dampers for semi-active seismic control," in *Proceedings, Third International Conference on Motion and Vibration Control*, vol. III, pp. 35–40, 1996.

[138] B. F. Spencer, S. J. Dyke, M. K. Sain, and J. D. Carlson, "Phenomenological model for magnetorheological dampers," *Journal of Engineering Mechanics*, vol. 123, no. 3, pp. 230–238, 1997.

[139] S. J. Dyke, B. F. Spencer, M. K. Sain, and J. D. Carlson, "Seismic response reduction using magnetorheological dampers," in *Proceedings, International Federation of Automatic Control, World Congress*, vol. 50, pp. 145–150, 1996.

[140] S. J. Dyke, B. F. Spencer, M. K. Sain, and J. D. Carlson, "Experimental verification of semi-active structural control strategies using acceleration feedback," in *Proceedings, Third International Conference on Motion and Vibration Control*, vol. III, pp. 291–296, 1996.

[141] S. J. Dyke, B. F. Spencer, M. K. Sain, and J. D. Carlson, "Modeling and control of magnetorheological dampers for seismic response reduction," *Smart Materials and Structures*, vol. 5, no. 5, p. 565, 1996.

[142] A. M. Reinhorn, S. Viti, and A. S. Whittaker, "Retrofit of structures: Strength reduction with damping enhancement," in *Proceedings, KEERC-MCEER Joint Seminar on Contributions to Earthquake Engineering, Multi-disciplinary Center for Earthquake Engineering Research*, 2002.

[143] S. Viti, G. P. Cimellaro, and A. M. Reinhorn, "Retrofit of a hospital through strength reduction and enhanced damping," *Smart Structures and Systems*, vol. 2, no. 4, pp. 339–355, 2006.

[144] G. P. Cimellaro, O. Lavan, and A. M. Reinhorn, "Design of passive systems for control of inelastic structures," *Earthquake Engineering & Structural Dynamics*, vol. 38, no. 6, pp. 783–804, 2009.

[145] H. Iemura and M. H. Pradono, "Advances in the development of pseudo-negative-stiffness dampers for seismic response control," *Structural Control and Health Monitoring*, vol. 16, no. 7-8, pp. 784–799, 2009.

[146] D. T. R. Pasala, A. A. Sarlis, S. Nagarajaiah, A. M. Reinhorn, M. C. Constantinou, and D. Taylor, "Adaptive negative stiffness: A new structural modification approach for seismic protection," *Journal of Structural Engineering, ASCE, DOI:10.1061/(ASCE)ST.1943-541X.0000615*, April, 2012.

[147] A. Reinhorn, O. Lavan, and G. Cimellaro, "Design of controlled elastic and inelastic structures," *Earthquake Engineering and Engineering Vibration*, vol. 8, pp. 469–479, 2009.

[148] A. M. Reinhorn, S. Viti, and G. P. Cimellaro, "Retrofit of structures: Strength reduction with damping enhancement," in *Proceedings of the 37th UJNR panel meeting on wind and seismic effects*, pp. 16–21, 2005.

[149] N. Gluck, A. M. Reinhorn, J. Gluck, and R. Levy, "Design of supplemental dampers for control of structures," *Journal of Structural Engineering, ASCE*, vol. 122, no. 12, pp. 1394–1399, 1996.

[150] A. A. Sarlis, *Adaptive seismic protection of systems*. PhD thesis, University at Buffalo, SUNY, Buffalo, New York, July 2012.

[151] A. A. Sarlis, D. T. R. Pasala, M. C. Constantinou, A. M. Reinhorn, S. Nagarajaiah, and D. P. Taylor, "Negative stiffness device for seismic protection of structures," *Journal of Structural Engineering, ASCE, DOI:10.1061/(ASCE)ST.1943-541X.0000616*, April, 2012.

[152] M. V. Sivaselvan and A. M. Reinhorn, "Hysteretic models for deteriorating inelastic structures," *Journal of Engineering Mechanics*, vol. 126, no. 6, pp. 633–640, 2000.

[153] Y. Ohtori, R. E. Christenson, B. F. Spencer, and S. J. Dyke, "Benchmark control problems for seismically excited nonlinear buildings," *Journal of Engineering Mechanics*, vol. 130, no. 4, pp. 366–385, 2004.

[154] N. Makris and C. J. Black, "Dimensional analysis of bilinear oscillators under pulse-type excitations," *Journal of Engineering Mechanics*, vol. 130, no. 9, pp. 1019–1031, 2004.

[155] N. Makris and C. J. Black, "Dimensional analysis of rigid-plastic and elastoplastic structures under pulse-type excitations," *Journal of Engineering Mechanics*, vol. 130, no. 9, pp. 1006–1018, 2004.

[156] W. Molyneaux, "Supports for vibration isolation," Technical Report ARC/CP-322, Aeronautical Research Council, Great Britain, 1957.

[157] D. L. Platus, "Negative-stiffness-mechanism vibration isolation systems," in *Proceedings of SPIE*, (San Jose, CA, USA), pp. 44–54, 1992.

[158] D. L. Platus, "Vibration isolation system," 2004. U.S. Classification: 248/603; International Classification: : F16F/1300.

[159] D. K. Kusumastuti, A. M. Reinhorn, and A. Rutenberg, "A versatile experimentation model for study of structures near collapse applied to seismic evaluation of irregular structures," tech. rep., University at Buffalo, SUNY, 2005.

[160] D. T. R. Pasala, A. A. Sarlis, A. M. Reinhorn, S. Nagarajaiah, M. C. Constantinou, and D. P. Taylor, "Simulated bilinear-elastic behavior in a SDOF elastic structure using negative stiffness device: Experimental and analytical study," *Journal of Structural Engineering, ASCE (under review)*, 2012.

[161] D. T. R. Pasala, A. A. Sarlis, A. M. Reinhorn, S. Nagarajaiah, M. C. Constantinou, and D. P. Taylor, "Apparent-weakening in SDOF yielding structure using negative stiffness device: Experimental and analytical study," *Earthquake Engineering and Structural Dynamics (under review)*, 2012.

[162] D. T. R. Pasala, A. A. Sarlis, S. Nagarajaiah, A. M. Reinhorn, M. C. Constantinou, and D. P. Taylor, "Negative stiffness device for seismic response control of multi-story buildings: Experimental study," *Earthquake Engineering and Structural Dynamics (under review)*, 2012.

[163] D. T. R. Pasala, A. A. Sarlis, S. Nagarajaiah, A. M. Reinhorn, M. C. Constantinou, and D. P. Taylor, "Negative stiffness device for seismic response control of multi-story buildings: Distributed isolation," *Earthquake Engineering and Structural Dynamics (under review)*, 2012.

[164] MATLAB, *version 7.10.0 (R2010a)*. Natick, Massachusetts: The MathWorks Inc., 2010.

[165] J. Ormondroyd and J. P. DenHartog, "The theory of the dynamic vibration absorber," *Transactions of ASME*, vol. APM-50, no. 7, pp. 9–22, 1938.

[166] S. Nagarajaiah and D. T. R. Pasala, "NEESR-adapt-struct: Semi-active control of ASD device adaptive length pendulum dampers," in *Proceedings of the* 19^{th} *Analysis and computation speciality conference, ASCE*, vol. CDROM, 2010.

[167] S. Nagarajaiah, D. T. R. Pasala, and C. Huang, "Smart TMD: Adaptive length pendulum dampers," in *Proceedings of the* 5^{th} *world conference on structural control and health monitoring*, vol. CDROM, (Tokyo, Japan), 2010.

[168] M. Abe and Y. Fujino, "Dynamic characterization of multiple tuned mass dampers and some design formulas," *Earthquake Engineering & Structural Dynamics*, vol. 23, no. 8, pp. 813–835, 1994.

[169] R. S. Jangid, "Optimum multiple tuned mass dampers for base-excited undamped system," *Earthquake Engineering & Structural Dynamics*, vol. 28, no. 9, pp. 1041–1049, 1999.

[170] J. C. H. Chang and T. T. Soong, "Structural control using active tuned mass dampers," *Journal of the Engineering Mechanics Division*, vol. 106, no. 6, pp. 1091–1098, 1980.

[171] Y. Ikeda, K. Sasaki, M. Sakamoto, and T. Kobori, "Active mass driver system as the first application of active structural control," *Earthquake Engineering & Structural Dynamics*, vol. 30, no. 11, pp. 1575–1595, 2001.

[172] S. K. Yalla, A. Kareem, and J. C. Kantor, "Semi-active tuned liquid column dampers for vibration control of structures," *Engineering Structures*, vol. 23, no. 11, pp. 1469–1479, 2001.

[173] M. Contreras, D. T. R. Pasala, and S. Nagarajaiah, "Adaptive length SMA pendulum smart tuned mass damper performance in the presence of real time primary system stiffness change," *Smart structres and systems (under review)*, 2012.

[174] L. Cohen, *Time-frequency analysis*. New Jersey: Prentice-Hall, 1^{st} edition ed., 1995.

[175] S. Nagarajaiah, N. Vardarajan, and S. Sahasrabudhe, "Variable stiffness and instantaneous frequency," in *Proceedings of Structures Congress, ASCE*, vol. 1, pp. 858–861, 1999.

[176] S. Narasimhan and S. Nagarajaiah, "Stft algorithm for semiactive control of base isolated buildings with variable stiffness isolation systems subjected to near fault earthquakes," *Engineering Structures*, vol. 27, no. 4, pp. 514–523, 2005.

[177] C. S. Mehendale and K. M. Grigoriadis, "Hysteresis compensation using LPV gain-scheduling," in *Proceedings of American Control Conference*, vol. 2, pp. 1380–1385, 2004.

[178] S. A. C. J. P. Salapaka, "S." and M. V. Salapaka, "High bandwidth nano-positioner: A robust control approach," *Review of scientific instruments*, vol. 73, pp. 3232–3241, 2002.

[179] X. Tan and J. S. Baras, "Adaptive identification and control of hysteresis in smart materials," Technical Report CDCSS TR 2003-3 (ISR TR 2003-40), University of Maryland, 2003.

[180] G. Song, J. Zhao, X. Zhou, and J. Garcia, "Tracking control of a piezoceramic actuator with hysteresis compensation using inverse preisach model," *IEEE Transactions on mechatronics*, vol. 10, no. 2, pp. 198–209, 2005.

[181] H. Oloomi and B. Shafai, "Weight selection in mixed sensitivity robust control

for improving the sinusoidal tracking performance," in *Proceedings 42nd IEEE conference on decision and control*, pp. 300–305, 2003.

[182] C. S. Mehendale, I. J. Fialho, and K. M. Grigoriadis, "Adaptive active microgravity isolation using LPV gain-scheduling methods," in *Proceedings of American Control Conference*, pp. 300–305, 2003.

[183] D. T. R. Pasala, S. Nagarajaiah, and K. M. Grigoriadis, "Gain scheduled control of hysteretic systems," in *Proceedings of SPIE, Smart Structure/NDE*, 2009.

[184] R. Venkataraman and P. S. Krishnaprasad, "Approximate inversion of hysteresis: Theory and numerical results," in *Proceedings of IEEE Conference on Decision and Control*, vol. 5, pp. 4448–4454, 2000.

[185] X. Tan, R. Venkataraman, and P. S. Krishnaprasad, "Control of hysteresis: Theory and experimental results," in *Proceedings of SPIE - The International Society for Optical Engineering*, pp. 101–112, 2001.

[186] R. C. Smith, "Inverse compensation for hysteresis in magnetostrictive transducers," *Mathematical and Computer Modelling*, vol. 33, pp. 285–298, 2001.

[187] A. Taware and G. Tao, *Control of sandwich nonlinear systems*. Springer-verlag, Heidelberg, 2001.

[188] W. S. Galinaitis and R. C. Rogers, "Control of a hysteretic actuator using inverse hysteresis compensation," in *Proceedings of SPIE - The International Society for Optical Engineering*, vol. 3323, pp. 267–277, 1998.

[189] C. S. Mehendale, *Advanced gain-scheduling for nonlinear control design using linear parameter varying systems theory*. PhD thesis, University of Houston,

Houston, 2005.

[190] P. Krejci and K. Kuhnen, "Inverse control of systems with hysteresis and creep," in *IEEE Proceedings of Control Theory and Applications*, vol. 148, pp. 185–192, 2001.

[191] F. Zhang, K. M. Grigoriadis, and I. J. Fialho, "Linear parameter-varying control for active vibration isolation systems with stiffness hysteresis," *Journal of vibration and control*, vol. 15, pp. 527–547, 2009.

[192] D. T. R. Pasala, "Repetitive control of hysteretic systems using robust h-infinity controller," 2009.

[193] D. T. R. Pasala, S. Nagarajaiah, and K. M. Grigoriadis, "Response control of saivs system using lpv gain-scheduling controller," in *Proceedings of Earth and Space conference (CD-ROM)*, 2008.

[194] W. J. Rugh and J. S. Shamma, "Research on gain scheduling," *Automatica*, vol. 36, pp. 1401–1425, 2000.

[195] G. S. Becker, *Quadratic stability and performance of linear parameter dependent systems*. PhD thesis, University of California, Berkley, 1993.

[196] F. Wu, X. H. Yang, A. Packard, and G. Becker, "Induced $\mathcal{L}_2$-norm control for lpv system with bounded parameter variation rates," in *Proceedings of American Control Conference*, vol. 3, pp. 2379–2383, 1995.

[197] P. Apkarian and R. J. Adams, "Advanced gain-scheduling techniques for uncertain systems," *IEEE Transactions in Automatic Journal*, vol. 6, pp. 21–32, 1998.

[198] Y. Bai, *Advanced controls of large scale structural systems using linear matrix inequaty methods*. PhD thesis, University of Houston, Houston, 2006.

[199] D. Mate, "Experimental and analytical study of semiactive variable stiffness control system," Master's thesis, University of Missouri, Columbia, 1998.

[200] Y. K. Wen, "Method for random vibration of hysteretic systems," *ASCE: Journal of Engineering Mechanics*, vol. 102, pp. 249–263, 1976.

[201] R. Bouc, "Forced vibration of mechanical systems with hysteresis," in *Proceedings of* 4^{th} *Conference on nonlinear oscillations*, vol. 3, pp. 2379–2383, 1967.

[202] D. T. R. Pasala, S. Nagarajaiah, and K. M. Grigoriadis, "Tracking control of variable stiffness hysteretic-systems using linear-parameter-varying gain-scheduled controller," *Smart Structures and Systems*, vol. 9, no. 4, 2012.

[203] F. Wu, *Control of linear parameter varying systems*. PhD thesis, University of California, Berkley, 1995.

[204] F. Wu, X. H. Yang, A. Packard, and G. Becker, "Induced $\mathcal{L}_2$-norm control for lpv systems with bounded parameter variation rates," *International journal of nonlinear and robust control*, 1997.

[205] D. J. C.", K. Glover, P. P. Khargonekar, and B. A. Francis, "State-space solutions to standard $\mathcal{H}_2$ and $\mathcal{H}_\infty$ control problems," *IEEE Transactions in Automatic Control*, vol. 34, pp. 831–847, 1989.

[206] P. Apkarian and P. Gahinet, "A convex characterization of gain-scheduled $\mathcal{H}_\infty$ controllers," *IEEE Transactions in Automatica Journal*, vol. 40, pp. 853–864, 1995.

[207] S. Skogestad and I. Postlethwaite, *Multivariable feedback control: Analysis and design*. John Wiley & Sons, New York, 1996.

[208] P. Apkarian, A. Nemirovski, A. Laub, and M. Chilali, *LMI Control Toolbox User's Guide*. The MathWorks Inc.: Natick, 1995.